KATHOLIEKE UNIVERSITEIT LEUVEN
FACULTEIT INGENIEURSWETENSCHAPPEN
DEPARTEMENT ELEKTROTECHNIEK (ESAT)
AFDELING PSI
Kasteelpark Arenberg 10, B-3001 Leuven-Heverlee (Belgium)

KATHOLIEKE UNIVERSITEIT LEUVEN
FACULTEIT GENEESKUNDE
DEPT. MEDISCH DIAGNOSTISCHE WETENSCHAPPEN
AFDELING NUCLEAIRE GENEESKUNDE
Herestraat 49, B-3000 Leuven (Belgium)

HIGH QUALITY IMAGE FORMATION OF SMALL ANIMALS USING EMISSION TOMOGRAPHY

Promotoren:
Prof. dr. ir. J. NUYTS
Prof. dr. ir. P. SUETENS

Proefschrift voorgedragen tot
het behalen van het doctoraat
in de ingenieurswetenschappen

door

Kathleen VUNCKX

Oktober 2008

KATHOLIEKE UNIVERSITEIT LEUVEN
FACULTEIT INGENIEURSWETENSCHAPPEN
DEPARTEMENT ELEKTROTECHNIEK (ESAT)
AFDELING PSI
Kasteelpark Arenberg 10, B-3001 Leuven-Heverlee (Belgium)

KATHOLIEKE UNIVERSITEIT LEUVEN
FACULTEIT GENEESKUNDE
DEPT. MEDISCH DIAGNOSTISCHE WETENSCHAPPEN
AFDELING NUCLEAIRE GENEESKUNDE
Herestraat 49, B-3000 Leuven (Belgium)

HIGH QUALITY IMAGE FORMATION OF SMALL ANIMALS USING EMISSION TOMOGRAPHY

Examencommissie:

Prof. dr. ir. P. Van Houtte, voorzitter
Prof. dr. ir. J. Nuyts, promotor
Prof. dr. ir. P. Suetens, promotor
Prof. dr. ir. F. Maes, assessor
Prof. dr. sc. P. Dupont, assessor
Prof. dr. ir. D. Vandermeulen
Prof. dr. sc. M. Defrise (Vrije Universiteit Brussel)

Proefschrift voorgedragen tot
het behalen van het doctoraat
in de ingenieurswetenschappen

door

Kathleen VUNCKX

U.D.C. 681.3∗I4

Oktober 2008

D/2008/7515/95
ISBN 978-90-5682-985-8

Voorwoord

Het begon allemaal tijdens de blokperiode van mijn laatste examenreeks aan de universiteit. Er viel een mailtje in de bus over een doctoraatsproject op nucleaire geneeskunde dat mij meteen enthousiast maakte. Na een eerste gesprek met mijn toekomstige promotor en collega's was ik verkocht. Het begin van vier rijk gevulde en leerrijke jaren! Ik was uiteraard nooit tot de eindmeet van dit doctoraat geraakt zonder de steun van vele mensen. Daarom hier een woordje van dank.

Vooreerst wil ik mijn promotoren *Prof. Johan Nuyts* en *Prof. Paul Suetens* bedanken om mij de kans te geven in de boeiende wereld van de medische beeldvorming te werken. Voor de dagelijkse begeleiding kon ik mij geen betere promotor inbeelden dan Johan. Zijn deur staat altijd open, je kan met vragen of problemen steeds bij hem terecht. Ook wanneer je denkt alle pistes uitgeprobeerd te hebben, blijft hij met oplossingen aankomen. Ik kijk daarom al uit naar onze verdere samenwerking.

Graag wil ik ook een woord van dank uitbrengen aan mijn assessoren *Prof. Patrick Dupont* en *Prof. Frederik Maes* die met interesse mijn werk gevolgd hebben. Tijdens mijn seminaries in het Louvre en na het lezen van mijn manuscript gaven ze mij tal van interessante bemerkingen. Bij Patrick kon ik ook altijd terecht voor een interessante discussie, die vaak uitmondde in een gezellige babbel over de meest uiteenlopende, al dan niet onderzoeksgerelateerde onderwerpen.

Prof. Michel Defrise en *Prof. Dirk Vandermeulen*, bedankt om in jullie drukke agenda tijd vrij te maken om te fungeren als lid van mijn jury. Jullie vele nuttige tips waren bijzonder welkom. Michel wil ik ook extra bedanken voor de interessante gesprekken tijdens het jaarlijkse IEEE NSS-MIC congres en de gezamenlijke projectvergaderingen. Uit onze samenwerkingen stak ik veel op.

Voorts wil ik *alle leden van de examencommissie* bedanken om niet op te zien tegen het kritisch nalezen van dit lijvige werk, dat als het ware meegroeide met mijn zwangere buikje. Bedankt ook *Prof. Paul Van Houtte* om als voorzitter de doctoraatsverdediging in goede banen te leiden.

Ook mijn collega's van de dienst nucleaire geneeskunde wil ik graag bedanken. Mijn diensthoofd, *Prof. Luc Mortelmans*, heeft ervoor gezorgd dat alle faciliteiten voorhanden waren om aan mijn doctoraat te kunnen werken. Voor het plannen van de talrijke experimenten op klinische camera's, kon ik steeds terecht bij de hoofdtechnologen, *Ludo Verhaegen* en *Carla Marteaux*. Ook *Peter Vermaelen*, *Stijn Dirix*, *Bert Vanbilloen*, *Dominique Vanderghinste*, *Christelle Terwinghe* en *Tjibbe*

de Groot zorgden mee voor het in goede banen leiden van de experimenten. Voor de installatie van de pinhole-collimatoren op een klinische camera konden we rekenen op *Ronnie (Ronald) Lubon* van *Siemens Medical Solutions*.

Van mijn collega-doctorandi verdienen velen een extra bedankje. Zo zorgde *Dirk Bequé* voor een vliegende start van mijn doctoraat. *Kristof Baete* stond altijd klaar met goede raad en zorgde voor geanimeerde discussies tijdens de lunch. *Cindy Casteels* en ik startten samen een doctoraat op de dienst, waardoor we vaak bij elkaar te rade konden omtrent het verloop ervan. Bij *Lily Plessers* kon ik steeds terecht voor een oppeppende babbel als ik in een dipje zat. *Catherine Lemmens*, die de voorbije drie jaar letterlijk aan mijn zijde zat, was uitgelezen persoon om over de technische en minder technische problemen van gedachte te wisselen. Bedankt voor de steun en het luisterend oor. I thank *Lin Zhou* for the many interesting discussions and owe her and *Ameya Atre* many thanks for helping me out with submitting my manuscript. *Humphrey Fonge*, *Marijke De Saint-Hubert* and *Kristof Prinsen* enriched my research experience by involving me in their preclinical experiments.

Verder wil ik *Stefaan Vleugels*, *Dominique Delaere*, *Bart De Dobbelaer* en *Francine Reniers* bedanken voor de technische en administratieve ondersteuning. Natuurlijk ook een welgemeend dank-je-wel aan de andere *collega's van nucleaire geneeskunde, radiofarmacie en MoSAIC* voor de goede samenwerking en leuke gesprekken.

De voorbije jaren legde ik vele nieuwe contacten. Zo waren de projecten met *de onderzoeksgroepen van de V.U. Brussel en de Universiteit Gent* zeer leerrijk. Many thanks also to *Samuel Matej* for drawing our attention to interesting questions concerning TOF PET and for the nice collaboration. *Pieter-Jan van Mullekom* en *Jurgen Willems* (*Nuclear Fields International B.V.*), *Tom Van Hemel* (*H. C. Starck*), en *Dirk Bastiaensen* en *Jan Peirs* (*departement Werktuigkunde, K.U. Leuven*) zorgen voor het vervaardigen van de pinhole-collimatoren en -platen.

Voor hun financiële steun aan dit werk dank ik het Fonds Wetenschappelijk Onderzoek - Vlaanderen (G.0174.03 en G.0569.08).

Naast het harde werken, was er ook nood aan ontspanning. Bedankt aan iedereen die - vooral tijdens het voorbije half jaar - ervoor gezorgd heeft dat ik af en toe eens van achter mijn bureau vandaan kwam. Nogmaals sorry voor de schromelijke verwaarlozing. Ik probeer het binnenkort weer goed te maken ;-)

Ook een dikke merci aan *mijn ouders* om er ondanks hun eigen drukke bestaan steeds voor te zorgen dat ik in de beste omstandigheden kon opgroeien en mij volledig kon ontplooien. Bedankt *Pieter* om je kleine zus zo op handen te dragen, je bent een grote steun. De voorbije 9 jaar hebben ook *mijn schoonouders en schoonzus Greet* mij van harte in hun familie opgenomen. Bedankt voor de vele aanmoedigingen en de luilekkerweekendjes in het verre West-Vlaanderen.

Tot slot heb ik goed nieuws voor mijn man *Lieven* en ons eerste kindje dat groeit in mijn buik. De tekst is af, het doctoraat is binnen! Nu komen jullie weer op de eerste plaats, waar jullie thuishoren. Lieven, bedankt voor het vele geduld dat je de voorbije jaren hebt moeten opbrengen en voor de steun bij de laatste loodjes.

Kathleen

Abstracts

High quality image formation of small animals using emission tomography

The past decade, both SPECT and PET have extensively been studied to improve the quality of functional imaging in small laboratory animals. In this work, we focused on small animal SPECT, which has many applications and the potential to outperform the spatial resolution of the micro-PET. The reconstruction software was improved by more accurately modeling the imaging process, yielding superior images. In addition, an efficient image quality evaluation method was developed, and validated for single and multipinhole SPECT. Using this technique, the influence of many pinhole collimator design parameters, including the amount of overlap in multipinhole projections, on the reconstruction image quality was investigated. Based on these results, a multipinhole design was optimized for mouse imaging, manufactured, and tested on a clinical gamma camera equipped with two pinhole collimators. The same method was also applied to study the properties of time-of-flight PET. Finally, an overview of our most important pinhole SPECT applications is provided, illustrating the image quality evolution.

Hoge kwaliteitsbeeldvorming van kleine dieren door middel van emissietomografie

De voorbije tien jaar zijn zowel SPECT als PET uitgebreid bestudeerd ter verbetering van de kwaliteit van functionele beeldvorming in kleine proefdieren. In dit werk hebben we ons toegespitst op SPECT van kleine dieren, wat veel toepassingsmogelijkheden heeft en de ruimtelijke resolutie van de micro-PET kan overtroeven. Het reconstructieprogramma werd verbeterd door het nauwkeuriger modelleren van het beeldvormingsproces, wat superieure beelden oplevert. Bovendien werd een efficiënte methode ontwikkeld voor beeldkwaliteitsevaluatie, die gevalideerd werd voor enkel- en meervoudige pinhole SPECT. Hiermee werd de invloed van vele ontwerpparameters voor pinhole-collimatoren op de reconstructiebeeldkwaliteit onderzocht, de hoeveelheid overlap in multipinhole SPECT projecties incluis. Op basis van die resultaten werd een multipinhole-ontwerp voor muisbeeldvorming geoptimaliseerd, vervaardigd, en getest op een klinische gammacamera uitgerust met twee pinhole-collimatoren. Dezelfde methode werd ook toegepast om de eigenschappen van time-of-flight PET te bestuderen. Tot slot werd een overzicht van onze belangrijkste pinhole SPECT toepassingen gegeven ter illustratie van de beeldkwaliteitsevolutie.

Hoge kwaliteitsbeeldvorming van kleine dieren door middel van emissietomografie

Inleiding

De nucleaire geneeskunde spitst zich toe op functionele beeldvorming, waarbij specifieke stofwisselingsprocessen gevisualiseerd worden. Hiertoe wordt een kleine dosis radioactief gemerkte moleculen als speurstof geïnjecteerd bij de patiënt. Deze krijgen eventueel de tijd om deel te nemen aan de processen in het lichaam, waarna de patiënt in een scanner geplaatst wordt. Door het radioactief verval worden, afhankelijk van het gebruikte isotoop, voortdurend fotonen of positronen uitgezonden, wat waargenomen kan worden met een gamma- of PET camera, respectievelijk. Deze gegevens worden meestal opgeslagen als een reeks van 2-dimensionale (2D) beelden, ook projectiebeelden genoemd. Voor sommige onderzoeken volstaan enkele van deze projectiebeelden voor het stellen van een diagnose. Voor andere dient men voldoende informatie te vergaren uit verscheidene hoeken om een 3D beeld van de moleculeverdeling in het lichaam van de patiënt te kunnen reconstrueren met behulp van wiskundige technieken. Bij 3D beeldvorming met isotopen die enkelvoudige fotonen uitzenden (SPECT) worden daarvoor één of meerdere vlakke detectoren rond de patiënt bewogen. Een PET camera voor de beeldvorming van positron-uitzendende isotopen bestaat meestal uit een ring van detectoren, omdat een positron bij de annihilatie met een elektron twee fotonen uitzendt in tegengestelde richtingen, die tegelijkertijd waargenomen moeten worden.

Voor de ontwikkeling van nieuwe radioactieve speurstoffen en voor het zoeken naar nieuwe therapieën voor o.a. neurodegeneratieve aandoeningen, hart- en vaatziekten, en kankers, is het nuttig SPECT en PET beeldvorming te doen bij kleine proefdieren. De ruimtelijke resolutie die verkregen wordt met klinische camera's is voor de meeste toepassingen voor kleine dieren echter ontoereikend. Bij SPECT beeldvorming wordt hiervoor meestal gebruikgemaakt van pinhole-collimatoren in plaats van de gebruikelijke collimatoren met parallelle gaten. Hierdoor wordt het projectiebeeld uitvergroot op de detector, zodat beelden met een hogere resolu-

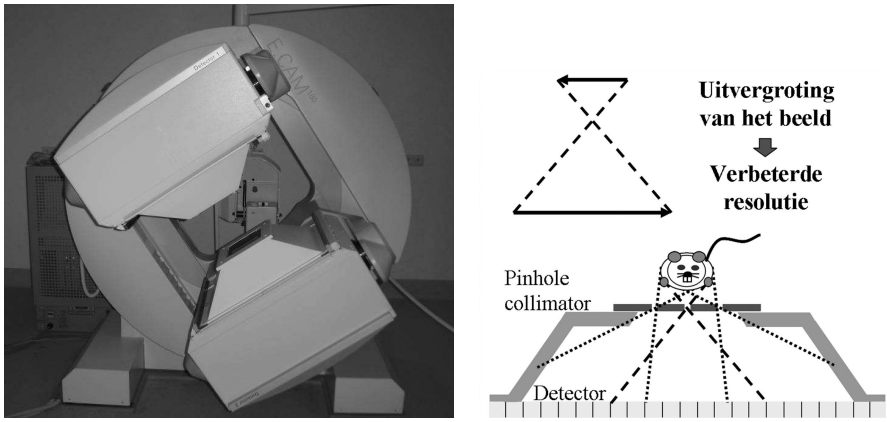

(a) Pinhole SPECT camera (b) Principe van pinhole-collimatie

Figuur 1: (a) Foto van onze pinhole SPECT camera, gebaseerd op een klinische camera en geïnspireerd op het systeem ontwikkeld door Schramm *et al.* [97]. (b) Illustratie van het pinhole-collimatieprincipe.

tie gereconstrueerd kunnen worden, weliswaar voor een kleiner gezichtsveld. Een voorbeeld van een dergelijke pinhole SPECT camera is getoond in Fig. 1(a). Het principe wordt verduidelijkt in Fig. 1(b). Een PET camera voor het scannen van proefdieren, een micro-PET camera, is meestal "simpelweg" een herschaalde versie van de klinische scanner.

Het doel van dit werk was een zo hoog mogelijke beeldkwaliteit te verkrijgen met een SPECT camera voor kleine proefdieren. Daarvoor werd zowel nieuwe software als hardware ontworpen. Al lag de focus vooral op pinhole SPECT op basis van een klinische camera, toch zijn de meeste voorgestelde technieken veel algemener toepasbaar. De bestaande software voor pinhole SPECT reconstructie werd uitgebreid en getest voor multipinhole SPECT met meerdere detectoren. Voorts werd de systeem- en gegevensmodellering op verscheidene vlakken uitgebreid en verbeterd. Op het gebied van hardware, werd enkel de pinhole-collimator geoptimaliseerd. Om verscheidene collimatoren snel met elkaar te kunnen vergelijken, werd een nieuw algoritme ontwikkeld om de beeldkwaliteit accuraat te voorspellen. Hiermee werd de invloed van de meeste pinhole-ontwerpparameters op de kwaliteit van het reconstructiebeeld nagegaan, zo ook van de hoeveelheid overlap in de projecties. Bij wijze van voorbeeld werd met deze methode vervolgens een optimale pinhole-plaat, die bevestigd kan worden op de bestaande pinhole-collimator, ontworpen voor één specifieke toepassing, vervaardigd en geëvalueerd met behulp van fantoom- en diermetingen. De methode werd ook toegepast om de kwaliteit van een ander soort systeem te evalueren, namelijk time-of-flight (TOF) PET. De bevindingen uit de theorie voor de verbetering van de pinhole SPECT beelden werden ook dadelijk vertaald naar aanpassingen in de praktijk, zodat de kwaliteit van de scans van kleine dieren, die uitgevoerd werden in het kader van preklinische studies, continu toenam.

Pinhole en multipinhole SPECT reconstructie

Doordat bij pinhole SPECT een andere collimator gebruikt wordt dan bij conventionele SPECT, vereist het simuleren van een pinhole SPECT meting een aantal specifieke acquisitiemodellen. Deze worden kort besproken in de sectie over cameramodellering. Bovendien ondervinden de pinhole SPECT metingen gelijkaardige fysische effecten, door interactie van de fotonen met materie, als de conventionele SPECT metingen. Correcties voor scatter, attenuatie, radioactief verval en overspraak werden daarom geïmplementeerd in de pinhole SPECT software, zodat een betere beeldkwaliteit en absolute kwantificatie mogelijk werden.

Cameramodellering

Zoals reeds eerder vermeld, zorgt een pinhole-collimator voor een uitvergroting van het projectiebeeld wanneer de afstand tussen de pinhole en het proefdier kleiner is dan de afstand tussen de pinhole en de detector (zie Fig. 1(b)). Hierdoor kan een betere ruimtelijke resolutie bereikt worden in de reconstructiebeelden in vergelijking met de resolutie van een conventionele SPECT scan. Het merendeel van de parameters die de geometrie van de camera beschrijven, wordt weergegeven door de commerciële camerasoftware. Deze zijn nauwkeurig genoeg voor de reconstructie van patiëntenmetingen, maar niet voor pinhole SPECT reconstructies. Voor single pinhole SPECT waarbij de detector een cirkelvormige baan aflegt rond de rotatieas, wordt de camerageometrie bepaald door 7 parameters. Om deze uniek te kunnen bepalen is een meting van 3 niet-colineaire punten nodig, waarvan 2 afstanden gekend zijn [11]. Deze calibratiemeting wordt onmiddellijk na de diermeting uitgevoerd met dezelfde acquisitie-instellingen. Aangezien we over meer informatie beschikken wanneer een multipinhole-collimator, d.w.z. met meerdere pinhole-openingen in één collimator, gebruikt wordt, kan het calibratiefantoom hiervoor nog verder vereenvoudigd worden. In [126] werd aangetoond dat slechts 2 puntbronnen, waartussen de afstand niet gekend hoeft te zijn, noodzakelijk zijn om de acquisitieparameters uniek te bepalen. Wij bekwamen hetzelfde resultaat via een equivalente afleiding op basis van de parameters die we reeds eerder gebruikten voor de beschrijving van single pinhole SPECT [121]. Uit onze eerste testen bleek echter dat het gebruik van extra informatie, zoals de afstand tussen de puntbronnen of tussen de pinhole-openingen, nuttig is om het calibratieproces te stabiliseren.

Niet elke detectorpixel meet evenveel activiteit van een vlakke, uniforme bron doorheen een pinhole-opening. Dit verschil in gevoeligheid moet in rekening gebracht worden tijdens de reconstructie. Omdat de meeste eenvoudige modellen niet nauwkeurig genoeg zijn, werd in dit werk een analytische methode uitgewerkt waarbij de gevoeligheid van elke detectorpixel analytisch berekend wordt op basis van de hoeveelheid materiaal die de straling doorkruist op haar weg naar de detector. Deze methode werd vervolgens succesvol vergeleken met Monte Carlo simulaties en metingen van een vlakke, uniforme bron. De kleine verschillen tussen de analytische en Monte Carlo methode enerzijds en de metingen anderzijds waren vooral te verklaren door fabricage-onnauwkeurigheden. Andere lichte afwijkingen ten op-

zichte van de simulaties en metingen vloeiden voort uit het niet modelleren van de eigenschappen van het detectorkristal en de niet-uniforme respons van de fotovermenigvuldigingsbuizen. De analytische methode is daarom vooral geschikt voor simulaties, bijvoorbeeld van nieuwe pinhole-collimatoren. Voor de reconstructie van pinhole SPECT metingen worden bij voorkeur de gemeten sensitiviteitsbeelden gebruikt.

Om gemeten gegevens te reconstrueren tot een 3D beeld wordt meestal de (geschatte) activiteit afwisselend voorwaarts en teruggeprojecteerd door de pinhole-opening(en). Dit vereist transformaties tussen het beeld- en het detectiedomein. Ofwel kijkt men hiervoor hoe elke beeldvoxel op de detector geprojecteerd wordt, ofwel modelleert men het volume dat vanuit elke detectorpixel bereikt wordt. Beide modellen kunnen gebruikt worden voor voorwaartse en terugprojectie. De laatste methode is op twee manieren geïmplementeerd in de pinhole SPECT software. De eerste bepaalt voor elke nieuwe projectie en terugprojectie 7 projectiestralen vanuit de detectorpixel door de pinhole-opening. De tweede berekent op voorhand welke beeldvoxels bijdragen tot de gemeten activiteit in een bepaalde detectorpixel en in welke verhouding. Dit wordt dan opgeslagen voor alle detectorpixels en geraadpleegd wanneer nodig, wat een beduidende tijdswinst oplevert t.o.v. de eerste methode.

Metingcorrecties

Door interactie met materie met een relatief lage densiteit, zoals menselijk weefsel en water, kunnen fotonen afbuigen en een deel van hun energie verliezen. Dit noemt men Comptonverstrooiing. Een foton kan ook botsen tegen een elektron in een dens materiaal, zoals het lood van de collimator, waardoor het elektron de energie van het foton kan opnemen en gebruiken om te ontsnappen uit het atoom. Een ander elektron uit het atoom met een hogere energiestatus kan dan diens plaats innemen door energie vrij te geven onder de vorm van een uitgezonden foton. Dit proces noemt men het foto-elektrisch effect en is een tweede vorm van fotonverstrooiing. Sommige van de verstrooide fotonen worden gedetecteerd, waardoor de beeldkwaliteit vermindert. Om deze te verbeteren, werden twee correctiemethodes geïmplementeerd in de pinhole SPECT software [56,58]. Met behulp van puntbronmetingen en Monte Carlo simulaties werd de hoeveelheid verstrooide fotonen verder onderzocht [103]. Hieruit bleek dat vooral voor metingen met het ^{123}I-isotoop, dat naast een fotopiek rond 159 keV ook fotonen met hogere energieën uitzendt, een beduidende vermindering bekomen kon worden door meer afschermingsmateriaal te gebruiken. Daarom werken we nu met dikkere pinhole-collimatoren.

De interactie van fotonen met materie zorgt er tevens voor dat een gedeelte van deze fotonen in het lichaam van de patiënt of het proefdier geabsorbeerd wordt. Indien een goede schatting gemaakt kan worden van het lichaam, kan op vrij eenvoudige wijze gecorrigeerd worden voor deze attenuatie. Deze schatting kan gebeuren op basis van de gegevens van de emissiescan, waarbij typisch de attenuatie van water aan alle lichaamsvoxels wordt toegekend, of met behulp van anatomische beelden, bekomen van een extra transmissie-, berekende tomografie- (CT) of magnetische

resonatie-scan (MRI).

Isotopen vervallen na verloop van tijd naar een stabiel element. Hierdoor vermindert de hoeveelheid radioactiviteit als functie van de tijd. Correctie voor dit verval werd mogelijk gemaakt in de pinhole SPECT software.

Voor sommige onderzoeken wil men twee functionele processen tegelijkertijd in beeld brengen. Daarvoor maakt men gebruik van twee isotopen die fotonen met een verschillende energie uitzenden. Deze energieën liggen echter vaak dicht bij elkaar, waardoor sommige fotonen toegekend worden aan het verkeerde isotoop. Naar aanleiding van een studie in konijnen, waarbij twee soorten celdood simultaan bestudeerd werden, werd een correctiemethode uitgewerkt voor de overspraak tussen de twee meest gebruikte SPECT isotopen, ^{99m}Tc en ^{123}I.

Kwantitatieve evaluatie van tomografische systemen

Voor hoge resolutie functionele beeldvorming van kleine dieren wordt vaak gebruikgemaakt van pinhole SPECT met een circulaire camerabeweging. Multipinhole SPECT voegt informatie toe door superieure bemonstering en kan de balans tussen resolutie en gevoeligheid verbeteren. Om verschillende pinhole-collimatorontwerpen te evalueren, is een efficiënte methode nodig die de reconstructiebeeldkwaliteit kwantificeert.

In dit werk hebben we een snelle, benaderende methode voorgesteld, die de kwaliteit onderzoekt van individuele beeldvoxels. Hierbij werd getracht hun gelineariseerde lokale impulsrespons (LLIR) en (co)variantie in een MLEM[1] gereconstrueerd beeld met laagdoorlaatfiltering nauwkeurig te voorspellen. Om verschillende systemen met elkaar te kunnen vergelijken werd een vooraf gedefinieerde doelresolutie opgelegd.

Ter validatie werd de contrast-ruisverhouding (CNR) in een aantal voxels van een homogene bol en van een realistisch, gesimuleerd rathersenfantoom berekend voor vele pinhole- en multipinhole-ontwerpen. Hierbij werd een goede overeenkomst waargenomen tussen de CNRs bekomen met de benaderende methode en deze verkregen met gefilterde MLEM reconstructies van gesimuleerde projecties met ruis.

Gebruikmakend van de benaderende methode werd vervolgens de invloed van telkens één variërende parameter op de CNR onderzocht in realistische pinhole- en multipinhole-ontwerpen. De bestudeerde parameters waren de diameter van pinhole-opening, de afstand tussen de openingen en de rotatieas, de focale afstand, de openingshoek, de positie van de openingen, de afstand waarop gefocust wordt en het aantal pinhole-openingen. De resultaten konden typisch verklaard worden door de verandering in gevoeligheid, de hoeveelheid uitsmering en de hoeveelheid overlap in de projecties. De methode werd toegepast op multipinhole-ontwerpen met openingen die op één enkel punt focusten, maar is evenzeer toepasbaar op andere ontwerpen.

[1] MLEM of maximale waarschijnlijkheid-verwachtingsmaximalisatie is een in de emissietomografie vaak gebruikt, iteratief reconstructie-algoritme [98]. Het is gedetailleerd beschreven in sectie 2.3.2 van deze doctoraatstekst.

Invloed van overlappende projecties op de reconstructiebeeldkwaliteit bij multipinhole SPECT

Zoals reeds vermeld, heeft multipinhole SPECT beeldvorming verscheidene voordelen t.o.v. enkelvoudige pinhole SPECT beeldvorming, waaronder een hogere gevoeligheid en verbeterde bemonstering. Het vinden van een goed ontwerp is echter een hele uitdaging gezien het grote aantal ontwerpparameters. Naast het bestuderen van de invloed van vele voor de hand liggende parameters op de reconstructiebeeldkwaliteit in de vorige sectie, werd tevens een bijzondere parameter, namelijk de hoeveelheid overlap in de projectiebeelden, bestudeerd tijdens dit doctoraat.

De evaluatie van de beeldkwaliteit werd zowel gebaseerd op de reeds eerder gebruikte benaderingsmethode voor de LLIR en de (co)variantie van een voxel, als op de systematische fouten in de reconstructie van ruisloze projectiegegevens. Er werden twee methodes voorgesteld om de overlap in het projectiebeeld te verwijderen door het tegenhouden van bepaalde projectiestralen met behulp van extra afscherming tussen de pinhole-plaat en de detector. Ook werden er twee maten gesuggereerd om de hoeveelheid overlap te kwantificeren.

Eerst werd de benaderende methode om de CNR te voorspellen gevalideerd door middel van MLEM reconstructies met een opgelegde doelresolutie. Vervolgens werden ontwerpen met verschillende hoeveelheden overlap geëvalueerd om de invloed van multiplexering na te gaan. Bovendien werd de CNR van elk pinhole-ontwerp ook vergeleken met deze van hetzelfde ontwerp, maar waarbij de overlap verwijderd was. Daarnaast werden de resultaten geïnterpreteerd met de overlapkwantificatiematen. Tenslotte werden de twee voorgestelde methodes om overlap te verwijderen met elkaar vergeleken.

Op basis van de resultaten konden we besluiten dat, vanaf het moment dat het hele detectoroppervlak gebruikt is, de door het multiplexen toegevoegde gevoeligheid enkel in staat is het verlies aan informatie te compenseren, maar de CNR niet kan verbeteren. Het verwijderen van de overlap kan echter wel de CNR doen toenemen. De winst is het belangrijkst in het centrale gezichtsveld, al gaat dat vaak ten koste van de CNR in een aantal voxels aan de randen, aangezien slechts weinig informatie overblijft voor hun reconstructie na overlapverwijdering. De reconstructiebeelden verschaften ons veel inzicht in de artefacten veroorzaakt door multiplexering en afknotting van projecties.

Geoptimaliseerd multipinhole-ontwerp voor muisbeeldvorming

In ons labo worden pinhole SPECT muisstudies voornamelijk uitgevoerd om de opname van nieuw ontwikkelde speurstoffen in o.a. de schildklier, een grote tumor, de lever, milt of nieren te bepalen. Daarom optimaliseerden we nieuwe multipinholeplaten voor gerichte muisbeeldvorming met hoge gevoeligheid.

Hiervoor werd opnieuw gebruikgemaakt van de efficiënte analytische methode om de CNR te voorspellen in veel punten van een homogene cilinder voor een groot aantal pinhole-ontwerpen met een bescheiden hoeveelheid overlap. Het ontwerp dat globaal gezien de beste CNR opleverde, een configuratie met 7 pinhole-openingen, werd geselecteerd. Vervolgens werd het patroon van de openingen lichtjes onregelmatig gemaakt om de artefacten, veroorzaakt door multiplexering, te verminderen. Twee identieke, maar gespiegelde 7-pinhole-platen werden vervaardigd. Daarnaast werd ook de calibratieprocedure geautomatiseerd en verfijnd om kleine afwijkingen t.o.v. de circulaire beweging in rekening te kunnen brengen.

Eerst werden de nieuwe platen getest door het reconstrueren van een gesimuleerde meting van een homogene cilinder. De meeste overlapartefacten werden onderdrukt door het onregelmatige patroon en verder verwijderd door de reconstructie te beperken tot het lichaamsvolume. Vervolgens werd een Jaszczakfantoom, gevuld met 37 MBq ^{99m}Tc, gescand op een tweekops gammacamera die uitgerust was met de nieuwe pinhole-collimatoren. Een vergelijking werd gemaakt tussen de beeldkwaliteit met en zonder verfijnde calibratie voor de beide koppen, zowel apart als tesamen gereconstrueerd. Voorts werden 20 korte scans van hetzelfde fantoom gemaakt met een enkelvoudige pinhole-collimator op de ene kop en een van de nieuwe multipinhole-collimatoren op de andere, zodat de verbeterde ruiseigenschappen van het nieuwe ontwerp onderzocht konden worden. Tenslotte werden nog twee normale muizen gescand met de nieuwe set van collimatoren om de bereikbare beeldkwaliteit in abdomen- en schildklierbeeldvorming te illustreren.

De simulatiestudie gaf aan dat het gebruik van informatie over het lichaamsvolume de overgebleven artefacten kan verwijderen. De verfijnde calibratie zorgde voor een verbeterde ruimtelijke resolutie, vooral in de reconstructiebeelden van de data verkregen met de tweede detectorkop. De ruis verminderde duidelijk door een nieuw multipinhole-ontwerp te gebruiken in plaats van een enkelvoudige pinhole. Daarenboven waren de eerste testscans succesvol, zodat we de nieuwe platen konden vrijgeven voor preklinische studies in muizen.

Pinhole SPECT: Toepassingen

Dit doctoraat had tot doel de reconstructiebeeldkwaliteit die bereikt kan worden met pinhole SPECT te onderzoeken en te verbeteren. Hiervoor werden zowel aanpassingen gedaan op het gebied van de pinhole SPECT software, door het (beter) modelleren van het acquisitiesysteem en de fysica van de radioactieve speurstof, als op het vlak van de hardware, namelijk door het verdikken van de eerste pinhole-collimator, het introduceren van een tweede collimator en het verbeteren van het pinhole-ontwerp. Zoals hierboven beschreven, was het bestuderen van de invloeden van deze veranderingen op een theoretische manier en met behulp van computersimulaties heel interessant. Door het valideren van deze resultaten met fantoommetingen, werd bovendien het gebruik van de pinhole SPECT camera voor beeldvorming van kleine dieren mogelijk gemaakt, zodat vele andere onderzoekers de mogelijkheid kregen om steeds betere in vivo SPECT beeldvorming uit te voeren

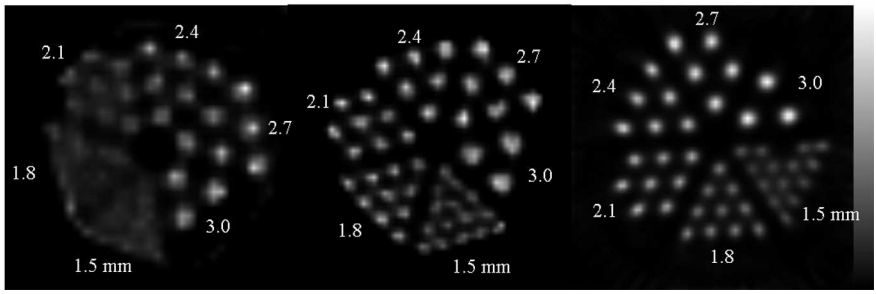

Figuur 2: Illustratie van de evolutie van de beeldkwaliteit over de tijd. Centrale, transaxiale snede door een resolutiefantoom met 6 secties van met ^{99m}Tc gevulde staafjes met een diameter tussen de 1.5 en 3.0 mm: (links) enkelvoudige pinhole met 3.0 mm diameter, (centraal) multipinhole met 7 openingen van 1.5 mm diameter, ontworpen voor beeldvorming van rathersenen (zie [10], p. 53) en (rechts) tweekops beeldvorming met de nieuwe set multipinhole-platen, halve acquisitietijd.

in het kader van hun preklinische experimenten. Dit kan gaan van het nagaan van de opname-eigenschappen van een nieuw ontwikkelde speurstof voor SPECT, over het bestuderen van metabolismen in bepaalde ziektemodellen in kleine dieren, tot het evalueren van behandelingen in dergelijke diermodellen.

Om een beeld te schetsen van de globale evolutie van de beeldkwaliteit, werd eerst de acquisitie en reconstructie van een Jaszczak-fantoom bestudeerd over de tijd. Dit is een plastieken cilinder met 6 spievormige secties die meerdere holle staafjes bevatten met een diameter tussen de 1.5 en 3.0 mm. Initieel hadden we slechts één pinhole-collimator ter beschikking en werd gescand met een enkelvoudige pinhole-plaat met een opening van 3.0 mm diameter. Een centrale, transaxiale snede door het resolutiefantoom, waarbij de meetgegevens gereconstrueerd werden met een vroege versie van de pinhole SPECT software, is getoond in Fig. 2 (links). Vervolgens werd overgeschakeld naar een multipinhole-plaat met 7 openingen van 1.5 mm diameter, die ontworpen was voor het scannen van rathersenen (zie [10], p. 53), en het centrale beeld in Fig. 2 opleverde. Het rechtse beeld in dezelfde figuur toont het resultaat van een recente meting van het fantoom, gebruikmakend van de nieuwe set multipinhole-platen, geoptimaliseerd voor muisbeeldvorming, op de twee pinhole-collimatoren, zodat de acquisitietijd gehalveerd kon worden.

De pinhole SPECT beeldvorming begon met het in beeld brengen van rathersenen. Door een normale rat achtereenvolgens met een 7-pinhole- en een enkelvoudige pinhole-collimator te scannen, werd duidelijk dat de eerste een betere resolutie opleverde, zodat de striata in de hersenen beter van elkaar gescheiden waren. De gevoeligheid van beide systemen was gelijkaardig. Vervolgens werden verscheidene reeksen konijnen gescand om de opname van een nieuwe speurstof voor ongeorganiseerde celdood na te gaan in verschillende hartinfarctmodellen. Hierbij werd gebruikgemaakt van transmissie en emissie micro-PET, pinhole SPECT met enkelvoudige pinhole(s) en CT. Voor de analyse van de beelden, dienden ze geregistreerd te zijn. Dit werd verwezenlijkt met behulp van markers en rigide en niet-rigide

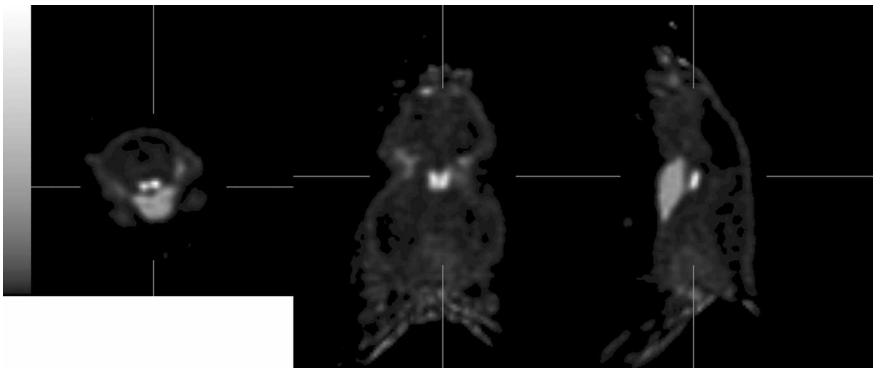

Figuur 3: Transaxiale (links), coronale (centraal) en sagittale snede (rechts) door de schildklier van een normale muis.

registratietechnieken. Voor een deel van de experimenten dienden twee speurstoffen gemerkt met verschillende isotopen, namelijk ^{99m}Tc en ^{123}I, tegelijkertijd gevisualiseerd te worden. Hiervoor werd overspraakcorrectie uitgewerkt. Tenslotte werden ook een aantal groepen muizen gescand, enerzijds voor het in beeld brengen van georganiseerde celdood in verscheidene muismodellen, anderzijds voor het visualiseren van de schildklier (zie Fig. 3).

In de nabije toekomst zullen verschillende groepen ratten gescand worden om andere nieuwe speurstoffen voor ongeorganiseerde celdood te testen in verscheidene infarctmodellen. Ook de ontwikkelde speurstof voor georganiseerde celdood zal verder bestudeerd en gebruikt worden in tumormuizen om vroege respons bij chemotherapie te onderzoeken.

Evaluatie van de beeldkwaliteit bij TOF PET

Om te illustreren dat de in dit doctoraat ontwikkelde benaderende methode voor de evaluatie van tomografische systemen zeer uitgebreide toepassingsmogelijkheden heeft in de emissie- en transmissietomografie, werd ze gebruikt bij het bestuderen van TOF PET. Het is reeds meermaals aangetoond dat het gebruik van TOF informatie tijdens de reconstructie van PET meetgegevens de beeldkwaliteit ten goede komt.

In dit doctoraat hebben we deze verbetering gekwantificeerd met behulp van twee methodes: (1) een gepubliceerde analytische uitdrukking die enkel geldt voor een centraal punt in een grote, uniforme, schijfvormige bron, en (2) onze efficiënte analytische benaderingen voor gefilterde MLEM reconstructie met een vaste doelresolutie, die de beeldkwaliteit in een pixel of een kleine regio kan voorspellen op basis van de Fisher-informatiematrix. Met behulp van deze laatste methode kon tevens de door Watson voorgestelde gewichtsfunctie [128] voor gefilterde terugprojectie reconstructie van TOF PET gegevens afgeleid worden.

De beeldkwaliteit werd onderzocht voor verschillende locaties in verscheidene softwarefantomen. Zowel vereenvoudigde als realistische fantomen, gemeten met TOF PET systemen alsook met een conventionele PET camera, werden gesimuleerd. Aangezien de tijdsresolutie van het systeem niet altijd accuraat gekend is, werd tevens het effect van het gebruik van een onnauwkeurige kernel tijdens de reconstructie op de beeldkwaliteit bestudeerd met behulp van de analytische benaderingen.

Eerst bevestigden we met deze methode dat de vermindering van de variantie in het centrum van een grote, uniforme, schijfvormige bron evenredig is met de schijfdiameter en omgekeerd evenredig met de tijdsresolutie. Vervolgens konden we een verbetering in beeldkwaliteit vaststellen in alle pixels door het gebruik van de TOF informatie, al steeg de CNR trager in eccentrische regio's en regio's met hoge activiteit dan in centrale en lage tot middelmatige activiteitsregio's. Tot slot had het onnauwkeurig (te smal of te breed) modelleren van de tijdsresolutie tijdens de reconstructie een daling van de CNR tot gevolg. Ondanks het redelijk vlakke optimum, moet ermee rekening gehouden worden dat het gebruik van een inaccuraat TOF model aanleiding geeft tot artefacten in het reconstructiebeeld.

Algemeen besluit

Belangrijkste bijdrages van dit werk

De hoofdbijdrages van dit werk kunnen opgedeeld worden in vier onderwerpen. Vanuit wetenschappelijk oogpunt is de belangrijkste waarschijnlijk de voorspelling en het onderzoek van de beeldkwaliteit. Hiervoor werd een efficiënte, benaderende methode ontwikkeld die de LLIR en de covariantiematrix voor een punt of kleine regio van een gefilterd MLEM reconstructiebeeld met een opgelegde doelresolutie nauwkeurig kan voorspellen. Deze methode werd in de eerste plaats gebruikt om de invloed van verscheidene pinhole-ontwerpparameters op de beeldkwaliteit te bestuderen. Ook het effect van overlap in de projectiebeelden werd hiermee grondig onderzocht. Ter illustratie van de algemene toepasbaarheid van de methode voor het evalueren van tomografische sytemen, werd tevens nagegaan in welke mate het gebruik van TOF informatie tijdens PET reconstructie de beeldkwaliteit kan verhogen en hoe belangrijk een goed model voor de tijdsresolutie is.

Gebaseerd op de kennis verworven door het bestuderen van de pinhole-ontwerpparameters en met behulp van de benaderende methode werd vervolgens een pinhole SPECT ontwerp geoptimaliseerd voor één specifieke toepassing, namelijk gerichte muisbeeldvorming. Een set van twee multipinhole-platen werd vervaardigd en getest met behulp van fantoomscans en muisexperimenten.

De verbeteringen van de pinhole SPECT reconstructie kunnen als een derde verwezenlijking van dit doctoraat beschouwd worden. Vooreerst werd een analytische methode geïmplementeerd voor het berekenen van de pinhole-gevoeligheid voor de activiteit van een vlakke, uniforme bron. Deze werd in samenwerking met de universiteit van Gent succesvol vergeleken met Monte Carlo simulaties en metingen [103],

en wordt intussen als standaard gebruikt voor alle computersimulaties van pinhole-metingen en -reconstructies. Voor de reconstructie van gemeten pinhole-gegevens worden bij voorkeur gemeten gevoeligheidsbeelden gebruikt. Daarnaast werden twee gelijkaardige scattercorrectiemethodes toegevoegd aan de pinhole SPECT software [56, 58]. Ook methodes om te compenseren voor attenuatie, verval en overspraak tussen ^{99m}Tc en ^{123}I werden geïmplementeerd en gevalideerd, en worden intussen routinematig gebruikt bij pinhole SPECT scans van kleine dieren. Al deze aanpassingen in combinatie met een correctiefactor bekomen uit de reconstructie van een gemeten homogeen fantoom, zorgen ervoor dat kwantitatief correcte beelden afgeleverd kunnen worden die de activiteitsverdeling in Bq/mm^3 weergeven. Bovendien werd de calibratiemethode geautomatiseerd en verfijnd door (kleine) afwijkingen van de cirkelvormige camerabeweging in rekening te brengen. Uit een theoretische studie volgde ook dat 2 puntbronnen op ongekende afstand van elkaar kunnen volstaan voor multipinhole-calibratie.

Tot slot hebben de vele dierscans, die uitgevoerd werden in het kader van preklinische studies, gefungeerd als drijvende kracht voor vele software- en hardwareverbeteringen. Naast de hierboven opgesomde verbeteringen voor de reconstructie, werden bijvoorbeeld ook onze eerste pinhole-collimator verdikt, een tweede aangekocht, nieuwe pinhole-platen ontworpen en vervaardigd, intramodaliteitsregistraties mogelijk gemaakt, etc. Dankzij al deze ingrepen werd de beeldkwaliteit continu verbeterd, zodat de pinhole SPECT camera heel wat aan populariteit heeft gewonnen in de voorbije 4 jaar.

Suggesties voor verder onderzoek

Tot dusver werd de benaderende methode voor het evalueren van de beeldkwaliteit vooral gebruikt om meer inzicht te krijgen in de pinhole-ontwerpparameters. Ze zou verder ook gebruikt kunnen worden om verschillende recent ontwikkelde micro-SPECT systemen met elkaar te vergelijken voor een bepaalde toepassing. Momenteel wordt in ons laboratorium met behulp van deze methode de prestatie van een roterende platencollimator (rotating slat) vergeleken met die van een collimator met parallelle gaten voor planaire scans en 3D SPECT [137]. Voorts hebben we de methode gebruikt om 2D TOF PET te evalueren. Als uitbreidingen zouden randoms en scatter gemodelleerd kunnen worden, alsook overgegaan naar 3D waarvoor de tijdswinst groter is.

In dit werk werd vooral de CNR beschouwd als maat voor de beeldkwaliteit. Artefacten door overlap en truncatie vertalen zich echter niet per se in een lagere CNR. Er wordt verwacht dat informatie over deze artefacten te vinden is in de covariantiematrix, maar hiervoor is meer onderzoek nodig. Een andere bemerking is dat de benaderende methode, in tegenstelling tot MLEM reconstructie, geen negatieve activiteit tegenhoudt. Hoe dit gemodelleerd kan worden is nog een open vraag.

Een ander toepassingsdomein voor de ontwikkelde methode is dat van de numerieke waarnemers, waarbij de opgelegde doelresolutie de vergelijking van verschillende systemen bij gelijke resolutie op eenvoudige wijze mogelijk maakt. Bovendien

kunnen de benaderingen gebruikt worden om na te gaan of de ordening van verschillende systemen of reconstructie-algoritmes varieert met de grootte van de bestudeerde regio's of verandert wanneer de beelden meer of minder gefilterd worden met een laagdoorlaatfilter.

Met behulp van de benaderende methode werd een set pinhole-platen ontworpen die geoptimaliseerd zijn voor gerichte muisbeeldvorming. Hierbij werd echter nog overlap toegelaten om de ontwerp- en productiefase te vergemakkelijken, al heeft ons onderzoek uitgewezen dat het verwijderen ervan betere beeldkwaliteit kan opleveren. Ook is men dan automatisch verlost van artefacten ten gevolge van multiplexering en wordt verwacht dat de reconstructie sneller zal convergeren. Het lijkt dus zinvol om een nieuwe set te ontwerpen zonder overlap. Bovendien worden binnenkort een aantal ratstudies gestart, zodat een geoptimaliseerd ontwerp voor ratbeeldvorming eveneens van pas zou komen.

Ook op het vlak van cameramodellering kunnen we nog een aantal mogelijkheden tot verbetering belichten. Voor multipinhole SPECT calibratie hebben we aangetoond dat twee puntbronnen op een ongekende afstand van elkaar volstaan voor het bepalen van de geometrische parameters van de camera. Deze theoretische afleiding dient echter nog verder bestudeerd en ondersteund te worden met behulp van simulaties en metingen. De projectie- en terugprojectiemodellen die we momenteel ter beschikking hebben, dienen nog uitgebreid te worden zodat ze rekening kunnen houden met de penetratie door de pinhole. De efficiënte projectiemethode die gebruikmaakt van voorafberekende gegevens werkt momenteel bovendien enkel voor een perfect cirkelvormige camerabeweging. Calibratieparameters die bijvoorbeeld een systematische draaiing of kanteling van de detector aangeven, kunnen met deze methode dus nog niet in rekening gebracht worden.

Het gebruik van extra informatie tijdens de reconstructie kan de beeldkwaliteit verder verbeteren. Het beperken van de reconstructie tot het lichaamsvolume was hier een illustratie van. Het bepalen van dit volume kan echter nog vereenvoudigd en geautomatiseerd worden, zodat het minder interactie met de gebruiker vereist. Indien anatomische informatie beschikbaar is, bijvoorbeeld van een CT- of MRI-scan, kan deze bovendien als prior-informatie gebruikt worden in een maximum a posteriori (MAP) reconstructie. Ook dit kan de pinhole SPECT reconstructies verbeteren.

Met de huidige reconstructiesoftware kunnen beelden afgeleverd worden die de activiteitsverdeling in Bq/mm^3 weergeven. Voor sommige studies is het echter belangrijk dat gecompenseerd wordt voor het effect van de geïnjecteerde dosis en het lichaamsgewicht, wat kan met een eenvoudige normalisatie. Bij kleine dieren zoals muizen blijft echter vaak een significant deel van de dosis achter op de plaats van injectie, namelijk de staart. Om hiervoor te corrigeren, kan bijvoorbeeld een snelle scan van de staart uitgevoerd worden. Hoe korter de scantijd per projectie, hoe groter de overhead wordt van het verplaatsen van de detector. Dit kan opgelost worden door de camera te laten meten terwijl deze aan een continue snelheid draait. De metingen binnen een bepaalde draaihoek worden dan in dezelfde matrix opgeslagen, zodat de dataverwerking onveranderd blijft. Ondanks de goede, initiële resultaten met deze techniek, verdient vooral de calibratie nog wat extra validatie.

List of acronyms

iD ..... i-dimensional
A ..... aperture acceptance angle
ALARA ..... as low as reasonably achievable
AOR ..... axis of rotation
CCW ..... counterclockwise
CNR ..... contrast-to-noise ratio
CRC ..... contrast recovery coefficient
cs ..... central sampling overlap removal method
CT ..... computed tomography
CW ..... clockwise
CZT ..... cadmium-zinc-telluride
D ..... aperture diameter
DA ..... distance between the aperture and the axis of rotation
DD ..... distance between the aperture and the detector
DEW ..... dual energy window
EM ..... expectation maximization
ET ..... emission tomography
F ..... focusing distance
FBP ..... filtered backprojection
FOM ..... figure of merit
FOV ..... field of view
FT ..... Fourier transform
FWHM ..... full width at half maximum
FWTM ..... full width at tenth maximum
HD ..... higher dimensional than 3D
I ..... inclination angle
LIR ..... local impulse response
LLIR ..... linearized local impulse response
LOR ..... line of response
LS ..... least squares
LSO ..... lutetium orthosilicate
LYSO ..... lutetium yttrium orthosilicate
mAb ..... monoclonal antibodies
MAP ..... maximum a posteriori

MIH ..... mono-iodohypericin
MIHA ..... mono-iodohypericin monocarboxylic acid
ML ..... maximum likelihood
MLEM ..... maximum likelihood expectation maximization
MoSAIC ..... molecular small animal imaging center
mph ..... multipinhole
MR, MRI ..... magnetic resonance imaging
ms ..... maximum sensitivity overlap removal method
NP ..... number of pinhole apertures
OS ..... ordered subsets
OSEM ..... ordered subsets expectation maximization
ovl ..... overlap
PA ..... angular position of the aperture with respect to the other apertures
PD ..... radial distance of the aperture to the central aperture, pinrad(ius)
PET ..... positron emission tomography
p.i. ..... post injection
PMT ..... photomultiplier tube
PSF ..... point spread function
RMSD ..... root mean squared deviation
RMSRD ..... root mean squared relative deviation
ROI ..... region of interest
SCID ..... severe combined immunodeficient
SD ..... standard deviation
SNR ..... signal-to-noise ratio
SPECT ..... single photon emission computed tomography
sph ..... single pinhole
SUV ..... standardized uptake value
T ..... pinhole aperture plate thickness
TEW ..... triple energy window
TOF ..... time-of-flight
VOI ..... volume of interest
WLS ..... weighted least squares

List of symbols

x, y, z ..... cartesian coordinates in the image space
$\Delta x, \Delta y, \Delta z$ ..... dimensions of the image voxels
r_j, α_j, z_j ..... cylindrical coordinates of point source j
g_x, g_z ..... cartesian coordinates of the grid sampling point
$\nu_x = \nu\cos\theta, \nu_y = \nu\sin\theta$ ..... coordinates in the Fourier space
u, v ..... cartesian coordinates in the detector space
$\Delta u, \Delta v$ ..... dimensions of the detector pixels
u_{ij}, v_{ij} ..... projection coordinates of point source j through aperture i
u'_{ij}, v'_{ij} ..... u_{ij}, v_{ij} corrected for twist angle

$\approx$ ..... is approximately equal to
$\propto$ ..... is proportional to
$\mapsto$ ..... mapping operation
∞ ..... infinity
* ..... complex conjugate
$^{-1}$ ..... matrix inverse
^{ps} ..... approximate pseudoinverse
^{T} ..... matrix transpose
$|.|$ ..... Jacobian determinant
$|\vec{x}|$ ..... vector norm
$\Re(.)$ ..... real part
∇^{20} ..... second partial derivative in the first parameter
∇^{11} ..... first partial derivative in the first and second parameter
∇_q ..... row gradient operator

a ..... amount of detected coincidences per unit area
a_{ij} ... probability that a photon emitted from image voxel j is detected in pixel i
ap ..... aperture index
ap_m ..... aperture causing multiplexed sensitivity
ap_u ..... aperture causing useful sensitivity
A, A^T ..... projection and backprojection operator
B, B^T projection and backprojection operator modeling the reconstruction TOF kernel with inaccurate time resolution
c ..... speed of light

C_{left} ..... amount of photons measured in the left scatter window
C_{prim} ..... amount of primary photons measured in the photopeak window
C_{right} ..... amount of photons measured in the right scatter window
C_{scat} ..... amount of scattered photons measured in the photopeak window
C_{total} ..... total amount of photons measured in the photopeak window
C_Y ..... covariance matrix of the phantom measurement Y
cf ..... correction factor
Cov ..... covariance matrix
Cov^j ..... covariance matrix of voxel j
$crosstalk_{Y\ in\ X-window}$ ..... fraction of crosstalk of isotope Y in the photopeak window of X
d ..... distance between the aperture and the axis of rotation
d ..... aperture diameter
d_{eff} ..... effective aperture diameter
D ..... disk source diameter
D_a ..... long axis diameter of ellipse phantom
D_b ..... short axis diameter of ellipse phantom
$D[.]$ ..... diagonal matrix
$dist_{fs}$ ..... distance between the pinhole aperture and the activity source
e^j ..... j-th unit vector
e_u, e_v ..... electrical shifts
e'_u, e'_v ..... electrical shifts corrected for twist angle
$E(.)$ ..... expected value
f ..... focal length
$\boldsymbol{F}$ ..... Fisher information matrix
$\boldsymbol{F}^j$ ..... shift-invariant approximation of the Fisher information matrix $\boldsymbol{F}$
$\boldsymbol{F}^j_{DC}$ ..... DC-value of $\boldsymbol{F}^j$
g ..... complete grid area
$\boldsymbol{G}$ ..... pseudoinverse of the Fisher information matrix $\boldsymbol{F}$
$\boldsymbol{G}^j$ ..... pseudoinverse of $\boldsymbol{F}^j$
$G(\nu \cdot \hat{u})$ ..... 1D Fourier transform of the Gaussian TOF kernel
$\text{Gauss}_{\text{iD}}\{\sigma_x^2\}$ ..... i-dimensional Gaussian with a standard deviation σ_x
i ..... detector pixel i
I ..... total number of detector pixels
$I(\nu)$ ..... 2D Fourier transform of the activity distribution in the object
j ..... image voxel j
J ..... total number of image voxels
l ..... projection line, line of response
l^j ..... (linearized) local impulse response of voxel j
l^{ROI} ..... linearized local impulse response of the ROI
l_k ..... intersection length of the projection ray with voxel k
L ..... logarithm of the likelihood
m, n ..... mechanical offsets
M ..... logarithm of the prior
$M(\theta, \nu)$ ..... 2D Fourier transform of the measured projection data at angle θ
M_{ap} ..... mapping function for the projection through aperture ap

M_α^j ..... total multiplexed sensitivity for voxel j at rotation angle α
M_{α,ap_u,ap_m}^j . multiplexed sensitivity of aperture ap_m seen in the pixel with U_{α,ap_u}^j
N ..... number of noise realizations
N_j ..... set of neighboring voxels of voxel j
original$_j$ ..... j-th voxel value in the original image
$p(.)$ ..... probability
$p(.|.)$ ..... conditional probability
$\boldsymbol{P}$ ..... post-smooth filter
$\boldsymbol{P}^j$ ..... j-dependent post-smooth filter
q_i ..... measured number of photons in detector pixel i
$\bar{q}_i$ ..... measured number of photons in detector pixel i without noise
Q ..... measurement or projection data
Q_{ap} ..... measurement through aperture ap
$\bar{Q}$ ..... noiseless sinogram
r ..... number of pixels in the ROI
r_i ..... expected number of photons to be measured in detector pixel i
R_α^j total remaining useful sensitivity for voxel j at rotation angle α after overlap removal
RA_0 ..... initial amount of radioactivity
RA_t ..... expected amount of radioactivity remaining after time t
recon$_j$ ..... j-th voxel value in the reconstructed image
S_{ap} ..... sensitivity of aperture ap
$sino_{X,corr}$ ..... sinogram of isotope X corrected for crosstalk
$sino_{X-window}$ ..... sinogram measured in the photopeak window of X
t ..... measurement time
$t_{1/2}$ ..... half-life of the isotope
th ..... pinhole aperture plate thickness
$\hat{u}$ ..... 2D unit vector in the projection direction at angle θ
$\hat{u}^\perp$ ..... 2D unit vector in the direction perpendicular to $\hat{u}$
$\boldsymbol{U}$ ..... Hessian of the log-prior M
U_α^j ..... total useful sensitivity for voxel j at rotation angle α
$U_{\alpha,ap}^j$ ..... useful sensitivity of aperture ap for voxel j at rotation angle α
Var^{ROI} ..... variance in the ROI
w ..... weighting factor
$W(\hat{u},\nu)$ 2D FT of the weighting function applied during backprojection
W_{left} ..... width of the left scatter window
W_{prim} ..... width of the photopeak window
W_{right} ..... width of the right scatter window
$\vec{x}=(x,y)$ ..... location vector in the spatial domain (2D)
y ..... distance between the aperture and voxel (x,y,z)
Y ..... phantom measurement

α ..... aperture acceptance angle
β ..... regularization parameter
δ ..... impulse or delta function
Δr ..... resolution of the reconstructed image

Δt ..... TOF time resolution
Δx ..... localization uncertainty of the TOF PET system
η ..... inclination angle of the pinhole w.r.t. the normal of the detector
θ ..... projection angle
κ ..... inclination angle of the projection ray w.r.t. the normal of the detector
λ_d ..... decay constant
λ_j ..... activity in image voxel j
Λ ..... activity distribution image
$\hat{\Lambda}$ ..... reconstruction image
μ ..... mean
μ ..... linear attenuation coefficient
μ_k ..... linear attenuation coefficient in voxel k
ϕ ..... detector tilt
Φ ..... objective function
ψ ..... detector twist
Ψ ..... area of the pinhole opening
Ψ_{eff} ..... effective area of the pinhole opening
ρ_{area} ..... flood source activity per unit area
ρ_{vol} ..... flood source activity per unit volume
σ ..... standard deviation
σ^2 ..... variance
σ_{obj} ..... standard deviation of an object with Gaussian shape
σ_{TOF} ..... standard deviation of the TOF kernel
τ ..... angle between the incoming projection ray and the normal on the detector
τ ..... TOF dimension

Contents

Chapter 1

Introduction

1.1 Positioning

Medical imaging can be divided into two main subgroups: anatomical imaging and functional imaging. In anatomical imaging, the differences between tissues are exploited to gather information about the anatomy of the patient. Depending on the acquired information, a 2D, 3D or even higher dimensional (HD) image can be obtained. Abnormalities, such as bone fractures or fluid accumulation, can be detected using such images. The two main modalities used for this type of imaging are computed tomography (CT) and magnetic resonance imaging (MRI). The latter is also often applied in the scope of functional imaging, where specific metabolic or physiological processes are visualized. A typical example is the comparison of the brain activity at the execution of two well-defined tasks.

Nuclear medicine techniques focus on functional imaging only. To this end, first a molecule is labeled with a radioactive ligand. Next, a very low dose of this radioactive tracer is administered to the patient, usually by intravenous injection. The tracer then takes part in certain metabolic processes. Gamma rays (or photons), measurable by one or more detectors, are emitted during the radioactive decay of the radionuclide. From these measurements, a 2D, 3D or HD[1] image of the tracer distribution, and thus of the metabolic processes can be reconstructed. Examples of such processes are blood perfusion to study the functionality of the heart, and uptake of glucose to detect and examine tumors.

In nuclear medicine two main kinds of radionuclides are used for diagnosis: single photon emitters and positron emitters. Positrons annihilate with an electron, causing the simultaneous emission of two photons in opposite directions, each with an energy of 511 keV, equivalent to the rest mass of an electron. Therefore, a positron emission tomography (PET) camera measures the number of emitted positrons by coincidence detection. In contrast, single photon emitters do not produce collinear

[1] In the rest of this work only 2D and 3D images are mentioned. Most statements and methods for 3D images can be straightforwardly extended to HD images.

photons, and the acquisition must rely on the detection of individual photons using a single photon emission computed tomography (SPECT) camera. Most single photon tracers have a photon energy in the range of 70 to 300 keV.

For the development of new tracers and for the investigation of new therapies for e.g. neurodegenerative disorders, cardiovascular diseases, and cancers, (small) animal studies are performed using representative animal models. As human scanners usually are not appropriate to provide sufficiently high quality images of small animals, dedicated cameras as well as special collimators (to convert a clinical scanner to a small animal imager) have been developed in the past. With these, similar relative detail can be visualized, compared to the human images. Depending on the animal and camera, spatial resolutions within the range of about 0.35 mm to 1.5 mm are currently achievable for small animal SPECT, whereas the resolution of small animal PET is restricted to 1-2 mm.

1.2 Aim

The global goal of this work was to investigate the properties of a pinhole SPECT camera for small animal imaging with respect to the reconstruction image quality. Based on the gathered knowledge, our pinhole SPECT system then had to be optimized to provide images of superior quality for preclinical studies in mice, rats and rabbits. Although the image quality properties were studied in general, the optimization of the prototype small animal SPECT system was subject to some restrictions as we started from a specific dual head clinical gamma camera (e.cam Fixed 180°, Siemens Medical Solutions). Hence, the specifications of the detector(s) were fixed. In addition, we preferred using one set of pinhole collimator supports with a well-chosen detector to pinhole aperture distance for all applications, to which easily interchangeable pinhole plates can be attached. This design principle was inspired by the work of Schramm *et al.* [97]. It facilitates image quality enhancement for various sizes of animals and field of views.

1.3 Objectives

More concrete, the objective of this work was to get more insight in the effect of the many single and multipinhole collimator design parameters on the reconstruction image quality. Therefore, an efficient image quality evaluation method was required. Although such expressions had been derived earlier [33,37,77,94], the two predicted figures of merit, resolution and variance, often have a counteracting influence on the image quality, making comparison e.g. between various pinhole SPECT systems difficult. Therefore, the aim was to derive a similar method in which one of both parameters can easily be fixed to a target value.

Once this approximate method for predicting the reconstruction image quality was thoroughly validated, it was to be used to address an often debated issue in the pinhole SPECT domain, namely the question whether the increased sensitivity

due to overlapping projections can compensate for the induced data ambiguity. By evaluating the image quality reachable with various pinhole collimator designs causing different amounts of overlap, the effect of overlap on the image quality could be investigated in this work.

Although the focus was mainly on a clinical gamma camera transformed to a micro-SPECT system by equipping it with pinhole collimators, many of the studied techniques and drawn conclusions are more generally applicable. To illustrate that, the image quality evaluation method was to be tested for a different type of tomographic system. Because some counterintuitive results were recently presented, concerning the influence on the image quality of the time resolution model used during time-of-flight (TOF) PET reconstruction, we decided to study the image quality of TOF PET in more detail.

Besides the theoretical investigation of the image quality of pinhole SPECT, the reconstructed images of the available pinhole SPECT camera were also to be enhanced. This could be done both by changes in the software and the hardware. The software improvements could be divided into two paths. On the one hand, the in-house implemented pinhole SPECT reconstruction software had to be extended and tested thoroughly for multi head multipinhole SPECT measured data. On the other hand, the system and data modeling needed to be further elaborated and improved. The accuracy of the system model is founded on that of the geometrical calibration as well as on that of the pinhole resolution and sensitivity modeling. In this work, we also aimed for improving the reconstruction image quality and quantitativeness by correcting the measured data for the effects of scatter, attenuation, decay, crosstalk (in case of multiple isotope scans), etc.

Hardware improvement can be seen as a very broad research area, ranging from pinhole collimator optimization to the investigation of new detector materials and the development of more accurate and faster electronics. Since in this work the adaptations were to be tested on an existing clinical camera, only the easily interchangeable collimators have been studied. Using the efficient image quality evaluation method for the comparison of many different (simulated) pinhole collimator designs, a pinhole design needed to be optimized for a specific application (as a proof of principle), manufactured and evaluated based on phantom and animal measurements.

1.4 Main contributions

The main emphasis of this work was put on the theoretical evaluation of the reconstruction image quality of a tomographic system. It consisted of the *derivation, validation and application of efficient, analytical approximations for tomographic image quality evaluation*. As the scope of this work was small animal emission tomography, these were primarily used to quantify the image quality of various pinhole SPECT systems. After investigating the influence of the various single and multipinhole collimator design parameters on the image quality in chapter 4, the method was applied to weigh the pros and cons of overlapping projections against each other

in a quantitative and task-dependent way. Hence, an answer could be formulated to this often posed question in the multipinhole SPECT community (see chapter 5). The more general applicability of the method was illustrated by investigating the image quality of TOF PET systems with it. Recently, some findings indicated that image quality would benefit from a reconstruction with an unmatched model for the TOF resolution (i.e. a slightly too wide Gaussian compared to the real one). With our analytical method, this statement was investigated and refuted. The best contrast-to-noise properties were obtained when using the accurate TOF resolution model during reconstruction. This result was supported by simulations performed in other research groups.

Using the developed image quality evaluation method, *a multipinhole collimator design was optimized* for a specific application, namely focused mouse imaging, within the constraints of the available hardware (see section 6). In addition, both hardware and software solutions were proposed to *reduce reconstruction artifacts*. The optimized design was manufactured and validated with phantom and animal experiments.

The in-house developed *pinhole SPECT reconstruction software* has been *extended* and thoroughly validated for processing multi head multipinhole SPECT data. As explained in chapter 3, *both the camera and data modeling were improved*. The former was enhanced by refining the geometrical calibration and the resolution and sensitivity models. To compensate for photon-matter interaction effects, such as scatter, attenuation, decay, and if necessary crosstalk, data correction methods were implemented. Thanks to these improvements in camera and measurement modeling, images of superior quality can now be provided.

The majority of software and hardware improvements described in this work were driven by the many *small animal pinhole SPECT scans* that were planned in the scope of preclinical experiments (see chapter 7). As support for these research projects, dedicated software for image registration and analysis has been developed.

1.5 Overview

Chapter 2 provides background information that is essential for understanding the subsequent chapters. First, the imaging modalities used in nuclear medicine are discussed and the correspondences and differences between human and small animal scanners are emphasized. Next, the most commonly used methods to reconstruct the activity distribution from a measurement are briefly explained. Finally, a short overview is given of the most important figures of merit and procedures to evaluate the quality of emission tomography images. In chapter 3, more practical issues of single and multipinhole SPECT reconstruction are discussed, including implementation guidelines. Suggestions for both proper camera modeling and measured data corrections are elaborated. In chapter 4, an efficient pinhole collimator design evaluation method is derived, validated and used to study the effects on the image quality of the most important pinhole collimator design parameters. An often discussed issue in the multipinhole SPECT field is whether or not overlap in the projection

images is beneficial for the reconstruction image quality. This topic is studied in more detail in chapter 5. Using the information gathered in these last two chapters and the image quality evaluation method of chapter 4, a multipinhole design is optimized for mouse imaging, starting from the available dual head pinhole SPECT camera. The optimization method, some improvements in multipinhole measurement processing and the optimized design are described in chapter 6. This design has been evaluated with simulations, phantom measurements and animal experiments. In chapter 7, a short overview of the most important studies, performed on the available pinhole SPECT system, is presented as an illustration of image quality evolution obtained thanks to the pinhole SPECT reconstruction software improvements and pinhole collimator optimizations discussed in this work. To demonstrate the more general applicability of the image quality evaluation method described in chapter 4, it has been applied to a different research area currently gaining much interest, namely time-of-flight (TOF) PET. The influence on the image quality of using TOF information during reconstruction is investigated in multiple, increasingly realistic, software phantoms (see chapter 8). In addition, the effect on the reconstructed image of using an inaccurate TOF model is studied. The main conclusions and contributions of this work, as well as some suggestions for future work are listed in chapter 9.

Chapter 2

Background

In this chapter, the basic principles and techniques used in the rest of this work are explained. First, the three main clinical cameras currently occupying the nuclear medicine department are described (section 2.1). Next, the adaptations necessary for imaging small animals are discussed (section 2.2). In section 2.3, the most popular reconstruction algorithms, used to process emission tomography data, are explained. Last, measures and methods to evaluate image quality are briefly summarized in section 2.4.

2.1 Functional imaging in nuclear medicine

The most important radioactive tracers used in nuclear medicine for diagnosis can be classified in two groups: *single photon emitters* and *positron emitters*. They differ in the way they decay. For the first group of tracers, the decay of the isotope causes the emission of photons with isotope-specific energies in random directions. These are imaged using a *gamma camera*, as explained in section 2.1.1. The by far most commonly used single photon emitting isotope is 99m-technetium (^{99m}Tc), with its main photopeak at 140 keV and a half-life of 6.01 h. The second group of tracers decays by emitting a positron, i.e. a nuclear particle with the properties of an electron, but with a positive rather than a negative charge. This positron annihilates with an electron, resulting in the emission of two photons with an energy of 511 keV each, in opposite directions. This effect can be imaged with a *positron emission tomography* or *PET camera* (see section 2.1.2). The most important PET isotope is 18-fluorine (^{18}F) with a half-life of 110 min.

2.1.1 Gamma camera

A clinical gamma camera consists of one, two or three detector heads containing a large scintillation crystal, usually of sodium iodine doped with thallium (NaI(Tl)). A collimator is positioned in front of the crystal to characterize the direction of the

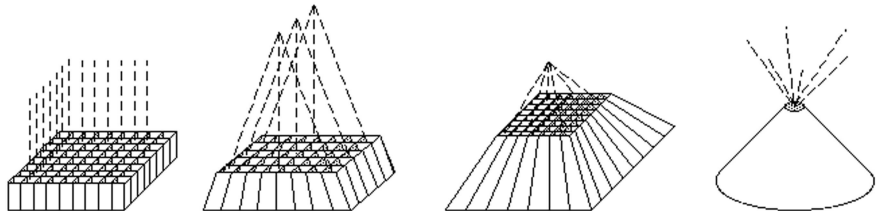

Figure 2.1: Illustration of the different collimator types: (a) parallel hole, (b) fan beam, (c) cone beam and (d) pinhole collimator.

(a) Clinical gamma camera (b) Clinical PET/CT camera

Figure 2.2: Pictures of two clinical cameras: (a) a gamma camera (e.cam Fixed 180°, Siemens Medical Solutions), and (b) a PET/CT camera (Biograph 16, Siemens Medical Solutions).

incoming photons. Many types of collimators are available. The most commonly used in clinical practice is the parallel hole collimator (see Fig. 2.1(a)). Fan beam, cone beam and pinhole collimators are less frequently used (see Fig. 2.1(b)-(d)). The latter, however, is of great importance for small animal imaging (see section 2.2.2). The detector heads are attached to a gantry and rotate in one plane around a bed on which the patient is positioned. The distance between the heads and the patient is adjustable and is taken as small as possible to obtain the best resolution.

Depending on the application, a gamma camera is used to obtain 2D or 3D images of the tracer (or activity) distribution in the patient. It is then called *planar* and *single photon emission computed tomography (SPECT) imaging*, respectively. A typical clinical dual head gamma camera is shown in Fig. 2.2(a). This is the one we currently use for pinhole SPECT imaging (see Fig. 2.3(a)).

Planar imaging

In case only a 2D visualization of the tracer distribution is required, a static image, also called projection or planar image, representing the number and detection location of the perpendicularly incoming, measured photons, is acquired in a 2D matrix on one or more detectors. The counts, i.e. detected photons, are accumulated over a time interval and then interpreted as such. The most common example of this is whole body bone imaging, where a detector head is located at both anterior and posterior position and the patient is steadily shifted through the camera gantry.

Single photon emission computed tomography

In order to obtain a 3D representation of the tracer distribution in the patient, more information is required. Therefore, the detector heads are rotated around the patient, usually in a finite number of steps. The data are then acquired in multiple 2D matrices, one for every projection angle or detector head position. Next, these 2D images are reconstructed to build a 3D volumetric image (see section 2.3).

2.1.2 Positron emission tomography camera

Since two photons traveling in opposite directions need to be detected simultaneously for the acquisition with positron emitters, a dedicated camera is used for *PET imaging*. Rather than having multiple detector heads rotating around the patient, it consists of one or more rings of detector blocks. The patient, lying on a translatable bed, is positioned in the center of the ring. No collimation is required, because the emitted photon pairs travel along a straight line, of which the direction can be retrieved if the two photons are detected simultaneously by a pair of detectors. Based on these lines of responses (LORs), a 3D image can be reconstructed.

Nowadays, PET cameras can hardly be bought without a CT module (see section 2.1.3). The complementary functional and anatomical information, obtained due to the combination of these two systems, facilitates and often even improves the diagnosis made by the physician. An example of a typical PET/CT system is shown in Fig. 2.2(b). For the same reasons, SPECT/CT cameras are currently gaining in popularity. In the near future, PET/MR scanners, and later on maybe SPECT/MR cameras, will become commercially available too.

Time-of-flight PET

The two photons of a photon pair usually travel different distances before reaching a detector. In the early 1980s, the first PET systems, able to measure this spatial difference corresponding to a time difference in the order of hundreds of picoseconds (ps), were being built [109]. Most of the gain in image quality induced by this technique was, however, counteracted by the low efficiency of the fast scintillators available at that time [17]. Thanks to the recent improvements in the development of fast detector crystals, TOF PET received renewed interest. In June 2006, Philips

introduced the first and so far only commercially available *time-of-flight (TOF) PET camera*, the GEMINI TF. It is a fully 3D TOF PET/CT system with lutetium yttrium orthosilicate (LYSO) crystals and a time resolution of about 585 ps ($\approx$ 9 cm) full width at half maximum (FWHM) [107]. This timing information provides a rough location estimate along the LOR and can improve the image quality if used during image reconstruction. The qualitative effects of TOF information are further discussed in chapter 8.

2.1.3 Computed tomography camera

As mentioned before, the *computed tomography* or *CT camera* was introduced in the nuclear medicine department for its anatomical information. Despite the fact that it is not a nuclear medicine technique, it has become indispensable in this department, especially in combination with PET. Therefore, it is briefly discussed in this section.

Instead of injecting a patient with a radioactive tracer, externally produced photons (*X-rays*) are fired at the patient and detected at the other side. A CT camera thus consists of an opposed X-ray tube and detector array, which rotate at equal, high speed around the patient. The ratio between the emitted and detected photons provides information about the attenuating properties of the tissues traveled through. Thanks to the rotation, one or more transaxial slices of the patient can be reconstructed.

2.2 Small animal functional imaging using emission tomography

All cameras discussed in the previous section, except for the TOF PET system, have found their equivalent in the small animal imaging field. Most of them simply correspond to a resized version of the original one. The similarities and differences are explained below.

2.2.1 Single photon planar imaging

In small animal imaging, planar imaging is often performed as a first, quick test to see whether a (newly developed) tracer has taken up as expected or to provide additional information to biodistribution studies. This can be done by putting the animal very close to or immediately onto the parallel hole detector of a clinical gamma camera; because the closer, the better the resolution. Unfortunately, the intrinsic resolution of such cameras is in the order of 4 mm FWHM, which is large for most laboratory animals. As only a small part of the detector area is used, either multiple animals can be scanned at the same time, or a pinhole collimator can be positioned in front of the crystal instead of the parallel hole collimator, enlarging the projection image of the animal on the detector (see Fig. 2.3(b)). This latter

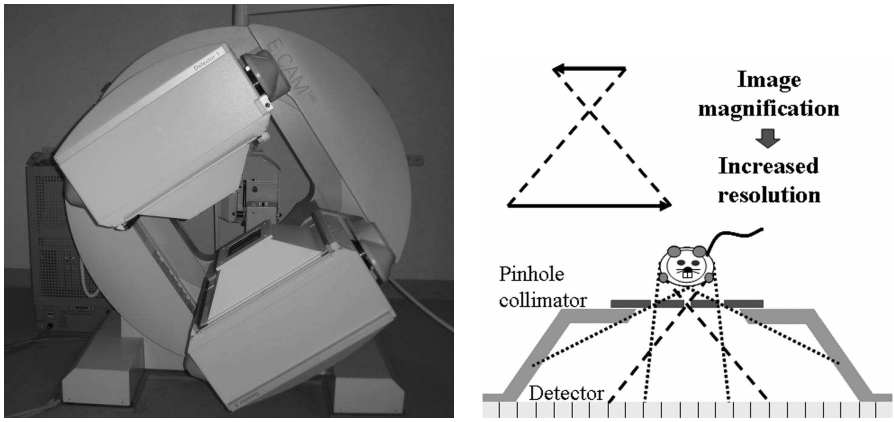

(a) Pinhole SPECT camera (b) Principle of pinhole collimation

Figure 2.3: (a) Picture of the pinhole SPECT camera used in this work, based on the clinical gamma camera shown in Fig. 2.2(a) and inspired by the system developed by Schramm *et al.* [97]. (b) Illustration of the pinhole collimation principle.

method is rarely used for planar imaging, though, because the strong deformations make the image difficult to interpret. For SPECT imaging, on the contrary, using pinhole collimation is common practice, as explained in the next paragraph. As an alternative, a detector with a better intrinsic resolution (around 2 mm FWHM), such as available in dedicated micro-SPECT cameras, can be used.

2.2.2 Micro-SPECT

In the early days of small animal SPECT imaging, a *clinical gamma camera* was *converted into a micro-SPECT system* by substituting one or more parallel hole collimators for single *pinhole collimators*. The design of the pinhole collimator(s) used in this work was based on the pinhole SPECT system described by Schramm *et al.* [97], and consists of a truncated lead pyramid with an interchangeable tungsten pinhole aperture plate on top (see Fig. 2.3). Since photons are stopped by dense materials, such as lead and tungsten, only the photons traveling through the pinhole can be detected. The foundations of pinhole imaging can be found in the principle of the *camera obscura*, the predecessor of the photo camera, where 3D objects illuminated by the sun were projected through a hole onto a wall, which later on was replaced by a 2D film or detector. In small animal imaging, the subject is magnified onto the large detector by choosing a greater distance between the pinhole and the detector than between the pinhole and the activity to be imaged (see Fig. 2.3(b)). Some 5 to 10 years ago, a shift occurred from one to multiple pinholes per collimator. The two main advantages of increased sensitivity and improved sampling are generally considered to result in higher reconstruction image quality, which was investigated in more detail in this thesis.

(a) NanoSPECT (Bioscan)

(b) U-SPECT-II (MILabs)

(c) FLEX Triumph^{TM} (Gamma Medica-Ideas)

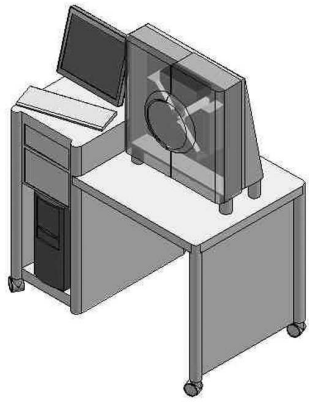

(d) LinoView^{TM} miniSPECT (Linoview Systems)

Figure 2.4: Pictures of dedicated micro-SPECT cameras of (a) Bioscan (NanoSPECT/CT), (b) MILabs (U-SPECT-II), (c) Gamma Medica-Ideas (FLEX Triumph^{TM}) and (d) Linoview Systems (LinoView^{TM} miniSPECT).

A more recent trend is that of the *dedicated micro-SPECT cameras*. These exploit among other things the latest developments in detector hardware, such as crystals with an improved intrinsic resolution (e.g. pixelated cadmium-zinc-telluride (CZT)). As these new crystals are more expensive than traditional large NaI(Tl) crystals, the detectors are usually smaller, allowing less magnification. Thanks to the superior detector resolution, the spatial resolution in the reconstruction image is usually not compromised, and often even slightly improved compared to that of micro-SPECT cameras with large NaI(Tl) detectors. Comparing cost and quality is

Figure 2.5: Picture of the micro-PET system available at the MoSAIC, the molecular small animal imaging center of the Katholieke Universiteit Leuven, Belgium (Focus 220, Siemens Medical Solutions).

essential in choosing the most appropriate camera. In addition, some dedicated systems such as the U-SPECT [9] are stationary, which eliminates the possibility of loss in spatial resolution due to improper modeling of the detector movement (see sections 3.1.1 and 6.5.2). In this case, enough apertures are required to assure sufficient sampling. The development and commercialization of dedicated micro-SPECT systems is currently receiving increased interest, with several promising players on the market, such as Bioscan with the NanoSPECT/CT (http://www.bioscan.com), MILabs with the U-SPECT-II (http://www.milabs.com), Gamma Medica-Ideas with the X-SPECT^{TM} and FLEX Triumph^{TM} (http://www.gammamedica.com) and Linoview Systems with the LinoView^{TM} miniSPECT (http://www.linoview.com). Pictures of these systems are shown in Fig. 2.4. Bioscan also provides clinical cameras equipped with multipinhole collimators, as in [97]. They call this concept HiSPECT. The design of the pinhole SPECT camera used in this work (Fig. 2.3(a)) was inspired by the same system and therefore looks very similar.

2.2.3 Micro-PET

The principle and composition of a *micro-PET system* is exactly the same as that of a clinical PET camera, except for its reduced size. Since the volume to be imaged is significantly smaller, both the detector crystal size and the radius of the detector ring(s) can be rescaled accordingly (see Fig. 2.5). Where for clinical PET the spatial resolution is dominated by the non-collinearity of the rays emitted by the photon pair (not perfectly 180°) and by the detector size, the effect of the non-collinearity on the resolution is largely reduced for small animal PET due to its small ring diameter. The spatial resolution of the latter system is therefore mainly influenced by the detector size and the positron range of the used isotope, i.e. the distance the positron travels between its origin (at decay) and its annihilation with

an electron, causing the emission of a photon pair [70]. As the positron range of ^{15}O is significantly larger than that of ^{18}F, namely 0.501 mm FWHM and 4.14 mm FWTM (full width at tenth maximum) versus 0.102 mm FWHM and 1.03 mm FWTM, the spatial resolution of any type of PET system is clearly worse when a ^{15}O-tracer is used [70]. Typically, a micro-PET camera has a spatial resolution of 1-2 mm, which is adequate for most small animal imaging applications. In contrast to the resolution of the micro-SPECT systems, this resolution can hardly be improved any further.

2.3 Image reconstruction

In emission tomography (ET), the continuous spatial distribution of the tracer uptake in the patient, also called activity distribution, is measured and typically stored in a 2D or 3D matrix (per time frame in case of a dynamic acquisition), or in list mode (storing each detected event as a separate entry). From these measurements, a 2D or 3D digital representation of this activity distribution can be reconstructed. The two approaches most often used in clinical practice and research are the analytical and the iterative methods, and are discussed below.

2.3.1 Analytical methods

As an illustration of analytical reconstruction methods, we discuss the 2D parallel beam *filtered backprojection* (FBP) algorithm, which can reconstruct the unknown activity distribution $\lambda(x, y)$ from the acquisition of a 2D transaxial plane or slice. This is a generally applicable method, because most fully 3D measurements in ET, such as 3D PET data, can be rebinned into 2D data sets [28]. For the other, intrinsically 3D reconstruction problems, such as pinhole SPECT, cone beam CT and helical CT, as well as for the fully 3D PET reconstruction, alternative analytical algorithms have been derived, which will not be discussed in this section [32,62,64].

The measurement $q(l, \theta)$ of photons emitted from a transaxial slice is usually stored in a 2D matrix, called sinogram, with the polar coordinates l and θ indicating the projection line and the projection or viewing angle, respectively. The projection operation, which is the transformation from the image to the sinogram space corresponding to the measurement, can (for the ideal case) be written as:

$$q(l, \theta) = \int_{(x,y) \in \text{projection line}} \lambda(x, y) dx dy. \tag{2.1}$$

In words, the values of the pixels crossed by projection line l in direction θ are accumulated and stored in $q(l, \theta)$.

The data can be perfectly reconstructed analytically in the ideal case, where no noise, scatter or attenuation are present, the tracer distribution is limited both in support and amount of activity, and the data are measured with sufficient sampling. This reconstruction can be calculated in many equivalent ways, all based on the

Fourier theorem, which states that the 1D Fourier transform (FT) of the projection acquired for angle θ is identical to the central profile along the same angle through the 2D FT of the original distribution.

The most popular analytical reconstruction algorithm is filtered backprojection or FBP. Before describing how it calculates the tracer distribution from the measured data, we first explain the backprojection operation, which is a transformation from sinogram to image space. For every projection angle θ, the measured value $q(l, \theta)$ is added to all pixels crossed by projection line l, or

$$\text{Backproj}(q(l,\theta)) = \int_0^\pi q(x\cos\theta + y\sin\theta, \theta)d\theta \tag{2.2}$$

To obtain the unknown activity distribution, we start from the definition of the inverse FT:

$$\lambda(x,y) = \int_{-\infty}^{+\infty}\int_{-\infty}^{+\infty} \Lambda(\nu_x,\nu_y)\exp^{\imath 2\pi(\nu_x x+\nu_y y)}\, d\nu_x d\nu_y, \tag{2.3}$$

with $\Lambda(\nu_x, \nu_y)$ the 2D FT of $\lambda(x, y)$ and $\imath = \sqrt{-1}$. Transformation from orthogonal to polar coordinates ($\nu_x = \nu\cos\theta$ and $\nu_y = \nu\sin\theta$) yields

$$\lambda(x,y) = \int_{-\infty}^{+\infty} d\nu \int_0^\pi |\nu| d\theta \Lambda(\nu\cos\theta, \nu\sin\theta)\exp^{\imath 2\pi\nu(x\cos\theta+y\sin\theta)}. \tag{2.4}$$

The Fourier theorem can be written as $Q(\nu, \theta) = \Lambda(\nu\cos\theta, \nu\sin\theta)$, with $Q(\nu, \theta)$ the 1D FT in l of $q(l, \theta)$, and because the integrals are interchangeable, (2.4) turns into

$$\lambda(x,y) = \int_0^\pi d\theta \int_{-\infty}^{+\infty} |\nu| d\nu Q(\nu,\theta)\exp^{\imath 2\pi\nu(x\cos\theta+y\sin\theta)}. \tag{2.5}$$

Taking the definition of the backprojection operation (2.2) into account, the expression for FBP is found:

$$\lambda(x,y) = \text{Backproj}\left(\int_{-\infty}^{+\infty} |\nu| Q(\nu,\theta)\exp^{\imath 2\pi\nu(x\cos\theta+y\sin\theta)}\, d\nu\right). \tag{2.6}$$

The algorithm thus consists of filtering the sinogram in the frequency domain with $|\nu|$, called the ramp filter, subsequently taking the 1D inverse FT and backprojecting the result. The ramp filter behaves as a high pass filter, canceling out the blurring effect of the backprojection.

The FBP algorithm could also be considered as an unweighted least squares method, where Gaussian noise distribution is assumed, because the same weight is applied for all viewing angles. It operates entirely linearly on the data. The two main drawbacks of these methods are that neither the Poisson variation underlying the data (i.e. two photon emissions are independent, thus also their measurement), nor the attenuation are taken into account, causing noisy images suffering from streak- and ring-like artifacts, and underestimated isotope concentration in the image center.

To take the effect of attenuation into account, a good estimate of its distribution over the scanned subject should be available. This can be obtained in various ways. From most to least accurate we mention the following techniques: CT acquisition, transmission measurement on a SPECT or PET system using an external source rotating around the patient or phantom, derivation of an attenuation map based on the consistency conditions [81, 129] and correction with a fixed attenuation coefficient (corresponding to water) assigned to all pixels within the body support which can be obtained from a (fast) reconstruction. In PET, the data can easily be precorrected for the effect of attenuation, because along one projection line all photons undergo the same attenuation. For SPECT data, however, attenuation correction is much more complex, due to its depth-dependency (i.e. activity in an image pixel far from the detector is attenuated more than the same activity close-by). As the FBP method is only briefly discussed in chapter 8 in the context of TOF PET, the problems of attenuation and quantification for SPECT reconstruction are not elaborated further. In addition, using the iterative reconstruction techniques, described in the next section, these problems can easily be solved.

2.3.2 Iterative methods

Although FBP is a simple and efficient method, it has several disadvantages when used for emission tomography reconstruction, as mentioned above. One of the problems is that it does not take into account the Poisson nature of the measured data. Therefore, statistical methods were derived that include the statistics of the acquisition in the model. To show how this is done, we start from the expression for the projection operation:

$$r_i = \sum_{j=1}^{J} a_{ij}\lambda_j \approx q_i, \quad i = 1, \ldots, I \tag{2.7}$$

$$\text{matrix notation: } R = A\Lambda \approx Q \tag{2.8}$$

with r_i the expected number of photons to be measured in detector pixel i, a_{ij} the probability that a photon emitted from image pixel j is detected in pixel i, λ_j the unknown activity in pixel j, q_i the measured number of photons in detector pixel i, and I and J the total number of detector and image pixels, respectively. Because the noise in ET is Poisson distributed, the probability, or *likelihood*, of measuring q_i photons if on the average r_i photons are expected can be written as

$$p(q_i|r_i) = \frac{e^{-r_i} r_i^{q_i}}{q_i!}. \tag{2.9}$$

Since the detection of one photon in detector pixel i has no influence on the detection of other photons in different detector pixels (independent data), the probabilities

can simply be multiplied:

$$p(Q|\Lambda) = \prod_i \frac{e^{-r_i} r_i^{q_i}}{q_i!} \tag{2.10}$$

$$\propto \prod_i e^{-r_i} r_i^{q_i}. \tag{2.11}$$

In the next section, it will be explained how this statistical model can be used to obtain a good estimate of the real activity distribution.

Maximum likelihood expectation maximization

The most popular iterative reconstruction method in ET is the *maximum likelihood expectation maximization* algorithm (MLEM) [98]. It consists of two main parts, namely the maximization of the likelihood function (ML), being the goal of the method, and the expectation maximization (EM) algorithm, which is the specific iterative method used to find this maximum.

To simplify the calculations, the logarithmic function is applied to the likelihood (see (2.10)) and combined with (2.7) to yield the expression for the *log-likelihood* $L(Q|\Lambda)$:

$$L(Q|\Lambda) = \sum_i (q_i \ln(r_i) - r_i) \tag{2.12}$$

$$= \sum_i (q_i \ln(\sum_j a_{ij}\lambda_j) - \sum_j a_{ij}\lambda_j). \tag{2.13}$$

Because the logarithmic function is a monotonically increasing function, maximizing the log-likelihood is equivalent to the maximization of the likelihood function. The $\ln(q_i!)$ was dropped because it is independent of λ_j, hence fixed during reconstruction and not contributing to the optimization of the (log-)likelihood. The maximization is done by setting the partial derivatives $\partial L/\partial\lambda_j$ equal to zero, subject to the Kuhn-Tucker conditions necessary and sufficient for non-negativity constrained maximization (i.e. the activity distribution cannot be negative anywhere):

$$\frac{\partial L}{\partial \lambda_j} = \sum_i a_{ij}\left(\frac{q_i}{\sum_k a_{ik}\lambda_k} - 1\right) \begin{cases} = 0, & \text{for } \lambda_j > 0, \\ \leq 0, & \text{for } \lambda_j = 0, \end{cases} \qquad \forall j = 1, \ldots, J. \tag{2.14}$$

These equations are nonlinear in λ_j, and can therefore not be solved directly. Iterative methods are typically used to handle this type of problem.

The most commonly used iterative algorithm in ET is the EM algorithm, because of its simplicity and its guaranteed convergence. This method consists of two steps, namely the *expectation* or *E-step*, and the *maximization* or *M-step*.

In [30] it was shown that to derive the formulas for both steps, a set of complete variables $X = \{x_{ij}\}$, with x_{ij} the unknown number of photons detected in i and originating from j, needs to be introduced. The expected value of x_{ij}, given Λ is

$$E(x_{ij}|\Lambda) = a_{ij}\lambda_j \tag{2.15}$$

The log-likelihood function of the complete variables X can be derived similarly to the log-likelihood of (2.12)-(2.13), and yields

$$L_x(X|\Lambda) = \sum_i \sum_j (x_{ij} \ln(a_{ij}\lambda_j) - a_{ij}\lambda_j). \tag{2.16}$$

In the E-step, the expectation of this new log-likelihood function, given the measurement Q and the current estimate of the activity Λ^{old} is computed:

$$E(L_x(X|\Lambda)|Q, \Lambda^{old}) = \sum_i \sum_j (n_{ij} \ln(a_{ij}\lambda_j) - a_{ij}\lambda_j), \tag{2.17}$$

$$\text{with} \quad n_{ij} = a_{ij}\lambda_j^{old} \frac{q_i}{\sum_k a_{ik}\lambda_k^{old}}, \tag{2.18}$$

and n_{ij} being the expected value of the unknown value x_{ij}. If λ^{old} would have been the perfect estimate of the real activity distribution, $\sum_k a_{ik}\lambda_k^{old}$ would have been equal to the number of measured photons q_i, and n_{ij} would have been equal to $a_{ij}\lambda^{old}$.

In the M-step, the new estimate of Λ, that maximizes the above expectation function, is calculated:

$$\frac{\partial}{\partial \lambda_j} E(L_x(X|\Lambda)|Q, \Lambda^{old}) = \sum_i (\frac{n_{ij}}{\lambda_j} - a_{ij}) = 0. \tag{2.19}$$

Thus,

$$\lambda_j = \frac{\sum_i n_{ij}}{\sum_i a_{ij}}, \tag{2.20}$$

and substitution of (2.18) into (2.20) yields the MLEM algorithm:

$$\lambda_j^{new} = \frac{\lambda_j^{old}}{\sum_i a_{ij}} \sum_i a_{ij} \frac{q_i}{\sum_j a_{ij}\lambda_j^{old}} \tag{2.21}$$

If all voxels of the starting image Λ^{old} are chosen non-negative, the final reconstruction image Λ^{new} will not contain any negative values either. Indeed, both the measurement Q and the probabilities a_{ij} are non-negative, hence the non-negativity contraint of the likelihood maximization is automatically fulfilled.

The EM algorithm for this problem can be seen as an iterative forward-backward projection technique. One rather attractive feature of this method is that the non-negativity constraint is automatically satisfied, providing the initial estimate is entirely non-negative. Pixels that are initially set equal to zero remain zero throughout the reconstruction.

Although MLEM provides superior images compared to FBP, its use is not widespread in clinical routine because of its slow convergence and corresponding long reconstruction times. The two most popular alternatives, being the *ordered subsets* (OS) [55] and the *maximum a posteriori* (MAP) method [50, 52], are elaborated next.

Ordered subsets expectation maximization

The rationale of the ordered subsets method is to group the projection data into an ordered sequence of subsets, each consisting of one or more projection images. Usually these subsets are processed with the EM algorithm (OSEM), but any iterative algorithm can be applied. During reconstruction, the likelihood is maximized as in MLEM, but for each subset the estimate obtained from the previous subset is used as its initial estimate for EM application. One (global) iteration of OSEM is defined as a single pass through all specified subsets. This procedure accelerates convergence by a factor proportional to the number of subsets.

In principle, a projection can be contained in more than one subset. However, it is common practice to use mutually exclusive and exhaustive subsets, in which case each OSEM iteration has a similar computation time to one standard EM iteration. Assigning all projections to a single subset, reduces OSEM to standard MLEM.

As mentioned above, OSEM is very closely linked to MLEM. Therefore, as is the case for MLEM, it is bounded by the natural non-negativity constraint and is applicable in both SPECT and PET. In SPECT, OSEM was proven to provide similar image reconstruction quality with an order of magnitude acceleration over EM [55].

It was found that OSEM reconstruction of noisy projection data does not converge. The convergence properties can be improved by dividing the projection data in balanced subsets, such that the activity of each pixel contributes similarly to any subset. A better balance can be obtained by reducing the number of subsets. A very large number of subsets also increases the noise in the reconstruction image. Thus, for a low number of counts, every subset should contain sufficient data, meaning the number of subsets should not be too high. In addition, it is beneficial to introduce new information as fast as possible. Therefore, projections corresponding to the greatest variability in the image are preferentially chosen first, the perpendicular ones second, and so on.

To assure convergence to an ML solution, OSEM can be applied at a sequence of growing subsets, ending with some iterations of standard MLEM. This *reduced ordered subsets* method is used for most reconstructions mentioned in the subsequent chapters.

Pinhole SPECT data require fully 3D reconstruction, as the projections cannot be rebinned into projection data for 2D reconstruction. The use of standard 3D MLEM is very unappealing, though, because of its long reconstruction time. Therefore, the development of 3D OSEM is recognized as an interesting alternative [116].

In the early days of pinhole SPECT, a 3D FBP algorithm was used to reconstruct the acquired data [32]. However, these deviate strongly from the assumptions FBP was derived for: ideal projections, shift-invariant point spread function and uniform data variance. The reconstruction images suffer therefore from significant streak artifacts. In [59], the standard MLEM iterative algorithm was found to improve the image quality of pinhole SPECT and to suppress the streak artifacts at the cost of long reconstruction time. Similar results were obtained with OSEM, but within

clinically acceptable times [116].

In pinhole SPECT, additional artifacts are present in the non-central slices due to truncation and due to the fact that circular orbit acquisition provides insufficient information for exact reconstruction [112]. Although these artifacts cannot be eliminated completely, (OS)EM can reduce these. With OSEM, also a significant improvement in resolution was established, especially in the axial direction [116]. The improvements in image quality due to OSEM instead of FBP reconstruction are more apparant for pinhole than for conventional parallel hole SPECT [116].

The convergence of OSEM is very non-uniform for pinhole SPECT, hence a high number of iterations is necessary for accurate quantification, and post-filtering with a shift-invariant Gaussian kernel is often required to reduce excessive noise.

Maximum a posteriori or penalized likelihood

There exist several methods to obtain good images with the EM method. The most straightforward one is running MLEM until convergence, followed by some Gaussian post-smoothing to reduce the high frequency noise. However, as mentioned above, this is impracticle due to its slow convergence, unless the OS algorithm is used. A possible, but arguable solution is to stop the reconstruction early, hence not giving the noise the opportunity to accumulate. As convergence is usually not reached, the image will look good, but will not accurately represent the activity distribution. A third, popular method uses a regularizer during reconstruction to speed up convergence and suppress the noise. Instead of maximizing the likelihood, its goal is to maximize the posterior probability $p(\Lambda|Q)$, which takes into account the a priori probability of the isotope concentration. It is therefore called the maximum a posteriori or MAP algorithm [50, 52].

From the rule of Bayes,

$$p(\Lambda|Q) = \frac{p(Q|\Lambda)p(\Lambda)}{p(Q)}, \tag{2.22}$$

we can see that this method includes two important probability models. The first one, the likelihood $p(Q|\Lambda)$, was discussed above. The second one, the prior probability $p(\Lambda)$, provides information about how realistic the current estimate of the isotope distribution is considered to be. It will often give low probability to images with many high frequencies, as they are assumed to be caused by noise. Most priors thus encourage local smoothness in the isotope concentration, e.g. quadratic priors. However, there probably exist as many different priors as there are researchers in this field. The most important ones are the Gibbs-Markov priors [45], among which the quadratic prior and the Huber prior [54] are the most commonly used. Which prior is most suitable for a certain application depends on the typical pattern of isotope concentrations in the examined organs. Indeed, although it is clear that we have some initial idea about the activity distribution, it is hard to translate that into an adequate prior. The probability $p(Q)$ is a fixed value, since the measured data Q do not change during reconstruction. Its value is unknown, but also irrelevant during the maximization process.

Some people give preference to working with a penalty, instead of with a prior distribution. E.g., if the activity distribution contains high frequencies, a penalty can be added to the possibly high (log-)likelihood to disfavor this solution compared to a more smooth one. Again, the sum is maximized iteratively. Such a *penalized likelihood* approach, however, yields exactly the same algorithms as the Bayesian approach discussed above. They are only based on a different philosophy.

As mentioned above, the description of a proper prior distribution $p(\Lambda)$ is difficult, because the uptake in and the location, shape and size of the organs is patient- and time-variant. Therefore, most priors only pairwise compare neighboring pixels, such that the posterior probability is only sensitive to local properties of $p(\Lambda)$ [50]. The most commonly used prior is the quadratic prior:

$$p(\Lambda) = \frac{1}{Z}\exp(-\beta M(\Lambda)), \tag{2.23}$$

$$\text{with } M(\Lambda) = \sum_j \sum_{k\in N_j} w_{jk}(\lambda_j - \lambda_k)^2, \tag{2.24}$$

Z a normalization factor, β the regularization parameter or the weight given to $M(\Lambda)$ the log-prior, N_j the set of neighboring pixels of pixel j, and w_{jk} the weighting factors, usually reflecting the distance to the neighboring pixel k.

The objective function that should be maximized during MAP reconstruction is

$$\Phi(\Lambda, Q) = L(Q|\Lambda) - \beta M(\Lambda). \tag{2.25}$$

Because the objective function is not quadratic, an iterative algorithm is required. As in the ML case, the EM algorithm can be used, albeit in an adapted version. Further details are omitted here, since they are out of the scope of this text.

2.4 Image quality evaluation

Image quality evaluation forms a broad research domain and objective assessment of image quality is not straightforward. Depending on the task, e.g. quantification accuracy or lesion detectability, different techniques and figures of merit (FOMs) should be applied [5]. In this text, we mainly focus on quantification and visualization of small structures.

In emission tomography, and medical imaging in general, the study of image quality can be grouped in three main contexts. First of all, if different cameras or camera setups, e.g. various collimators, are available to image a patient or phantom, one wants to know which one will provide the best image quality. This is, as mentioned above, application-/task-dependent, because the image quality is highly influenced by the size of the subject to be imaged, the tracer uptake and distribution, the energy of the tracer, etc.

Second, it might be interesting to investigate the influence of the acquisition protocol on the image quality. Several parameters could be optimized, such as the

injected dose, the ideal scanning period and the duration of the scan. Although both an increase in injected dose and in scan duration would reduce the noise in the reconstructed image, a trade-off between patient safety and comfort and image quality should be made. Following the ALARA principle (*as low as reasonably achievable*), the amount of radioactivity administered to a patient (or injected in a phantom, which needs to be handled by one or more researchers) should be as low as possible without hampering the image diagnosis.

In addition, for each specific imaging task and tracer, the ideal protocol should be determined before it is used routinely. For flow studies one usually starts the scan simultaneously with the tracer injection, whereas for other studies it might be more interesting to scan when the activity distribution in the regions of interest (ROIs) is stable. This plateau phase can be determined by acquiring data of one subject over a long period of time, i.e. several hours, and plotting the uptake of the tracer in the ROIs as a function of time in a time-activity curve.

Last, the used reconstruction algorithm (see section 2.3) will have a large influence on the image quality. FBP is known to yield an estimate with minimal bias of the activity distribution and provides good quantification accuracy for PET, but suffers from severe streak artifacts. MLEM delivers often biased, but artifact-free images.

In this work, image quality will be studied to evaluate different pinhole SPECT designs (see chapters 4-6) and to compare a conventional PET system to current and future generation TOF PET cameras (see chapter 8) in images with an imposed, uniform target resolution.

The evaluation of image quality can be split up in two main steps, namely the data collection and the data analysis. These will be discussed separately in sections 2.4.1 and 2.4.2, respectively.

2.4.1 Data collection

Before investigating the quality of an image, one should have a clear idea about the study setup, meaning a description of the camera, the imaging protocol, the patient or phantom to be scanned, the tracer used, etc. In addition, it is important to select the data collection method: will the image quality be examined based on *measured data*, or using a simple or more advanced *simulation* technique?

Measurements

The investigation of image quality by measurements (mainly phantom scans) is appealing, since there is nothing more representative to data acquisition than a real measurement. The figure of merit (FOM) under investigation determines the kind of phantom that will be used. Line sources and hot rod phantoms are especially useful for resolution measurements, whereas homogeneous phantoms are more relevant for detecting quantification inaccuracies, artifacts, inhomogeneity, etc. Phantoms

might also contain hot and cold regions with a known contrast compared to a warm background. These are often used for contrast-noise studies.

Simulations

Measurements have the advantage of being very realistic, but they are also quite costly, time-consuming and the results are often noisy, due to the limited acquisition time and activity or due to the small number of scans (for repeated measurements, see section 2.4.2). Computer simulations are therefore a welcome alternative. Additional advantages are the known ground truth and the complete parameter setting freedom.

Simulating a SPECT or PET acquisition can range from modeling the most important camera parameters and responses (see section 3.1) to incorporating all statistical effects encountered by the emitted photons, as in *Monte Carlo simulations*. In conventional computer simulations, typically the camera geometry, the point spread function (PSF) and the sensitivity are modeled. Examples of additional parameters are attenuation, detector response, scatter and decay. Most of these are discussed in section 3.2. In Monte Carlo simulations, millions of photons are simulated and tracked starting from their emission, and taking into account the photon-electron interactions in the patient body and in the detector.

2.4.2 Data analysis

Image quality can be quantified using many different FOMs [5]. Below, we give a brief overview of the image quality quantification measures most often used in emission tomography.

Bias

If an estimator is *biased*, it means that it systematically over- or underestimates the real value of the parameter. This corresponds to positive and negative bias, respectively. Another term for bias is systematic error.

For an image reconstructed from (noiseless) simulated data, the bias can be calculated based on the known true activity distribution. Typically, the difference image between the reconstructed and the true image is plotted next to the true one, to investigate the spatial distribution and the severity of the bias. To quantify the bias as a single value, however, there exist many different approaches. The most simple technique is to take the mean value of the difference image. Alternative options are e.g. the root mean squared deviation (RMSD) and the root mean squared

relative deviation (RMSRD):

$$\text{RMSD} = \sqrt{\frac{\sum_j (\text{recon}_j - \text{original}_j)^2}{J}}, \tag{2.26}$$

$$\text{RMSRD} = \sqrt{\frac{\sum_j (\frac{\text{recon}_j - \text{original}_j}{\text{original}_j})^2}{J}}, \tag{2.27}$$

with recon_j and original_j the j-th pixel value in the reconstructed and original image, respectively, and J the total number of image pixels. The former is most adequate for homogeneous images, whereas the latter might be more appropriate for images with high contrast values.

Resolution

Some phantoms are especially designed for determining the *resolution* of an imaging system, e.g. line sources. Resolution is typically expressed in terms of the full width at half maximum (FWHM) or full width at tenth maximum (FWTM) of profiles through the point spread function or line spread function. This FWHM and FWTM can be calculated as the distance between the two points at which the curve reaches half or one tenth of the curve's maximum. For a Gaussian-shaped curve, the FWHM corresponds to $2\sqrt{2 \ln 2\sigma^2}$, with σ^2 the variance of the Gaussian distribution.

In an image either the FWHM is calculated from the (interpolated) profile through the resolution element (e.g. line source), or a Gaussian is fitted to this profile to get a more accurate estimate, at least if the shape is expected to be Gaussian-like.

Impulse response - contrast recovery coefficient

Another measure to test the quality of an imaging system or reconstruction method is the *impulse response*. It shows how all image pixel values react on a small change in one pixel. The response in that pixel is called the *contrast recovery coefficient (CRC)*. If the impulse response is Gaussian-shaped, as is often approximately the case in emission tomographic images, the CRC-value corresponds to a certain resolution expressed in FWHM, and vice versa. A method to predict the impulse response analytically is discussed later in this section.

For ET, we have to evaluate the system response locally, because of the shift-variant character of both the reconstruction and the imaging system. Therefore, it is no option to work with global measures, such as the modulation transfer function (MTF), which describes the response of a system to an image decomposed into sine waves (having an infinite extent).

Variance

To quantify the noise on the data or in an image, one usually relies on the *variance*. It is a property of the data distribution, expressing how much the data are spread around the mean value. Depending on the information available on the data, three definitions for the variance are commonly used, namely the population variance, the sample variance and the bias-corrected sample variance.

For a variable X with a known distribution $p(x)$, the variance is called the *population variance* σ^2, which is defined as

$$\sigma^2 = \mathrm{Var}(X) = E((X-\mu)^2) = \sum_{i=1}^{N} p(x_i)(x_i-\mu)^2, \tag{2.28}$$

with μ the population mean and $p(x)$ a discrete distribution with N possible values of x_i. For a continuous distribution $p(x)$, the variance can be written as

$$\sigma^2 = \int p(x)(x-\mu)^2 dx. \tag{2.29}$$

If both the mean and the variance have to be estimated from the data themselves, the *sample variance* s_N^2 can be calculated as

$$s_N^2 = \frac{1}{N}\sum_{i=1}^{N}(x_i-\bar{x})^2, \tag{2.30}$$

with $\bar{x}$ the sample mean. This is a biased estimator of the variance. Therefore, the *bias-corrected sample variance* s_{N-1}^2 has been defined:

$$s_{N-1}^2 = \frac{1}{N-1}\sum_{i=1}^{N}(x_i-\bar{x})^2 \tag{2.31}$$

In this work, we decided to use the sample variance as the variance estimator, without bias correction, because we use the noiseless reconstruction as the mean image, which in ET is generally assumed to be a very good estimator for the mean image [6, 19, 130]. Throughout this text, σ^2 is used to denote variance.

Covariance matrix

If one is also interested in how the variation in one variable (e.g. one image pixel value) influences the other variables, and vice versa, one can calculate the *covariance matrix*. It is built up with the covariances between each pair of variables:

$$\mathrm{Cov}(x_i, x_j) = E((x_i-\mu_i)(x_j-\mu_j)) \tag{2.32}$$

An accurate estimation of the variance and covariances requires the reconstruction of multiple replicates of the same sinogram corrupted with different noise realizations. This is also called *repeated simulations*. The relative error on the obtained

standard deviation, i.e. the square root of the variance, is $1/\sqrt{2 * N}$, with N the number of noise realizations.

Another, more efficient, but less accurate method to estimate the variance, is to calculate the variance in a region around the pixel of interest. The large number of pixels in the region cancels the need for repeated simulations. This method should only be applied if the neighboring pixels are uncorrelated, and if the region is truly uniform.

Signal-to-noise ratio and contrast-to-noise ratio

In imaging, usually a trade-off is required between the quantification accuracy and the noise. Therefore, the properties of both are often combined in one FOM, namely the signal-to-noise ratio (SNR), or alternatively, the contrast-to-noise ratio (CNR). The former is used to study how well a signal, e.g. the activity in a voxel or region of interest (ROI), can cope with noise; the latter compares this activity to the surrounding activity. If no background activity is present, or if the signal is defined as the difference with the background, SNR and CNR are identical. Noise is often measured in a ROI in the background, although the variability in the voxel or ROI itself provides a better estimate.

In this work, we calculate the CNR from the properties of the impulse response:

$$\mathrm{CNR} = \frac{\mathrm{CRC}}{\sqrt{\mathrm{variance}}} \tag{2.33}$$

Analytical image quality evaluation methods

Most reconstruction algorithms in ET implicitly define the estimator, which is the reconstruction image $\hat{\Lambda}$. Indeed, it is the maximizer of the likelihood or the posterior probability, and cannot be written as an explicit expression. This means that the properties of the estimator, such as its mean, impulse response or covariance, cannot be expressed analytically either. Therefore, one can either resort to computational methods to calculate these, or try to find approximate analytical expressions for them. In [33, 37], Fessler *et al.* derived such approximations that are generally applicable to implicitly defined estimators, and illustrated their usability for transmission and emission tomographic algorithms. A recapitulation of the derivation of the approximations is given below.

We start from the general expression for a reconstruction algorithm, which is designed to maximize a certain objective function $\Phi(\Lambda, Q)$:

$$\hat{\Lambda}(Q) = \arg\max_{\lambda \geq 0} \Phi(\Lambda, Q) \tag{2.34}$$

The reconstruction algorithm in fact tries to solve $A\Lambda = Q$, with A the system matrix, which corresponds to the projection operation. Because we only consider continuous objective functions, for which the maximum can be found by setting the

first partial derivatives with respect to the first parameter (λ_j) to zero, we can write

$$\frac{\partial}{\partial\lambda_j}\Phi(\Lambda,Q)\bigg|_{\Lambda=\hat{\Lambda}(Q)} \begin{cases} =0, & \text{for } \lambda_j>0, \\ \leq 0, & \text{for } \lambda_j=0, \end{cases} \qquad \forall j=1,\ldots,J. \tag{2.35}$$

For the ease of derivation, we will ignore the non-negativity constraint and the corresponding Kuhn-Tucker conditions further on. By differentiating (2.35) also with respect to the second parameter (q_i) and applying the chain rule, the partial derivatives of an implicitly defined function can be calculated, so

$$\sum_k \frac{\partial^2}{\partial\lambda_j\partial\lambda_k}\Phi(\hat{\Lambda},Q)\frac{\partial}{\partial q_i}\hat{\lambda}_k(Q)+\frac{\partial^2}{\partial\lambda_j\partial q_i}\Phi(\hat{\Lambda},Q)=0. \tag{2.36}$$

In matrix notation, (2.36) becomes

$$\nabla^{20}\Phi(\hat{\Lambda},Q)\nabla_q\hat{\Lambda}(Q)+\nabla^{11}\Phi(\hat{\Lambda},Q)=0, \tag{2.37}$$

where the (j,k)th element of the $J\times J$ operator ∇^{20} is $\frac{\partial^2}{\partial\lambda_j\partial\lambda_k}$, ∇_q denotes the row gradient operator, and the (j,i)th element of the $J\times I$ operator ∇^{11} is $\frac{\partial^2}{\partial\lambda_j\partial q_i}$. If we assume that the symmetric matrix $-\nabla^{20}\Phi(\hat{\Lambda},Q)$ is positive definite, (2.37) can be solved for $\nabla_q\hat{\Lambda}(Q)$. For the special case where the measurement Q equals the noiseless sinogram $\bar{Q}$, it yields

$$\nabla_q\hat{\Lambda}(\bar{Q})=[-\nabla^{20}\Phi(\hat{\Lambda}(\bar{Q}),\bar{Q})]^{-1}\nabla^{11}\Phi(\hat{\Lambda}(\bar{Q}),\bar{Q}) \tag{2.38}$$

This outcome will be useful for the derivation of approximations for the mean, impulse response and covariance.

Mean. In [33], the approximation for the mean of an implicitly defined estimator was shown to be a complex combination of higher-order partial derivatives, and will not be discussed here. However, for ET, the MLEM and MAP reconstruction of the noiseless sinogram $\bar{Q}$ are considered to be very good estimates for the mean of many noisy projection data sets [6, 19, 130]. Therefore, they can be assumed to be locally linear.

$$\mu(\hat{\Lambda}(Q))\approx\hat{\Lambda}(\bar{Q}) \tag{2.39}$$

Impulse response. As in ET the MLEM and MAP reconstructions are shift-variant and nonlinear, the global impulse response cannot be described and we need to resort to the use of the *local impulse response*, which is defined as

$$\begin{aligned} l^j(\Lambda) &= \lim_{\delta\to 0}\frac{\mu(\hat{\Lambda}(Q(\Lambda+\delta e^j)))-\mu(\hat{\Lambda}(Q(\Lambda)))}{\delta} \\ &= \frac{\partial}{\partial\lambda_j}\mu(\hat{\Lambda}(Q)) \end{aligned} \tag{2.40}$$

with e^j denoting the j-th unit vector, which is an array of length J with a value 1 in the element corresponding to pixel j and 0 in all others. Substituting (2.39) into

(2.40), yields the more efficient *linearized local impulse response* (LLIR)

$$\begin{aligned} l^j(\Lambda) &\approx \lim_{\delta \to 0} \frac{\hat{\Lambda}(\bar{Q}(\Lambda + \delta e^j)) - \hat{\Lambda}(\bar{Q}(\Lambda))}{\delta} \\ &= \frac{\partial}{\partial \lambda_j} \hat{\Lambda}(\bar{Q}(\Lambda))) \end{aligned} \tag{2.41}$$

Applying the chain rule to (2.41) and substituting (2.38) in it, provides the following general approximation for the LLIR of an estimator $\hat{\Lambda}(Q)$ [37]

$$\begin{aligned} l^j(\hat{\Lambda}) &\approx \nabla_q \hat{\Lambda}(\bar{Q}(\Lambda)) \frac{\partial}{\partial \lambda_j} \bar{Q}(\Lambda) \\ &= [-\nabla^{20} \Phi(\hat{\Lambda}(\bar{Q}), \bar{Q})]^{-1} \nabla^{11} \Phi(\hat{\Lambda}(\bar{Q}), \bar{Q}) \frac{\partial}{\partial \lambda_j} \bar{Q}(\Lambda) \end{aligned} \tag{2.42}$$

For MAP reconstruction, the objective function $\Phi(\Lambda, Q)$ is defined as in (2.25):

$$\Phi(\Lambda, Q) = L(Q|\Lambda) - \beta M(\Lambda) \tag{2.43}$$

with $L(Q|\Lambda)$ the log-likelihood function of (2.13). From these equations, we can calculate the partial derivatives required for the LLIR approximation:

$$-\nabla^{20} L(Q|\Lambda) = A^T D \left[\frac{q_i}{\bar{q}_i^2(\Lambda)} \right] A \tag{2.44}$$

$$\nabla^{11} L(Q|\Lambda) = A^T D \left[\frac{1}{\bar{q}_i(\Lambda)} \right] \tag{2.45}$$

where A and A^T represent the projection (see (2.8)) and backprojection operator, respectively, and $D[.]$ is a diagonal matrix. Substitution of the above equations into (2.42) yields

$$l^j(\hat{\Lambda}) \approx \left[A^T D \left[\frac{\bar{q}_i(\Lambda)}{\bar{q}_i^2(\hat{\Lambda}(\bar{Q}))} \right] A + \beta \boldsymbol{U}(\hat{\Lambda}(\bar{Q})) \right]^{-1} A^T D \left[\frac{1}{\bar{q}_i(\hat{\Lambda}(\bar{Q}))} \right] A e^j, \tag{2.46}$$

with $\boldsymbol{U}$ the Hessian of the log-prior. As the projection is a smoothing operation, the expected measurement of the unknown activity distribution is very similar to the expected measurement of noiseless data reconstruction ($\bar{Q}(\Lambda(Q)) \approx \bar{Q}(\hat{\Lambda}(\bar{Q}))$). Therefore, in the specific case of emission tomography, the LLIR approximation for MAP estimators is

$$l^j(\hat{\Lambda}) \approx \left[\boldsymbol{F} + \beta \boldsymbol{U}(\hat{\Lambda}(\bar{Q})) \right]^{-1} \boldsymbol{F} e^j, \tag{2.47}$$

$$\text{with} \quad \boldsymbol{F} = A^T D \left[\frac{1}{\bar{q}_i(\Lambda)} \right] A, \tag{2.48}$$

which is called the Fisher information matrix $\boldsymbol{F}$.

The Fisher information measures the amount of information that an observable random variable, here the measurement Q, carries about an unknown parameter, in our case the activity distribution Λ. Its calculation is based on the second derivative of the log-likelihood function $L(Q|\Lambda)$ to the unknown parameter:

$$F(\Lambda) \triangleq -E\left(\frac{\partial^2 L(Q|\Lambda)}{\partial \Lambda^2}\right) \tag{2.49}$$

As reconstruction corresponds to the maximization of the likelihood, which is equivalent to setting all first derivatives to zero (see (2.14)), the information about the quality of the estimator is contained in the second derivatives. The Fisher information can thus also be seen as a measure of the sharpness of the peak of the (log-)likelihood curve plotted as function of Λ, so of the curvedness near the maximum likelihood estimate $\hat{\Lambda}$. A rather flat curve corresponds to a low second derivative and a low amount of information. A sharp maximum, on the contrary, indicates that the observable random variable, i.e. the measurement Q, contains much information, or alternatively, that the reconstruction problem is well-posed. Also interesting to remark, is that the inverse of the Fisher information defines the lower bound on the variance of estimators of a deterministic parameter λ. This means that the variance of any unbiased estimator $\hat{\lambda}$ is at least as high as the inverse of the Fisher information:

$$\mathrm{Var}(\hat{\lambda}) \geq \frac{1}{F(\lambda)} \tag{2.50}$$

This inequality is also known as the Cramér-Rao lower bound [25]. If there is more than one parameter, e.g. matrix Λ, the above can be generalized by saying that

$$\mathrm{Var}(\hat{\Lambda}) - F(\Lambda)^{-1} \tag{2.51}$$

is positive semidefinite, with $F(\Lambda)$ the Fisher information matrix.

Covariance. To find an appromation for the covariance matrix, we start from the first-order Taylor expansion of the estimator $\hat{\Lambda}(Q)$

$$\hat{\Lambda}(Q) \approx \hat{\Lambda}(\bar{Q}) + \nabla_q \hat{\Lambda}(\bar{Q})(Q - \bar{Q}) \tag{2.52}$$

Taking the covariance of both sides, results in

$$\mathrm{Cov}(\hat{\Lambda}(Q)) \approx \nabla_q \hat{\Lambda}(\bar{Q}) \cdot \mathrm{Cov}(Q) \cdot [\nabla_q \hat{\Lambda}(\bar{Q})]^T \tag{2.53}$$

Combining (2.38) with (2.53) yields the general approximation for the covariance matrix of an estimator $\hat{\Lambda}(Q)$ [33]

$$\begin{aligned} \mathrm{Cov}(\hat{\Lambda}(Q)) \quad \approx \quad & [-\nabla^{20}\Phi(\hat{\Lambda}(\bar{Q}), \bar{Q})]^{-1} \cdot \nabla^{11}\Phi(\hat{\Lambda}(\bar{Q}), \bar{Q}) \cdot \mathrm{Cov}(Q) \\ & \cdot [\nabla^{11}\Phi(\hat{\Lambda}(\bar{Q}), \bar{Q})]^T \cdot [-\nabla^{20}\Phi(\hat{\Lambda}(\bar{Q}), \bar{Q})]^{-1} \end{aligned} \tag{2.54}$$

Inserting (2.44) and (2.45) into (2.54) and assuming that $\bar{Q}(\Lambda(Q)) \approx \bar{Q}(\hat{\Lambda}(\bar{Q}))$, yields the covariance matrix approximation for MAP estimators in the special case of ET:

$$\mathrm{Cov}(\hat{\Lambda}(Q)) \quad \approx \quad \Big[\boldsymbol{F} + \beta \boldsymbol{U}(\hat{\Lambda}(\bar{Q}))\Big]^{-1} \boldsymbol{F} \Big[\boldsymbol{F} + \beta \boldsymbol{U}(\hat{\Lambda}(\bar{Q}))\Big]^{-1} \tag{2.55}$$

Note. Above we discussed the derivation of efficient approximations for the LLIR and the covariance of a voxel. To compare two systems, however, one should fix e.g. the resolution of the system response. As this response is shift-variant, a method is required to impose a fixed target resolution in every voxel. In chapter 4, we proposed similar approximations for the LLIR and the covariance, which use an isotropic post-smoothing filter as a regularization parameter instead of the above used prior, and thus approximate post-smoothed MLEM instead of MAP, because this makes fixing the resolution straightforward. Although with this method the image quality obtainable with a system can be optimized for a specific spatial resolution, this method can also be used to evaluate the performance of such optimized system at other resolutions.

2.5 Conclusion

The basic principles of functional imaging in nuclear medicine have been discussed in this chapter. After providing an overview of the various cameras, for human as well as for small animal imaging, the most commonly used reconstruction algorithms for emission tomography have been explained with their advantages and disavantages. Difference was made between analytical and iterative methods. Finally, the main topic of this work, image quality evaluation, has been presented. The problem was split up into two steps, namely data collection and data analysis. For the former, the importance of realism, obtained with measurements, was weighted against the parameter freedom and the availability of the golden standard with simulations. For data analysis, the most often used figures of merit were briefly explained, together with some simple and efficient methods to calculate them.

Chapter 3

Single and multipinhole SPECT reconstruction

Due to the different collimator design, pinhole SPECT has its own specific properties concerning image acquisition and reconstruction, compared to conventional SPECT. Therefore, adapted models for the camera geometry, the sensitivity and the forward and backward projection are required. These are discussed in section 3.1. Obviously, the acquired data also suffer from the same, or at least very similar, physical detrimental effects as regular SPECT measurements, mainly due to interaction of photons with matter. Correction methods for scatter, attenuation, decay and crosstalk, that were implemented in the pinhole SPECT software to improve the reconstruction image quality and to enable quantification, are described in section 3.2.

3.1 Camera modeling

3.1.1 Camera geometry modeling

Equipping a gamma camera with a pinhole collimator allows imaging with a spatial resolution superior to the intrinsic detector resolution R_i. Indeed, if the subject to be imaged is positioned close to the collimator compared to the distance between the collimator and the detector, the projection of the activity distribution is magnified onto the detector (see Fig. 2.3(b)), hence reducing the influence of R_i on the system spatial resolution. This magnification restricts the field of view (FOV) to a smaller volume, limiting the use of pinhole SPECT for patients to e.g. thyroid imaging, but making it ideal for small animal imaging. In the case of a clinical camera, the commercial software provides the geometrical acquisition parameters with sufficient accuracy for regular patient imaging with a resolution of 5-10 mm FWHM. However, for high-resolution pinhole SPECT imaging, a more accurate estimate of these parameters is required.

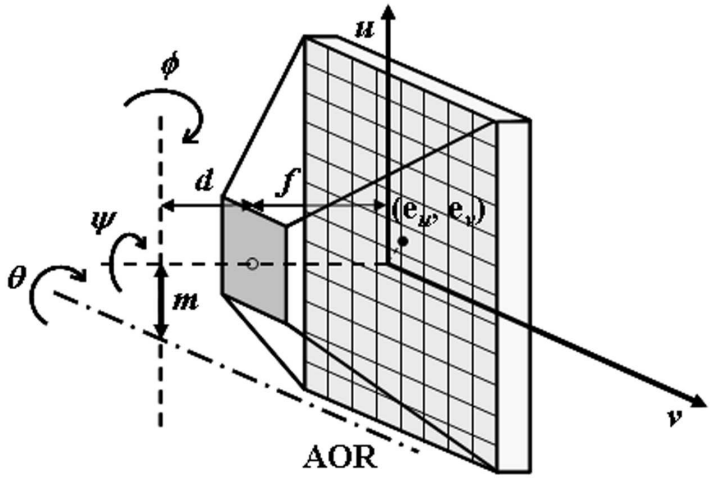

Figure 3.1: Illustration of the acquisition geometry parameters.

For the description of the acquisition geometry of a single aperture system with a detector performing a perfect circular motion, 7 parameters are sufficient and required [83, 96]. This can easily be understood as follows. A camera detector has 6 degrees of freedom (3 translations and 3 rotations), and a pinhole has 3 additional degrees of freedom (3 translations). The rotation angle θ around the axis of rotation (AOR) can however be incorporated by fixing the starting angle. The position along the axial direction can be chosen arbitrarily. Consequently, 7 degrees of freedom remain, which can be parameterized in many ways. Our choice of parameters is illustrated in Fig. 3.1. They can be divided into two groups. The *intrinsic parameters* are the focal length f, i.e. the distance between the aperture and the detector, and the electrical shifts e_u and e_v, which represent the global shift of the projection image with respect to the detector pixels, caused by drift of the detector hardware. These parameters are independent of the detector position. The *extrinsic parameters* d, m, ϕ and ψ depend on the position of the detector with respect to the AOR. Parameter d defines the distance between the aperture and the AOR, measured along the central ray (which is defined as the pinhole projection ray orthogonal to the detector), m is the mechanical offset, being the distance between the central ray and the AOR. The tilt angle ϕ and twist angle ψ represent the rotation in a plane parallel to the rotation axis and the central ray, and the rotation of the detector around the central ray, respectively. Here, all parameters are assumed to remain constant during acquisition. An extended procedure to deal with parameter variation is presented later.

Single pinhole calibration

The topic of single pinhole calibration of a circularly rotating camera detector has extensively been studied in the past, not only for pinhole SPECT, but also in the

context of cone beam CT. Mathematically, these two problems are identical. In [11], Bequé *et al.* showed that the acquisition of three non-collinear point sources, with 2 distances between the point sources known, is necessary and sufficient to uniquely determine all 7 parameters. Assuming that the camera motion is reproducible, we scan the calibration phantom immediately after the animal SPECT scan, using the same collimator and acquisition setup (except for shorter scan duration). To derive the geometrical parameters from the measurement, a projection based on an initial guess of the parameters is simulated, and fitted to the centers of the measured point projections using a simple least squares Powell algorithm (see section 10.5 in [91]). Due to the noise on the data, the fit might get stuck in a local optimum, but in practice very good image quality is obtained with this calibration method. It was seen that some parameters are heavily correlated [11], but that correlated errors usually have little influence on the image quality.

Because of the large magnification, small deviations from the circular orbit (e.g. due to gravity) might have a significant effect on the image quality and spatial resolution. Several methods have been developed to cope with these deviations, either by modeling the global additional movements, or by estimating the small translations and rotations in every projection angle based on the measurement. In [12], e.g., the oscillation of the detector was modeled by a sinusoidal variation of the tilt angle as a function of the projection angle. This model was adequate for the presented single head DSX camera (SMV). Of course, the deviations are very camera-dependent, hence a good model for one system, might be useless for another. In [29], a more generally applicable method was proposed. After an initial regular calibration, assuming perfect circular motion, the deviations modeled as small translations and rotations are calculated for every viewing angle using a singular value decomposition. A similar method, using a least squares fitting algorithm, is presented in section 6.2.3.

Multipinhole calibration

When the pinhole collimator consists of multiple apertures, additional information is available for geometrical calibration. Wang *et al.* showed that for multipinhole SPECT two point sources are generally sufficient, without the need to know the distance between them [126]. This means that a simultaneous animal and calibration scan becomes more feasible, and requires nothing more than two easily discernable point sources to be attached to the animal bed. In the appendix of [121], we gave an equivalent derivation, based on the parameters of Fig. 3.1 and the parameterization of [11]. A more extended explanation is provided in appendix A.

In [126], good results were reported with this simplified calibration method. In our, so far limited, experience with this method, we noticed that the addition of knowledge about either the distance between the point sources or the distance between the apertures strongly stabilized the optimization problem in the presence of noise. Additional simulation and phantom experiments are required to study the properties of this calibration procedure in more detail.

Although the above described calibration methods have mainly been tested for

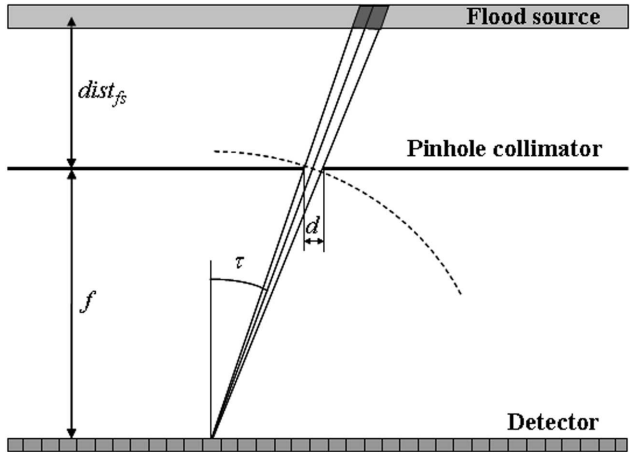

Figure 3.2: Illustration of the pinhole sensitivity calculation for one detector pixel, in the case of an ideal single pinhole collimator.

data of clinical gamma cameras equipped with pinhole collimators, they are equally well suited for dedicated micro-SPECT systems using rotating or stationary planar detectors.

3.1.2 Sensitivity

Sensitivity is commonly defined as the probability that the activity in point j is detected on the detector. However, in this work, we define the *pinhole sensitivity* as the amount of activity measured through the pinhole aperture when a flood source (i.e. a homogeneous planar source) of 1 Bq/unit area is positioned in front of the pinhole collimator (at a random distance). It has the advantage to be easily measurable and it can be used to calculate the point source sensitivity.

Analytical modeling

In the case of an ideal pinhole collimator (an infinitely thin, perfect absorber with a circular opening, see Fig. 3.2), the pinhole sensitivity can easily be calculated analytically for every detector pixel i. If we first assume that the detector pixel is infinitely small and that the flood source thickness is relatively small compared to its distance to the detector, the detectable activity area (of the dark gray part in Fig. 3.2) is:

$$\text{area} = \left(\frac{dist_{fs} + f}{f}\right)^2 \Psi, \tag{3.1}$$

with $dist_{fs}$ and f the distance from the pinhole to the activity source and to the detector (i.e. the focal distance), respectively, $\Psi = \pi(d/2)^2$ the area of the pinhole

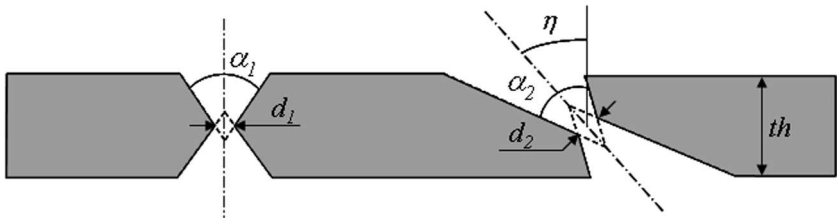

Figure 3.3: Illustration of the typical pinhole apertures: (left) non-inclined and (right) inclined aperture.

opening, and d the aperture diameter. This detectable area is independent of the angle τ between the incoming ray and the normal on the detector. One should note that, because photons are emitted isotropically, the amount of photons emitted from this area and measured in an infinitely small pixel i is equal to the amount of photons that would be detected in this area if all activity present in the detectable area was positioned in pixel i. From the latter point of view, the calculation of the pinhole sensitivity is straightforward. Indeed, the measured amount of photons is then determined by the fraction of the area of a sphere, with its origin in pixel i and radius $(dist_{fs} + f)/\cos\tau$, that is covered by the detectable area (= last factor of the equation):

$$\text{sensitivity in pixel } i = \iint_i dudv \cdot \rho_{area} \cdot \frac{\text{area} \cdot \cos\tau}{4\pi \left(\frac{dist_{fs}+f}{\cos\tau}\right)^2} \tag{3.2}$$

$$= \rho_{area} \cdot \frac{\Psi \cos^3\tau}{4\pi f^2} \cdot \Delta u \cdot \Delta v \tag{3.3}$$

with ρ_{area} the flood source activity per unit area, which is assumed 1 Bq/unit area in sensitivity calculations, and Δu and Δv the dimensions of the detector pixels. As can be seen from this equation, the sensitivity, as it is discussed here, is not a function of the distance between the source and the pinhole collimator ($dist_{fs}$). Note that this is different from the more frequently used definition of pinhole sensitivity.

Real pinhole collimators, however, have a finite thickness th, and the pinhole apertures usually consist of two mirrored, coaxial, truncated cones (see Fig. 3.3). In multipinhole collimators, some of the pinholes might be inclined to image the same FOV as the central one (see Fig. 3.3 (right)). These two kinds of pinholes are most common and are called *knife-edge pinholes*. The top angle of such truncated cone is called the *acceptance angle* α of the pinhole. The inclination angle with respect to the normal is denoted as η. Because of the finite thickness of the collimator, some rays will penetrate through the material, with a probability that decreases exponentially with increasing length of penetrated collimator material. Therefore, (3.3) is not a realistic model for the sensitivity. In [99], suggestions were made about how to include the penetration in the model. As the penetrating rays make the pinhole seem larger, an effective diameter d_{eff} can be calculated and used

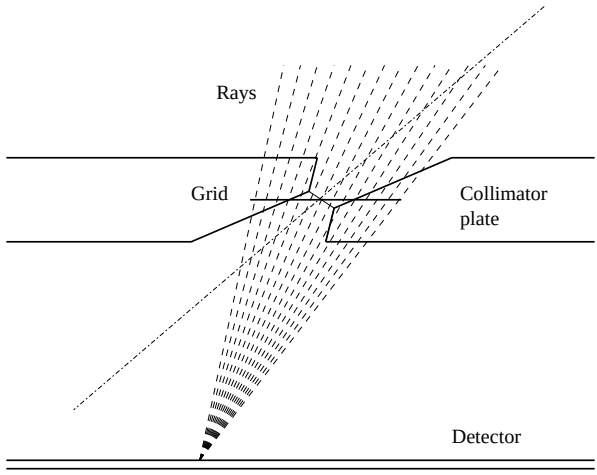

Figure 3.4: Illustration of the sensitivity calculation method for realistic pinhole apertures.

instead of the exact diameter d. In addition, the penetration depends on the angle of the incoming ray τ. Therefore, the third power of the cosine is better replaced by $n_p > 3$, which can be found by fitting the sensitivity to a measurement. Thus, (3.3) becomes

$$\text{sensitivity in pixel } i = \rho_{area} \cdot \frac{\Psi_{eff} \cos^{n_p} \tau}{4\pi f^2} \cdot \Delta u \cdot \Delta v \tag{3.4}$$

with $\Psi_{eff} = \pi(d_{eff}/2)^2$. Unfortunately, this simple model is not really appropriate for inclined apertures and/or apertures with a small α. In addition, it cannot be used to predict the sensitivity for new pinhole aperture designs, since it requires a fit to a measurement. Hence, there is a need for a more accurate sensitivity model.

If the geometry and the material of the pinhole collimator are known, the sensitivity can be calculated analytically, using a ray-tracing method. We have implemented a method that is very similar to the one described in [97], but starts from a detector pixel instead of an image voxel. The principle is shown in Fig. 3.4. Starting from each detector pixel, a finite number of rays through a rectangular grid is considered. This grid lies in the plane through the pinhole center and parallel to the collimator planes (and the detector), and is centered around the pinhole center. The fraction of photons that penetrates through the collimator material is calculated by defining the intersection length l_r of each ray with the pinhole collimator:

$$\text{penetration fraction} = \exp(-\mu l_r), \tag{3.5}$$

with μ the linear attenuation coefficient for the collimator material, usually tungsten. As the pinhole aperture is now sampled by a grid of rays, the effective aperture

area can be defined as

$$\Psi_{eff} = \iint_{g} dg_x dg_z w(g_x, g_z, \tau), \tag{3.6}$$

with g the complete grid area, g_x and g_z the coordinates of the grid sampling point, and $w(g_x, g_z, \tau)$ the penetration fraction of the ray under angle τ through point (g_x, g_z) as calculated from (3.5). The effective area thus depends on the angle τ of the incoming rays, hence it should be recalculated for every single detector pixel to obtain the complete sensitivity image. To speed up the calculation time, one can exploit the symmetry of the pinhole aperture in some cases. For each individual pinhole aperture of a single or multipinhole collimator, the sensitivity is calculated individually. For symmetrical designs, the sensitivity of an aperture can be reused for another aperture by a simple mirroring operation.

Sensitivity measurements

If one wants to compare the calculated sensitivity for a pinhole aperture to a measured sensitivity image, the activity of the flood source ρ_{area} (in Bq/unit area), the measurement time t and a correction factor cf need to be taken into account. This correction factor compensates for the branching factor (i.e. the expected number of emitted photons with photopeak energy per disintegration) and for the finite thickness of the crystal, for example. The activity that will be measured in detector pixel i then yields

$$\text{measurement in pixel } i \ = \rho_{area} \cdot t \cdot cf \cdot \iint_{g} \frac{dg_x dg_z w(g_x, g_z, \tau) \cos^3 \tau}{4\pi f^2} \cdot \Delta u \cdot \Delta v \tag{3.7}$$

where $\cos^3 \tau$ is written instead of $\cos^{n_p} \tau$, because the angle-dependent penetration is contained in $w(g_x, g_z, \tau)$.

In collaboration with the university of Ghent, the accuracy of this analytical sensitivity calculation method was investigated by comparing it to Monte Carlo simulations and measurements [103]. In Fig. 3.5, horizontal (left column) and vertical profiles (right column) through the sensitivity images are shown for both a central, non-inclined (top row) and an eccentric, inclined pinhole aperture (bottom row). These profiles were normalized to their respective integral for qualitative comparison. For the central pinhole, the profiles closely match. For the inclined aperture, the mismatches between the different methods are somewhat larger. The main differences between the measured sensitivity on the one hand and the simulated and calculated sensitivity on the other hand can be attributed to fabrication errors and inaccuracies. A clear example is shown in Fig. 3.6, where a measured sensitivity (left) is compared to the calculated sensitivity (center). The difference image (right) indicates the location of the manufacturing error where the aperture deviates from the assumed conical shape. Tungsten, which is most commonly used for pinhole collimation because of its high attenuation coefficient, is difficult to process. First, the central hole is drilled. Next, either the knife edges are produced

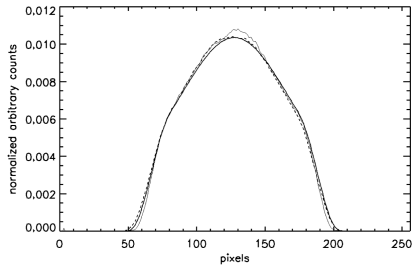

(a) Central, non-inclined pinhole; horizontal profile (row = 100)

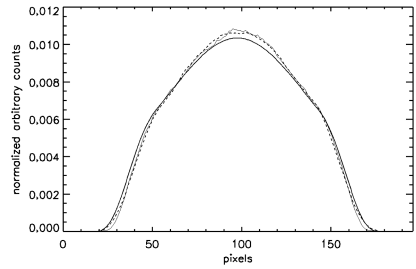

(b) Central, non-inclined pinhole; vertical profile (column = 128)

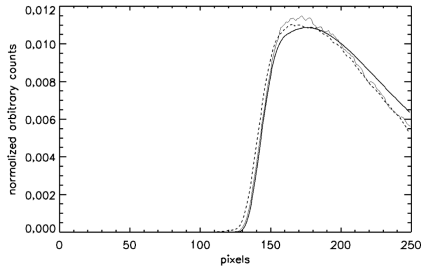

(c) Eccentric, inclined pinhole; horizontal profile (row = 170)

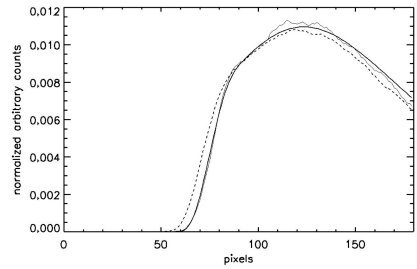

(d) Eccentric, inclined pinhole; vertical profile (column = 200)

Figure 3.5: Horizontal and vertical profiles through the sensitivity images of a central, non-inclined ((a) horizontal profile (row = 100) and (b) vertical profile (column = 128)) and an eccentric, inclined pinhole aperture ((c) horizontal profile (row = 170) and (d) vertical profile (column = 200)). Three methods to obtain the pinhole sensitivity are compared: calculation (thick line), Monte Carlo simulation (normal line) and measurement (dashed line) (see Fig. 2 in [103]).

using a cone-shaped drill, or using a technique called *spark erosion*. Heavily inclined pinholes have a very short and a very long edge (see Fig 3.3 (right)) and are therefore more prone to production errors. Most mechanical job-shops recommend spark erosion to produce these apertures, because accurately drilling at such angles is hard and the cones of standardized drills are not long enough to create the long edge. For spark erosion, the maximum allowed angle with respect to the normal is usually 45°. Another possibility is to make use of inserts [8,108]. This is especially interesting when very small diameters are required (< 1 mm). Often gold is used for these inserts, because of its superior photon-stopping power compared to tungsten [108,113]. Indeed, the (knife-)edge penetration becomes increasingly important with decreasing aperture diameter. Thanks to the relatively small amount of material necessary for the inserts, compared to the whole pinhole plate, a gold-tungsten combination might still be affordable for some pinhole designs, given the current record prices for gold. However, the multipinhole designs proposed in this work

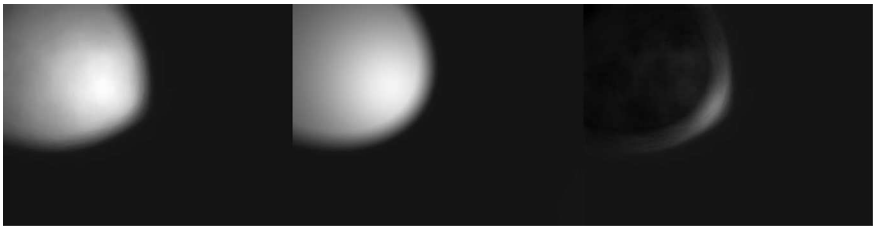

Figure 3.6: Example of difference between measured and calculated sensitivity due to manufacturing errors: (left) measurement, (center) calculated sensitivity and (right) difference image.

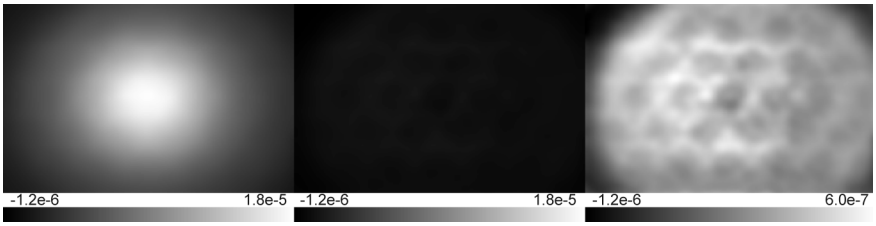

Figure 3.7: Example of the non-uniform response of the PMTs to a ^{99m}Tc flood source measured with a single pinhole collimator with 3 mm aperture diameter: (left) sensitivity measurement, (center) difference image between measurement and calculation using the same scale as for the measurement, and (right) difference image rescaled to its own minimum and maximum.

consist of apertures with very large inclination angles, and therefore would require a significantly large amount of gold, resulting in a high additional cost. The mismatch of the calculated sensitivity with respect to the other two sensitivity images is probably due to the lower efficiency at the edges of the crystal. The analytical calculation method does not model the material properties of the NaI(Tl) crystal, but assumes a perfect absorber. This assumption is least accurate at the detector edges. In the Monte Carlo simulation, the crystal was included in the model, hence the corresponding profiles better match those of the measurement at the detector edges than the profiles of the calculated sensitivity. A measurement can also suffer from the non-uniform response of the photomultiplier tubes (PMTs) to flood source irradiation, as illustrated in Fig. 3.7. At the left, a sensitivity measurement (^{99m}Tc) through a 3-mm diameter single pinhole is shown. In the center, the difference between the measurement and the calculated sensitivity is plotted using the same scale. At the right, this same image is presented after rescaling it to its own extrema. In this image, the non-uniform PMT response is clearly visible (each circle corresponds to one PMT). The central image indicates its very low contribution, though.

Because of these often present deviations between the calculated and measured sensitivity, the latter one is standardly used for reconstructions of measured pinhole

SPECT data. Another advantage of using the measured pinhole sensitivity is that it intrinsically contains information about the non-uniform detector response. The sensitivity needs to be acquired for every aperture separately (or multiple in parallel, if their projection images do not overlap), and the measurement has to be repeated for every different isotope-energy window setting combination. Next, these measured projection images are processed as follows. If necessary, the projection image is first masked to discard activity elsewhere on the detector seen through other pinholes. For our measurements, the data are acquired in a 256×256 matrix. However, the pinhole collimator blocks part of the crystal, such that the image can be cropped. Furthermore, the measurement is corrected for scatter and decay (see sections 3.2.1 and 3.2.3). To reduce the noise in the measurement, a high amount of tracer activity is measured for a sufficiently long period of time, usually around 37 MBq (= 1 mCi) in a recipient of 22.1 mm diameter ($\approx$ 96 kBq/mm^2 = 2.6 μCi/mm^2) during 10 min/aperture. To normalize the sensitivity image to represent a measurement of a flood source with an activity of 1 Bq/unit area, both a time and a flood source activity and area correction is applied (see (3.7)). The correction factor cf can then be found by analytically calculating the sensitivity image and scaling it to the measurement with a least squares fit. It gives an idea about the activity passing through the crystal. For ^{99m}Tc cf is about 0.7, whereas it is about 0.35 for ^{123}I. The latter has the additional difficulty that the dose is hard to calibrate accurately in a dose calibrator optimized for ^{99m}Tc. Depending on the shape and material of the recipient, e.g. a syringe or a vial, already a factor of two in dose can be perceived. Care must thus be taken when calculating a correction factor. To further suppress the noise, a broad median filter is used for the data acquired in the photopeak energy window (to preserve the steap edges of the sensitivity profiles) and a modest Gaussian smoothing filter was applied to the data acquired in the scatter energy window(s) before scatter correction (see section 3.2.1 for an explanation on the different energy windows).

To assure the reconstructed images will be quantitatively correct, a homogeneous cylinder with known activity concentration is measured and reconstructed using the processed measured sensitivities. Because cf is quite sensitive to the noise, it can slightly vary over the different apertures of the same pinhole collimator, although the same flood source was used for all of them. Therefore, the measurements were not corrected for the fitted cf and used as such during projection and backprojection. As the concentration in the cylinder is accurately known, a global scale factor can be calculated to correct the values in the reconstruction. This scale factor is applicable for all measurements performed with the same pinhole collimator, isotope and energy window setting.

3.1.3 Projection/backprojection

As was already explained in section 2.3, image reconstruction requires a good model for the projection and the backprojection. This corresponds to finding a mapping operation from the image space to the sinogram space and back. Two main approaches can be followed: *voxel-driven* and *ray-driven*.

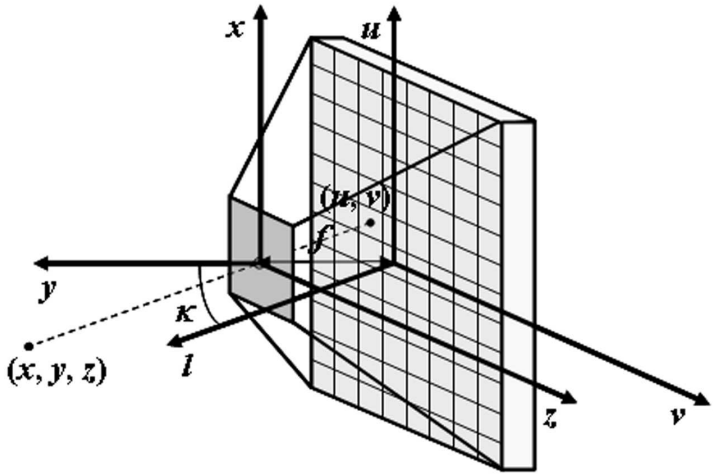

Figure 3.8: Illustration of the different coordinate systems for the voxel-driven and the ray-driven method.

Voxel-driven approach

In the voxel-driven approach, it is determined for every image voxel where it is projected on the detector. The activity of that voxel will then be assigned to that detector location during the projection operation. This location can be one detector pixel (nearest neighbor interpolation), 4 pixels with a weight obtained with bilinear interpolation, or, even better, a larger region of pixels by modeling the size of the pinhole aperture. This mapping operation from the image to the projection space is denoted with $M_{ap}((x, y, z) \mapsto (u, v))$. Because in pinhole SPECT every voxel is seen with a different sensitivity, a 3D sensitivity map $S_{ap}(x, y, z)$, representing the probability that a photon emitted in voxel (x, y, z) is detected through aperture ap, should be calculated and stored for every aperture. For ease of calculation, the coordinate system is fixed to the pinhole collimator (see Fig. 3.8) and the reconstruction image Λ is rotated by projection angle $\pm\theta$ in each forward and backprojection step. Hence, the same mapping operation and sensitivity map can be used for every projection angle. The projection $Q_{ap}(u, v, \theta)$ through that aperture at projection angle θ can then be expressed as:

$$Q_{ap}(u, v, \theta) = \iiint dxdydz \cdot S_{ap}(x, y, z) \cdot \Lambda(x, y, z, \theta) \cdot M_{ap}((x, y, z) \mapsto (u, v)) \quad (3.8)$$

$\Lambda(x, y, z, \theta)$ is written as a (synthetic) 4D image, but can be calculated from the 3-dimensional activity distribution by rotating it by every projection angle θ. As mentioned above, M_{ap} is the mapping function, indicating which voxels contribute to the projection and to what extent. For each aperture ap, the sensitivity of the

detector for voxel (x, y, z) can be calculated very similarly to (3.4) and (3.6):

$$S_{ap}(x,y,z) = \rho_{vol} \cdot \frac{\Psi_{eff} \cos^3 \tau}{4\pi y^2} \cdot \Delta x \cdot \Delta y \cdot \Delta z, \tag{3.9}$$

$$\text{with } \Psi_{eff} = \iint\limits_{g} dg_x dg_z w(g_x, g_z, \tau), \tag{3.10}$$

where ρ_{vol} is the activity per unit volume in the voxel, y is the distance between the aperture and voxel (x, y, z), and Δx, Δy and Δz are the dimensions of the voxels. Equation (3.9) shows that indeed the sensitivity is distance-dependent for the voxel-driven method. In section 3.1.2, it was explained that even a 2D sensitivity image calculation is very time-consuming. One could argue that it can be calculated in advance and stored. However, the distance between the pinhole collimator and the center of rotation varies from scan to scan. Hence, a sufficiently large 3D sensitivity map should be available and extra interpolation errors will be introduced by positioning it correctly in the image space. In addition, analytical sensitivity modeling is not always sufficiently accurate, especially for multipinhole systems (see section 3.1.2), and measuring the detector response throughout the image space is very unpractical. Therefore, we preferred the ray-driven approach.

Ray-driven approach

In the ray-driven approach, the mapping problem is considered from the opposite side. From every detector pixel, a ray is drawn through the pinhole center and all image voxels encountered by this ray are taken into consideration for the projection or backprojection. The main difference with the voxel-driven approach is that the sampling of the image space is not equidistant anymore, but along diverging projection lines l with equations:

$$\begin{cases} f \cdot x + u \cdot y &= 0 \\ f \cdot z + v \cdot y &= 0 \end{cases} \tag{3.11}$$

with (u, v) the coordinates on the detector of the projection of point (x, y, z) through a pinhole at a focal distance f from the detector (see Fig. 3.8). The v- and z-axis are parallel to the AOR if the detector underwent no tilt nor twist. The integration over $dxdzdy$ thus becomes an integration over $dudvdl$ by

$$dxdzdy = \begin{vmatrix} \frac{\partial x}{\partial u} & \frac{\partial x}{\partial v} & \frac{\partial x}{\partial l} \\ \frac{\partial z}{\partial u} & \frac{\partial z}{\partial v} & \frac{\partial z}{\partial l} \\ \frac{\partial y}{\partial u} & \frac{\partial y}{\partial v} & \frac{\partial y}{\partial l} \end{vmatrix} dudvdl \tag{3.12}$$

$$= \begin{vmatrix} -\frac{y}{f} & 0 & 0 \\ 0 & -\frac{y}{f} & 0 \\ 0 & 0 & \cos\kappa \end{vmatrix} dudvdl \tag{3.13}$$

$$= \frac{y^2}{f^2} \cos\kappa \tag{3.14}$$

with $|\cdot|$ the Jacobian determinant and κ the inclination angle of the projection ray with respect to the normal of the detector (see Fig. 3.8). Applying this transformation to the sensitivity of the voxel-driven method (3.9), introduces the correction factor $(y^2/f^2)\cos\kappa$ in the sensitivity for the ray-driven method $S_{ap}(u,v,l)$:

$$S_{ap}(u,v,l) = \rho_{vol} \cdot \frac{\Psi_{eff}\cos^3\tau}{4\pi y^2}\frac{y^2}{f^2}\cos\kappa \cdot \Delta u \cdot \Delta v \cdot \Delta l \tag{3.15}$$

$$= \rho_{area} \cdot \frac{\Psi_{eff}\cos^3\tau\cos\kappa}{4\pi f^2} \cdot \Delta u \cdot \Delta v = S_{ap}(u,v) \tag{3.16}$$

and thus eliminates the y-dependence. As was seen in section 3.1.2, the activity per unit area is also independent of the distance, hence $\rho_{vol} \cdot \Delta l$ could be substituted by ρ_{area}. It should be noted that (3.16) corresponds to (3.4), the 2D sensitivity image multiplied by $\cos\kappa$. For realistic single and multipinhole collimators, the same sensitivity calculation method as described in section 3.1.2 can thus be used, or alternatively, flood source measurements for every pinhole aperture separately. However, during projection and backprojection one should not forget the additional factor $\cos\kappa$. Notice that for the ideal single pinhole sensitivity calculation angle κ equals angle τ. Using the more accurate method, however, τ corresponds to the angle of the ray through one of the grid points, whereas κ denotes the angle of the ray through the aperture center. Due to the large detector-aperture distance compared to the aperture diameter, the difference between τ and κ is negligible, though.

The projection $Q_{ap}(u,v,\theta)$ through aperture ap can now be written as:

$$Q_{ap}(u,v,\theta) = S_{ap}(u,v) \cdot \int dl \cdot \Lambda(u,v,l,\theta) \tag{3.17}$$

Again, nearest neighbor interpolation, bilinear interpolation or resolution modeling can be applied. Two distinct methods for modeling the effect of the pinhole aperture on the resolution are discussed below. The first method only precalculates very limited information about the projection rays. Most of the projection rays have to be (re)calculated on-the-fly for every projection and backprojection. The second method calculates all data necessary for projection and backprojection in advance.

7-ray/21-ray method. Because often the amount of information required for appropriate resolution modeling during projection and backprojection is too high to be stored and retrieved efficiently, a simple method that calculates it on-the-fly was developed in the university of Brussels [12]. Instead of considering one projection ray through the pinhole center, 7 rays through the pinhole aperture were calculated, positioned in a hexagonal pattern with one in the center. Their location and weight was based on a standard quadrature method for 2D integration on a disk (see [12]). Hence, for projection, the value of each detector pixel equals the weighted average of the projections along its corresponding 7 rays. For backprojection, that value is then simply redistributed over these rays using the same weights. Septal or edge penetration can be modeled by assuming the aperture diameter is slightly larger, and thus positioning the outer rays closer to the edge. The calculation

is similar to that of the effective diameter in section 3.1.2. This extension has been implemented, but still requires validation. To increase the accuracy, a 21-ray variant is also available. This is only recommended for very large pinhole diameters, though, because the difference with the 7-ray method will be small otherwise and the calculation time goes up with a factor of three. The 7-ray method is already about a factor of seven slower than the projector-backprojector without resolution recovery. As the reconstruction time for multipinhole SPECT became unpractically high, a faster alternative was required, at least for simulations. Therefore, a method precalculating most of the data necessary during projection and backprojection was developed, as described in the next paragraph.

Precalculation method. The major challenge of developing a precalculation method is to keep the required storage space limited. Three methods with increasing modeling accuracy have been implemented. In the first one, nearest neighbor interpolation is used to determine which voxels to consider during projection and backprojection. Hence, only the index of the voxels crossed by the (single) projection ray need to be stored per detector pixel, typically number of rows elements per aperture. The reconstruction image is rotated before projection and after backprojection, making sure that only index storage for one projection angle is required. The second method is very similar, but uses bilinear instead of nearest neighbor interpolation in each plane of image voxels crossed by the projection ray. As a result, for each encountered voxel 4 indices and 4 weights need to be stored, corresponding to a factor of 8 increase in (the still very limited) memory usage. However, neither of these two methods models the resolution induced by the pinhole properly. Therefore, a third method was implemented, providing accurate resolution modeling. For each detector pixel, the volume of interest for projection is modeled by a cone, defined by the detector pixel location as its top and the pinhole circular aperture as one of its conic sections. Hence, for each x-z image plane its cross-section with this cone is calculated, and the indices of all voxels inside this ellipse are stored as well as all corresponding weights. Depending on the number of detector pixels, the size of the FOV, the image voxel size, the number of pinholes and their diameters, the required storage space varies between tens of megabytes and some gigabytes. If attenuation correction needs to be performed, storage of some additional parameters is required for each ray. So far, edge penetration is not modeled yet. It goes without saying that this will increase the memory usage even further. The acceptance angle of the pinhole apertures is not taken into consideration in the calculation of the cone and its intersections with the planes. However, during both the projection and backprojection operation, the projection image is multiplied with the 2D sensitivity map, which solves this issue without increasing the complexity of the resolution modeling. The sensitivity map can also be applied to reduce the required memory. Indeed, all detector pixels unsensitive to a certain pinhole aperture can be ignored during the projection and backprojection operation through that aperture, and consequently do not require storage of the cone intersection information.

3.2 Measurement corrections

3.2.1 Scatter correction

In nuclear medicine, the photons emitted due to radioactive decay interact with matter by collisions with electrons. Due to the interaction with low density materials, such as human tissue and water, the photon might lose some or all of its energy to the hit electron. The total kinetic energy before and after the interaction will stay the same, but the more energy is released to the electron, the larger the scatter angle of the photon, i.e. the deviation from its original path, will be ($0° \leq$ scatter angle $\leq 180°$) and the further the electron can travel. This effect is called *Compton scatter* and is the main cause of patient scatter in SPECT and PET measurements. When a photon hits an electron in a dense material, such as lead of the collimator, it is more probable that the electron absorbs the energy of the photon to escape from the atom. Another electron of the atom with a higher energy status can then take its place by releasing energy in the form of an emitted photon. This process is known as the *photo-electric effect* and is a second kind of photon scatter.

As due to scatter the energy of the photon decreases, it seems easy to discern scattered photons from *primary* or *direct photons*. All detected photons with an energy below the photopeak energy[1] can be classified as scattered photons. However, the energy resolution of a detector is not perfect, meaning the energy of the photon cannot be measured with infinite accuracy. A typical NaI(Tl) camera has an energy resolution of about 10% FWHM. PET cameras have an even worse energy resolution ($> 25\%$ FWHM). Therefore, all detected photons with an energy within a certain range around the photopeak energy, called the *energy window*, are regarded as primary photons. However, many of those are actually scattered photons.

For measurements with ^{99m}Tc or other isotopes with only one main photopeak, the amount of scatter in the photopeak energy window is typically estimated from the amount of measured photons in a scatter energy window [58]. This window is positioned at the left side of the photopeak energy window, i.e. at lower energies, because due to the interaction with an electron the photon loses energy. For isotopes with multiple photopeaks, some of the scattered high energy photons can be measured in the lower photopeak energy window. Therefore, this *dual energy window* (DEW) scatter correction method is not adequate. In [56], a simple technique to estimate and correct for the scatter was proposed and validated for several typical SPECT isotopes, including those with multiple photopeak energies. This method is called *triple energy window* (TEW) scatter correction, because it measures the emitted photons in three energy windows. The main window is the energy window centered around the (main) photopeak of the isotope. At the left and the right of this photopeak window, a scatter window is positioned to estimate the amount of scattered photons with energies lower and higher than the photopeak energy, respectively. The amount of scattered and primary photons measured in the photopeak

[1] The photopeak energy is the energy of the photons emitted during radioactive decay of the isotope. Some isotopes, such as ^{123}I, emit photons of two or more different energies. Usually, only the photons with the lowest energy are measured as direct photons.

Figure 3.9: Illustration of the 4 point source locations for scatter measurement.

Table 3.1: Scatter fractions for ^{99m}Tc and ^{123}I in plexi and in air.

% scatter	in plexi	in air
^{99m}Tc point source	27.3	11.1
^{123}I point source	43.5	36.7

window, C_{scat} and C_{prim}, respectively, are then estimated as:

$$C_{scat} \approx \left(\frac{C_{left}}{W_{left}} + \frac{C_{right}}{W_{right}}\right)\frac{W_{prim}}{2} \tag{3.18}$$

$$C_{prim} \approx C_{total} - C_{scat} \tag{3.19}$$

with C_{left} and C_{right} the amount of photons measured in the left and right scatter window, respectively, and W_{prim}, W_{left} and W_{right} the widths of the three windows. C_{total} corresponds to the total amount of measured photons in the photopeak window. For isotopes with one main photopeak, such as ^{99m}Tc, C_{right} can then be assumed to be equal to zero. However, for isotopes such as ^{123}I and ^{201}Tl, the TEW cannot be reduced to the DEW setting, because of their additional high-energy photopeaks.

For pinhole SPECT, we currently use DEW scatter correction for ^{99m}Tc measurements, with a 20% photopeak window (i.e. the window width equals 0.2 times the photopeak (or central) energy) and a lower scatter window of equal width. For ^{123}I, TEW scatter correction is performed with a 20% photopeak window and 15% lower and upper scatter windows.

To study the scatter in pinhole SPECT a little further, a point source was positioned at a distance of about 4.5 cm from the single pinhole collimator. Static measurements were performed of the point source at 4 different locations with respect to the aperture (see Fig. 3.9), and with a DEW and TEW setting for a ^{99m}Tc and a ^{123}I point source, respectively. Using the above described scatter correction method, the amount of primary and scattered photons in the photopeak window, as well as the scatter fraction can be determined. In this experiment the scatter was mainly caused by the collimator. To evaluate the influence of soft tissue on the scatter fraction, the measurements were repeated with the point source between two plexi plates of 2 cm thickness each, modeling the body of a small laboratory animal and the results are plotted with respect to the point source location for the case

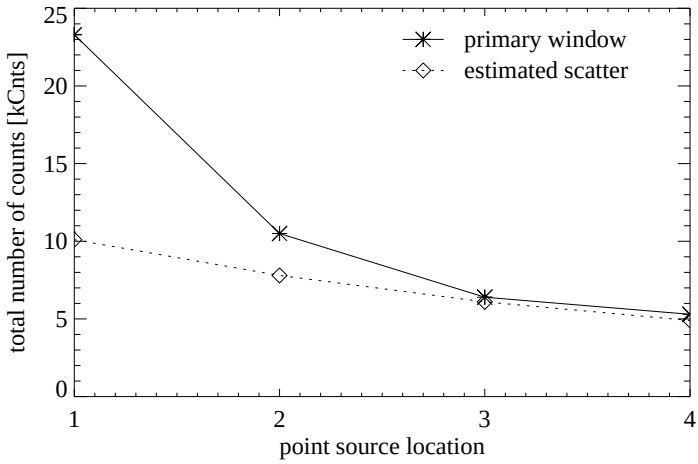

Figure 3.10: Plot of the amount of scatter in the photopeak energy window estimated with the TEW method (dotted line) and of the total amount of photons measured in this window (solid line) with respect to the ^{123}I point source location (see Fig. 3.9). For these measurements the point source was positioned in between two plexi plates of 2 cm thickness, each.

of ^{123}I in Fig. 3.10. Table 3.1 presents the results of the point sources located in front of the pinhole (position 1 in Fig. 3.9). These indicate that the scatter induced by the plexi is not negligible, especially not in the case of ^{99m}Tc due to its low photon energy. In addition, the share of the scatter in the photopeak window is much bigger for ^{123}I than for ^{99m}Tc, both in plexi and in air. This can be explained by the high energy peaks in the ^{123}I spectrum. In collaboration with the university of Ghent, the effect of the collimator thickness on the amount of scatter was investigated with a Monte Carlo simulation study [103]. From a simulated measurement of a 1 cm high, 6 cm diameter water cylinder filled with 37 MBq ^{123}I, they found that increasing the collimator plate thickness from 6 mm to 20 mm yielded a linear decrease of the share of the scatter fraction measured in the photopeak window. Further increasing the thickness had little influence. Because ^{123}I is a frequently used isotope for small animal SPECT studies, we decided to order new pinhole plates with a thickness of 12 mm rather than 6 mm and to thicken the most important walls of the available lead pinhole collimator (serving as support for the pinhole plate), as shown in Fig. 3.11. The increase in thickness was kept within limits for cost and weight reasons. These two adaptations resulted in clearly reduced scatter. As an example, the amount of collimator scatter, measured from a point source positioned in air on top of a 6 mm thick tungsten plate (attached to the not yet thickened support), could be diminished by a factor of 3.2 by just doubling the thickness of the tungsten plate.

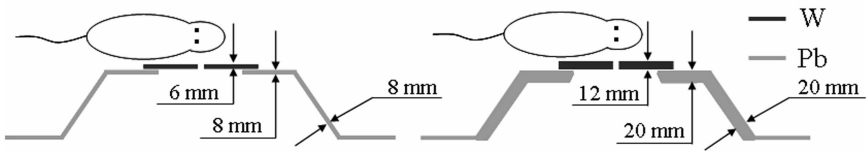

Figure 3.11: Illustration of the initial (left) and final thickness of the pinhole collimator (right), which was thickened to reduce the amount of scattered photons.

3.2.2 Attenuation correction

Due to the interaction with matter, a fraction of the photons traveling through the body of a subject is absorbed. This process is called *attenuation* and can be described by its (inverse) exponential behaviour (see (3.5)). Due to this effect, the amount of detected photons is less than expected from the amount of emitted photons and the camera geometry. During reconstruction, one should correct for the effect of attenuation both in the forward and in the backward projection step. As the backprojection operation is known to be the transpose of the projection operation, the attenuation correction is applied very similarly in both steps. Hence, here only the forward projection is discussed.

In SPECT, a photon is attenuated by all matter encountered between its origin and the detector. Therefore, activity emitted from a point close to the detector will be attenuated less than activity emitted far from the detector. Every image voxel k induces a certain amount of attenuation, expressed by attenuation coefficient μ_k which is stored in an attenuation map. The activity in every voxel j can then be corrected for attenuation by cumulating $\mu_k l_k$ for all voxels k encountered between voxel j and the detector, with l_k the intersection length of the projection ray with the voxel k, and applying (3.5).

Attenuation correction hence requires a good estimate of the subject's 'material' composition. As was explained very briefly in section 2.3.1, various methods are used in practice. They can be split-up in two groups, namely the *emission-based* and the *anatomy-based attenuation maps*. Both are discussed below.

Emission-based attenuation correction

Because the large majority of the human (or small animal) body consists of water, the most basic attenuation correction approach starts by estimating the body support, i.e. all image voxels representing a part of the body, from the emission data. This support can either be obtained from the sinogram itself [46] or from a (fast) image reconstruction. Next, an attenuation map is built by assigning the linear attenuation coefficient of water at the energy of the used isotope to all voxels of this body support. For some specific applications, additional information can be assigned to the attenuation map. A nice example is human brain imaging, where based on the emission sinogram the head contour can be defined and the attenuation of the skull can be included by modeling it as an ellipse with a certain constant

thickness [111] at or near the edge of the head. For pinhole SPECT, we restricted ourselves to homogeneous attenuation maps, though.

The main advantage of this method is that it does not require an additional scan to acquire attenuation information. However, it can only be used if sufficient non-specific uptake is present all over the (investigated part of the) body, hence allowing body support determination. In addition, the inaccuracy of the estimate for bone and air might introduce quantification errors and artifacts.

Anatomy-based attenuation correction

A more accurate estimate of the distribution of the attenuating tissue can be obtained by performing an extra scan, be it a transmission scan on the same camera using an external gamma emitting source, or a CT scan. Because the energy of the external source (emitting γ- or X-rays) is usually different from that of the injected tracer, and because of the energy-dependence of the attenuation coefficient, a conversion is often required from the reconstructed transmission or CT image to an attenuation map appropriate for the emission scan with the current isotope. Unfortunately, these two are related non-linearly. Usually, the relationship is approximated by a piece-wise linear transformation with on the edge points the corresponding values for the most important tissues, such as air, plexi, water, soft tissue and bone [13, 65]. The resulting attenuation map can then be applied during reconstruction in the exact same way as the homogeneous attenuation map described in the previous paragraph.

This correction method is more accurate than the first one, but might require image registration. In addition, for some small animals, such as rats and especially mice, the attenuation is rather limited because of the very short path length of the photon traveling through the body. Therefore, attenuation correction is often omitted for these animals, even if quantification is required.

3.2.3 Decay correction

As mentioned before, a radioactive tracer used for diagnosis in nuclear medicine consists of a molecule labeled with an isotope, which decays to another isotope or to a stable element by the emission of photons (or γ-rays), next to other particles, to release the excess energy set free during decay. Because the final state of the element is a stable, non-radioactive state, the amount of radioactivity (and thus the amount of emitted photons) gradually decreases. Depending on the used isotope and the scan time, this difference between the start and the end of the scan can be significant, such that decay correction is required. The decay is a statistical process, meaning that the exact amount of radioactivity after a certain period of time cannot be predicted. However, the expected value decays exponentially at a constant (mean) rate λ_d, the *decay constant*, hence the expected amount of radioactivity RA_t remaining after time t, can be calculated from the initial amount RA_0 as

$$RA_t = RA_0 \exp(-\lambda_d t) \tag{3.20}$$

From this formula, the *half-life* of an isotope, which is the time to reduce RA_0 to half of it, can easily be obtained:

$$t_{1/2} = \frac{\ln 2}{\lambda_d} \tag{3.21}$$

To correct for the effect of decay, either each detected photon (or photon pair) is immediately compensated for the elapsed time using (3.20) (typically for PET imaging), or each accumulated projection image is decay corrected to the start time of the scan. Global decay correction to a certain point in time can also be performed after reconstruction.

The half-life of each isotope is known. SPECT isotopes generally live longer than PET isotopes, e.g. ^{99m}Tc (6.01 h) and ^{123}I (13.2 h) versus ^{18}F (110 min) and ^{13}N (10 min). Therefore, decay correction is especially important for the short-living PET isotopes, but it might also be helpful for the longer-living SPECT isotopes in case of long study times or multiple scans spread over time with one tracer injection. In the latter case, recalculating all scans to the same time point might be interesting to facilitate uptake comparison.

3.2.4 Crosstalk correction

In some clinical and pre-clinical studies, one is interested in imaging two functional processes at the same time. Two examples are perfusion and necrosis (cell death) in the heart, and apoptosis and necrosis (organized and non-organized cell death) in tumors. The most common approach is to inject two tracers labeled with different SPECT isotopes, e.g. ^{201}Tl (70 keV) and ^{99m}Tc (140 keV), or ^{99m}Tc (140 keV) and ^{123}I (159 keV). Although the latter two are the two most commonly used SPECT tracers, discrimination between photons originating from the ^{99m}Tc tracer and those of the ^{123}I tracer is rather difficult, because their photopeak energies are very close to each other. As the energy resolution of a gamma camera is limited to about 10% FWHM, some of the ^{99m}Tc photons will be measured in the ^{123}I energy window, and vice versa. This phenomenon is called *crosstalk*. In this section, we focus on ^{99m}Tc-^{123}I crosstalk correction, because in chapter 7, this correction was applied for the simultaneous visualization of necrosis and apoptosis in the infarcted region of the left heart ventrical of a rabbit.

To measure both ^{99m}Tc and ^{123}I as accurately as possible, the energy windows for collecting photons of each isotope separately were chosen as wide as possible, without allowing overlap between the two windows. For each isotope, an energy window of 11% width centered around their respective photopeak energy was set, as shown in Fig. 3.12. In addition, a lower and upper scatter window were positioned just outside the 20% width regular photopeak window of the two isotopes. They were assigned a width of 15% with respect to their central energy.

As was shown in table 3.1, the measured spectrum of an isotope strongly changes due to additional scatter in the subject, compared to measurements in air. The pinhole collimator causes extra scatter as well. Therefore, it is important during

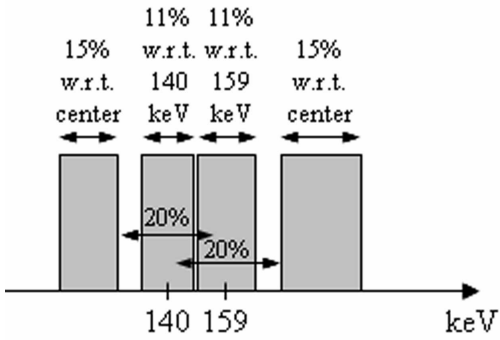

Figure 3.12: Energy window setting for a dual isotope (^{99m}Tc-^{123}I) measurement.

Table 3.2: Calculated crosstalk fractions for ^{123}I and ^{99m}Tc in plexi and in air.

% crosstalk	in plexi	in air
^{123}I in ^{99m}Tc window	6.2	6.0
^{99m}Tc in ^{123}I window	8.1	6.7

the crosstalk measurement to model the (scatter in the) subject and to perform the measurement with the pinhole collimator instead of the parallel collimator. Because dual isotope SPECT scans were planned only for rabbits, a ^{99m}Tc and an ^{123}I point source were positioned in between two plexi plates of about 5 cm thickness each. Three subsequent planar pinhole scans were performed at a typical distance for a rabbit study. First, only the ^{123}I point source was put in between the plexi plates in the central FOV. Second, the ^{99m}Tc was positioned next to it. Last, the ^{123}I point source was removed. During setup change, care was taken not to move the position of the point source remaining for the next scan, hence no registration was necessary before the image processing. The same scans were performed for the same setup, but outside the plexi to enable studying the effect of object scatter.

From the single point source measurements, the percentage crosstalk can easily be calculated. First, the pixels with a relevant measurement value are selected by simply thresholding in the photopeak window (i.e. the ^{99m}Tc-window for ^{99m}Tc). These will be further denoted by ROI (region of interest). Next, the crosstalk fraction is defined as the mean value in that ROI measured in the crosstalk window (i.e. the ^{123}I-window for ^{99m}Tc), divided by the mean value in the same ROI measured in the photopeak window. An overview of the crosstalk fractions for both isotopes in plexi and in air is presented in table 3.2. Last, these fractions are used to correct for the crosstalk in the dual point source measurement, using:

$$\text{sino}_{Tc,corr} = \text{sino}_{Tc-window} - \text{crosstalk}_{I\ in\ Tc-window} \cdot \text{sino}_{I-window} \quad (3.22)$$

$$\text{sino}_{I,corr} = \text{sino}_{I-window} - \text{crosstalk}_{Tc\ in\ I-window} \cdot \text{sino}_{Tc-window} \quad (3.23)$$

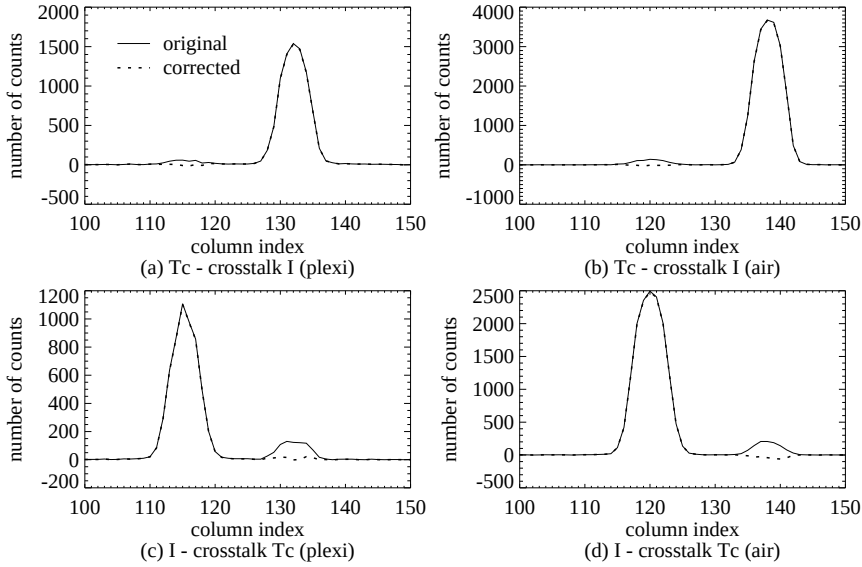

Figure 3.13: Profiles through the dual isotope point sources measurement. The ^{99m}Tc point source was positioned at the right of the ^{123}I point source. The measured counts in the ^{99m}Tc-photopeak (top row) and in the ^{123}I-photopeak (bottom row) energy window are shown before (solid line) and after crosstalk correction (dotted line). The left column plots the results in plexi, the right column those in air.

with $\text{sino}_{X,corr}$ the sinogram of isotope X corrected for crosstalk, $\text{sino}_{X-window}$ the sinogram measured in the photopeak window of X, and $\text{crosstalk}_{Y\ in\ X-window}$ the fraction of the crosstalk of isotope Y in that window. The results of the crosstalk correction for the dual point source measurements are shown in Fig. 3.13. Usually the sinograms are cut-off at zero.

Currently, the sinograms are precorrected as explained in (3.22) and (3.23). However, ideally the crosstalk should be modeled as a contamination of the sinogram during iterative reconstruction, similar to the way the scatter is. This means that before comparing the projection of the estimated activity distribution to the measurement, the estimated crosstalk is added to the calculated projection. Preferentially this summed image is Poisson distributed and the estimate of the crosstalk is noise-free, which will not be the case. The precorrection, which is somewhat easier to implement, is assumed to be acceptable here, because of the relatively small values in table 3.2. In addition, no scatter correction is applied, because too little information is available in the measured data. No further scatter investigation was performed, because of the already strongly reduced scatter fraction thanks to the increased collimator thickness (see section 3.2.1).

3.3 Conclusion

In this chapter, both the pinhole SPECT specific camera modeling and the more generally applicable measurement correction methods, necessary to obtain accurate and quantitatively correct reconstruction images, have been described. These have all been implemented and included in the in-house developed single and multipinhole SPECT software, which is used routinely for the reconstruction of small animal and phantom measurements. Many examples of these high quality images can be found in chapter 7.

Chapter 4

Single and multipinhole collimator design evaluation method for small animal SPECT

[1]High resolution functional imaging of small animals is often obtained by single pinhole SPECT with circular orbit acquisition. Multipinhole SPECT adds information due to its improved sampling, and can improve the trade-off between resolution and sensitivity. To evaluate different pinhole collimator designs an efficient method is needed that quantifies the reconstruction image quality. In this chapter, we propose a fast, approximate method that examines the quality of individual voxels of a post-smoothed MLEM reconstruction by studying their linearized local impulse response (LLIR) and (co)variance for a predefined target resolution. For validation, the contrast-to-noise ratios (CNRs) in some voxels of a homogeneous sphere and of a realistic rat brain software phantom were calculated for many single and multipinhole designs. A good agreement was observed between the CNRs obtained with the approximate method and those obtained with post-smoothed MLEM reconstructions of simulated noisy projections. This good agreement was quantified by a least squares fit through these results, which yielded a line with slope 1.02 (1.00 expected) and a y-intercept close to zero (0 expected). 95.4% of the validation points lie within three standard deviations from that line. Using the approximate method, the influence on the CNR of varying a parameter in realistic single and multipinhole designs was examined. The investigated parameters were the aperture diameter, the distance between the apertures and the axis of rotation, the focal

[1]This chapter has been published as a full article in *IEEE Transactions on Medical Imaging*: K. Vunckx, D. Bequé, M. Defrise and J. Nuyts. Single and multipinhole collimator design evaluation method for small animal SPECT. *IEEE Trans. Med. Imag.*, 27(1):36-46, 2008. Only minor changes concerning notational consistency and lay-out have been performed.

distance, the acceptance angle, the position of the apertures, the focusing distance and the number of pinholes. The results can generally be explained by the change in sensitivity, the amount of post-smoothing and the amount of overlap in the projections. The method was applied to multipinhole designs with apertures focusing at a single point, but is also applicable to other designs.

4.1 Introduction

Single pinhole collimated SPECT is regularly used nowadays for high resolution functional imaging of small animals. High resolution can be achieved, but the sensitivity is rather low and the data acquired with a circular orbit have been proven to be incomplete [112]. The use of a multipinhole collimator can increase the sensitivity without loss of resolution and the additional information can reduce the incompleteness. Mathematical analysis can only verify, however, whether the data are complete or not [112]. To be able to compare different single and multipinhole collimator designs a method is needed that quantifies how much information is missing. Pinhole collimator designs are usually compared based on their resolution and their sensitivity, calculated analytically, using Monte Carlo simulations or phantom measurements [3, 18, 57, 97, 100]. In this chapter, we propose a new technique to evaluate single and multipinhole collimator designs with respect to the quality of each reconstructed voxel.

Quantifying the quality of a reconstructed voxel is typically done by exploring the properties of its linearized local impulse response (LLIR). In order to achieve a fixed (and more isotropic) target resolution for the LLIRs, we replace the usual maximum a posteriori (MAP) approach [37,79,93,94] by an efficient post-smoothed maximum likelihood expectation maximization (MLEM) approach. A similar, but slightly different approach, was proposed in [77], where a modified uniform Cramer-Rao bound with a resolution constraint was derived to be able to compare different multipinhole designs.

This chapter is organized as follows. The new analytical pinhole collimator evaluation method, its usefulness and the reference method, used for the validation of the proposed efficient approximations, are explained in section 4.2. Section 4.3 describes some simulation experiments. On the one hand, the experiments are meant to validate the new method. On the other hand, the influence of the most important design parameters on the image quality is investigated. First, some general parameters, such as the aperture diameter, are tested both for single and multipinhole designs. Second, the effects of multipinhole-specific design parameters are examined. The results of these experiments are presented in section 4.4 and are further discussed in section 4.5.

4.2 Theory

4.2.1 Linearized local impulse response

For linear and shift-invariant imaging systems and reconstruction algorithms, the properties of the mean reconstruction image can be described by the (global) impulse response (in the spatial domain) or by the frequency response (in the Fourier domain). However, since the MLEM or MAP reconstruction $\hat{\Lambda}$ of the unknown activity distribution Λ for emission tomography is shift-variant and nonlinear in the projection data Q, an alternative approach is required. In [37] a generalization of the impulse response for emission tomography, called the local impulse response (LIR) l^j has been proposed[2]:

$$\begin{aligned} l^j(\Lambda) &= \lim_{\delta \to 0} \frac{\mu(\hat{\Lambda}(Q(\Lambda + \delta e^j))) - \mu(\hat{\Lambda}(Q(\Lambda)))}{\delta} \\ &= \frac{\partial}{\partial \lambda_j} \mu(\hat{\Lambda}) \end{aligned} \tag{4.1}$$

where $\mu(x)$ denotes the mean of x, e^j is the j-th unit vector and j is the index of the voxel in the reconstructed image. The impulse response is local in two ways. First, due to the shift-variant character of the reconstruction and of the imaging system, the shape of the impulse response is a function of j. Second, it is object-dependent, or equivalently, nonlinear in the projection data, reflected by the argument Λ in equation (4.1).

To allow a more efficient calculation of the LIR, one can assume the reconstruction is locally linear [37]. Then the mean of many reconstructions of noisy projection data can be replaced by the reconstruction of noiseless projection data $\bar{Q}$, as was experimentally confirmed by Wilson *et al.* [130]:

$$\mu(\hat{\Lambda}) \approx \hat{\Lambda}(\bar{Q}(\Lambda)) \tag{4.2}$$

The substitution of (4.2) in (4.1) results in the following definition of the linearized local impulse (LLIR) [37]:

$$\begin{aligned} l^j(\Lambda) &\approx \lim_{\delta \to 0} \frac{\hat{\Lambda}(\bar{Q}(\Lambda + \delta e^j)) - \hat{\Lambda}(\bar{Q}(\Lambda))}{\delta} \\ &= \frac{\partial}{\partial \lambda_j} \hat{\Lambda}(\bar{Q}(\Lambda)) \end{aligned} \tag{4.3}$$

which will be taken as a starting point in the next section.

[2]The local impulse response l^j is a function of the voxel j, the unknown activity distribution Λ and the reconstruction algorithm. In order to keep the expressions readable, we limited the notation to $l^j(\Lambda)$.

4.2.2 Reconstruction quality quantification

The goal of this chapter is to find an efficient method that quantifies the image reconstruction quality induced by a single or multipinhole collimator design, such that many different designs can be compared quickly and easily. The properties of the LLIR, as described in the previous section, could - in principle - be used for this purpose.

The calculation of the LLIR and the (co)variance in a voxel using an iterative reconstruction algorithm and multiple noise realizations of the projection data, however, is very time-consuming. To calculate the LLIR in a voxel j, two reconstructions are required (one of the projection data of the object with an extra impulse in voxel j and one without impulse), as can be seen from equation (4.3). For each extra voxel that needs to be examined, an extra reconstruction is necessary. The computation of the covariance matrix of that voxel j involves the reconstruction of a large number N of noisy projection data sets. These data sets are obtained by computing N different Poison noise realizations of the simulated noise-free projection data of the phantom without impulse[3]. The relative error on the standard deviation is estimated to be $\sqrt{1/(2N)}$, assuming that the standard deviation is Gaussian distributed. This approach will be called the *reference method* in the rest of this work.

Yet, optimizing the design of a multipinhole collimator for a specific application is practically infeasible using the reference method. Therefore, a much faster computational method is required. In [33, 37, 94] the following - more efficient - approximations for the LLIR and its covariance matrix after convergence of a MAP reconstruction have been formulated:

$$l^j(\Lambda) \approx [\boldsymbol{F} + \beta \boldsymbol{U}]^{-1} \boldsymbol{F} e^j \tag{4.4}$$

$$\mathrm{Cov}^j(\Lambda) \approx [\boldsymbol{F} + \beta \boldsymbol{U}]^{-1} \boldsymbol{F} [\boldsymbol{F} + \beta \boldsymbol{U}]^{-1} e^j \tag{4.5}$$

$$\text{with} \qquad \boldsymbol{F} = \boldsymbol{A}^T \mathrm{diag}(\boldsymbol{Q})^{-1} \boldsymbol{A} \tag{4.6}$$

where $\boldsymbol{F}$ is the Fisher information matrix, which - in emission tomography - can be calculated by a projection $\boldsymbol{A}$, weighted by the projection data $\boldsymbol{Q}$ (where $\mathrm{diag}(\boldsymbol{Q})$ is a diagonal matrix with the elements of $\boldsymbol{Q}$ on the diagonal), and followed by a backprojection $\boldsymbol{A}^T$ (where ^{T} denotes transpose), β is the smoothing parameter and $\boldsymbol{U}$ is the Hessian of the quadratic prior, used for regularization.

The calculation of the LLIR in equation (4.4) requires the inversion of the JxJ matrix ($\boldsymbol{F}$+$\beta\boldsymbol{U}$), in which J represents the total number of image voxels. Given the relatively high number of image voxels in emission tomography, this solution is not feasible in practice. If $\boldsymbol{F}$ would be shift-invariant, however, it would be a circulant matrix (except for edge effects) and equations (4.4) and (4.5) would reduce to subsequent convolutions of the perturbation e^j with the convolution masks defined by $\boldsymbol{F}$ and $[\boldsymbol{F}$+$\beta\boldsymbol{U}]^{-1}$. Although single and multipinhole projections are not

[3]The (co)variance matrix for a voxel j is generally presumed to be equal for a phantom with and without impulse. This has as an advantage that these reconstructions (which are responsable for the main share of the computation time) can be reused for all voxels.

shift-invariant, and thus neither is $\boldsymbol{F}$, local shift-invariance could be assumed. This would only introduce a small error near the impulse in voxel j. This assumption has been proposed earlier in [36,94] in the context of shift-variant PET, and in [79] for multipinhole SPECT. The Fisher information matrix $\boldsymbol{F}$ could then be approximated by a matrix $\boldsymbol{F}^j$ of which the rows are replaced by shifted versions of the j-th row. In this way $\boldsymbol{F}$ is turned into a circulant matrix $\boldsymbol{F}^j$ and the calculation of equations (4.4) and (4.5) can be done by convolutions in the spatial domain, as stated above, or by simple and even more efficient multiplications in the Fourier space.

To be able to easily compare different pinhole collimator designs, we choose to impose a fixed target resolution in the reconstruction image. For MAP reconstruction Stayman *et al.* [104] and Nuyts *et al.* [86] proposed methods that yield reconstructed images with isotropic, uniform resolution. Fessler [35] proposed a simpler analytical approach to get an isotropic spatial resolution. These methods are in fact equivalent to MLEM reconstruction run to convergence and post-smoothed to reach the imposed target resolution (see [104] for more details). Therefore we replaced the MAP regularization prior by a post-smooth filter $\boldsymbol{P}^j$ [119]. For each voxel j, this filter $\boldsymbol{P}^j$ is chosen to be the isotropic Gaussian that makes the approximation $\boldsymbol{T} \approx \boldsymbol{P}^j\boldsymbol{G}^j\boldsymbol{F}^j$ as accurate as possible, with $\boldsymbol{T}$ the isotropic Gaussian with a full width at half maximum (FWHM) equal to the target resolution and $\boldsymbol{G}^j$ the pseudoinverse of $\boldsymbol{F}^j$. The analytical approximations for the LLIR and the covariance of voxel j (in the spatial domain) then become:

$$l^j(\Lambda) \approx \boldsymbol{P}^j\boldsymbol{G}^j\boldsymbol{F}^j e^j \tag{4.7}$$

$$\mathrm{Cov}^j(\Lambda) \approx \boldsymbol{P}^j\boldsymbol{G}^j\boldsymbol{F}^j\boldsymbol{G}^{jT}\boldsymbol{P}^j e^j \tag{4.8}$$

$$= \boldsymbol{P}^j\boldsymbol{G}^{jT} l^j(\Lambda) \tag{4.9}$$

We have slightly adapted the convolution mask represented by $\boldsymbol{F}^j$ in order to reduce the influence of the edge effects caused by the circulant approximation. This step was inspired by the triangular function proposed in the appendix of [136]. Approximations (4.7)-(4.9) predict very well the LLIR and covariance in voxel j close to this voxel, but become less accurate if the distance from j increases. Therefore, the elements of $\boldsymbol{F}^j$ are multiplied (in the spatial domain) by a weight that decreases with increasing distance from j. Empirically, the weight was set to one in voxel j and to zero at a distance from j equal to the number of columns in the reconstructed image. A linear decline was found to give accurate approximations.

In equations (4.7)-(4.9) matrix $\boldsymbol{G}^j$ represents an approximate pseudoinverse of matrix $\boldsymbol{F}^j$, since the inverse usually does not exist. Indeed, pinhole SPECT data acquisition is incomplete; hence the reconstruction will not be unique and $\boldsymbol{F}^j$ will not be of full rank. In the MAP algorithm this is solved by adding a prior for regularization, as in equations (4.4) and (4.5). For MLEM we propose the following approximation $\mathbf{G}^j$ of the pseudoinverse (in the Fourier domain):

$$\mathbf{G}^j = \frac{\mathbf{F}^{j*}\max\left(\Re(\mathbf{F}^j), 0\right)}{\mathbf{F}^{j*}\mathbf{F}^j\max\left(\Re(\mathbf{F}^j), 0\right) + \epsilon} \tag{4.10}$$

with $\mathbf{G}^j$ and $\mathbf{F}^j$ the Fourier transform[4] of $\boldsymbol{G}^j$ and $\boldsymbol{F}^j$, respectively, * the complex conjugate, $\Re(\mathbf{F}^j)$ the real part[5] of $\mathbf{F}^j$ and $\epsilon = 10^{-10}|\mathbf{F}^j_{DC}|^3$, where $\mathbf{F}^j_{DC}$ denotes the DC-value of $\mathbf{F}^j$ in the Fourier domain, or the mean value of the corresponding image in the spatial domain. Regularizing effects were obtained by removing the negative frequencies and by choosing an appropriate ϵ.

As measures for the reconstruction quality in voxel j the contrast recovery coefficient (CRC) and the variance of the LLIR in voxel j (which are the j-th element of l^j and Cov^j, respectively) are commonly used. The CRC can be seen as a measure of resolution [93]. Thanks to the fixed resolution after post-smoothing, the CRC should be more or less constant. The only parameter to optimize then is the variance. As an alternative the contrast-to-noise ratio (CNR) can be optimized as well, since

$$\mathrm{CNR} = \frac{\mathrm{CRC}}{\sqrt{\mathrm{variance}}}. \tag{4.11}$$

In the rest of this chapter, the CNR is taken as the image quality measure.

4.2.3 Collimator design parameters

When designing a single pinhole collimator, only a few parameters have to be taken into consideration, namely:

- The aperture diameter (D).
- The distance between the aperture and the axis of rotation (AOR), abbreviated as DA.
- The distance between the aperture and the detector (DD), also called focal distance.
- The aperture acceptance angle (A).
- The pinhole aperture plate thickness (T).
- The linear attenuation coefficient of the pinhole aperture plate, depending on the material (usually tungsten) and the energy of the isotope used.

These will be classified as the *general pinhole design parameters*.

The addition of pinhole apertures, however, causes a dramatic increase in the collimator design complexity. Extra parameters are:

- The position of the aperture (in polar coordinates) with relation to the other apertures (PD and PA, see Fig. 4.1).

[4] Before performing the Fourier transform (and the above mentioned weighting) the image is zero padded.

[5] Note that, for the calculation of $\Re(\mathbf{F}^j)$, the image has to be shifted before Fourier transformation, such that the DC-value is located at [0, 0, 0].

- The focusing distance (F), which is the distance between the apertures and the point at which the apertures focus (i.e. the point where the central axes of the apertures intersect each other).

This second group of parameters are *multipinhole-specific design parameters*. Remark that, in this chapter, we force all apertures to focus at one point (on the central axis of the central pinhole), since we are only interested in imaging a small region (e.g. the brain), not the whole body. This means that the inclination angle I of each aperture can be derived from the focusing distance F and the position of the aperture (PD and PA). If the apertures would not focus all at the same point, two additional parameters for each aperture - instead of the fixed focusing distance F - would be necessary to specify the geometry of the design uniquely.

All above described parameters, except for the aperture diameter, are visualized in Fig. 4.1.

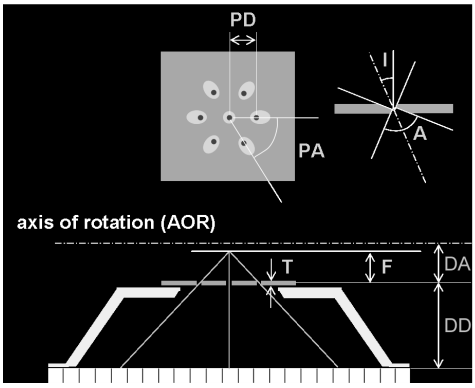

Figure 4.1: Illustration of the pinhole collimator design parameters.

To reduce the complexity of the multipinhole designs, we restrict the apertures (a) to lie in the same plane parallel to the detector (which is supposed to be parallel to the AOR), (b) to focus at one point (i.e. the image center if not specified otherwise), and (c) to form a regular polygon around a central pinhole. In addition, the parameters D, A and T are chosen equal for all pinhole apertures. Of course, it is possible that other designs result in a better reconstruction quality, but this is beyond the scope of this chapter.

4.3 Experiments

The rationale of the experiments presented in this section is twofold. On the one hand, these experiments are meant to validate the proposed approximations for the CRC and the variance, which are presumed to quantify the image quality, for various single and multipinhole collimator designs (section 4.3.1). On the other hand, the experiments are set up to examine the influence of the different design

parameters on the reconstruction image quality, by varying one parameter while keeping all others fixed (section 4.3.2).

4.3.1 Validation of the approximate image quality quantification method

Some efficient approximations to calculate the LLIR and its covariance in an image voxel j were proposed in section 4.2.2. Before these analytical approximations can be applied routinely to evaluate and optimize single and multipinhole designs, they should be validated with respect to the reference method, based on post-smoothed MLEM iterative reconstructions (see section 4.2.2 for more details on the reference method).

Many different designs (see section 4.3.2) were simulated and tested for their corresponding image quality. A subset of the experiments presented in this chapter was performed twice: once using the approximate method (equations (4.7)-(4.10)) and once more - for validation - with the reference method. For each validation experiment, the outcome of both methods will be compared and discussed in section 4.4. Many designs were validated to be sure the approximate method was not only valid (by chance) for a specific test design.

Two different software phantoms, a homogeneous sphere and a rat brain phantom (see Fig. 4.2), were used in the experiments to show that the new method is accurate independently of the imaged object. Although the method was mainly tested for a homogeneous sphere, it should be valid for any object.

The homogeneous sphere had a radius of 17.5 mm and was simulated in an image space with 65x65x65 cubic voxels of 0.8 mm. The activity in the sphere was set to 5 kBq/mm^3. A coronal slice of this sphere is shown in Fig. 4.2(a) and the six investigated voxels are pointed out with a number. To avoid overloading the graphs, only the results of the three most extreme voxels (indicated with a diamond, a triangle and a rectangle (points 1, 3 and 6, respectively)) are shown in sections 4.4.1 and 4.4.2. In section 4.4.3 the results of all six voxels are plotted.

The rat brain phantom has been built based on the reconstruction of a real rat brain measurement with ^{123}I-FP-CIT to visualize the striata (as in [68]). This three-dimensional image was thresholded to segment it into regions with similar activity uptake. These regions are (in order of increasing uptake): the body of the rat, the brain, the striata in the brain, the glands behind the eyes, called Harderian glands, and the salivary gland (outer and inner region). The body was filled with a homogeneous background activity, although in reality there is not uptake everywhere. All segments contained realistic amounts of activity. Again an image space with 65x65x65 cubic voxels of 0.8 mm was simulated. A transaxial, coronal and sagittal slice of the software phantom are shown in Fig. 4.2(b)-(d). The same voxels as for the homogeneous sphere were considered.

Both the approximate and the reference method start from a simulated forward projection of the activity in the chosen software phantom (with or without an impulse in the voxel of interest) onto the detector, which is assumed to be an infinitely

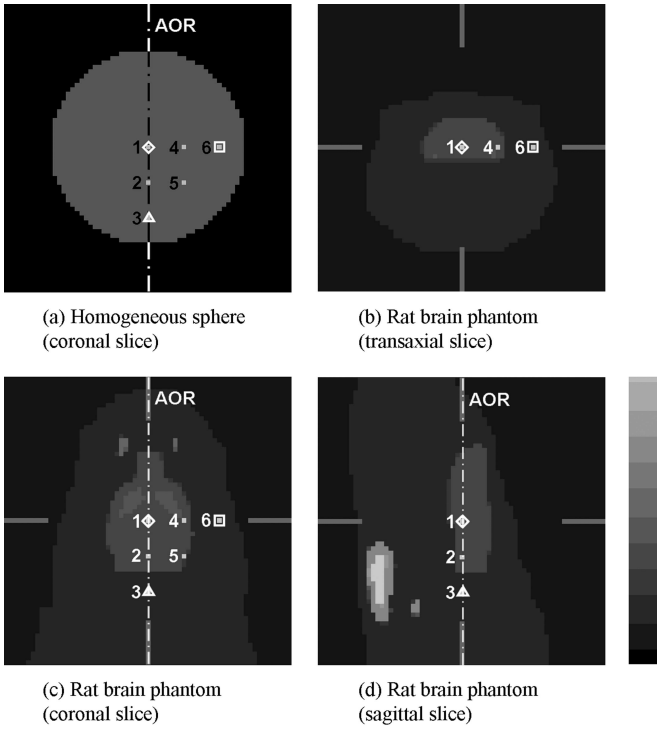

Figure 4.2: Illustration of the homogeneous sphere (coronal slice) and the rat brain phantom (transaxial, coronal and sagittal slice). The examined voxels where depicted.

thin, perfect absorber with an intrinsic resolution of 4 mm. The projection method defines for each detector pixel and for each aperture a cone through the field of view (FOV) which contains all voxels that contribute to the intensity measurement of that pixel. The contribution of each voxel is weighted by a factor, which depends on the distance between the voxel and the detector. These weights are calculated once beforehand, and are used for all forward and backward projections in the approximate, as well as in the reference method. In this way, the resolution and sensitivity of the pinhole apertures are modeled. However, our current implementation of the projection method does not allow edge penetration modeling yet. Effects due to scatter and attenuation were neglected.

For the reference method, a series of independent noise realizations was computed using a pseudo-random Poisson noise generator. The sets of noisy data were reconstructed using MLEM with relaxed ordered subsets (OS) [55, 98, 116]. An equivalent of 472 MLEM iterations were performed, to reach an estimate near convergence. The reconstructed images were post-smoothed in order to obtain a resolution of 2.4 mm FWHM in the voxel of interest. The calculation of the variance

(using the reference method) was based on 150-300 noise realizations[6].

4.3.2 Effect of pinhole collimator design parameters

The presented method will be useful in many ways. Our two main purposes are: (a) to gain insight in the influence of the different design parameters on the image quality, and (b) to optimize the collimator design for specific applications. The former will be elaborated in more detail in this section, and will be useful for the latter, the design phase, which is subject of ongoing research in our lab.

To examine the effect of the different pinhole design parameters, we started for each experiment from the same realistic single pinhole design or from one of two realistic multipinhole designs. While keeping all other parameters fixed, the parameter of interest was varied. We investigated the following parameters: the aperture diameter (D), the distance between the pinholes and the AOR (DA), the focal distance (DD), the acceptance angle (A), the distance between the central aperture and the surrounding ones (PD), the focusing distance (F) and the number of pinhole apertures (NP). The first 4 parameters, the *general pinhole design parameters*, were both investigated for single and multipinhole designs. The last 3 parameters are only applicable to multipinhole designs. They were categorized under the name *multipinhole-specific design parameters*.

Fixed parameters

Since at our lab we focused on rat brain imaging using a Siemens e.cam camera, we fixed the parameters to realistic values as well for the pinhole collimator design as for the camera parameters and the phantom size. In this chapter we use only one of the two detector heads, since the reference method is very time-consuming and the extension from one to more detector heads is straightforward and has no influence on the accuracy of the approximate method.

The simulated SPECT scanner acquired the data in a 256x200 matrix with square pixels of 1.95 mm. The intrinsic resolution of the detector was 4.0 mm FWHM. The distance between the detector and the AOR was 218 mm. A perfect circular orbit with 64 equally spaced projection angles was assumed. Each projection image was acquired in 60 s.

The pinhole collimator design was inspired by and very similar to the design proposed by Schramm *et al.* in [97]. It consists of a lead pyramid with a tungsten pinhole insert plate (thickness 12 mm) on top of it. The knife-edge pinhole aperture of the single pinhole design was positioned centrally with respect to the detector at a focal distance of 173 mm. The aperture had a diameter of 1.5 mm, an acceptance angle of 60° and its central axis was perpendicular to the detector plane.

Two different multipinhole collimator designs were taken as a starting point for the experiments. To image the homogeneous sphere, a 7-pinhole collimator was

[6]Due to the very long calculation time of the reference method, only for a small part of the designs more than 150 noise realizations were performed.

Table 4.1: Main pinhole collimator design parameters

	1-pinhole	4-pinhole	7-pinhole
D	1.5 mm	1.5 mm	1.2 mm
DA	45 mm	45 mm	45 mm
DD	173 mm	173 mm	173 mm
A	60°	60°	60°
PD		25 mm	25 mm
F		45 mm	45 mm

simulated. Six pinholes were uniformly distributed over a circle with a radius PD of 25 mm around the central aperture. In the rest of this work, this radius will be called the *pinradius*. Three apertures were located on a line parallel to the AOR. All pinholes had an aperture diameter of 1.2 mm, an acceptance angle of 60°, and focused at a point at 45 mm from the central one (i.e. at the image center). These parameters were chosen because they result in a good detector filling with modest overlap between the projections through the different apertures.

To reduce the simulation time for the validations, the rat brain phantom was imaged with a pinhole collimator with only 4 apertures, one central and three on the vertices of a regular triangle. Again a pinradius of 25 mm was chosen. One of the outer apertures was positioned on the line through the central pinhole and parallel to the AOR. The aperture diameter was taken 1.5 mm. The rest of the design parameters were equal to those of the 7-pinhole collimator.

A summary of the three above specified pinhole designs can be found in table 4.1.

Varying parameters

As explained earlier in this section all design parameters were kept fixed, except one. For the global pinhole design parameters D, DA, DD and A, both a single and a multipinhole experiment was performed. First, the diameter D was varied from 0.6 to 2.4 mm with an interval of 0.3 mm. Second, distances between the apertures and the AOR (DA) from 30 to 60 mm, in steps of 5 mm, were considered. Third, the focal distance was varied from 113 to 233 mm in steps of 20 mm. Fourth, the acceptance angle was changed from 20° to 80° with intervals of 10°.

For the multipinhole-specific design parameters several multipinhole designs were tested. First, the pinradius was increased from 15 to 45 mm in steps of 5 mm. Next, the focusing distance was varied from 30 to 60 mm with an interval of 5 mm. Finally, designs with 5 to 13 pinholes were compared.

An overview of the experiments is given in table 4.2. As can be seen from the penultimate column, the homogeneous sphere and the rat phantom were used alternatingly in the experiments.

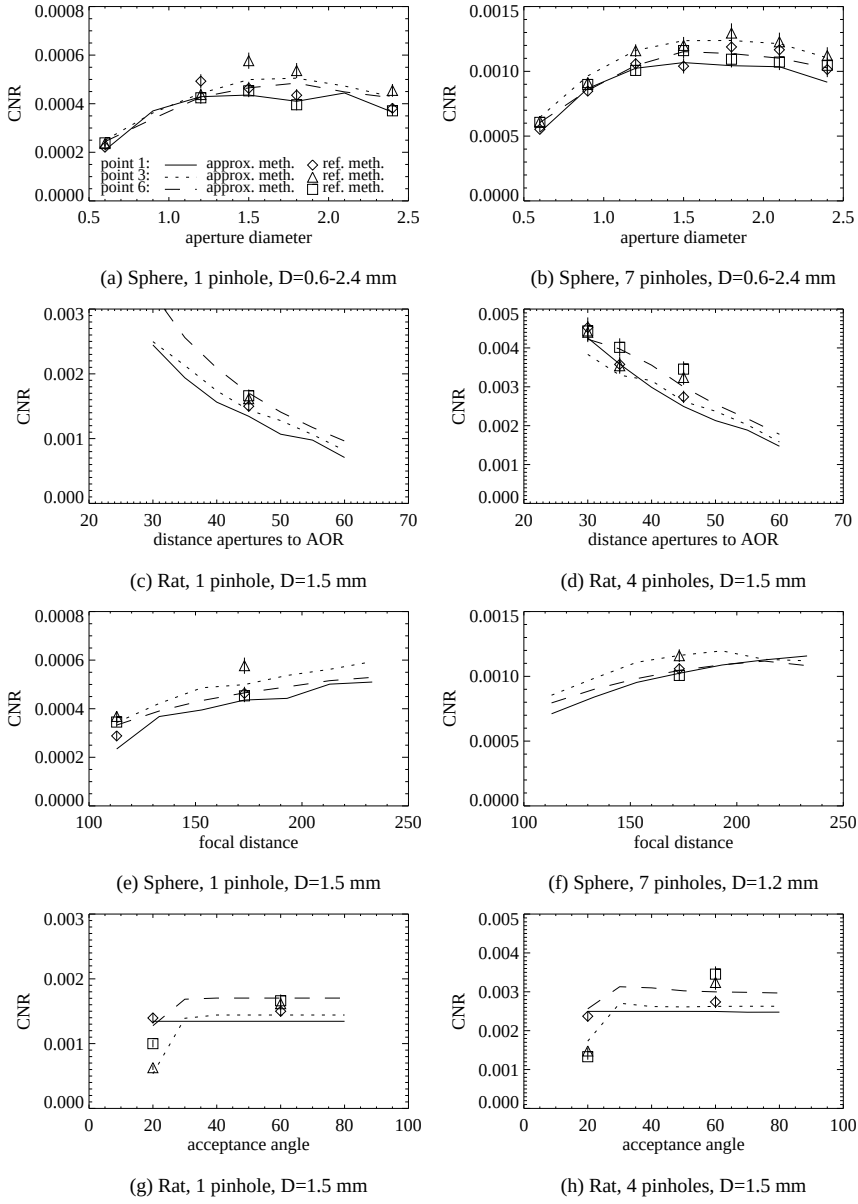

(a) Sphere, 1 pinhole, D=0.6-2.4 mm

(b) Sphere, 7 pinholes, D=0.6-2.4 mm

(c) Rat, 1 pinhole, D=1.5 mm

(d) Rat, 4 pinholes, D=1.5 mm

(e) Sphere, 1 pinhole, D=1.5 mm

(f) Sphere, 7 pinholes, D=1.2 mm

(g) Rat, 1 pinhole, D=1.5 mm

(h) Rat, 4 pinholes, D=1.5 mm

Figure 4.3: Evaluation of the influence of the different global pinhole design parameters on the reconstruction quality of a homogeneous sphere or a rat brain phantom. Left: single pinhole designs, right: multipinhole designs. The error bars indicate one standard deviation. The target resolution was 2.4 mm.

Table 4.2: Varying pinhole collimator design parameters

	Interval	Step	Phantom	Starting design
D	0.6-2.4 mm	0.3 mm	sphere	1-pinh. and 7-pinh.
DA	30-60 mm	5 mm	rat	1-pinh. and 4-pinh.
DD	113-233 mm	20 mm	sphere	1-pinh. and 7-pinh.
A	20°-80°	10°	rat	1-pinh. and 4-pinh.
PD	15-45 mm	5 mm	sphere	7-pinhole
F	30-60 mm	5 mm	rat	4-pinhole
NP	5-13 pinh.	1 pinh.	sphere	7-pinhole

4.4 Results

In sections 4.4.1 and 4.4.2, the results of many different pinhole designs, evaluated with the presented approximate method, are shown and discussed. For validation, part of these designs were evaluated with the reference method as well. In section 4.4.3, all validation points are gathered to get a global overview of the agreement between the new method and the reference method.

4.4.1 Effect of general pinhole design parameters

Aperture diameter (D)

For the single and multipinhole SPECT setups (with an aperture diameter between 0.6 mm and 2.4 mm), the reconstruction image quality in three voxels of the homogeneous sphere (see Fig. 4.2(a) points 1, 3 and 6) are displayed in Fig. 4.3(a) and (b) respectively. The solid, dotted and dashed line connect the results for point 1, 3 and 6, respectively, obtained with the approximate method. The results acquired with the reference method are displayed as diamonds, triangles and rectangles for point 1, 3 and 6, respectively.

Fig. 4.3(a) and (b) show that, for a target resolution of 2.4 mm, the CNR reaches a (rather flat) maximum at an aperture diameter of about 1.5-1.8 mm. The results show a very similar behavior for single and multipinhole collimators, but the CNR is much higher with the multipinhole design, as expected. The graphs also reveal good agreement between the analytical prediction and the reference method.

Two complementary effects contribute to variance reduction. First, increasing the aperture diameter leads to increased sensitivity and hence reduced variance. Second, post-smoothing the MLEM reconstruction reduces the variance as well. Apparently, the optimal variance reduction is obtained with a combination of both contributions. When the aperture diameter is further increased, the corresponding reduction of the post-smoothing (required to reach the target resolution) leads to a net increase of the variance. Similar findings were reported by Fessler [34]. In addition, as the optimum is relatively flat, it might be interesting to take a slightly larger aperture diameter in order to reduce the influence of collimator scatter.

Distance apertures to AOR (DA)

Decreasing the distance between the aperture(s) and the rotation axis should lead to improved resolution and sensitivity. Because the resolution is kept constant at the target resolution by post-smoothing, the CNR is expected to increase due to a reduction of the variance. This is confirmed by Fig. 4.3(c) and (d).

For the points studied in the rat phantom, the distance DA can be reduced until the aperture plate touches the phantom without noticeable degrading effects due to truncation of projections. To illustrate the effect of truncation, the experiments were repeated with a reduced acceptance angle (40° instead of 60°). As shown in Fig. 4.4(a) and (b), the reduction of the FOV and the according increase in truncation now limit the increase of the CNR at small distances for the eccentric points (numbers 3 and 6).

As shown in Fig. 4.3(d), three multipinhole designs were validated. The approximations again agree very well with the results obtained with the post-smoothed MLEM reconstructions. As in the previous experiment, the CNR is higher for the multipinhole designs because of the three extra apertures.

Focal distance (DD)

Varying the focal distance modifies the magnification, but has little influence on the sensitivity. This is in contrast with the previous parameter (DA), which strongly influences the sensitivity. This difference between the two parameters explains the observation that the CNR varies more slowly when varying DD (see Fig. 4.3(e) and (f)) than when varying DA, as in Fig. 4.3(c) and (d).

For the single and multipinhole designs the same trends are found. Though, one should note that for multipinhole designs with a very large focal distance the quality of the eccentric points starts to degrade. The cause is twofold. On the one hand, the large magnification, induced by the large focal distance, results in overlapping projections to which the eccentric points are more susceptible than the central points. For a detector pixel gathering activity from more than one aperture, i.e. for a pixel in a region of overlap, uncertainty about the origin is introduced and the photon count will be worth less than in the case without overlap. On the other hand, the magnification can cause projection truncation. If a voxel is seen through less apertures, its image quality is obviously degraded.

Two single pinhole designs were validated as can be seen in Fig. 4.3(e). The CNRs obtained with the reference method confirm those calculated with the new efficient method.

Acceptance angle (A)

To test the influence of the acceptance angle on the image quality, we varied the angle between 20° and 80°. The rat phantom was used in the simulations.

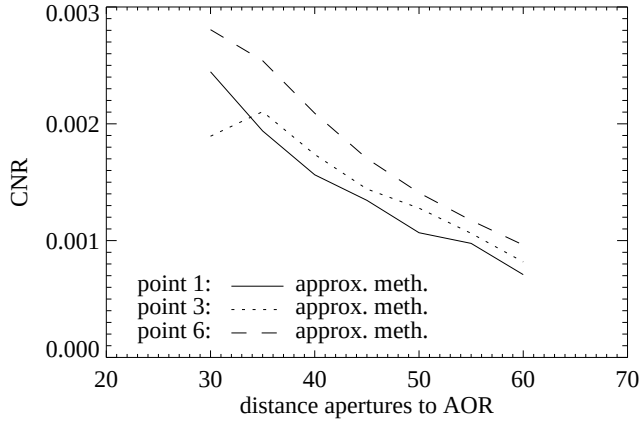

(a) Rat, 1 pinhole, D=1.5 mm, A=40°

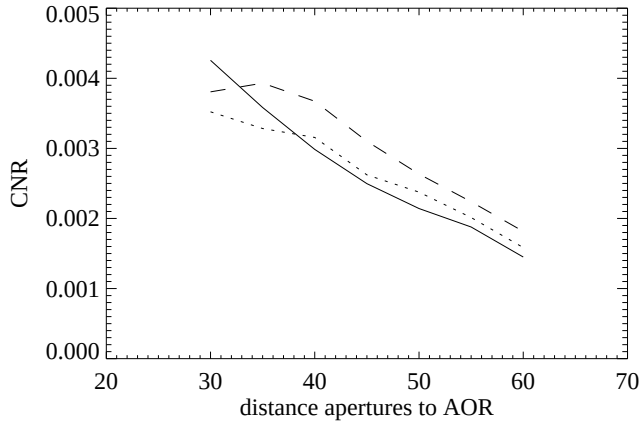

(b) Rat, 4 pinholes, D=1.5 mm, A=40°

Figure 4.4: Illustration of the reduction of the image quality (in points 3 and 6) due to the truncation effect in case of a small distance between the apertures and the AOR (DA=30 mm) and a small acceptance angle (A=40°). Top: single pinhole designs, bottom: multipinhole designs.

From the results, shown in Fig. 4.3(g) and (h), we can conclude that for the investigated voxels in the rat phantom - given the current design parameters - an acceptance angle of 40° is sufficiently large. Further reduction of the acceptance angle leads to loss of information in the eccentric voxels, due to the reduced FOV. Enlarging the acceptance angle might be interesting if one would like to scan also larger animals with the design, or if larger parts of the animal are of interest.

Increasing the acceptance angle in multipinhole designs increases the amount of overlap between the projections acquired through different pinholes. This results in a slight decrease of the CNR (see Fig. 4.3(h)).

For both experiments two designs were validated. The approximate method again predicted well the CNRs found with the reference method.

Note that in Fig. 4.3 the CNR for point 1 is generally lower than the CNR for points 3 and 6. This can intuitively be explained as follows. Because of its central location in the phantom (both in the sphere and in the rat brain phantom), any line of response (LOR) through voxel 1 also contains many other high intensity voxels. As a result, all information about voxel 1 is superimposed on a high intensity 'background' from the other contributing voxels. The contribution of voxel 1 to these measurements is therefore hardly separable from the measurement noise, resulting in a high variance for voxel 1. As voxels 3 and 6 generally have less intense voxels on their LORs, their variance is lower compared to the variance for voxel 1. This can also be verified with equations (4.6), (4.9), (4.10) and (4.11), which confirm that the CNR decreases for increasing count $\boldsymbol{Q}$.

4.4.2 Effect of multipinhole-specific design parameters

Pinradius (PD)

Predicting the effect of changing the distance between the central and the surrounding apertures is very difficult, because the image quality is affected by many counteracting influences. First, as the pinradius increases, the sensitivity drops, because the (mean) distance from a random voxel to the pinhole apertures increases. This induces obviously a decrease in image quality in that voxel. Second, the amount of overlap between the projection images, and thus also the number of voxels that are projected onto the detector in an overlap region, reduces with a growing pinradius, which should be beneficial. Third, an increasing pinradius causes the projections of a voxel to move outward. Therefore some projections might fall outside the detector area, again reducing the CNR.

In this work, the reconstruction quality is evaluated in individual voxels. Therefore, the effect of the change in pinradius, and thus also the effect of the above mentioned influences, is examined for each voxel of interest separately. For this reason we studied the behavior of the projections of the activity in the voxel of interest through the different apertures, while changing parameter PD.

All investigated voxels in the homogeneous sphere reach their maximum image quality at a pinradius of 25 mm (see Fig. 4.5(a)). However, these points experience the increase in distance between the apertures very differently. The projections of the central voxel (point 1) start to overlap with other projections for a pinradius of 20 mm. Projection truncation begins at 40-45 mm. Therefore, below 20 mm and above 40 mm the quality is expected to decrease rapidly. The slight decrease in between (see solid line in Fig. 4.5(a)) can be explained by the reduction in sensitivity. The eccentric voxel on the AOR (point 3) suffers already from overlap at a pinradius of 25 mm and some projections of the point start to fall outside the detector area from a PD of 30-35 mm. The optimum (see dotted line in Fig. 4.5(a)) is, as expected, more clear. The eccentric point in the central plane (point 6) is not influenced by any overlap any more at a PD of 35 mm, but from a PD of

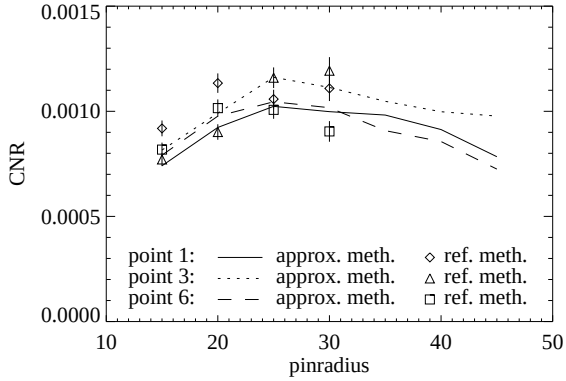

(a) Sphere, 7 pinholes, D=1.2 mm

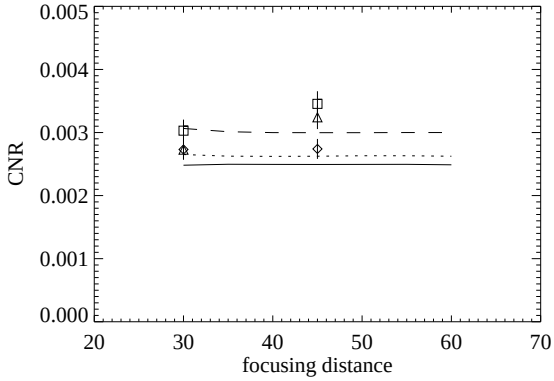

(b) Rat, 4 pinholes, D=1.5 mm

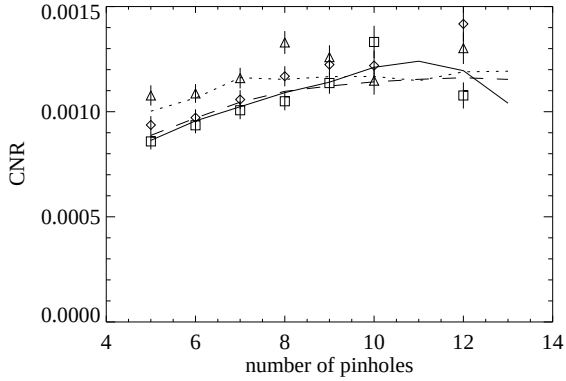

(c) Sphere, 5-13 pinholes, D=1.2 mm

Figure 4.5: Evaluation of the influence of the different multipinhole-specific design parameters on the reconstruction quality of a homogeneous sphere or a rat brain phantom. The error bars indicate one standard deviation. The target resolution was 2.4 mm.

30-35 mm the information drops due to truncated projections. Fig. 4.5(a) (dashed line) suggests that for this voxel the higher sensitivity for designs with a PD of 25 or 30 mm manages to compensate for the deteriorating influence of the overlap.

The four designs with the smallest pinradius were successfully validated with the reference method.

Focusing distance (F)

From Fig. 4.5(b), it can be concluded that the effect of the focusing distance on the reconstruction quality of the rat brain phantom is negligible. This is due to the fact that the acceptance angle is still large enough to cover the investigated points.

The two validated designs gave satisfactory results.

Number of pinholes

The effect of the addition of pinholes can be studied from Fig. 4.5(c). As expected, at first the CNR increases with the number of pinhole apertures thanks to the increased sensitivity. However, due to overlap, the extra sensitivity does not simply stand for increased information and a saturation point will be reached, as was also observed by Cao *et al.* [18]. For the central voxel (point 1) the image quality is best for 11 apertures. Adding more pinholes reduces the CNR. The axially eccentric voxel (point 3) does not benefit from using more than 7 apertures. However, this does not degrade the image quality either. For the eccentric voxel in the central plane (point 6) the curve starts flattening around 9 pinholes.

For most designs the CNR was also calculated using the reference method. Most predictions match well with the validation results. The latter show the above discerned trends less clearly due to noise. For the first 5 designs between 250 and 300 noise realizations were simulated instead of 150, hence their shorter error bars.

4.4.3 Method validation: overview

All validation points are shown in one graph (see Fig. 4.6(a)), which plots the CNR calculated with MLEM reconstructions with respect to the predicted CNR. The solid line was fitted to minimize the least squares distance to these points. The dashed lines indicate distances of one and two standard deviations from the fitted line. The standard deviation on the CNR could be found from the relative standard deviation on the variance, since the CRC was calculated from noiseless data. Hence, for most points the relative standard deviation on the CNR is $\sqrt{1/(2*150)} = 0.058$.

As shown in Fig. 4.6, the fitted line is slightly inclined towards the y-axis (slope 1.02, y-intercept $6.1{*}10^{-6}$), which means that the approximate method systematically underestimates the CNR a little. In addition, 49.4%, 82.8% and 95.4% of the points are located in the 68.3%, 95.4% and 99.7% confidence interval (one,

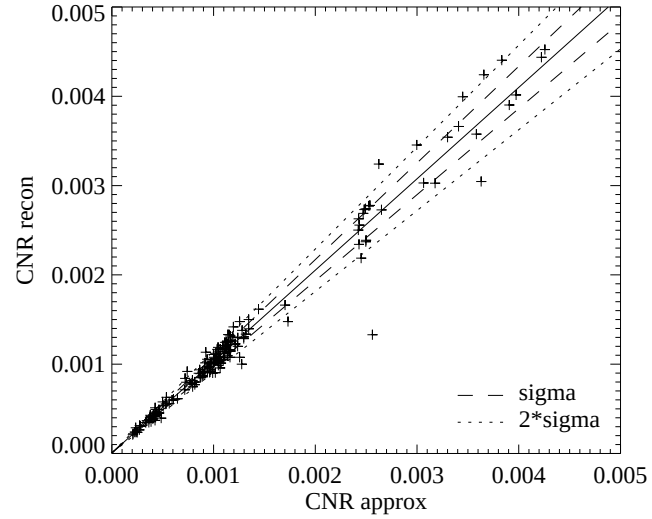

(a) All validation points

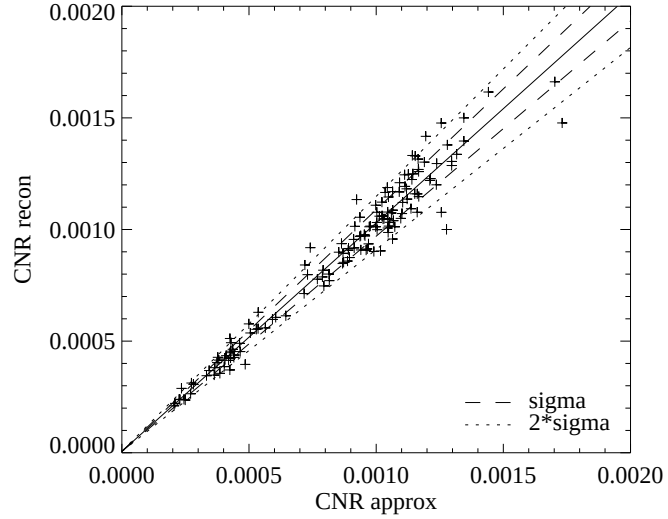

(b) Zoomed-in part of figure (a)

Figure 4.6: Plot of the CNR calculated using the reference method versus the CNR obtained with the approximate method. (a) all validated designs, (b) a zoomed-in part of (a).

two and three standard deviations), respectively. These results show that the new approximate method predicts successfully the reconstruction quality of a voxel.

4.5 Discussion

Although it has not been thoroughly tested yet, the reconstruction quality quantification method, presented in section 4.2.2, should also be valid for multiple head multipinhole SPECT. In addition this method can be applied to PET and other SPECT applications as well.

Our method differs from the methods presented in [79, 93, 94] by the use of post-smoothed MLEM instead of MAP. However, if the regularization term $\beta \boldsymbol{U}$ is designed in such a way that $[\boldsymbol{F}+\beta \boldsymbol{U}]^{-1} = \boldsymbol{P}^j \boldsymbol{G}^j$, like in [104], the difference between MAP and post-smoothed MLEM fades away and equations (4.4) and (4.5) become equations (4.7) and (4.8). With our method we can easily impose a uniform target resolution, which has the advantage that different designs can be compared at the same resolution and that only one parameter has to be considered for optimization, i.e. the variance in the voxel of interest, or equivalently its CNR.

Some previously published methods, like [93], go even further in their approximations. They try to isolate shift-invariant factors, like the geometric projection matrix for positron emission tomography (PET) imaging. Since it is the same for all voxels, it only has to be calculated once. This saves a lot of computation time. For a pinhole system, however, it seemed impossible to distinguish and isolate shift-invariant factors. Another possibility is to isolate the matrices that are independent of the object, like the camera geometry matrix in [94], such that it is sufficient to calculate them in advance (just once). However, this is not useful for collimator design or for the examination of design parameters, since each camera geometry is only tested once. Therefore, we have been using the earlier stated approximations that are less efficient, but still much faster than the reference method. Nevertheless, calculating the impulse response and the covariance matrix, rather than only the CRC and the variance in the investigated voxel (as in [93, 94]), supplies extra - possibly useful - information. It might for example be interesting to know the exact shape of the impulse response or to see which points covariate heavily with the voxel of interest (e.g. to predict artifacts).

To discuss the performance of the suggested approximate method, we list the most time-consuming steps. For each examined voxel 1 projection, 1 backprojection, 1 3D Fourier transformation, 2 inverse 3D Fourier transformations and 2 3D convolutions (for post-smoothing) are required. It is obvious that the efficiency is much higher than that of the reference method, for which 152 post-smoothed MLEM reconstructions (2 of noise-free and 150 of noisy projection data) with 472 iterations (using relaxed ordered subsets) have to be executed for the first voxel and one more for each additional voxel. These 472 iterations used 61 main iterations (with a varying number of subsets), which require 61 forward and backward projections on the whole data set. As the main computational load is due to the forward and backward projections, the efficiency gain is about a factor 152*61 for the first point, and about a factor 61 for all next points. The time gain is thus huge if only a few points (up till several 100s) are under investigation. However, if one is interested in variance images of the complete phantom, a faster method, such as [136], is recommended.

Our approximation of the pseudoinverse $\mathbf{G}^j$ (in the Fourier domain) includes a factor $\max(\Re(\boldsymbol{F}^j), 0)$ both in the numerator and in the denominator. In our experience, frequencies with $\Re(\boldsymbol{F}^j) < 0$ have a negative influence on the accuracy and the stability of the approximations. This is probably because they are mostly caused by approximations and round-off errors, since the true Fisher information matrix is positive semidefinite.

To get a fixed resolution throughout the object, the post-smoothing filter was calculated for each voxel separately in this chapter, since pinhole SPECT is shift-variant. For the reconstruction of real data, however, this is not practical. Though, since reconstruction near convergence is assumed, the difference in resolution between the voxels will be rather small after post-smoothing with a fixed filter.

If the software phantom is a centered homogeneous sphere, it is sufficient to investigate all voxels of a halfplane containing the rotation axis. Because of the circular symmetry of the reconstruction properties, this halfplane provides all information about the reconstruction of the entire sphere. For a central single pinhole or a multipinhole design that is symmetrical with respect to the central transaxial plane, a quarter plane (containing the rotation axis and the image center) is even sufficient. Of course, neighboring voxels are usually very alike, such that only a subset of voxels should be investigated. Furthermore, the less regular and homogeneous the software phantom, the more voxels should be examined.

From the validation studies we could remark that the CRC and the variance were more sensitive to the number of iterations (for the reference method) and to the choice of ϵ in equation (4.10) (for the approximate method) than the CNR. If too few iterations were performed or if ϵ was chosen too high, equations (4.7)-(4.10) became less accurate to approximate the CRC and the variance. Fortunately, an increase or decrease in CRC usually accords with an increase or decrease, respectively, in the variance, such that it has only a minor impact on the approximation of the CNR. This inaccuracy can be explained as follows: the higher the number of iterations, or equivalently, the smaller ϵ, the more high frequencies are included, which results in a better approximation of the pseudoinverse and a sharper impulse response. In that case, the large(r) amount of post-smoothing can more easily moderate small inaccuracies. For the same reason the inaccuracy also increases when enlarging the aperture diameter, since the resolution of the impulse response is already large with respect to the imposed target resolution. However, these pinhole diameters are not relevant for pinhole collimator design anyway, because the target resolution cannot be reached for these diameters.

The problem also becomes more complex if the shape of the impulse response resembles less an (isotropic) 3D-Gaussian. A possible solution to reduce this inaccuracy, is to allow more degrees of freedom to the post-smooth filter P^j, e.g. by allowing different FWHM in the three directions or by changing the shape of P^j. However, since the approximation of the CNR is acceptably accurate and in practice we post-smooth with an isotropic Gaussian, we decided to proceed with the CNR (instead of the CRC and the variance) as the reconstruction image quality measure and with an isotropic Gaussian as post-smooth filter.

A target resolution of 2.4 mm might seem a little high at first sight, but from

Fig. 4.3(b) it can be seen that the optimal pinhole diameter is only 1.5-1.8 mm. We preferred to keep the apertures large enough in order to guarantee sufficient sensitivity, as we were mainly interested in designs for low count rat brain studies.

4.6 Future work

In our simulations edge penetration was neglected. The effect of this approximation becomes increasingly important if the pinhole apertures get smaller, if the inclination angle becomes larger, and if the energy of photons emitted by the isotope used to image the phantom/animal gets higher. For the imaging of tracers labeled with ^{99m}Tc with pinhole apertures around 1.5 mm and acceptance angles around 60°, the effect of edge penetration on the relative performance of different designs is expected to be modest compared to the effect of varying the different pinhole design parameters considered in our study. Therefore, we presume that the global trends will remain the same, although e.g. a slight shift towards a lower optimal diameter might be expected, since the effective diameter is underestimated. In the future, we intend to extend our projection method with edge penetration modeling and to study its effect on the image quality.

The presented approximations will be used in the future to find a good design for rat brain imaging. Many different designs will be tested keeping the effects of the different design parameters in mind. The best design will be realized in practice and compared with our current 7-pinhole design (with aperture diameters of 1.5 mm, acceptance angles of 60°, a pinradius of 39 mm and a focal distance of 170 mm).

While searching for a better design, the following considerations should be kept in mind. Firstly, the image quality is shift- and object-variant. A well defined problem statement is the first step in the optimization process: for which application will the design be used, for which portion of the FOV should the quality be optimized, etc. Secondly, it still is an approximate method. Therefore it is useful to verify the quality of (some of) the best designs with the reference method. Finally, a trade-off is often necessary between the degree of quality improvement and the feasibility, or equivalently, the complexity of the design.

Another important issue is the positioning of the pinhole apertures in a multipinhole design. In this work we ignored the fact that regular patterns might cause artifacts in the reconstruction image in case of overlapping projections (see [3,119,125]) in the form of points (*ghost points*) or circular shapes (*ghost circles*). Positioning the apertures in an irregular pattern can help to reduce these artifacts. This was already observed in the 1970's [49], when one introduced the nonredundant arrays[7] to reduce the high correlations between different voxels. In chapter 5 we will have a closer look at the effect of these artifacts on the reconstruction image quality. It should be verified whether these artifacts are translated adequately into a lower CNR or whether they are only reflected in the covariance matrix of the reconstruction.

[7] In a nonredundant array one imposes that the displacement between every two pinholes appears once and only once.

As mentioned during the discussion of the results in section 4.4, the overlapping projections do not only cause artifacts. They also influence the reconstruction image quality, since some projected activity cannot be linked one-to-one any more with a particular pinhole aperture. It is therefore not straightforward to value the extra sensitivity obtained by allowing projections to overlap. Using the method presented in this chapter, the influence of overlap is studied in the next one. Preliminary results were already described in [122].

4.7 Conclusion

An accurate and efficient method is proposed to evaluate different single and multi-pinhole collimator designs for a particular application and a fixed target resolution. The quality of the reconstruction of each voxel can be quantified efficiently based on the contrast recovery coefficient of the linearized local impulse response and the variance. This method has been validated using post-smoothed MLEM reconstructions. The effect of changing a collimator design parameter, such as the aperture diameter, the focal distance or the number of pinholes, has been investigated.

Chapter 5

Effect of overlapping projections on reconstruction image quality in multipinhole SPECT

[1]Multipinhole SPECT imaging has several advantages over single pinhole SPECT imaging, including an increased sensitivity and an improved sampling. However, the quest for a good design is challenging, due to the large number of design parameters. The effect of one of these, the amount of overlap in the projection images, on the reconstruction image quality, is examined in this chapter. The evaluation of the quality is based on efficient approximations for the linearized local impulse response and the covariance in a voxel, and on the bias of the reconstruction of the noiseless projection data. Two methods are proposed that remove the overlap in the projection image by blocking certain projection rays with the use of extra shielding between the pinhole plate and the detector. Also two measures to quantify the amount of overlap are suggested. First, the approximate method, predicting the contrast-to-noise ratio (CNR), is validated using post-smoothed MLEM reconstructions with an imposed target resolution. Second, designs with different amounts of overlap are evaluated to study the effect of multiplexing. In addition, the CNR of each pinhole design is also compared with that of the same design where overlap is removed. Third, the results are interpreted with the overlap quantification measures. Fourth, the two proposed overlap removal methods are compared. From the results we can conclude that, once the complete detector area has been used, the extra sensitivity due to multiplexing is only able to compensate for the loss of

[1]This chapter has been published as a full article in *IEEE Transactions on Medical Imaging*: K. Vunckx, P. Suetens and J. Nuyts. Effect of overlapping projections on reconstruction image quality in multipinhole SPECT. *IEEE Trans. Med. Imag.*, 27(7):972-983, 2008. Only minor changes concerning notational consistency and lay-out have been performed.

information, not to improve the CNR. Removing the overlap, however, improves the CNR. The gain is most prominent in the central field of view, though often at the cost of the CNR of some voxels at the edges, since after overlap removal very little information is left for their reconstruction. The reconstruction images provide insight in the multiplexing and truncation artifacts.

5.1 Introduction

Over the past decade research on small animal imaging has gained a lot of interest. For SPECT, multipinhole collimation methods are receiving increased attention over single pinhole collimators because they are expected to provide superior image quality. However, the complexity of designing such a multipinhole collimator increases dramatically with the number of pinhole apertures. The influence of many of these design parameters, such as the focal distance, the aperture diameter and the position of the apertures, has already been investigated in the previous chapter. Another design parameter is the amount of overlap (also called multiplexing) allowed for the projections through the different pinhole apertures. Two extreme cases are coded aperture collimation with a high degree of multiplexing (Meikle *et al.* [75]) and no overlap at all (Beekman *et al.* [9]), with in between a moderate amount of overlap (Schramm *et al.* [97]). Although overlap has been studied previously (e.g. [76,78,80]), its effects are not yet completely understood. In this work we try to find the answer to the question: "Is it better to have *more sensitivity* thanks to overlapping projections or to *remove the overlap* (and thus reduce the sensitivity) in order to have unambiguous information in each detector pixel?" For a certain pinhole design, the overlap can be removed by putting extra collimation material between the pinhole plate and the detector, such that each detector pixel only receives counts from one single aperture. We investigate the effect of multiplexing on the reconstruction image quality of each voxel. As a measure of image quality the contrast-to-noise ratio (CNR) of the linearized local impulse response (LLIR) in a voxel of the reconstructed image is used. The efficient approximate method to calculate the CNR was presented earlier in section 4.2.2. A recapitulation of this method can be found in section 5.2.1. Also the bias in the reconstruction image is studied. In section 5.2.2 we propose two different ways to remove the overlap in the projection image. To analyze its influence on the image quality, it is useful to have some measures that quantify the amount of overlap. Some suggestions are made in section 5.2.3. In section 5.3 several simulation studies are described. First, a validation study is presented. Second, the effect of overlap on the image quality is studied based on a number of multipinhole designs with a varying degree of multiplexing. Each design is also compared with the same design, but with extra shielding such that the overlap is removed. Third, the overlap quantification measures are used to explain some of the results. Finally, the two overlap removal methods are compared. The results are presented in section 5.4 and discussed in section 5.5.

5.2 Theory

5.2.1 Reconstruction image quality quantification

One way to quantify image quality in emission tomography is to examine the properties of the linearized local impulse response (LLIR) l^j [37]:

$$l^j(\hat{\Lambda}) = \lim_{\delta \to 0} \frac{\hat{\Lambda}(\bar{Q}(\Lambda + \delta e^j)) - \hat{\Lambda}(\bar{Q}(\Lambda))}{\delta} \tag{5.1}$$

$$= \frac{\delta}{\delta \lambda_j} \hat{\Lambda}(\bar{Q}(\Lambda)) \tag{5.2}$$

where $\bar{Q}$ is the expectation of the projection data Q, $\hat{\Lambda}$ is the reconstruction of the unknown activity distribution Λ, e^j is the j-th unit vector, and j is the index of the voxel in the reconstruction image.

The calculation of the LLIR (l^j) and its covariance (Cov^j) for each voxel j using an iterative reconstruction method and multiple noise realizations, called *reference method* in the rest of this work, is very time-consuming. Therefore some efficient analytical approximations were proposed by Fessler *et al.* [33, 37] and Qi *et al.* [94] for converged maximum a posteriori (MAP) reconstruction:

$$l^j(\hat{\Lambda}) \approx [\boldsymbol{F} + \beta \boldsymbol{U}]^{-1} \boldsymbol{F} e^j \tag{5.3}$$

$$\mathrm{Cov}^j(\hat{\Lambda}) \approx [\boldsymbol{F} + \beta \boldsymbol{U}]^{-1} \boldsymbol{F} [\boldsymbol{F} + \beta \boldsymbol{U}]^{-1} e^j \tag{5.4}$$

where $\boldsymbol{F}$ is the Fisher information matrix, which is a function of $\bar{Q}$, β is the smoothing parameter and $\boldsymbol{U}$ is the Hessian of the quadratic prior, used for regularization.

We derived very similar approximations for converged post-smoothed maximum likelihood expectation maximization (MLEM) reconstruction with an imposed target resolution:

$$l^j(\Lambda) \approx \boldsymbol{P}^j \boldsymbol{G}^j \boldsymbol{F}^j e^j \tag{5.5}$$

$$\mathrm{Cov}^j(\Lambda) \approx \boldsymbol{P}^j \boldsymbol{G}^{jT} l^j(\Lambda) \tag{5.6}$$

with $\boldsymbol{P}^j$ the isotropic Gaussian post-smooth filter, $\boldsymbol{G}^j$ the approximate pseudoinverse of $\boldsymbol{F}^j$, which is the local shift-invariant approximation (see [36, 94]) of $\boldsymbol{F}$, and ^{T} denoting transpose. More details can be found in section 4.2.2.

A fixed spatial resolution enables the comparison between different pinhole collimator designs. This could also be achieved with a MAP method, e.g. using the analytical approach presented in [35]. As shown in [104], MAP and post-smoothed MLEM have the same noise performance when the same uniform resolution is imposed.

As a reconstruction image quality measure the contrast-to-noise ratio (CNR) in voxel j is used, which can be calculated from the contrast recovery coefficient

(CRC) and the variance of the LLIR in that voxel (which are the j-th element of $l^j(\Lambda)$ and $\mathrm{Cov}^j(\Lambda)$, respectively):

$$\mathrm{CNR} = \frac{\mathrm{CRC}}{\sqrt{\mathrm{variance}}}. \tag{5.7}$$

One should however take into consideration that pinhole SPECT is incomplete tomography. Due to the insufficient sampling there is no unique solution for the reconstruction problem. For multiplexing pinhole designs this causes the reconstruction image to suffer from artifacts (see [3, 78, 119, 125]) in the form of points (*ghost points*) or circular shapes (*ghost circles*). If no overlap is allowed, the probability for truncation artifacts increases.

Because it is not guaranteed that these image degrading effects influence the CNR, we found it useful to examine the reconstructed image as well, either by visual inspection of the image, or by evaluating the root mean squared relative deviation (RMSRD) of the post-smoothed reconstructed image from the original post-smoothed phantom, which is calculated as follows:

$$\mathrm{RMSRD} = \sqrt{\frac{\sum_{j\in\mathrm{VOI}} \left(\frac{\mathrm{recon}_j - \mathrm{phantom}_j}{\mathrm{phantom}_j}\right)^2}{J}}, \tag{5.8}$$

with j indicating a voxel in the image space, VOI the volume of our interest (at least excluding all voxels for which $\mathrm{phantom}_j = 0$) and J the total number of voxels in the VOI. Because the reconstruction is based on a noise-free sinogram and because of the matched post-smoothing, the RMSRD is mostly due to bias (artifacts). In this work we mainly focus on the variation in CNR.

5.2.2 Overlap removal methods

The amount of overlap in the projection images can be varied in different ways, such as:

- by varying the number of pinhole apertures,
- by varying the distance between the pinhole apertures,
- by varying the focal distance,
- by varying the acceptance angle,

or a combination of the above. However, these methods induce a change in image quality in two interacting ways. On the one hand, the activity will be seen with a different sensitivity due to the altered design parameter(s). On the other hand, the amount of multiplexing will differ. Therefore, in addition, each design is considered twice. Once just as it is, i.e. producing overlapping projections on the detector (see Fig. 5.1(a)), and once more with additional shielding between the pinhole plate and the detector (see Fig. 5.1(b) and (c)), which stops projection rays that otherwise

would cause multiplexing. This overlap removal can be obtained in many different ways. In this section, two methods are presented.

The sensitivity of an aperture will be measured as the projection image of a uniform plane source through that particular aperture. In Fig. 5.1(a) the black dashed and dotted curves depict profiles through the projection images corresponding to the central and eccentric apertures, respectively. It can be proven that the distance between the planar source and the pinhole plate has no influence on the projection images. In the rest of this work such a projection image will be called the "sensitivity image[2]", or simply the "sensitivity" of the corresponding aperture. The white solid curve in Fig. 5.1(a) shows a profile through the total sensitivity image. As can be seen, the overlapping projections cause an increased total sensitivity.

The sensitivity is readily calculated analytically (similar to [97]). Knowing the sensitivity for each aperture in each detector pixel, it is straightforward to detect and/or remove overlapping sensitivities in simulation studies.

The two overlap removal methods, proposed here and used to compare designs with and without multiplexing, are:

Maximum sensitivity

The most obvious way to remove multiplexing is to keep the highest sensitivity in each detector pixel. All other sensitivities in that pixel are set to zero. Intuitively, this seems a good solution, since sensitivity and reconstruction image quality go hand in hand. This principle is illustrated in Fig. 5.1(b), where the black dotted and dashed curves represent profiles through the new sensitivity images of the three pinhole apertures, and the white solid curve depicts a profile through the total sensitivity image. The extra shielding prevents the projections from overlapping. It is designed in such a way that the transition from one pinhole to the next happens at equal sensitivity in order to retain the highest sensitivity in each detector pixel.

Central sampling

Another useful approach could be to optimize the performance for the central field of view (FOV), by giving preference to extra sampling of central voxels over sampling of more eccentric voxels. For that purpose, the distances between the reconstruction image center and the backprojection lines starting from the detector pixel through the center of each pinhole aperture are computed. The sensitivity of the aperture corresponding to the smallest distance is preserved, all others are set to zero. For an illustration, see Fig. 5.1(c), where for one detector pixel in a former overlap zone (see Fig. 5.1(a)) the backprojection lines through the two involved apertures are drawn in gray. The backprojection line through the central pinhole lies closer to the image center than the line through the right pinhole. Therefore, the shielding is designed

[2]Note that this "sensitivity image" only provides the sensitivity as a function of two dimensions. It does not include the effect of the distance between the point source and the pinhole plane, and differs therefore from the more commonly used definition of sensitivity.

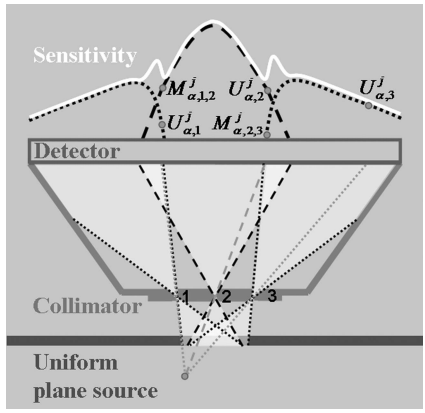

(a) With overlap

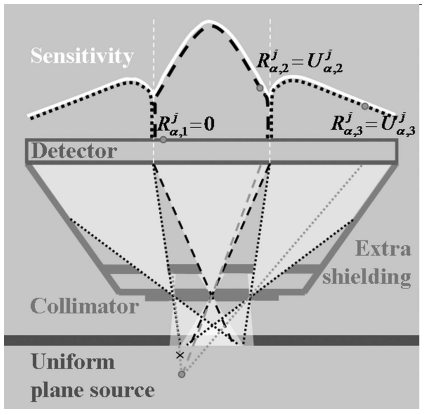

(b) Overlap removed with maximum sensitivity method

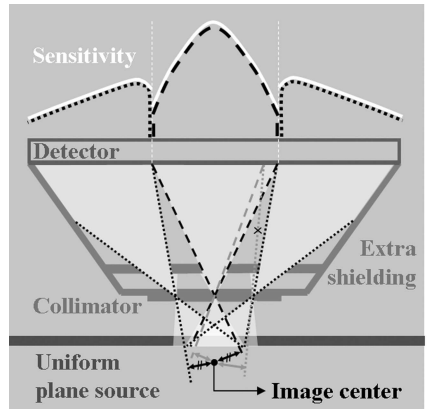

(c) Overlap removed with central sampling method

Figure 5.1: Graphical explanation of the "sensitivity" (a) for a simple multipinhole configuration and illustration of the two proposed overlap removal methods: (b) maximum sensitivity and (c) central sampling.

such that the former line is allowed to pass through, while the latter is stopped by collimator material. In other words, the sensitivity of the central aperture is maintained, whereas that of the right aperture is set to zero. The black backprojection lines corresponding to the black arrows originate from a detector pixel where the transition of one sensitivity to another takes place, since the distances to the center of the image are equal.

5.2.3 Overlap quantification measures

An intuitive method to quantify the amount of multiplexing consists of determining for each detector pixel from how many pinhole apertures it is gaining information and averaging this number over all pixels. This is a basic approach with several disadvantages. First, it does not take into account the degree of multiplexing in terms of the relative contribution of the involved apertures to the measurement. Second, it only represents the global amount of overlap in the detector space. It is not related to the voxels (in the image space), such that it is impossible to know which voxels and how many might suffer from this ambiguous information collection.

Therefore overlap quantification is envisaged from a different perspective here. Since the main purpose of this work is to investigate the influence of overlapping projections on the CNR in each reconstructed voxel, the amount of overlap is computed for every individual voxel.

The following measure of overlap is proposed:

$$\text{amount of overlap for voxel } j = 1 - \frac{\sum_\alpha U_\alpha^j}{\sum_\alpha (U_\alpha^j + M_\alpha^j)}, \tag{5.9}$$

where j is the voxel under consideration, and U_α^j and M_α^j represent the total "useful" and the total "multiplexed" sensitivity, respectively, both at rotation angle α. To compute U_α^j, a point source in j is projected through the center of each aperture ap (at rotation angle α) onto a single detector pixel, and detected with the useful sensitivity $U_{\alpha,ap}^j$ corresponding to that pixel (see Fig. 5.1(a)). Subsequently, these sensitivities are summed, i.e. $U_\alpha^j = \sum_{ap} U_{\alpha,ap}^j$. Averaging over all rotation angles gives an idea of the total amount of information that could have been available during reconstruction, if no overlap would have been present in the projections. However, in the case of multiplexing, activity originating from other image voxels and projected through other apertures might also be detected by the same detector pixels. As an example, in Fig. 5.1(a) the pixel detecting the activity in voxel j through aperture 1 with useful sensitivity $U_{\alpha,1}^j$ also detects other activity seen through aperture 2 with a multiplexed sensitivity $M_{\alpha,1,2}^j$. To account for this, all multiplexing sensitivities are accumulated as well, yielding $M_\alpha^j = \sum_{ap_u} \sum_{ap_m \neq ap_u} M_{\alpha,ap_u,ap_m}^j$ for angle α, with ap_u and ap_m the apertures causing the useful and the multiplexed sensitivities, respectively.

As a result, for non-multiplexing designs the amount of overlap equals zero for every voxel j. For designs with overlapping projections, it will be between zero and one for some voxels and zero for all others. In addition, a higher degree of multiplexing results in a higher value, both in the case where overlap is caused by an increasing number of apertures, and in the case where the share of the multiplexed sensitivity becomes larger with respect to that of the useful sensitivity.

Another issue that should be taken into consideration, however, is the fact that overlap removal can reduce the total sensitivity for a voxel, because one or more projection lines are blocked by the extra shielding (see Fig. 5.1). Therefore we

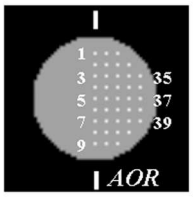

(a) Homogeneous sphere, transaxial slice (used for validation)

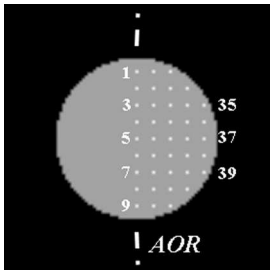

(b) Homogeneous sphere, transaxial slice (used for simulations)

(c) Rat brain phantom, transaxial slice

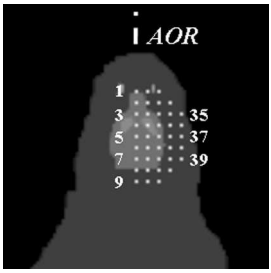

(d) Rat brain phantom, coronal slice

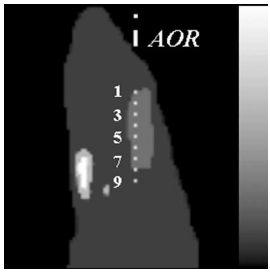

(e) Rat brain phantom, sagittal slice

Figure 5.2: The investigated voxels (in a slice containing the AOR) in two homogeneous spheres with a radius of (a) 17.5 mm and (b) 23.0 mm, respectively, and in a rat brain phantom: (c) transaxial, (d) coronal and (e) sagittal slice through the AOR.

suggest a second measure:

$$\text{loss of useful sensitivity for voxel } j = 1 - \frac{\sum_\alpha R_\alpha^j}{\sum_\alpha U_\alpha^j} \tag{5.10}$$

with R_α^j the total "remaining useful" sensitivity for voxel j after overlap removal (at rotation angle α). An example is shown in Fig. 5.1(b), where the same configuration as in Fig. 5.1(a) is depicted, but with the overlap removed following the maximum sensitivity method. Since the projection line through pinhole 1 is blocked, $R_{\alpha,1}^j$ equals zero. For the other two apertures the useful sensitivity before and after overlap removal is the same. Consequently, the total loss equals zero if the introduction of extra collimation does not affect the sensitivity for voxel j, and increases (to maximum one) when more (or all) useful sensitivity is discarded.

5.3 Simulation setups

5.3.1 Validation of the image quality quantification

In section 5.2.1 some efficient approximations for the LLIR in an image voxel and its covariance were described to quantify the image quality after post-smoothed MLEM reconstruction. These have been validated in the previous chapter for various designs differing in aperture diameter, focal distance, acceptance angle, positioning of the pinholes, number of pinholes, etc. In this chapter, we study another pinhole design parameter, the influence of overlapping projections, in more detail. Although it was already implicitly studied and validated in chapter 4, a more thorough investigation was needed, and an extra validation study for designs with explicit overlap removal was still considered to be relevant. Therefore, for a well-chosen multipinhole design, investigated before and after overlap removal (central sampling method, see section 5.2.2), the approximate method was compared with respect to the - very slow - reference method calculating the post-smoothed MLEM reconstructions of a large number of noisy projection data sets.

The multipinhole design consisted of 7 pinhole apertures with an aperture diameter of 1.8 mm and an acceptance angle of 60°. All apertures were located in a plane parallel to the detector. The 6 apertures surrounding the central one were uniformly distributed over a circle with a radius of 15 mm. This radius is also called *pinradius* in this work. Three pinholes were positioned on a line parallel to the axis of rotation (AOR). All apertures focused on the image center, i.e. the axes of symmetry of all apertures intersect at the image center. The distances from the detector to the center of the pinhole plate and to the AOR were 173 mm and 218 mm, respectively. The data were acquired in a matrix of 256×200 square pixels with a pixel size of 1.95 mm. The intrinsic resolution of the detector, which was assumed to be an infinitely thin, perfect absorber, was modeled as a Gaussian with a full width at half maximum (FWHM) of 4.0 mm.

For a homogeneous sphere with a radius of 17.5 mm and an activity of 5 kBq/mm^3 the CNR in 39 equally spaced voxels (as shown in Fig. 5.2(a)) was examined with the approximate method as well as with the reference method. The simulated SPECT acquisition consisted of 64 rotation angles (60 s each) measured over 360°. The image space consisted of 65×65×65 cubic voxels with a size of 0.8 mm and a target resolution of 2.4 mm was imposed.

The resolution and sensitivity effects of the pinhole apertures were modeled in the projection method as follows. For each detector pixel-aperture combination a cone through the FOV, which contains all voxels that contribute to the intensity measurement of that pixel, is defined. Each voxel's contribution is weighted by a factor dependent on the distance between the voxel and the detector. These weights are calculated in advance, and are used for all forward and backward projections. Our current implementation does not allow edge penetration modeling yet. Scatter and attenuation effects were neglected.

For the reference method, the iterative MLEM reconstructions were accelerated using ordered subsets (OSEM) [55, 116]. An equivalent of 472 iterations were cal-

culated to run MLEM close to convergence. The FWHM of the post-smooth filter was chosen such that the impulse response reached the target resolution. For the calculation of the (co)variance 250 noise realizations were simulated.

5.3.2 Effect of overlap on reconstruction image quality

To investigate the effect of overlap on the reconstruction image quality, we compare several realistic multipinhole designs with different degrees of multiplexing. For each design, the CNR was calculated for 39 voxels of a homogeneous sphere with a radius of 23.0 mm and an activity of 5 kBq/mm^3 (see Fig. 5.2(b)), using the approximate method. Afterwards, these designs were also tested for a digital rat brain phantom with realistic dimensions and activities (see Fig. 5.2(c)-(e)) to examine the effects of imaging another (more relevant) phantom with a different morphology.

All investigated designs had the same main parameters as the designs described in the previous section. They differ only in the number of apertures and/or in the distance between the central and the surrounding pinholes (pinradius). The projection images were also acquired in the same way as in the validation study, however including attenuation modeling this time (linear attenuation coefficient of ^{99m}Tc in water: 0.015 mm^{-1}). The image space was enlarged to 95×95×95 voxels of 0.8 mm and the target resolution was kept fixed to 2.4 mm.

Three groups of multipinhole designs were examined. The first group consisted of three designs with an increasing number of pinholes (5, 10 and 15 apertures), and thus an increasing amount of overlap. For each design the pinradius was 25 mm. For the second group three 10-pinhole designs were investigated of which the distance between the apertures was varied (a pinradius of 35, 25 and 15 mm). In this case the overlap increases with decreasing pinradius. The last group contained four designs, again with a varying number of apertures (9 to 15), but with a slightly different positioning of the apertures with respect to the first two groups. The pinhole apertures surrounding the central one were alternatingly divided over two concentric circles, the first one with pinradius 20 mm, the second one with pinradius 30 mm. This was done to improve the filling and the usage of the detector.

All designs were also investigated for the case where the overlap was completely removed, using either method of section 5.2.2. In this way two kinds of overlap reduction were examined, i.e. a reduction by decreasing the number of pinholes or by putting the apertures farther apart, and a removal by adding extra shielding to avoid overlap.

The CNR is insensitive to (low frequency) artifacts. Therefore, the noiseless projection data were also reconstructed with post-smoothed OSEM (an equivalent of 129 iterations). The RMSRD was calculated using equation (5.8). The VOI was defined by all voxels of the post-smoothed phantom that were higher than 50% of the (background) activity inside the object. For the rat phantom shown in Fig. 5.2(c)-(e), all pixels more distant from the image center than 23 mm were discarded as well.

5.3.3 Interpretation of the effect of overlap

In this simulation study, the effect of (the amount of) overlap in the projection images, as well as the influence of overlap removal, will be investigated with the help of the two new measures for overlap quantification, described in section 5.2.3 (see equations (5.9) and (5.10)). For this purpose, three 7-pinhole designs with a varying degree of multiplexing were examined using the approximate method. Next, these same three designs were reconsidered after removing the overlap. Last, the reconstructed image and the corresponding RMSRD were calculated, as described in the previous section.

The main system parameters were equal to the parameters stated above (section 5.3.2). The pinradius ranged from 35 mm (little overlap) to 15 mm (large overlap). The CNR, the amount of overlap and the loss of useful sensitivity were calculated for the same voxels of the large homogeneous sphere described previously (see Fig. 5.2(b)).

5.3.4 Comparison of overlap removal methods

In order to investigate how sensitive the CNR and the RMSRD are to the way overlap is removed, the third group of designs of section 5.3.2 (9 to 15 pinholes with alternating pinradius of 20 and 30 mm) was studied in more detail. The CNRs and RMSRDs that were obtained after overlap removal with the central sampling method are now compared to those found after maximum sensitivity overlap removal. Differences between the two presented overlap removal methods can only be explained by differences in loss of useful sensitivity which is calculated from equation (5.10).

5.4 Results

5.4.1 Validation of the image quality quantification

The results of the validation study, presented in section 5.3.1, are shown in Fig. 5.3. The CNR of each investigated point of the homogeneous sphere shown in Fig. 5.2(a) is plotted with respect to its point number. The solid and the dashed-dotted line connect the results obtained with the reference method for the 7-pinhole design before ('with overlap') and after ('no overlap') overlap removal, respectively. The dashed and the dotted line plot the corresponding CNRs estimated with the approximate method. The relative standard deviation on the CNR is expected to be $\sqrt{1/(2 \times 250)} = 4.5\%$. When the new approximate method is compared to the reference method, one can see a fair match of the absolute values and an excellent agreement for the performance ranking (overlap versus no overlap). Using the least squares fit through the validation points of the previous chapter (slope 1.02, y-intercept 6.1×10^{-6}, see Fig. 4.6), 47.4%, 87.2% and 94.9% of the points lie in a 1, 2 and 3 standard deviation range from the estimated value, respectively.

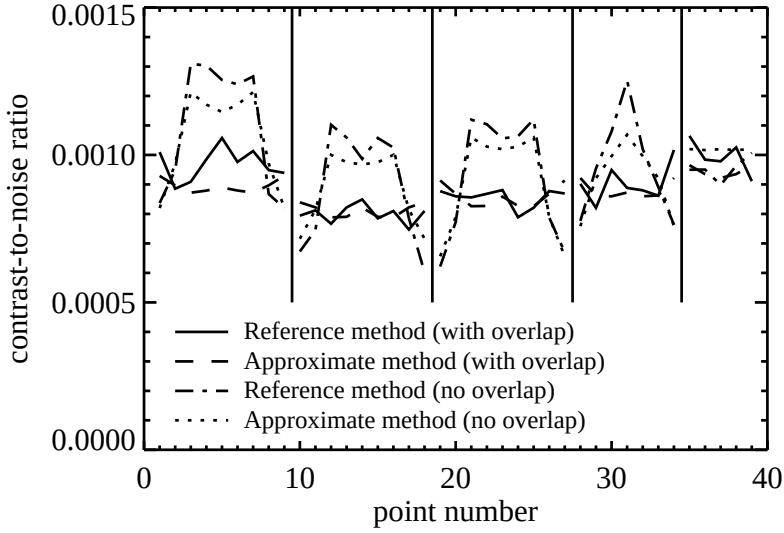

Figure 5.3: Validation of the approximate image quality quantification method with the reference method. The CNR obtained with a 7-pinhole design with a pinradius of 15 mm, with and without overlap (central sampling method), was calculated in 39 voxels of a small homogeneous sphere (Fig. 5.2(a)).

5.4.2 Effect of overlap on reconstruction image quality

The aim of the study presented in section 5.3.2 is to answer the question: is an amount of overlap in the projections beneficial or should it be reduced, and if so, how?

Fig. 5.4(a) shows the CNR in the examined voxels of the large homogeneous sphere of Fig. 5.2(b) for the first group of multipinhole designs. This graph already highlights multiple effects of multiplexing. First of all, it shows that if the overlap is maintained (solid lines), adding pinholes is beneficial up to about 10 apertures. Using a higher amount of apertures has almost no influence on the CNR. However, if the overlap is removed[3] (dashed lines), the CNR increases steadily with the number of pinholes for central voxels, but decreases for voxels at the edge of the FOV. Finally, all designs perform better after overlap removal, except for the most eccentric voxels. For the rat phantom (Fig. 5.4(b)) very similar results are found, though without decrease in CNR at the edges if compared to the designs with overlapping projections. For both phantoms, much less difference can be seen between imaging with and without overlap if a 5-pinhole design is used instead of a 15-pinhole design.

The investigation of the reconstruction images and the RMSRDs of the first group of designs (listed in table 5.1) indicates a very nice reconstruction quality for

[3] Unless mentioned otherwise, the plotted CNRs for designs without overlap were obtained using the central sampling overlap removal method.

Table 5.1: Overview of all RMSRDs corresponding to the four groups of designs tested in the simulation studies. The left three columns show the RMSRDs (designs allowing overlap (left), and after overlap removal with the maximum sensitivity (center) and the central sampling method (right)) for the large sphere. The right three columns show the RMSRDs for the rat brain phantom.

	large homogeneous sphere			rat brain phantom		
	RMSRD_{ovl}	RMSRD_{ms}	RMSRD_{cs}	RMSRD_{ovl}	RMSRD_{ms}	RMSRD_{cs}
ph 5, pinradius 25 mm	1.85%	1.78%	1.80%	2.46%	2.42%	2.41%
ph 10, pinradius 25 mm	7.70%	12.88%	15.30%	3.92%	2.83%	3.60%
ph 15, pinradius 25 mm	9.51%	14.65%	18.78%	5.32%	2.84%	3.96%
ph 10, pinradius 35 mm	6.81%	3.38%	44.99%	4.26%	4.67%	7.17%
ph 10, pinradius 25 mm	7.70%	12.88%	15.30%	3.92%	2.83%	3.60%
ph 10, pinradius 15 mm	10.33%	7.41%	7.20%	5.45%	2.78%	2.86%
ph 9, pinradius 20/30 mm	4.09%	1.83%	3.33%	4.44%	2.17%	2.36%
ph 11, pinradius 20/30 mm	5.25%	3.05%	14.31%	4.29%	2.57%	3.12%
ph 13, pinradius 20/30 mm	8.60%	6.94%	11.00%	5.85%	2.98%	3.78%
ph 15, pinradius 20/30 mm	13.17%	17.87%	22.26%	6.51%	3.16%	3.37%
ph 7, pinradius 35 mm	8.43%	1.95%	21.68%			
ph 7, pinradius 25 mm	6.29%	6.67%	7.15%			
ph 7, pinradius 15 mm	11.35%	5.46%	5.22%			

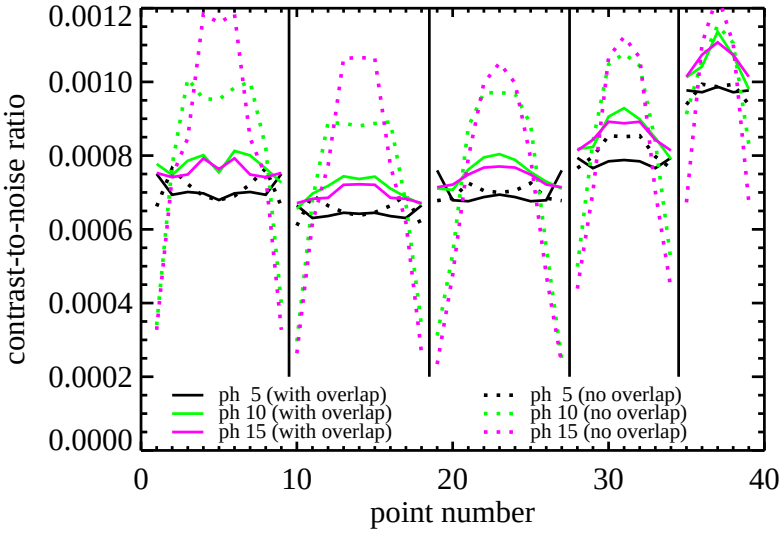

(a) Sphere, number of pinholes 5-15, pinradius 25 mm

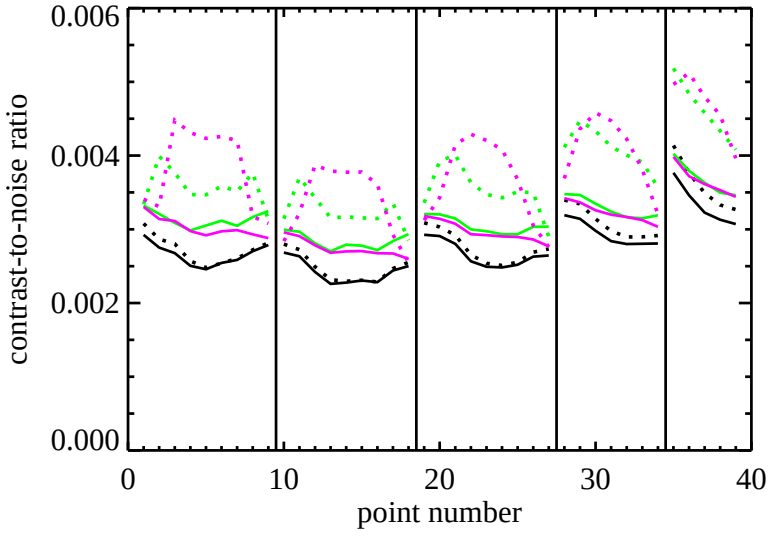

(b) Rat, number of pinholes 5-15, pinradius 25 mm

Figure 5.4: Evaluation of the first group of multipinhole designs with different degrees of overlap and without overlap (central sampling method). The number of apertures is varied from 5 to 15 and pinradius is 25 mm. The CNR of each voxel indicated in Fig. 5.2(b)-(e) is plotted with respect to its point number. The top graph (a) plots the results for a large homogeneous sphere, the bottom graph (b) those for a rat brain phantom.

all rat brain phantoms, as well as for the homogeneous sphere imaged with the 5-pinhole designs. Scanning this sphere with the multiplexing 10- or 15-pinhole design, the reconstruction image suffers quite heavily from ghost points and ghost circles causing inhomogeneity, but the sphere could be reconstructed completely. After overlap removal, truncation made it impossible to reconstruct the most eccentric axial planes and induced bias, resulting in a high RMSRD.

Similar conclusions, but from a different perspective, can be drawn from the second group of designs (see Fig. 5.5(a) and (b)). In this second part of the study, the difference in amount of overlap is caused by a variation in the positioning of the pinhole apertures. In the first design the apertures lie much farther from the central one and from one another than in the last design, which corresponds to less multiplexing in the former case with respect to the latter case. The design with overlap with the best CNR had its surrounding apertures positioned at a large distance from the central one (pinradius of 35 mm), and had thus the least overlap. The central FOV of the sphere seems to benefit most from this reduction in degree of multiplexing. For the rat phantom the transition from a pinradius of 35 to 25 mm has little influence. For the designs where overlap is removed, the pinholes can be put closer to one another, i.e. 25 mm pinradius (or even 15 mm pinradius if only the central voxels are of interest as for the rat phantom), but the larger the pinradius, the more homogeneous the CNR over the entire FOV. Also from these results a general improvement can be seen if the overlap is removed, except for some eccentric points. The largest difference occurs of course for the biggest overlap reduction.

As expected, designs with a higher amount of overlap have a higher RMSRD, due to the more severe multiplexing artifacts. An example of modest multiplexing artifacts is shown in the top row images of Fig. 5.6, which are central slices through the reconstruction image obtained with the 35 mm pinradius design with overlap allowed. Imaging with a design without overlapping projections causes usually more truncation and bias when the pinradius becomes larger (see Fig. 5.6, bottom row). The design with pinradius 35 mm where overlap was removed with the maximum sensitivity method does not follow this trend, though, and provides a very good image quality (see Fig. 5.6, central row). All reconstructed images of the rat brain phantom were very accurate within the VOI.

The last group of designs aimed for improvement in CNR by a more sensible usage of the detector area. Due to the distribution of the pinhole apertures over two circles, instead of one, more (interesting) information is to be expected in the non-overlapping parts of the projection images. From Fig. 5.7(a) and (b) the same general conclusions can be drawn as from Fig. 5.4(a) and (b), i.e. allowing overlap, the number of apertures has little influence on the (quasi uniform) CNR, and if overlap is removed, a steady increase in CNR can be perceived with increasing number of pinholes at the sacrifice of a decrease at the edge of the FOV.

For the homogeneous sphere the multiplexing artifacts become more pronounced with increasing amount of overlap. After overlap removal more truncation artifacts and bias occur if the number of pinholes increases. So, for all designs the RMSRD (see table 5.1) increases with increasing number of apertures. For the 9-pinhole

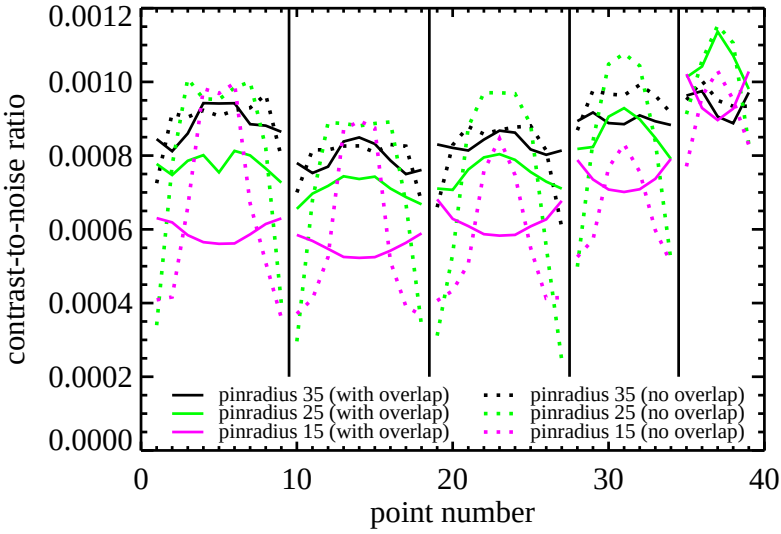

(a) Sphere, number of pinholes 10, pinradius 35-15 mm

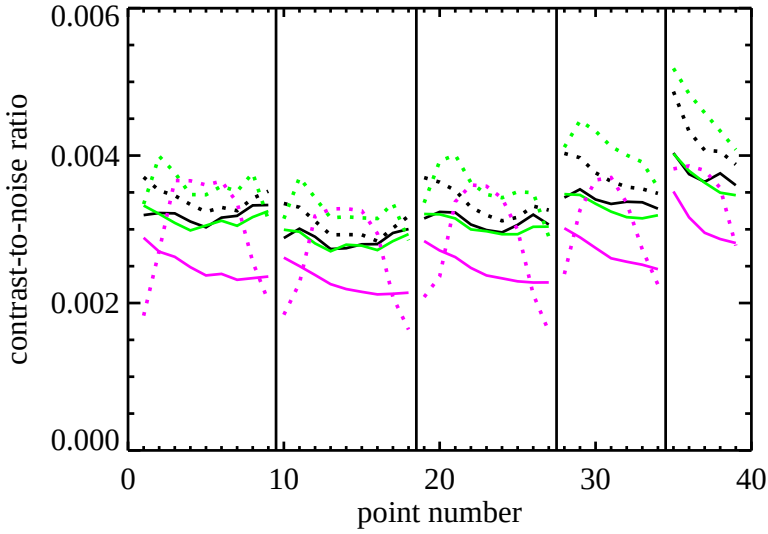

(b) Rat, number of pinholes 10, pinradius 35-15 mm

Figure 5.5: Evaluation of the second group of multipinhole designs with different degrees of overlap and without overlap (central sampling method). The number of pinholes is 10 and pinradius decreases from 35 to 15 mm. The CNR of each voxel indicated in Fig. 5.2(b)-(e) is plotted with respect to its point number. The top graph (a) plots the results for a large homogeneous sphere, the bottom graph (b) those for a rat brain phantom.

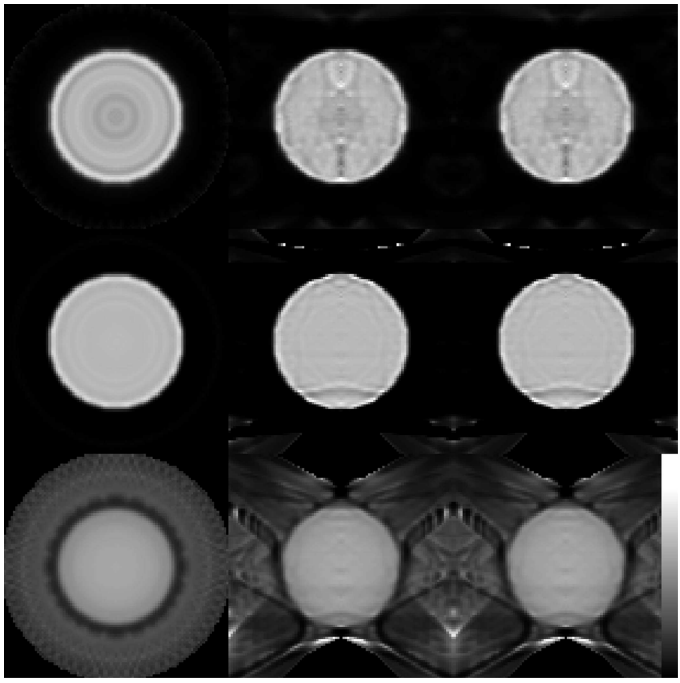

Figure 5.6: Reconstructed images of the large homogeneous sphere imaged with the 10-pinhole designs with a pinradius of 35 mm. First row: design allowing overlapping projections. Second row: design after maximum sensitivity overlap removal. Third row: design after central sampling overlap removal. The three columns depict the central transaxial (left), coronal (center) and sagittal slice (right).

design, the RMSRD improves if the overlap is removed, whereas a better RMSRD is obtained with overlap for the 15-pinhole design. The rat brain phantom could again be reconstructed quasi perfectly for all designs, especially for those without overlap.

Finally, we compare the results of the 15-pinhole design with two pinhole circles (Fig. 5.7(a) and (b)) with those of the 15-pinhole design with one pinhole circle, lying in between the previous two (Fig. 5.4(a) and (b)). For central voxels the results are very similar, but the high CNR is now also apparent for a larger extent of voxels. From the reconstruction images it is hard to decide which images are better. The RMSRDs favor the single circle design.

5.4.3 Interpretation of the effect of overlap

In the previous section many multipinhole designs were evaluated in order to get a feeling for the impact of overlapping projections on the CNR in the reconstruction image. From the results it became clear that it is better to reduce or, if possible, even

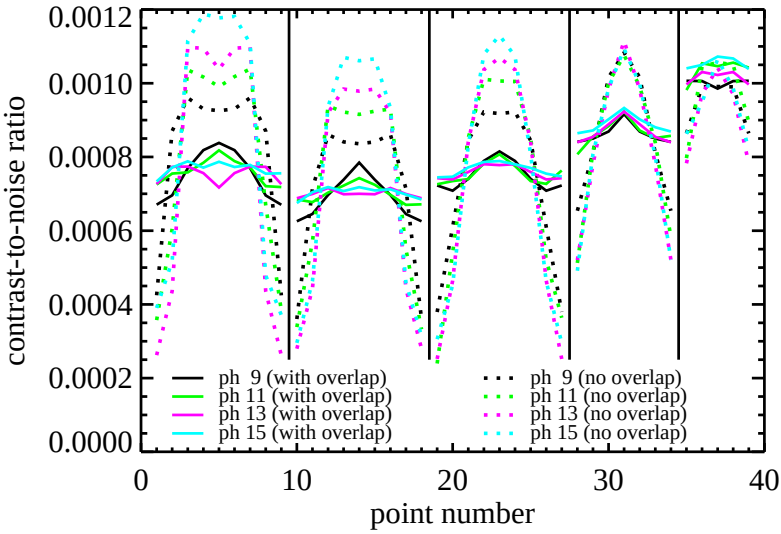

(a) Sphere, number of pinholes 9-15, pinradius 20/30 mm (alternatingly)

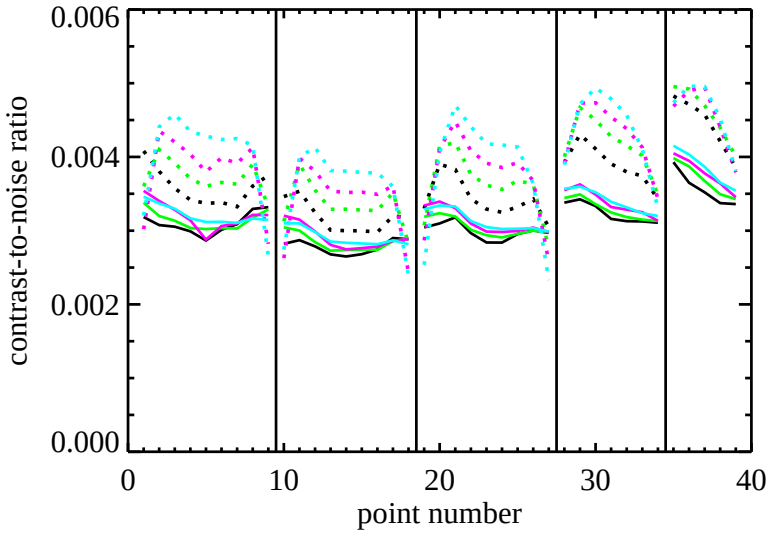

(b) Rat, number of pinholes 9-15, pinradius 20/30 mm (alternatingly)

Figure 5.7: Evaluation of the third group of multipinhole designs with different degrees of overlap and without overlap (central sampling method). The number of apertures ranges from 9 to 15 and pinradii are 20 and 30 mm alternatingly. The CNR of each voxel indicated in Fig. 5.2(b)-(e) is plotted with respect to its point number. The top graph (a) plots the results for a large homogeneous sphere, the bottom graph (b) those for a rat brain phantom.

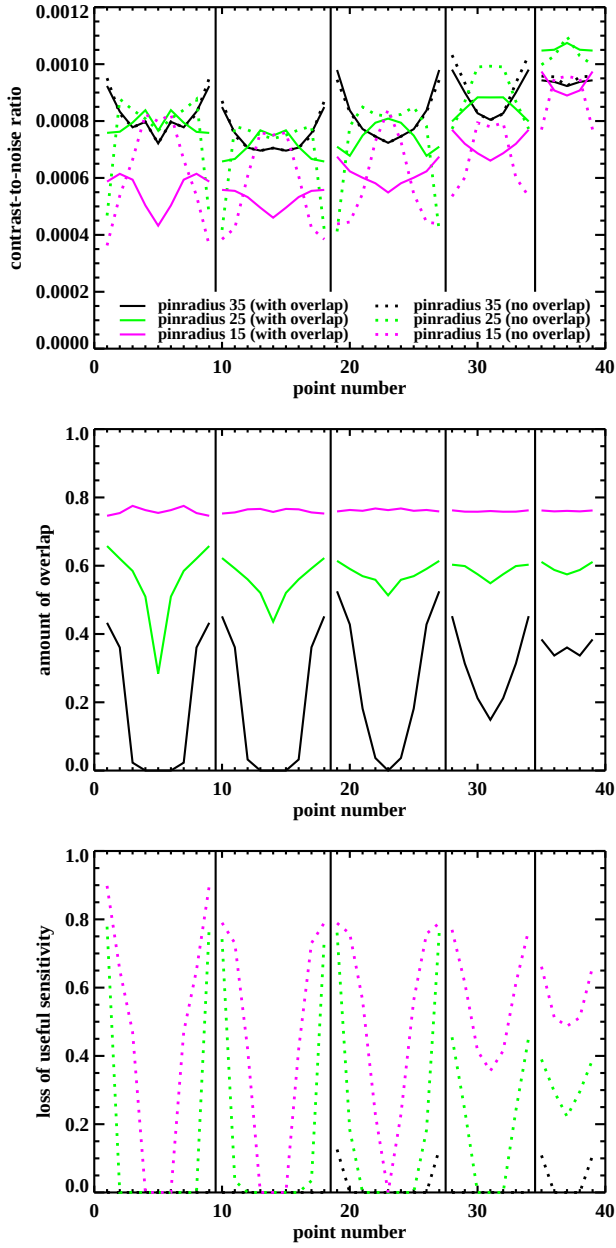

Figure 5.8: Evaluation of three 7-pinhole designs with different degrees of overlap and without overlap (central sampling method) to interpret the effect of overlap on the CNR in a homogeneous sphere. The three graphs plot for each voxel shown in Fig. 5.2(b) their contrast-to-noise ratio (top), amount of overlap (center), and loss of useful sensitivity after overlap removal (bottom).

to remove overlap. However, the amount of overlap was only described qualitatively (low, medium or high). Here a more quantitative approach is proposed, based on the two overlap quantification measures presented in section 5.2.3.

In order to discover some of the underlying reasons for the preference for non-multiplexing designs, we look more thoroughly at the influence of the variation of the distance between the central and the surrounding pinholes for three different 7-pinhole designs, and at the effect of overlap removal for these designs. In the top graph of Fig. 5.8 the CNR is plotted with respect to the examined voxels of the large homogeneous sphere, as in the previous section. The central graph shows the amount of overlap in the detector pixels that get information from voxel j (equation (5.9)), and the bottom graph plots the loss of useful sensitivity for voxel j (equation (5.10)).

The central graph of Fig. 5.8 shows that all voxels are seen with a similar, large amount of overlap through the design with pinradius 15 mm, whereas only the eccentric voxels suffer from some overlap if the design with pinradius 35 mm is used. That is why the difference due to overlap removal is largest in the former case and zero in the most central voxels in the latter case.

For the two designs with the smallest pinradius the CNR steeply decreases at a certain distance from the center of the FOV. In the bottom graph of Fig. 5.8 these same voxels show a large loss of useful sensitivity. This 'critical' distance is larger for designs with a larger pinradius.

Inspection of the reconstructed images and the RMSRDs results in the same conclusions as were drawn for the second group of designs studied in the previous section.

5.4.4 Comparison of overlap removal methods

The CNR obtainable with the third group of designs of section 5.4.2 (9 to 15 pinholes with alternating pinradius) was already shown for the central sampling overlap removal method in Fig. 5.7(a). The CNR was also calculated after overlap removal based on the maximum sensitivity. The results for both overlap removal methods are shown next to each other in Fig. 5.9(a) and Fig. 5.10(a). A remarkable difference in CNR can be noticed, especially in the central FOV. The gain in CNR initially decreases rapidly with increasing eccentricity using the maximum sensitivity method, whereas the central sampling method gives rise to an improved CNR in a larger (central) FOV, at the cost of the CNR of points at the border of the FOV (especially those far from the central plane).

As the designs, and therefore also their amount of overlap, were the same before overlap removal, only the difference in remaining useful sensitivity is responsible for the different results. As shown in Fig. 5.9(b) and Fig. 5.10(b), the loss in useful sensitivity is also much higher in most non-central voxels for the maximum sensitivity method than in the case where the central sampling method is used, except for the most eccentric ones.

In contrast with the results for the CNR, the maximum sensitivity method outperforms the central sampling method in terms of RMSRD.

5.5 Discussion

Realistic values were chosen for the collimator, camera geometry and acquisition parameters, based on the current parameters of our pinhole SPECT system used for rat brain imaging. For the validation study, the apertures were positioned close to one another to have much overlap, such that the results from the design before and after overlap removal are clearly distinguishable. In addition, a smaller sphere was simulated in a reduced image space compared to the other simulations in order to keep the calculation time of the reference method (close to 300 iterative reconstructions per design) reasonable. Attenuation was neglected for the same reason. The size of the large homogeneous sphere was chosen such that the reconstruction images obtained with the original designs (with overlap) did not suffer from truncation artifacts. Needless to say that this could not be guaranteed for all designs after overlap removal.

As could be expected from the results in the previous chapter, the validation study shows that the approximate method predicts the CNRs fairly well, both for a design with, and for a design without overlap. In general, the approximate method seems to slightly underestimate the CNR that can be obtained by post-smoothed MLEM. This was also observed in Fig. 4.6, where the least squares fit through the validation points inclined a little towards the reference method. A possible explanation might be that MLEM has more knowledge due to the built-in non-negativity constraint, which is ignored in the approximate method. The distribution of the new validation points is comparable to that of the first validation study.

As indicated in section 5.2.1, the CNR is not always a complete measure for the image quality, because it is insensitive to low frequency artifacts. This is not due to inaccuracies of the approximative method, though. In the presence of multiplexing artifacts, the estimated CNRs were confirmed in the validation study discussed above. In the presence of truncation artifacts, a successful validation was done for the 'ph 10, pinradius 35 mm' design with central sampling overlap removal, imaging the large homogeneous sphere (see Fig. 5.6(bottom row); validation results not shown). So far, we used the RMSRD as a measure of the bias in the reconstructed image.

From the simulation studies we can conclude that designs with overlapping projections (1) should keep the number of pinholes low enough, (2) should put their apertures farther apart compared to the same designs where overlap is removed, and (3) lead to inferior CNRs compared to their overlap-free equivalents. All three points indicate the same trend: overlap reduction/removal improves the CNR. This is especially the case in the center of the FOV. For the voxels at the border of the FOV the CNR tends to decrease, however.

Increasing the number of apertures in a multiplexing design was found to be useless once the detector area is completely filled. To validate this statement, the third

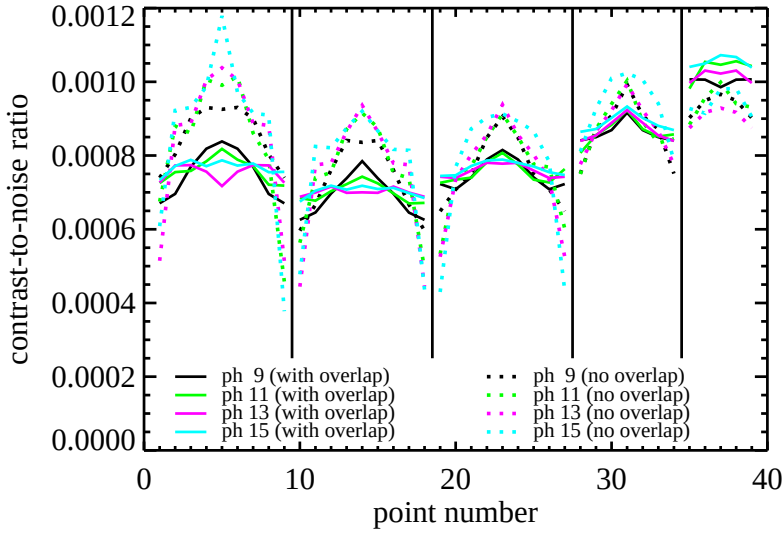

(a) Contrast-to-noise ratio (maximum sensitivity)

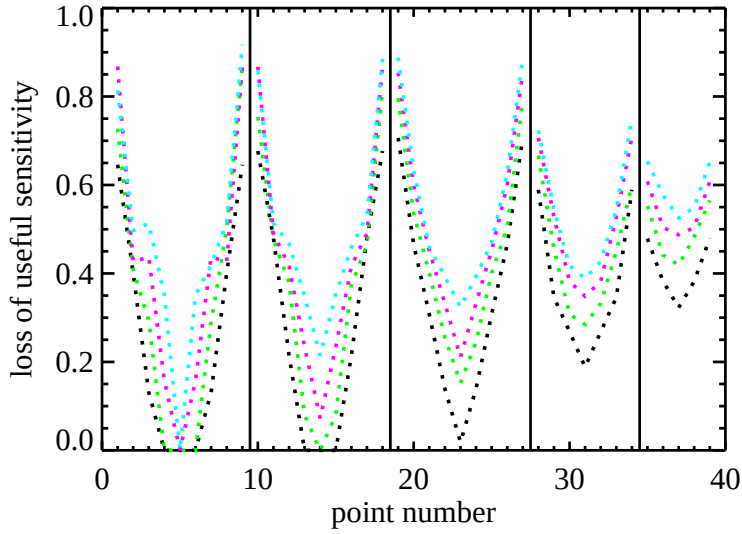

(b) Loss of useful sensitivity for voxel j (maximum sensitivity)

Figure 5.9: Comparison between the two overlap removal methods: (this figure) maximum sensitivity and (Fig. 5.10) central sampling. The CNRs (top images) in the large homogeneous sphere (see Fig. 5.2(b)), imaged with the designs of the third group consisting of 9 to 15 apertures at a pinradius of 20 and 30 mm alternatingly, as well as the loss of useful sensitivity due to overlap removal (bottom images) are shown.

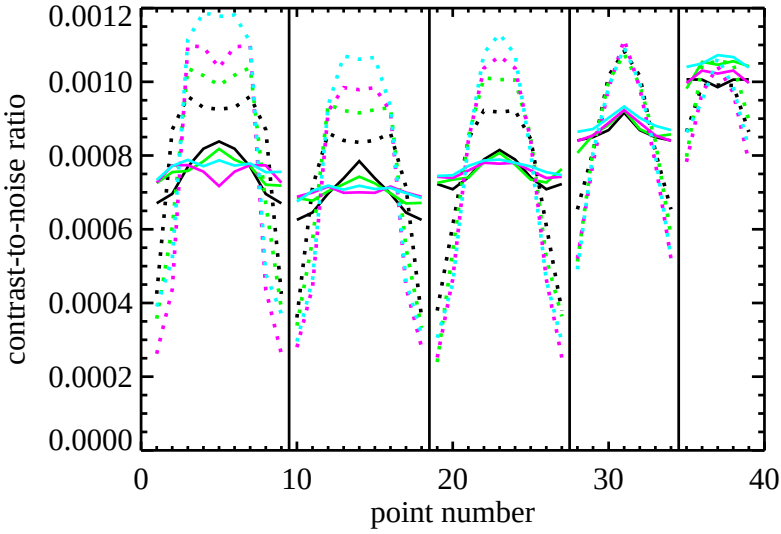

(a) Contrast-to-noise ratio (central sampling)

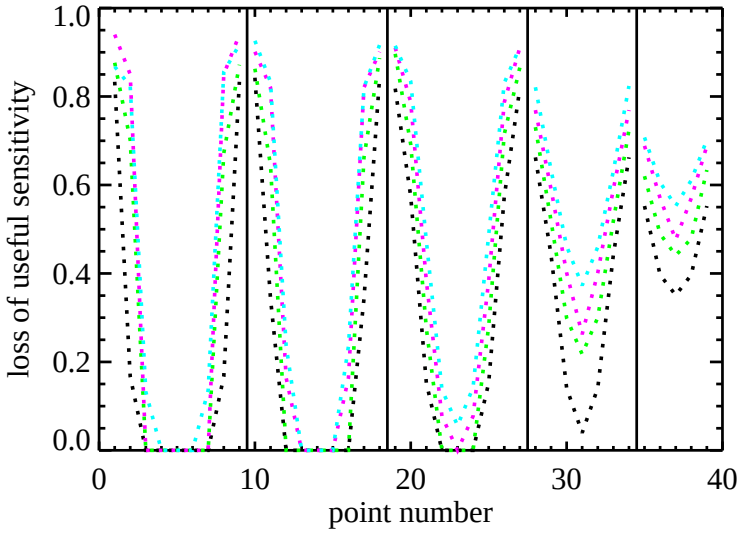

(b) Loss of useful sensitivity for voxel j (central sampling)

Figure 5.10: Comparison between the two overlap removal methods: (Fig. 5.9) maximum sensitivity and (this figure) central sampling. The CNRs (top images) in the large homogeneous sphere (see Fig. 5.2(b)), imaged with the designs of the third group consisting of 9 to 15 apertures at a pinradius of 20 and 30 mm alternatingly, as well as the loss of useful sensitivity due to overlap removal (bottom images) are shown.

group of designs was extended with a 21-pinhole design. Even for this extremely multiplexing design, the CNR remained unchanged (results not shown). Therefore we can conclude that the extra sensitivity can only compensate for the decrease in information due to overlap. No gain, nor loss in CNR is obtained. Similar conclusions were drawn in [18,78]. Removing overlap, however, creates a gain in the center of the FOV, at the cost of the CNR at the edge. Depending on the application one can conclude whether or not this can be considered as a general improvement. It is foregone that overlap removal has more influence if the amount of overlap was higher.

Studying the reconstruction images obtained with the designs that allow overlap, we observed an increased bias with increasing number of pinholes (as in [18]), because there are more pinhole pairs to cause artifacts and larger groups of pinholes might confirm the same ghost points or circles. The reprojection of the reconstructed activity is very similar to the original projection data, which indicates that these artifactuous images are nearly exact solutions of the ill-posed reconstruction problem.

Another interesting topic is the comparison between the CNR obtainable with single and multipinhole designs, respectively. One advantage of single pinhole collimation is the significantly larger achievable magnification, as the single projection image can fill the complete detector area. A second advantage is that in some applications, e.g. rat brain imaging, it can be positioned much closer to the animal than a multipinhole design. Due to this reduced distance, this single pinhole has a higher sensitivity. Its CNR was found to be similar, but not higher than that of the (non-optimized) multiplexing multipinhole designs simulated for this chapter (results not shown). However, most non-overlapping multipinhole designs discussed in this chapter easily outperform an optimized single pinhole design in terms of CNR. Only the voxels farthest from the AOR gain slightly in CNR using the single pinhole design. Reducing the distance between the pinhole and the AOR also has the disadvantage of degrading the sampling in the off-center planes, though, which results in good image quality in the central planes, but very poor image quality in all other planes. Multipinhole imaging might help here to ameliorate the off-center sampling, thereby improving the global image quality.

In Fig. 5.5(a), 5.5(b) and 5.8(top) one can see that, after overlap removal, designs with a large pinradius have a good CNR in a larger part of the FOV than designs with a small pinradius. This is because a larger pinradius induces less multiplexing before overlap removal, such that less projections are blocked, or equivalently, more useful sensitivity is maintained (see Fig. 5.8(bottom)). However, if the pinradius is too large or the voxel is too eccentric, some projections might fall outside the detector area, which reduces the CNR again.

For pinhole SPECT, especially multipinhole SPECT, one usually tries to use the detector area as efficiently as possible, meaning measuring data from as many angles and in as many pixels as possible. The measurement might then consist of line integrals only intersecting a volume of interest totally contained inside the phantom or animal. In other words, all projections are truncated at both sides, resulting in incomplete sampling of the entire body contour. This is called the

interior problem, for which the reconstruction is non-unique. We tried to avoid this problem for most designs by carefully choosing the size of the phantoms and their distance to the pinhole plate, because solving this interior problem is a research topic on its own [66, 71, 87]. Removing the overlap often induces or increases the truncation problem, particularly when using the central sampling method, since only importance is given to the sampling of the central FOV (see Fig. 5.6(bottom row)). We have observed that the reconstruction artifacts can be suppressed tremendously by forcing the reconstruction to be zero outside the body contour (results see next chapter). This is in agreement with the recent findings of Kudo *et al.* in [66], where it was shown that the solution to the interior problem is unique if a tiny a priori knowledge is available, i.e. if some of the activity distribution inside the region of interest is known. Due to its different shape, the rat brain phantom is easier to reconstruct than the homogeneous sphere. The asymmetry of the body with respect to the AOR indeed enables the measurement of the body contour with all designs, explaining the low RMSRDs for this phantom.

It is known that overlap removal increases the value of the useful sensitivity by eliminating the ambiguity of the information in a detector pixel. For the voxels in the central FOV this is usually the only or dominating factor that influences the CNR (see Fig. 5.8(bottom)). On the contrary, for more eccentric voxels, especially those farther from the central plane, another factor, the loss of sensitivity, gets into play and becomes increasingly important with increasing eccentricity. Detector pixels in overlap regions are assigned to only one pinhole aperture, such that their sensitivity for voxels (often the less central ones) seen through other apertures is thrown away. As a consequence, the gain of information due to unambiguity is counteracted by the loss of information due to stopped photons (by extra shielding), which might result in a decrease in CNR, instead of an increase.

The overlap quantification measures, proposed in section 5.2.3 were very helpful to investigate the main influences of multiplexing. We do not claim, however, that the two presented measures have a predictive value. They were only meant as an aid to interpret the results (CNR) found by the approximate method; not to replace this method. Moreover, one should note that these measures are based on the sensitivity images and not on the projection images. Therefore, they are more reliable if the phantom/animal to be scanned fills the FOV, such that the overlap in both images is comparable. The effects of overlap removal are smaller for smaller phantoms because much less multiplexing occurs in the projection images.

Two methods to remove the overlap in the projection images were presented in section 5.2.2. All CNR values shown in this chapter were calculated using the second method (central sampling), except for those in Fig. 5.9(a) and (b). The first method (maximum sensitivity) gave in most cases a very similar or slightly inferior CNR in the central FOV and a slightly better one at the edges. However, for the designs with two pinhole circles with different pinradii, the results were clearly different (see section 5.4.4). The CNR near the center of the FOV was higher for the central sampling method. However, the reconstructions obtained with the maximum sensitivity method were more uniform, and suffered less from bias and truncation artifacts in the off-center planes.

From these results, we can conclude that taking the highest sensitivity, which seems most straightforward, does not guarantee the best CNR, but yields a good overall image quality. Depending on the objective of the imaging task a different overlap removal strategy should be followed. If one aims e.g. for a really large FOV with a good CNR, some additional tricks are required, such as adapting the positioning of the apertures in order to better fill the detector area (e.g. two surrounding circles instead of one, or irregular patterns), letting the apertures focus at different points, or varying the acceptance angle of the apertures.

Despite the rather mathematical definition of the overlap removal methods, we believe practical solutions can be found, such as the addition of septa in between the pinhole plate and the detector (as in the U-SPECT-I [8]), since the sensitivity areas corresponding to the different pinhole apertures form closed entities, one for each aperture. However, some additional research is required to find a simple and robust way to translate the mathematical methods into an accurate and easy to develop shielding.

During pinhole collimator design, one should keep in mind that the estimated CNR is shift- and object-variant. Therefore, it is very important to clearly state the goal of the design (kind of application, typical size and activity distribution of the phantom/animal, size of the FOV, etc.) before passing on to the design phase. Furthermore, for small quality improvements, it is important to verify whether the change in image quality is worth the often increased complexity of the design. In addition, due to the approximate character of the evaluation method, small changes might be caused by inaccuracies. Hence, it might be useful to verify the results for (some of) the best design(s) with the reference method. As mentioned above, also a reconstruction image (or its RMSRD) is necessary to evaluate the effect of multiplexing and/or truncation artifacts.

In the simulations of this chapter, the pinhole apertures were positioned in a regular pattern, namely all apertures equally distributed over one or two circles around one central pinhole. This can have an extra degrading effect on the image quality, since parallel aperture pairs reinforce the multiplexing artifacts [119]. Less regular designs might reduce, but not eliminate the artifacts, because the artifacts are just more spread over the reconstruction image. This is illustrated for the design that is optimized for focused mouse imaging in chapter 6. An additional advantage of overlap removal is the elimination of these artifacts.

The designs discussed in this chapter were all focusing at the center of a small FOV. This study could, however, easily be extended to investigate any other type of pinhole design, e.g. with apertures focusing at different locations for whole body imaging (as in [117]).

Our main conclusion that the CNR decreases and the image reconstruction bias increases with increasing degree of multiplexing is in agreement with the findings in [78, 80].

5.6 Conclusion

In this chapter the influence of overlapping projections on the reconstruction image quality in multipinhole SPECT has been investigated. The contrast-to-noise ratio was used as a quality measure and was calculated based on efficient analytical approximations for the properties of the linearized local impulse response. To evaluate the effect of multiplexing, the CNR was calculated for a number of voxels in a homogeneous sphere and in a realistic digital rat brain phantom imaged by several multipinhole SPECT designs with different amounts of overlap. In addition, these designs were also examined after overlap removal, which could be obtained by putting extra shielding between the pinhole plate and the detector. Two intuitive overlap removal methods were proposed. The results indicate that, once the detector area is entirely used, the CNR neither improves, nor decreases with increasing degree of multiplexing. The increase in sensitivity only compensates for the increased ambiguity. In contrast, the elimination of overlap in the projection images improves the CNR at the center of the field of view, while the CNR of voxels at the edge of the FOV often decreases. This is because after overlap removal the ambiguity of the previously multiplexed data is removed for the central voxels, while for the eccentric ones the amount of useful sensitivity is also reduced. Two measures to quantify the overlap were suggested to help with the interpretation of the results. Since the CNR was found to be insensitive to bias in the reconstruction image, a reconstruction of the noiseless projection data was also calculated and studied for each design, revealing information about possible multiplexing and truncation artifacts.

Chapter 6

Optimized multipinhole design for mouse imaging

The majority of the mouse pinhole SPECT studies in our lab focus on the uptake of newly developed tracers in e.g. the thyroid, a large tumor, the liver, spleen or kidneys. Therefore, new multipinhole plates, optimized for focused mouse imaging with high sensitivity, are designed. A fast analytical method was used to predict the contrast-to-noise ratio (CNR) in many points of a homogeneous cylinder for a large number of pinhole designs with modest overlap. The design providing the best overall CNR, a configuration with 7 pinholes, was selected. Next, the pinhole pattern was made slightly irregular to reduce multiplexing artifacts. Two identical, but mirrored 7-pinhole plates were manufactured. In addition, the calibration procedure was automated and refined to cope with small deviations of the camera from circular motion. First, the new plates were tested by reconstructing a simulated homogeneous cylinder measurement. Most multiplexing artifacts were suppressed by the irregular pattern and further diminished by restricting the reconstruction to the body support. Second, a Jaszczak phantom filled with 37 MBq ^{99m}Tc was imaged on a dual head gamma camera, equipped with the new pinhole collimators. The image quality before and after refined calibration was compared for both heads, reconstructed separately and together. Next, 20 short scans of the same phantom were performed with single and multipinhole collimation to investigate the noise improvement of the new design. Finally, two normal mice were scanned using the new multipinhole designs to illustrate the reachable image quality of abdomen and thyroid imaging. The simulation study indicated that using body support information removes the remaining multiplexing artifacts. Refined calibration improved the spatial resolution, especially for the second detector head. Depending on the location in the phantom, the CNR increased with a factor of 1 to 2.5 using the new instead of a single pinhole design. The first proof of principle scans were successful, hence the new plates were released for preclinical studies in mice.

6.1 Introduction

The design of multipinhole collimators is often founded on experience, simulations or phantom studies [3, 9, 18, 31, 43, 48, 53, 57, 76, 78, 97, 100]. Comparison and evaluation are usually based on the measured or predicted resolution, sensitivity, bias or noise. In this work, we discuss the optimization of a multipinhole design using the previously developed, analytical image quality evaluation method based on Fisher information (see chapter 4). The application under consideration is focused mouse imaging, where only a restricted part of the mouse is under investigation, e.g. thyroid, a large tumor, liver, spleen or kidneys. Most mouse studies performed in our lab are conducted to investigate the uptake of a newly in-house developed tracer. Sometimes relatively low tracer uptake is expected based on biodistribution, however, hence high sensitivity is very important. Previously, the mice were scanned using a multipinhole plate with apertures having 1.5 mm diameter. The obtained resolution was considered sufficient for the majority of studies. Therefore, the aperture diameters of all tested pinhole designs were fixed to 1.5 mm.

In section 6.2, the pinhole design evaluation method, developed in chapter 4, is shortly revisited [120], and an approach to optimize a single and multipinhole design for a specific application is proposed. In addition, an automatic calibration data processing procedure and a more accurate calibration method, based on [29], are explained. The optimized designs are described in section 6.3. The setups of the simulations, phantom measurements and animal experiments are reported in section 6.4. The results are analyzed in section 6.5 and discussed in section 6.6.

6.2 Theory

6.2.1 Design evaluation method

In [37, 94] efficient approximations were proposed to rapidly predict resolution and noise characteristics of images obtained with maximum a posteriori reconstruction. In chapter 4, this approach was used to predict the contrast-to-noise ratio (CNR) for a small set of voxel values in images produced with post-smoothed maximum likelihood expectation maximization (MLEM), that have a predefined uniform spatial resolution. The CNR of voxel j is calculated as the value of the impulse response in voxel j divided by its standard deviation. This method enables fast and automated comparison of a large set of (slightly different) tomographic systems, such as a gamma camera with different pinhole collimators.

6.2.2 Optimization method

Application specification

Before starting any design process, it is important to clearly specify the application it will be designed for. In this work, the goal is to optimize the image quality in

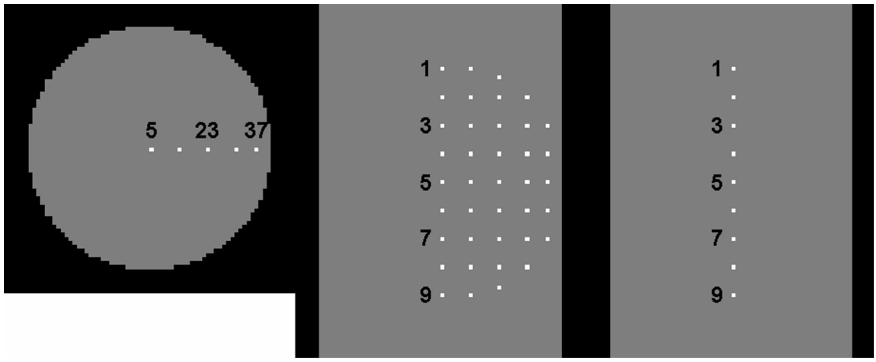

Figure 6.1: Central transaxial (left), coronal (center) and sagittal (right) slice through the homogeneous cilinder, used as mouse model during design optimization. The white points indicate the voxels for which the CNR was predicted.

a restricted part of a mouse. As a simple mouse model, a centered homogeneous cylinder (5 kBq/mm^3) with a radius of 18 mm and length of 52.8 mm (full length in the image space of 72×72×88 voxels with cubic size of 0.6 mm) was used. Only the image quality in the central sphere with a radius of 18 mm was considered to be important. Due to the symmetry of the phantom, investigation of the image quality in an axial half-plane containing the axis of rotation (AOR) is sufficient (see white points in Fig. 6.1). The outer activity was modeled to include its influence on the CNR in this volume of interest (VOI). This model could be seen as a worst case scenario, in which the whole field of view (FOV) is filled with homogeneous activity. In reality, some organs will have higher uptake than surrounding tissue, making reconstruction of these somewhat easier. As these plates will be used for any non-whole body mouse scan, meaning tracer uptake and distribution are unpredictable, optimizing the design for the most difficult case seems the best option.

General acquisition and design specifications

In our lab, we use a clinical dual head gamma camera (e.cam Fixed 180°, Siemens Medical Solutions) equipped with pinhole collimators (Nuclear Fields International B.V.) for micro-SPECT imaging, as was done in [97]. The parameters of these collimators are to be designed for the available detector, which is modeled as an infinitely thin perfect absorber with an intrinsic resolution of 4.0 mm full width at half maximum (FWHM). The data are usually acquired in a 256×200 matrix with square pixels of 1.95 mm, hence these parameters were used during simulation for the 64 projection images measured over 360° (60 s/view).

As it is well known that a smaller distance between the center of the (central) pinhole and the AOR, called *fdist* in the rest of this work, yields improved image quality, the fdist is taken as small as practically achievable. For this purpose, the

pinholes were positioned asymmetrically in a 12 mm thick tungsten pinhole plate[1]. Assuming a plastic bed of 2 mm thickness, a front thickness of the pinhole plate of 3 mm and 2 mm clearance between the bed and the pinhole plate to enable collimator rotation, an fdist of 25 mm was chosen. The aperture diameter was set to 1.5 mm for all designs, as was discussed in the introduction.

Single pinhole design

Single pinhole collimation is still often considered as a possibly good candidate for small animal imaging, because it has the advantage of larger magnification over multipinhole collimation, as it may use the whole detector area for a single projection. Therefore, we will first optimize the parameters of a single pinhole collimator for the above described application. This will allow later comparison with the optimized multipinhole collimator design (see next section). Since the diameter was already fixed to 1.5 mm, only the best acceptance angle-focal distance combination needs to be found.

For single pinhole design, it seems straightforward to increase the pinhole magnification factor until the complete detector area is filled. This reduces indeed the influence of the detector intrinsic resolution. Starting from the preset fdist, one can calculate the acceptance angle necessary to cover the entire VOI (see Fig. 6.1), and its corresponding focal length required to fill the whole detector. Due to the rectangular shape of the detector (width > height), either the upper and lower part of the VOI are truncated (width as restriction) or some detector area is left unused (height as restricting factor).

In addition, the acceptance angle could be chosen in many ways. Here, we only consider two methods: either it is defined by the line tangential to the VOI, or by the line through the cross-section of the VOI with the AOR, as also in that case each point within the VOI is at least detected once. The combination of acceptance angle and focal distance providing the best overall CNR, predicted with the approximate method described in section 6.2.1, will be chosen as the optimal single pinhole design.

Multipinhole design allowing overlap

Because multipinhole design involves a high number of design parameters, we restricted the search space by fixing the aperture diameter, the focal distance and the fdist. The aperture diameter was set to 1.5 mm. The focal distance was taken equal to those of our current pinhole plate supports, which are lead pyramids to which interchangeable pinhole plates can be attached [97], incremented with the backside thickness of the new pinhole insert, i.e. 167 + 9 = 176 mm. Again the minimal achievable fdist was set to 25 mm, including the 3 mm frontside thickness of the pinhole plate. The design parameters remaining for optimization were the number

[1] The plate thickness was chosen 12 mm to reduce the high energy scatter of ^{123}I [103], a SPECT isotope often investigated in our lab [21, 42].

of apertures, the positioning and inclination of the pinholes and their acceptance angles.

Next, a large group of designs was tested by predicting the CNR in the 39 points inside the VOI (see Fig. 6.1). Designs ranging from 2 to 13 apertures were evaluated, with acceptance angles between 17.5° and 90°. The distance between the central pinhole and the surrounding ones was taken within a 12.5-40 mm range. Usually, these non-central pinholes were spread equally over a circle. The apertures focused at a distance 15-60 mm from the pinhole center. In addition, also somewhat more exotic designs were investigated, e.g. with two 'central' pinholes surrounded by multiple apertures, with more than one focal point, with different acceptance angles for different apertures, with the surrounding pinholes in non-circular setups or spread over multiple concentric circles, etc.

When the whole group of designs is evaluated, a selection of the best few is made and used as a starting point for a finer tuning of the design parameters. This process is repeated for several iterations. Finally, the design resulting in the best overall CNR is chosen. However, this was only the first, nevertheless major step in the design process. Since overlap was not prohibited for ease of design and manufacturing, multiplexing artifacts are to be expected [3,119]. Hence, in a second step, the eccentric apertures are slightly displaced along a circle around the central one, in order to provoke as few and unintense artifacts as possible. Especially pinhole pairs on a line parallel to the AOR, causing point artifacts, and sets of pinhole pairs on parallel segments of equal length are avoided [119]. Next, the most promising irregular designs are tested both with respect to their CNR and to the artifacts visible in the reconstruction image obtained from simulated projection data. Finally, the best one is chosen to be manufactured as a prototype.

The best irregular design found for the first collimator, will also be used for the second one, but mirrored over the line through the central pinhole and perpendicular to the AOR. The advantages of using two different, both optimal designs, are the further reduction of multiplexing artifacts and improved sampling. This statement was verified by comparing the CNRs and the artifacts in the reconstruction images obtained with two identical plates to those found with a mirrored combination.

6.2.3 Experimental data processing

Increasing the complexity of the pinhole design also has its implications on the data processing. This is for example the case for the processing of the calibration scan (see Fig. 6.2 (top image)), a measurement of three non-collinear point sources (also called Bequé phantom), necessary to obtain an accurate estimate of the geometrical acquisition parameters when using a clinical gamma camera for small animal imaging [11] (see also section 3.1.1). Previously, every point source projection had to be assigned to the originating point and aperture before the geometrical parameters could be fit, which is illustrated in the bottom images of Fig. 6.2. At the left side, all point source projection centers for all projection angles are plotted in the same space. At the right side, a simulation of the projection data is shown, where the red, green and yellow diamonds were fitted to the projection points of

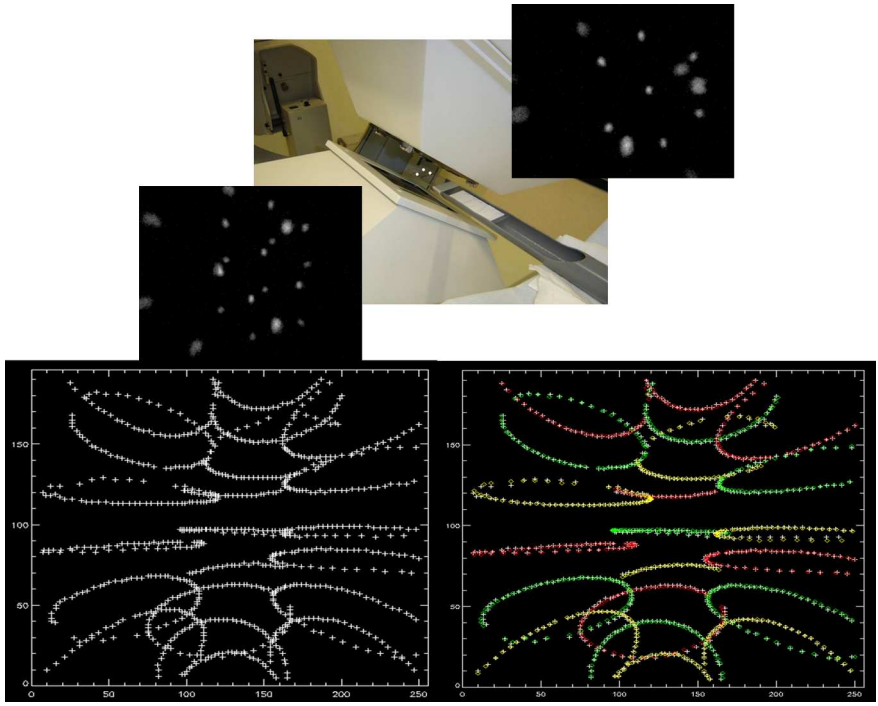

Figure 6.2: Illustration of a calibration measurement (top) with the three point sources indicated in white, and a projection image shown for both 7-pinhole collimators (many points are projected outside the detector area). At the bottom left, a combined plot of all point source projection centers for all projection angles is depicted. At the bottom right, a simulation of the projection data is shown, where the red, green and yellow diamonds were fitted to the projection points of the three point sources through the 7 apertures.

the three point sources through the 7 apertures. This semi-automatic assignment becomes more difficult and time-consuming with increasing pinhole design complexity. Therefore, an automatic processing method combining the assignment with the fit was developed and is presented in this section.

In addition, in comparison with single pinhole, calibration of multipinhole SPECT cameras with this Bequé phantom is expected to be more stable, because more information is available. Either one can use this extra information to reduce the number of point sources (two points without known distance can be sufficient [121,126]), to make the calibration less sensitive to noise, or to more accurately estimate small deviations from the modeled gantry trajectory. The latter is called refined calibration and a simple method applicable to both single and multipinhole SPECT is briefly discussed at the end of this section.

Automatic calibration data processing

Calibration data processing can be split-up into two parts: projection point detection and fitting the simulated data points to the measured ones. For both, many good solutions can be found. Here only one is discussed.

In the projection point detection step, up to (number of point sources) $\times$ (number of apertures) distinct projection blobs should be automatically discerned in each projection image. A simple method, often used in computer vision for blob detection, is to use the properties of the difference between two Gaussians. If an image smoothed with a wide Gaussian is subtracted from the same image smoothed with a narrow Gaussian, the local maxima are emphasized, reducing the detection of these maxima to a simple thresholding operation. Currently, we use this technique to determine the projection centers of the point sources.

Once these projection points have been detected, the originating point source and aperture should be identified for each of them. This would facilitate the fit of the simulated projection points, which are based on the current estimate of the geometrical parameters and the point source locations, to the measured ones. However, if a good initial parameter estimate is available, the identification and fitting step can be combined. In every projection image and for every measured point, the closest simulated point is determined and the sum of the distances between the measured and closest simulated points are minimized by iteratively updating the estimated parameters using a least squares fitting method. In practice, a sufficiently accurate initial guess can be provided, based on the results of previous scans.

Refined calibration

If the orbit followed by the detector heads of a gamma camera slightly deviates from the assumed perfect circle, the resolution will be suboptimal using a calibration method based on circular gantry motion like [11]. Therefore, we implemented a refined calibration method similar to the one presented in [29]. First, the conventional calibration method [11] is applied to the projection data of a Bequé phantom to find an initial estimate of the geometrical parameters (see above for a practical approach). Next, the detector and pinhole collimator are seen as one rigid object subject to small translations and rotations (both in 3 directions). For every projection angle, these 6 parameters describing the rigid camera motion are determined with a penalized least squares fitting procedure, such that they better explain the point source projections. As the deviations from the circular orbit are expected to be small, a penalty discouraging large translations and rotations was introduced.

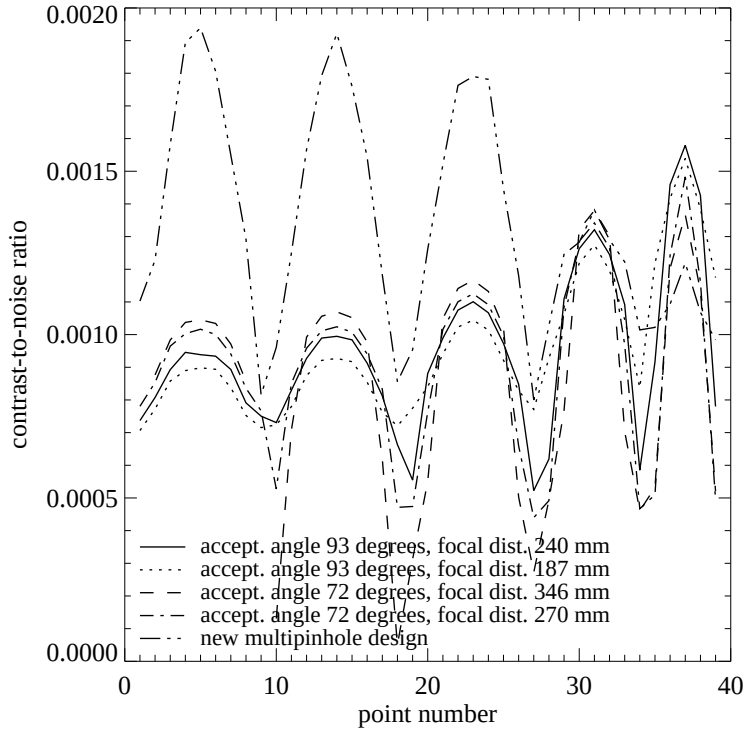

Figure 6.3: Contrast-to-noise ratio versus point number of the investigated points in the homogeneous cylindrical phantom shown in Fig. 6.1. Results were shown for the 4 tested single pinhole designs and the optimal multipinhole plate (all for one head).

6.3 Optimized designs

6.3.1 Single pinhole design

The acceptance angles required for covering the whole VOI were found to be 93° and 72° for the tangential line and the line intersecting the VOI on the AOR, respectively. The corresponding focal lengths were 240 mm and 346 mm, respectively, if the width was taken as restriction, and 187 mm and 270 mm, respectively, if the height was the rectricting measure.

Based on the predicted overall CNR, the best single pinhole design was obtained by choosing the acceptance angle from the line tangential to the VOI and using the height of the detector as restriction. The optimal single pinhole then had an acceptance angle of 93° and a focal distance of 187 mm (dotted line in Fig. 6.3).

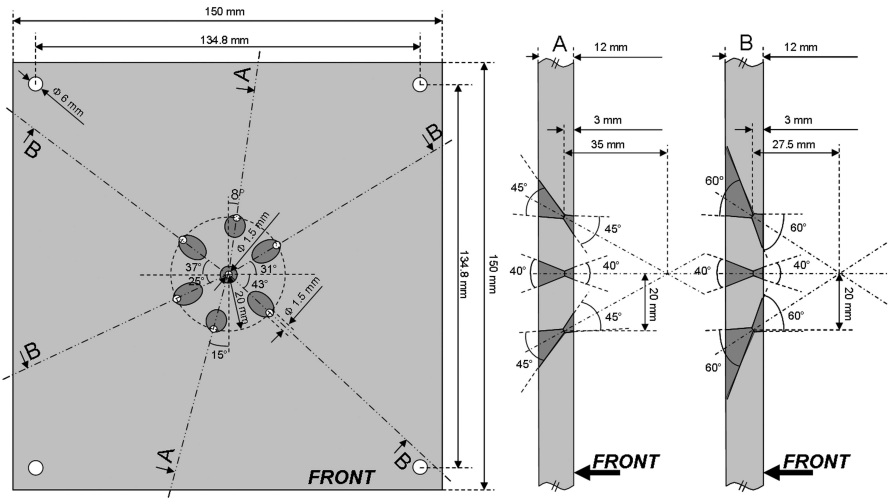

Figure 6.4: Technical drawing of the prototype plate for head 1.

6.3.2 Multipinhole design allowing overlap

The optimized multipinhole design consists of 7 apertures with a diameter of 1.5 mm, 6 on a circle with radius 20 mm around the central one. In the initial, regular design, these 6 apertures were equally spread over the circle, and two of these were positioned on a line through the central pinhole parallel to the AOR. These two apertures had an acceptance angle of 45° and focused at a point at 35 mm distance, whereas the other four had an acceptance angle of 60° and focused at 27.5 mm. The central pinhole had an acceptance angle of 40°.

To reduce the multiplexing artifacts that are expected because some overlap was allowed, the 6 surrounding pinholes were displaced along the circle. From the top one clockwise the apertures were rotated over 8°, -1°, 13°, 15°, 5° and 7° with respect to their original location (> 0° meaning clockwise), as can be seen in the drawing of Fig. 6.4. As mentioned earlier, the second plate was taken identical to the first one, but mirrored around the line through the central pinhole and perpendicular with respect to the AOR. A photo of the front- and backside of both prototype plates, manufactured by Nuclear Fields International B.V., are shown in Fig. 6.5. To illustrate the amount of overlap between the projections through the different apertures, a projection image of the homogeneous phantom, described in the first paragraph of section 6.2.2 and depicted in Fig. 6.1, is shown in Fig. 6.6. The CNR that can be obtained in the examined voxels of this phantom is plotted in Fig. 6.3 (dashed-triple dotted line) and seen to be on the average a factor of 1.41 better than the best single pinhole (dotted line), with a maximum of 2.16.

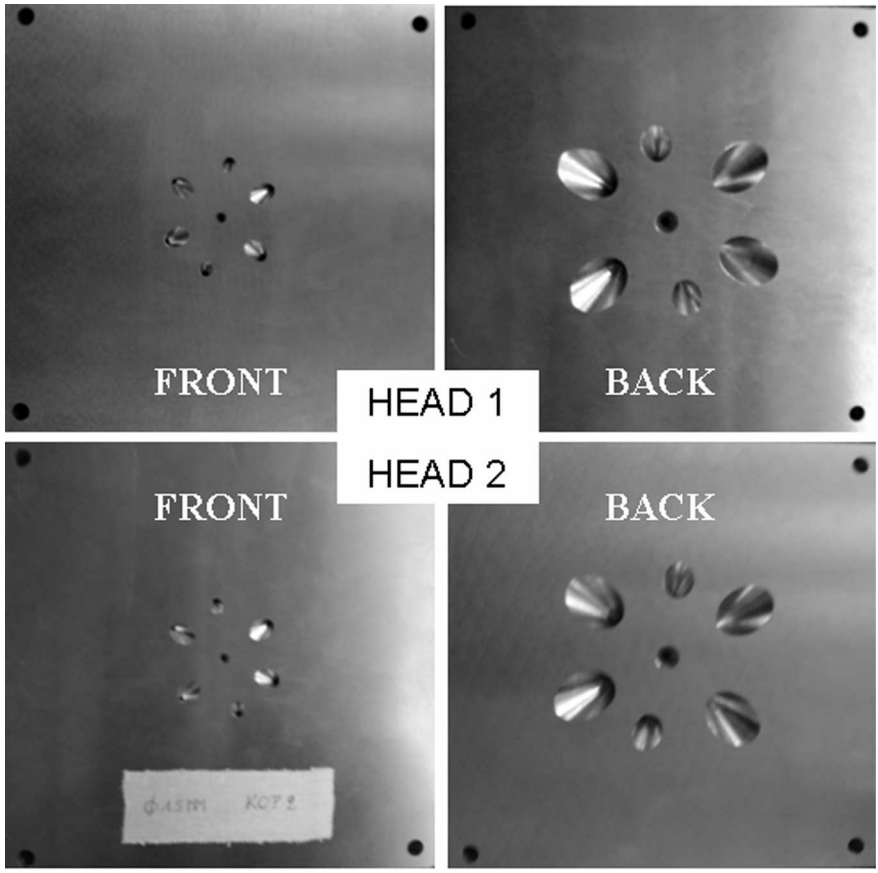

Figure 6.5: Photos of the front- and backside of the prototype plate for head 1 (top) and head 2 (bottom).

6.4 Experiments

6.4.1 Simulations: homogeneous phantom

To visually inspect the overall image quality of a dual head gamma camera equipped with the newly designed pinhole plates, the acquisition of a homogeneous cylindrical phantom was simulated. The phantom with a radius of 12.5 mm and a length of 96 mm was positioned centrally in a 72×72×160 image space with 0.6 mm cubic voxels (see Fig. 6.7(a)). The fdist of both pinhole collimators was 25 mm and the focal distance was 176 mm. 64 projection images over 360° with 256×200 square pixels of 1.95 mm were simulated by forward projecting the phantom and generating pseudo-random Poisson noise on the projection data. An intrinsic detector resolution of 4 mm FWHM was modeled. The ordered subsets expectation maximization (OSEM) algorithm with 5 iterations of 16 subsets was used to re-

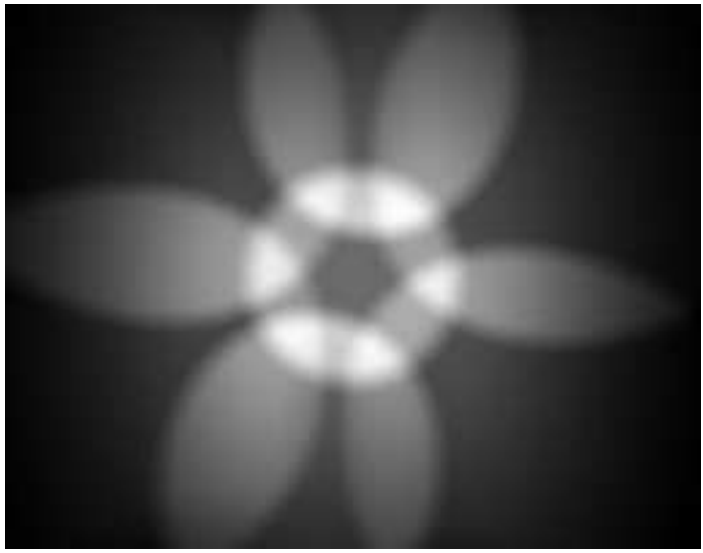

Figure 6.6: Projection image of the homogeneous phantom, shown in Fig. 6.1, through the pinhole collimator with the prototype plate for head 1.

construct the data [55, 116]. Resolution recovery was performed using the 7-ray method described in [1] (see also section 3.1.3) and the sensitivity was calculated analytically using a ray-tracing technique similar to the method explained in [97] (see section 3.1.2). Attenuation and scatter were not taken into account.

First, a pair of single pinhole designs with a diameter of 1.5 mm and an acceptance angle of 120°, covering a large FOV, was simulated. Next, the image quality obtainable with the optimized multipinhole plates was examined. To investigate the influence of the regularity of the aperture pattern, we start with the simulation of a pair of the regular multipinhole collimator design, from which the optimized pair was derived (see section 6.3.2). Subsequently, a pair with two times the same irregular pattern (see Fig. 6.4) was simulated, and both reconstruction images were compared to the image yielded from the optimized pair, especially examining the artifacts. The projection data obtained with the optimized pair were also reconstructed with 5 times more iterations to guarantee convergence.

Since overlap was not completely avoided, indeed the artifacts will not be eliminated completely and different solutions to suppress them are proposed. As these artifacts appear because measured activity is backprojected through one or more wrong apertures, one should find a method to reduce the chances of chosing the wrong aperture. From some initial reconstructions, we noticed that some activity is deposited outside the boundaries of the phantom or animal. Because activity is known to be absent there, it might originate from such a wrongly backprojected measurement. Therefore, if part of the image space is known to be free of activity, it is straightforward that restricting the assignment of activity to the other pixels will improve the reconstruction accuracy.

To attain this goal, first the contour of the phantom or animal should be found. A first approach is to grow a region from the image center of a fast initial reconstruction (e.g. 1 iteration of 64 subsets). Because taking the contour too narrow might introduce new artifacts, a second body support is derived by dilation with a 5×5 circular structure, and a third one by post-smoothing the initial support with a Gaussian with a FWHM of 5 pixels. After determining this body contour, a practical method to restrict activity assignment to inner pixels during reconstruction is required. An easy way is to use the body support, with all outer pixels equal to zero, as the starting image of the iterative reconstruction algorithm, because once a pixel is set to zero, no more activity can ever be assigned to it by the MLEM algorithm. The results of using the different forementioned body supports are compared to those obtained using the perfect phantom boundaries.

Another approach to improve the knowledge about the object boundaries could be replacing one of the two multipinhole collimators by a large FOV single pinhole. Although sensitivity is sacrificed, image quality could be improved compared to using the optimized multipinhole pair, because the backprojection of the single pinhole measurement is unambiguous. Therefore, the multiplexing artifacts are expected to be eliminated.

6.4.2 Phantom measurements: Jaszczak phantom

Spatial resolution

As a first experiment, a Jaszczak phantom was scanned using the dual head gamma camera described in section 6.2.2 equipped with two lead pyramids to which any of our available pinhole plates can be attached. The new multipinhole designs were then fixed to these and positioned as close as possible to the phantom. This phantom consists of a plastic cylinder with an outer diameter of 40 mm and 6 wedge-shaped sections with multiple hollow rods having a diameter ranging from 1.5 mm to 3.0 mm in steps of 0.3 mm. The rods are positioned at a center-to-center distance equal to their diameter from each other. The phantom was filled with 37 MBq ^{99m}Tc and scanned in step-and-shoot mode with the same parameters as used for the simulations (see section 6.4.1). Each projection image was acquired in 30 s. The activity distribution was reconstructed in a 72×72×88 image space with 0.6 mm cubic voxels. A gradually reduced OS iteration scheme of 2×16, 2×8, 2×4, 3×2, 4×1 (global iterations × number of subsets) was executed. The pinhole blurring was modeled using the 7-ray method [1].

For accurate sensitivity modeling, a planar source measurement was performed for every aperture separately, by making the planar source small enough to be seen through that particular pinhole only. The noise in the measurement was reduced by performing an acquisition over a long time and median filtering the image (see also section 3.1.2).

To accurately retrieve the acquisition geometry, an identical, but faster scan (10 s/view) of a calibration phantom was performed immediately after the phantom

scan [11]. This calibration phantom consisted of three point sources of 1.85 MBq ^{99m}Tc each, at known distances from each other.

To evaluate the effect of the refined calibration, described in section 6.2.3, the phantom was reconstructed twice. First, based on the basic calibration method [11], assuming a perfect circular camera motion, and second, using the geometrical parameters obtained with the refined calibration method. As the two camera heads are not guaranteed to be equally stable, the reconstructions were repeated for both heads separately.

Noise

The noise properties of the optimized multipinhole collimator are investigated by comparing them to those of the large FOV single pinhole collimator described in section 6.4.1 (aperture diameter 1.5 mm, acceptance angle 120°). To facilitate a fair comparison the Jaszczak phantom was scanned simulataneously with the single and the multipinhole collimator on head 1 and 2, respectively. Both collimators were positioned as close as possible to the centered phantom, aiming for an equal fdist, but the focal distance of the single pinhole collimator was 6 mm less, i.e. 170 mm instead of 176 mm, because the available single pinhole plate was symmetrically drilled and only 6 mm thick. Twenty subsequent scans were performed in continuous mode, alternatingly rotating clockwise (CW) and counterclockwise (CCW), and stored in 64 views (5 s/view). The measurement time was gradually increased for each scan to compensate for decay, hence keeping the noise at a constant level.

To enable comparison, the spatial resolution in the reconstruction images should be matched. Therefore, the number of iterations necessary for convergence is determined for the single and the multipinhole data separately. OSEM reconstructions with 1 to 30 iterations of 8 subsets are evaluated for their spatial resolution in an image space with the same dimensions as in the previous study. For the single and multipinhole, CW and CCW acquisition, the FWHM of the Gaussian post-smooth filter is determined by post-smoothing the reconstructed image until it best fits the perfect, homogeneously filled rod phantom convolved with a 3D isotropic Gaussian with 1.8 mm FWHM (target resolution). As the phantom was positioned with the rods parallel to the AOR, multiple planes can be summed to reduce the noise for the resolution measurements. Next, the noise in the different rods is evaluated by calculating the mean and variance on the mean in the regions of interest (ROIs), centered on the reconstructed rods and having a diameter equal to the physical diameter of the corresponding rod.

6.4.3 Focused mouse imaging

Within the scope of a preclinical study, a normal 25 g mouse was injected with ±15.0 MBq ^{99m}Tc-labeled annexin A5 and scanned 1 hour post injection (p.i.) using the same acquisition protocol as in section 6.4.2 (30 s/view). The measured data are reconstructed using the OSEM algorithm with an equivalent of 66 global

iterations in an image space of 96×96×120 cubic voxels of 0.8 mm. A computed tomography (CT) scan was performed immediately after the SPECT scan, enabling rigid registration between both images, since the mouse was fixed to a transportable bed and sufficient anatomical information was visible in the SPECT image. The body support could easily be derived from the CT image and used to avoid or reduce multiplexing artifacts and background activity in the SPECT reconstruction image.

To illustrate that the spatial resolution obtainable with the new multipinhole collimator designs is sufficient for most applications, the thyroid of a normal mouse was scanned. Typically the two tiny lobes of a mouse thyroid are only about 2 mm apart (center-to-center). The mouse was scanned 10 min after ±29.6 MBq pertechnetate ($^{99m}TcO_4^-$) was injected in the tail vein. Again the same acquisition protocol was used. The measured data are reconstructed using the OSEM algorithm with an equivalent of 155 global iterations in an image space of 96×96×120 cubic voxels of 0.6 mm. No CT scan was taken, because the only aim was to visualize the two thyroid lobes with our micro-SPECT system. The body support, used to improve the reconstruction image quality, was therefore derived from the reconstructed SPECT image.

6.5 Results

6.5.1 Simulations: homogeneous phantom

The central slices through the reconstruction images of the simulations described in section 6.4.1 are shown in Fig. 6.7(b)-(k). When two single pinhole collimators were used to acquire the data, a large, central part of the phantom could be nicely reconstructed (Fig. 6.7(b)), whereas the reconstruction images obtained with the new multipinhole designs (regular as well as irregular patterns) suffer from multiplexing artifacts (Fig. 6.7(c)-(e)), because modest overlap in the projections was allowed. To show that the irregular pattern of the new multipinhole plates reduced the artifacts as intended, its images (Fig. 6.7(e)) are compared to those obtained with the initial regular design on both collimators (Fig. 6.7(c)) and to those from two identical irregular designs (Fig. 6.7(d)). Using the regular designs results in very severe hot and cold point and circular artifacts. These are clearly reduced by making the aperture arrangement less regular. The use of a mirrored version as second pinhole plate further improves the image quality. As can be noted from Fig. 6.7(f), the artifacts are a possible sign of non-convergence. If enough information is available, as is the case here, the artifacts can be reduced and even eliminated by iterating very long.

Restricting the activity to the body support during reconstruction can also successfully diminish the multiplexing artifacts, as illustrated in Fig. 6.7(g). This support was grown in an image, obtained after 1 iteration of 64 subsets OSEM. An overestimation of the activity at the edges is apparent, however, indicating that the body contour was taken too narrow. Therefore, it was enlarged by dilation with a 5×5 circular structure and by post-smoothing with a Gaussian with a FWHM

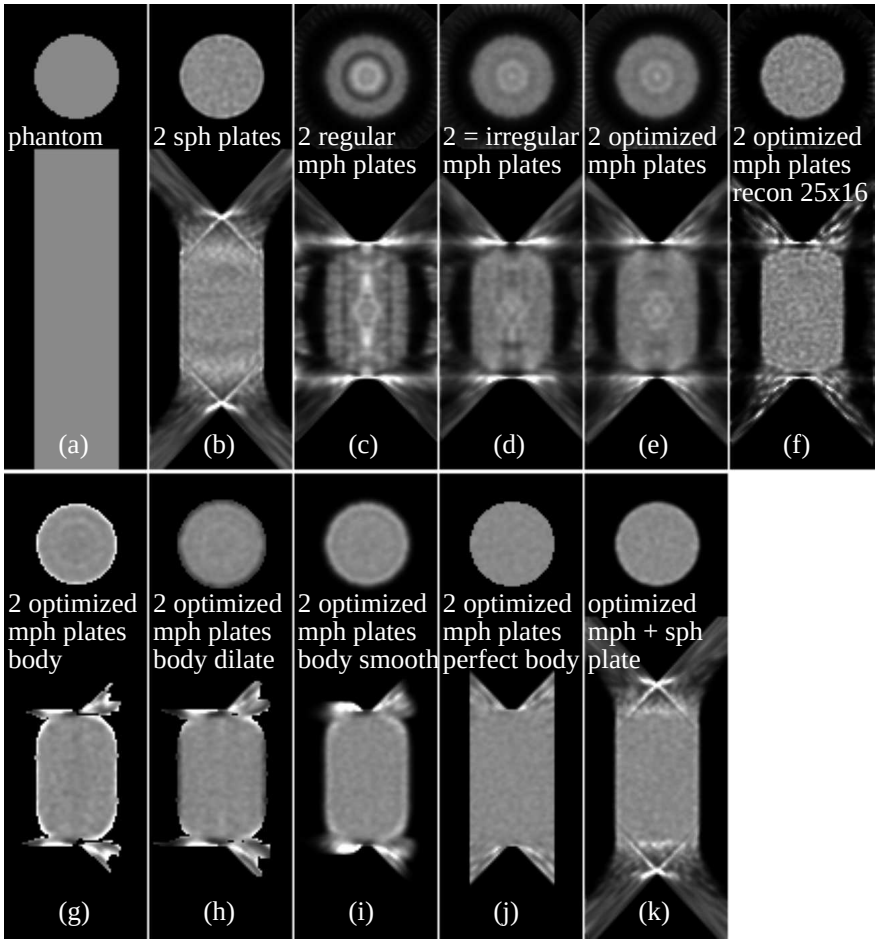

Figure 6.7: Central transaxial (top) and coronal (bottom) slices through (a) the homogeneous cylinder with 12.5 mm radius and (b)-(k) the reconstruction images corresponding to the simulation setups, described in section 6.4.1: (b) two large FOV single pinhole (sph) plates; (c) regular version of the optimized pair of multipinhole (mph) designs; (d) two times the same (irregular) plate of the optimized pair of mph plates; (e) optimized pair of mph plates; (f) same as (e), but reconstructed with 25 iterations of 16 subsets; (g) same as (e), but using body support found from fast reconstruction; (h) same as (g), but with dilated body support; (i) same as (g), but with smoothed body support; (j) same as (e), but using phantom as body support; (k) one optimized mph plate combined with a large FOV sph plate. All images were clipped at the same maximum.

of 5 pixels (or 3.0 mm), yielding the images of Fig. 6.7(h) and (i), respectively. If the exactly known support is used, a perfect, artifact-free reconstruction of this homogeneous phantom is obtained (Fig. 6.7(j)). Unfortunately, this knowledge is

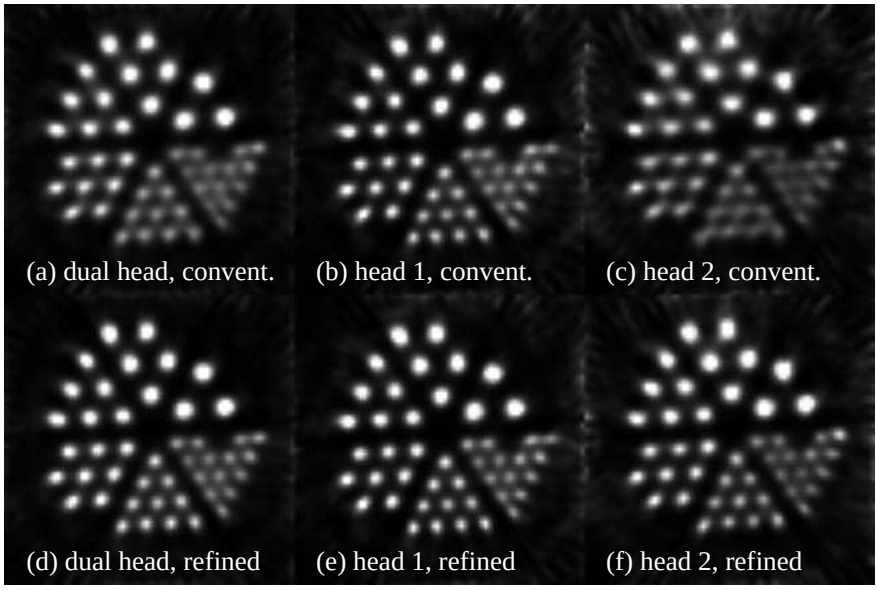

Figure 6.8: Central transaxial slice through the reconstructed Jaszczak phantom scanned with the new multipinhole designs (64 views, 30 s/view, step-and-shoot mode): using (a)-(c) conventional and (d)-(f) refined calibration. The reconstructions were based on the combined data (left), the data of head 1 (center) and those of head 2 (right). All images were clipped at the same maximum.

only available in simulation studies. From Fig. 6.7(k), we can conclude that a large FOV single pinhole collimator provides enough unambiguous information about the support to reconstruct the major part of the phantom without artifacts.

6.5.2 Phantom measurements: Jaszczak phantom

Spatial resolution

In Fig. 6.8 the central transaxial slices through the different reconstruction images of the Jaszczak phantom are shown. First, the calibration was done with the standard method, assuming perfect circular gantry motion. In the images obtained from the dual head measurement, all rods can be distinguished (Fig. 6.8(a)). One of the smallest rods is invisible due to an air bubble. Using only the data of head 1 provides even better resolution (Fig. 6.8(b)), already indicating the reconstruction of the head 2 data will be inferior. This is confirmed in Fig. 6.8(c), where the image quality of most rods decreased and some of the smallest rods cannot be separated.

In a second step, the geometrical parameters obtained with the previous calibration method are used as input for the refined calibration. New reconstruction images are generated based on the obtained parameters. Comparing the images of the dual head data obtained with the two calibration methods (Fig. 6.8(a) and

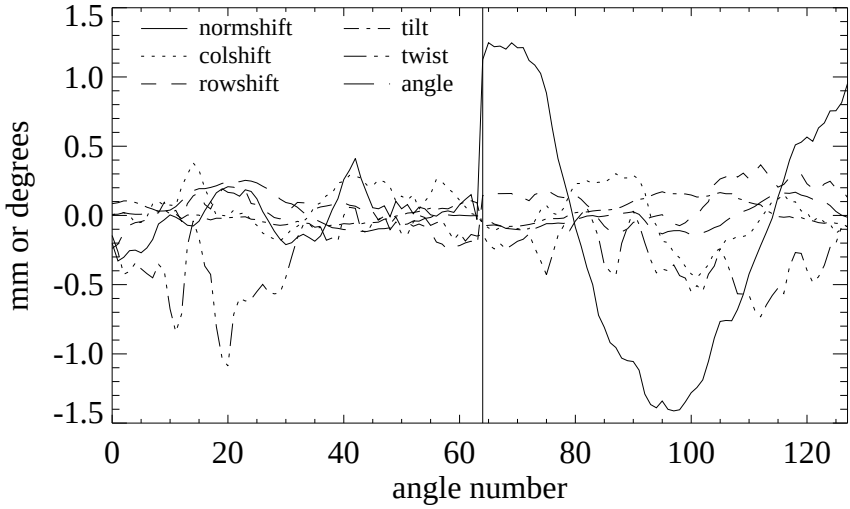

Figure 6.9: Plot of the refined calibration parameters (3 translations + 3 rotations) versus the projection number (angles 0-63 for head 1, angles 64-127 for head 2). The translations are expressed in mm, the rotations in degrees.

(d)), the resolution clearly improved using the refined method. The rods are better separable and more circular-shaped. The same, but less pronounced improvement is seen in the new image for head 1 (Fig. 6.8(e)). Now also similar image quality and resolution is obtained from the data of head 2. For this detector, refined calibration was required to compensate for deviations from circular motion and to achieve high quality images.

To gain insight into the deviations of the camera, the three translations and three rotations are plotted with respect to the projection angle in Fig. 6.9. The deviations were convolved with a kernel $[1/3, 1/3, 1/3]$ to suppress the noise effect. As expected, the deviations were greater for head 2 than for head 1, although all were spread within the small [-1.5, 1.5] range (in mm or degrees). The most important deviation was a translation of head 2 in the direction perpendicular to the detector. It shows a nice sine pattern. As it was initially positioned at the bottom and a positive offset corresponds to an outward movement, this shift can easily be explained by gravity.

Noise

Investigation of the spatial resolution in the original and post-smoothed images reconstructed with increasing number of iterations revealed that OSEM reconstruction with 30 iterations of 8 subsets leads to sufficient convergence for both single and multipinhole data. The smallest rods (diameter of 1.5 mm) are not taken into account in the analysis, because they are smaller than the target resolution of

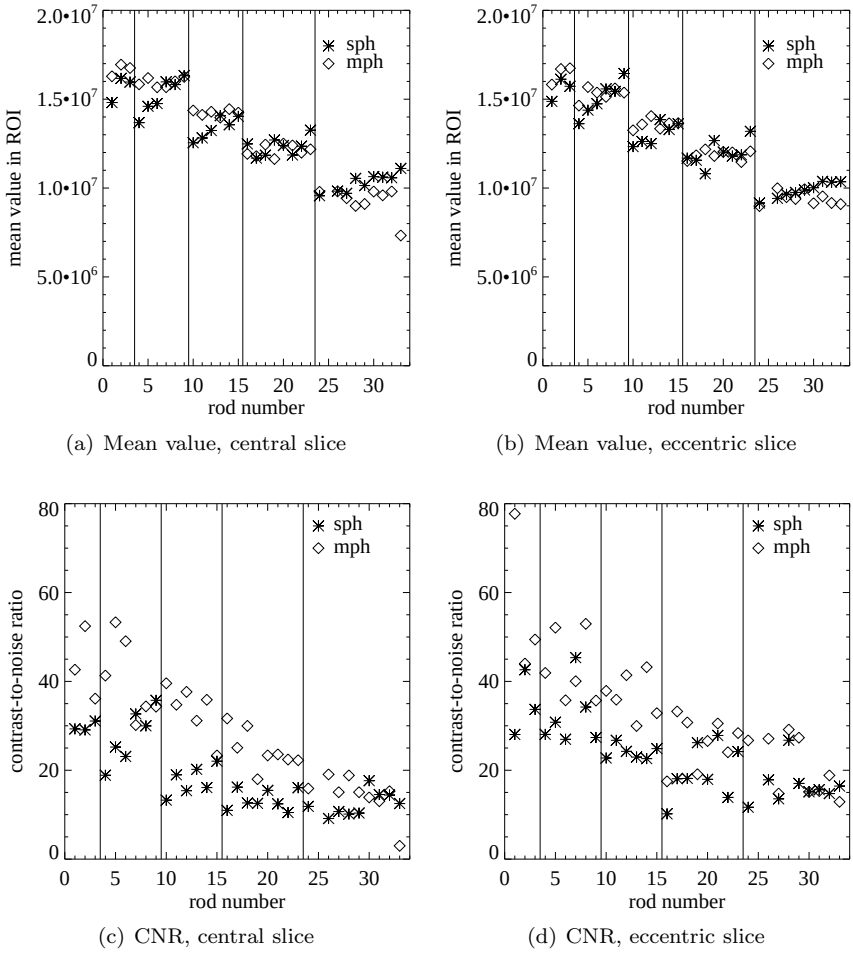

(a) Mean value, central slice

(b) Mean value, eccentric slice

(c) CNR, central slice

(d) CNR, eccentric slice

Figure 6.10: Plot of the mean value in the ROIs (top row), centered on the rods in the 20 reconstruction images of the single pinhole data (stars) and the multipinhole data (diamonds), respectively, versus the rod number. On the bottom row, the contrast-to-noise ratio in the rods is plotted with respect to the rod number. (a) and (c) depict the results for the central slice, (b) and (d) show the results for the eccentric slice. The rods are sorted per diameter (3.0 to 1.8 mm). In each sector, i.e. between two vertical lines, the rods are sorted from most central outwards.

1.8 mm. Gaussian post-smoothing with a FWHM of 1.06 mm for the single pinhole acquisitions (both CW and CCW) and 1.59 mm and 1.56 mm for the multipinhole CW and CCW acquisitions, respectively, needed to be applied to the reconstructions to achieve the target resolution. To reduce the noise, the 6 most central planes are summed, as well as 6 eccentric planes at about 7.2 mm distance from the central plane, in either direction. The average of these two eccentric slices is taken to

further reduce the noise, and to minimize the influence of the multipinhole design asymmetry.

In Fig. 6.10(a) and (b), the mean value in each ROI in the central and eccentric slice, respectively, averaged over the reconstruction images of the 20 scans, is plotted with respect to its rod number. The rods are sorted by decreasing diameter, and within each sector they are ranked from most central to most eccentric. The smallest rods are again ignored. Also the results for the second rod with diameter 1.8 mm (rod 25) were omitted, because of its low activity caused by an air bubble. Due to the imposed target resolution, the mean value is expected to be constant for rods of equal size and to decrease with decreasing diameter. From the single pinhole data (stars), we can conclude that the spatial resolution is quite shift-variant, since the outer rods have higher mean values, and thus better resolution, compared to the more central ones. Not correcting for the attenuation might also result is slightly higher values in the outer rods, although this effect is expected to be limited because of the small dimensions and low density of the phantom. The resolution in the multipinhole image is more or less constant per sector, though (see diamonds). The mean values for the eccentric slice are marginally smaller compared to those for the central one, both in the single and the multipinhole reconstruction.

To cover the effect of both the resolution and the noise in one figure of merit, the CNR is considered. The increase in CNR, due to the use of the multipinhole instead of the single pinhole collimator is visualized in Fig. 6.10(c) and (d), for the central and the eccentric slice, respectively. The CNRs yielded from the single and multipinhole image are again plotted as stars and diamonds for every ROI with respect to its corresponding rod number. The most significant gains are obtained for the most central rods, whereas only few of the most eccentric rods lose some CNR. In Fig. 6.10(d), the CNRs for both data sets are slightly higher, because of the lower variance due to the combination of the two eccentric slices.

6.5.3 Focused mouse imaging

A transaxial, coronal and sagittal slice of the first mouse image obtained with the new multipinhole designs are shown in Fig. 6.11. The body support, provided by the registered CT image, was used to counteract possible multiplexing artifacts. The goal was to image the liver and the kidneys. The bladder fell outside the reconstructable FOV, hence it was slightly truncated and its uptake values cannot be trusted. The liver is seen to be homogeneous and the cortical wall of the kidneys is clearly visible. No post-smoothing was applied.

In Fig. 6.12, a transaxial, coronal and sagittal slice of the reconstructed image of the thyroid of a normal mouse are depicted. The bilobal structure of the thyroid is clearly visible, as well as the salivary gland. The high image quality indicates that the injected dose could be strongly reduced, which is recommended as both a large radiation dose and a large injected mass (chemical quantity) can alter the outcome of the study [44, 67]. For follow-up studies it is important not to induce therapeutic effects.

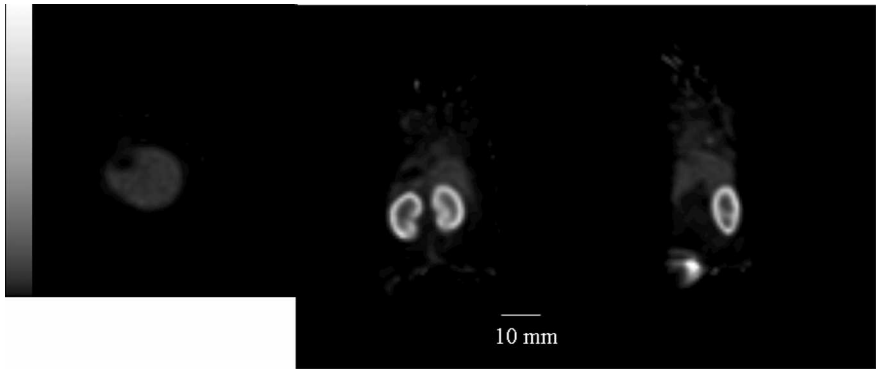

Figure 6.11: First mouse image with the new multipinhole design: (left) transaxial, (center) coronal and (right) sagittal slice of a normal mouse (1 h p.i.), injected with 15.0 MBq of ^{99m}Tc-labeled annexin A5 (64 views, 30 s/view, reconstruction voxel size 0.8 mm).

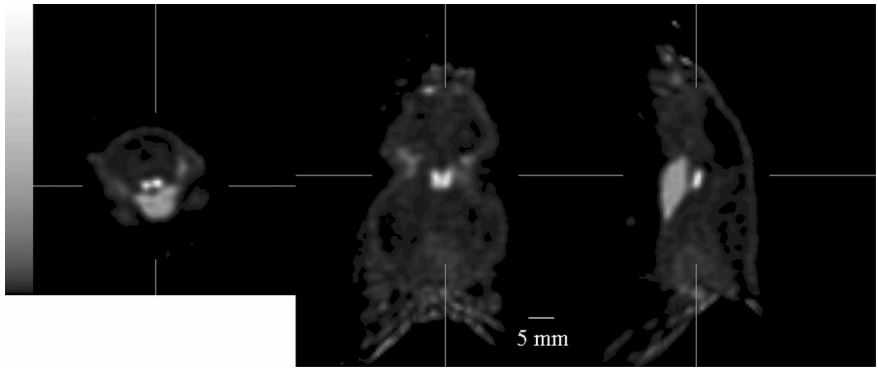

Figure 6.12: Transaxial (left), coronal (center) and sagittal slice (right) through the thyroid of a normal mouse (10 min p.i.), injected with ±29.6 MBq of $^{99m}TcO_4^-$ (64 views, 30 s/view, reconstruction voxel size 0.6 mm).

6.6 Discussion

In this work, the CNR is used as the figure of merit for the image quality, although it does not contain information about artifacts and bias (see chapter 5). This is not because the approximations used to predict the CNR are not accurate enough, though it is intrinsic to the CNR. Investigating the additional image quality measures (artifacts and bias) would require a reconstruction for every design, slowing down the design process significantly. Therefore, these measures were only evaluated for the best design.

Modest overlap was allowed for the new design for several reasons. First, many different theoretical methods to remove overlap in the projection images can be

devised. Two examples were described in section 5.2.2. This makes the parameter space for multipinhole design, which was already huge, many times larger. Second, it is not straightforward to translate such an overlap removal method into a simple and accurate collimation setup. Last but not least, this extra shielding should be easy to manufacture and to attach to and detach from the collimator frame, as the pinhole plates are often changed, depending on the animal being studied. Nevertheless, it would be a useful exercise to optimize a multipinhole design without allowing overlap for the same application, hence showing whether and to what degree it can improve the image quality compared to the design presented here.

The apertures of the optimized multipinhole collimator design focus at two different points. This is probably due to the rectangular size of the detector, which is smaller in the direction of the AOR compared to the perpendicular direction. Therefore, the apertures along this line have to project the activity closer to the activity seen through the central pinhole, hence their focusing point is located further from the collimator than that of the other apertures. For the same reason, their acceptance angle had to be reduced.

From Fig. 6.7(b) it was seen that using single pinhole collimators provides good image quality in the central FOV. However, in the off-center slices a decreased, and further apart an increased activity is perceived. In addition, it is well-known that the axial sampling decreases rapidly with increasing distance from the central slice. Adding pinholes improves this sampling [117].

As was illustrated in Fig. 6.7(c)-(e), making the pinhole pattern irregular, strongly reduces the multiplexing artifacts, but does not succeed in eliminating them. To check whether it might be a matter of convergence, the data were reconstructed with more iterations. Only after 5 times the initial number of iterations, i.e. an equivalent of 400 global MLEM iterations, the artifacts were eliminated. The same procedure was followed for the mouse model of Fig. 6.1, a similar cylinder but with a larger diameter. For this case, even such a long reconstruction was not sufficient to make the image artifact-free.

From Fig. 6.7(g)-(j) we can conclude that knowledge about the body support provides enough information to reconstruct the data with minor or even without artifacts. This can be linked to the findings in [66] if one assumes that this body support eliminates enough ambiguity to correctly reconstruct a part of the phantom. In that case, also the remainder of the relevant part of the phantom has a unique reconstruction. It is, however, still an open question how this knowledge about the support is gathered best, e.g. by region growing with or without post-processing, from a CT image, etc., and whether it is applicable and can be fully automated for any type of mouse scan. For instance, some tracers are very specific, making registration with the CT image impossible without the use of fiducial markers.

Also replacing one of the multipinhole plates by a large FOV single pinhole design is a solution to eliminate the artifacts and to remove the background activity. The single pinhole measurement indeed provides unambiguous information about the activity and therefore counteracts backprojection through wrong apertures of the multipinhole design. Furthermore, some of the detector pixels do not measure any activity. As MLEM is very good at reconstructing contours if some background

is measured, this speeds up convergence, both inside and outside the object. As a drawback, the single pinhole design reduces the sensitivity significantly. From simulations, the sensitivity for a central voxel was found to be 0.1% for an optimized multipinhole plate, compared to 0.02% for a large FOV single pinhole collimator (assuming a branching factor of 1 and a perfect absorbing detector). This is a reduction by a factor of 4.6 for that head, roughly corresponding to a halvation of the CNR. The total sensitivity for the central FOV of our optimized dual head multipinhole SPECT system is thus 0.2%, or about one tenth of the central FOV sensitivity of a micro-PET system. The above mentioned properties of the single pinhole collimator, however, suggest that inclining some pinholes to look at the edges of the animal or increasing their viewing angle might be useful to reduce the artifacts, without giving in much on sensitivity and CNR.

For the reconstruction of experimental data, an analytically calculated sensitivity model could be used. The calculated image could be fitted to the sensitivity measurement to improve its correspondence. However, small manufacturing errors and detector deficiencies (e.g. inhomogeneous detector response) cannot be included in this model (see section 3.1.2). Therefore, it might introduce additional artifacts in the reconstruction images, hence the measured model was used in our reconstructions.

Both from the reconstructed images of the Jaszczak phantom (Fig. 6.8) and from the plot of the deviations (Fig. 6.9), it became clear that the refined calibration had a minor impact on the reconstruction of the head 1 data, but was essential to yield high resolution images from the data of the second detector. Furthermore, a multipinhole measurement of the calibration phantom is expected to provide a more accurate estimate of the deviations than a single pinhole acquisition, because of the higher amount of information available. Thus, to ensure a fair comparison, the single pinhole collimator was attached to head 1 for the noise experiment of section 6.4.2.

The refined calibration procedure described in section 6.2.3 is very similar to the one derived in [29]. They both start from an initial calibration method that models the assumed camera motion, e.g. [11], and subsequently determine for every projection angle the best set of translations and rotations to be applied to the rigid detector-collimator unit. They only differ in the approach to calculate these deviations. In [29], the optimization problem is linearized, and the three translation and three rotation parameters are found from a singular value decomposition, neglecting the smallest eigenvalues. It is a very fast method, restricted to small deviations due to the linearization approximation. However, in practice, this is not expected to be a limiting factor, as the aberrations are usually small. The least squares fitting method used in this work, is somewhat slower, but still fast compared to the initial calibration step. It is easier to implement and could also be used for larger shifts and rotations. Currently, a penalty is used to disfavor all large deviations. However, depending on the camera, some translations or rotations might be more apparant. Then, simple penalty tuning is required to allow a larger deviation of that specific parameter. Due to the noise on the measured data, both methods might get stuck in a local optimum, but good results are obtained with either method.

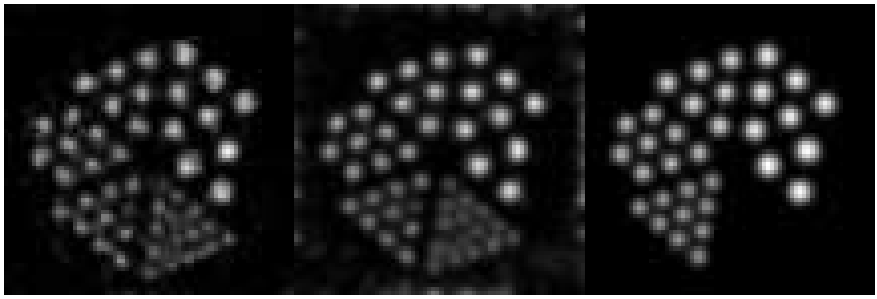

Figure 6.13: Sum image of the 6 most central planes of the post-smoothed image of the first scan (64 views, 5 s/view, continuous mode), reconstructed from (left) the single pinhole and (center) the multipinhole data, respectively. (Right): the ideal rod image, convolved with the target Gaussian (FWHM 1.8 mm). The smallest rods were omitted, because they were not taken into consideration during analysis as their diameter was below the target resolution.

In [11], it was noted that some geometrical parameters are highly correlated, e.g. the electrical shift and the tilt. This means that the measurements might be explained in several ways. Therefore, it is not surprising that there is also quite some variation on the deviation parameters between two projection angles. As it is more probable that the detector heads follow a more or less continuous path instead of a fluctuating one, and because the parameters are correlated in the same way for all viewing angles, it seems reasonable to slightly smooth the translational and rotational parameters. The reconstructed images obtained with and without parameter smoothing were compared visually and no apparant differences were observed.

From the mean values plotted in Fig. 6.10(a) and (b) it could be concluded that the single pinhole data yield clearly shift-variant resolution in the transaxial direction, which is best close to the boundaries of the phantom, because there the single pinhole collimator is most sensitive (and the activity is less attenuated). This can only be solved by using a shift-variant post-smooth filter. The multipinhole image is more shift-invariant thanks to improved sampling. In the axial direction, the resolution seems more or less constant. The resolution is not always accurately represented by the mean value, however, because of the often non-Gaussian shape of the impulse response. This is especially true for the single pinhole results, as can be seen in Fig. 6.13. From left to right, the central slice of the Jaszczak phantom (6 accumulated planes), reconstructed from the single and multipinhole data, respectively, and the ideal slice convolved with a 1.8 mm FWHM Gaussian are depicted. In the right image the smallest rods were omitted, because they were not taken into consideration during analysis as their diameter was below the target resolution. The multipinhole reconstruction image (center) has a clearly improved correspondence with the ideal post-smoothed case (right), compared to the single pinhole reconstruction (left). Indeed, the rods in the latter image are not circular-shaped; another advantage of the optimized design over the single pinhole design.

Most CNRs obtained with the optimized multipinhole design are a factor of

1 to 2.5 larger than those yielded from the single pinhole data. The gain was largest in the center of the FOV and smallest at the phantom boundaries. These results are in agreement with the gain predicted with the Fisher information-based approximations.

6.7 Conclusion

A new multipinhole design was optimized for focused mouse imaging, and evaluated using simulations, phantom measurements and mouse experiments. Some overlap between the projections was allowed to facilitate both the design process and the manufacturing. This led to multiplexing artifacts, which were reduced by making the arrangement of the apertures slightly irregular and different for the two detector heads. The remaining artifacts can be further diminished or even eliminated by iterating much longer, restricting the tracer uptake to the region enclosed by the object boundary during reconstruction, or replacing a multipinhole by a single pinhole collimator. Compared to a single pinhole design, the optimized design was found to increase the sensitivity by a factor of 4.6 in the center of the FOV, to improve the CNR by a factor of 1 to 2.5, depending on the location in the FOV, and to enhance the shape of the impulse response. In combination with the refined calibration method, pinhole SPECT with this optimized set of multipinhole collimators produces excellent reconstructions.

Chapter 7

Pinhole SPECT: Applications

In this PhD thesis, the aim was to investigate and to enhance the image reconstruction quality obtainable with pinhole SPECT. This was achieved by improving the pinhole software, i.e. modeling the acquisition system and the physics of the radioactive tracer, as well as the hardware, namely by thickening the first collimator, introducing a second collimator and improving the pinhole design. Studying the effects of these adaptations in theory or using computer simulations is very interesting, but validating these results with phantom measurements enabled the use of the pinhole SPECT camera for small animal imaging studies, hence providing many other researchers the opportunity to perform in vivo SPECT imaging for their preclinical experiments. This can range from the investigation of the uptake properties of a newly developed SPECT tracer, over metabolic studies of disease models in small animals, to treatment evaluation in such animal model. In the first section, the acquisition and reconstruction of a certain phantom is studied over time to illustrate the general evolution of the image quality. In the subsequent sections (sections 7.2-7.4), an overview of the most important pinhole SPECT studies, performed during the last 4 years (sorted over time), is provided. Next, the small animal SPECT imaging experiments planned for the near future are briefly explained (section 7.5). Finally, the impact of the used pinhole collimator(s) on the radiation dose given to the small animals is discussed.

7.1 Phantom studies

In this section, we want to illustrate how the image quality has evolved during the last four years. To this end, the central transaxial slice through three images of the same phantom, scanned with different pinhole collimators and protocols, and reconstructed using the software available at the time of the scan, are shown next to each other in Fig. 7.1. The phantom was a plastic cylinder containing 6

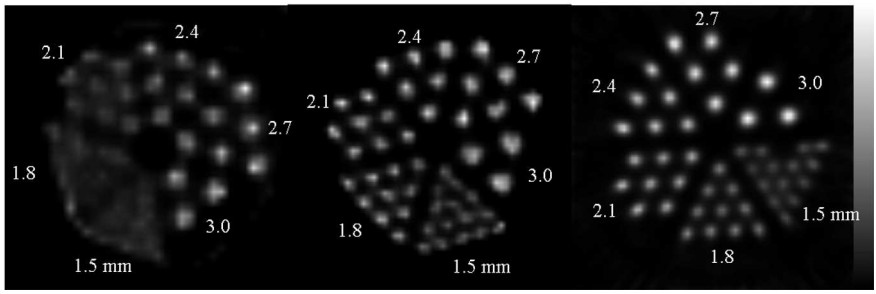

Figure 7.1: Illustration of the image quality evolution over time. Central transaxial slice of a resolution phantom with 6 sections of ^{99m}Tc-filled rods (±37 MBq) with a diameter between 1.5 and 3.0 mm: (left) single pinhole with 3.0 mm aperture diameter, (center) multipinhole with 7 apertures of 1.5 mm diameter, designed for rat brain imaging (see [10], p.53) and (right) dual head imaging with the new set of multipinhole plates (see chapter 6), half of the acquisition time. The acquisition and reconstruction parameters are summarized in table 7.1.

Table 7.1: Acquisition and reconstruction parameters of the resolution phantom scans (images see Fig. 7.1).

	scan 1	scan 2	scan 3
# of pinholes × diameter	1 × 3.0 mm	7 × 1.5 mm	7 × 1.5 mm (× 2)
dist. pinhole to AOR	38 mm	54 mm	34 mm
voxel size	1.2 mm	0.8 mm	0.6 mm
# of iterations	645	430	66
scan time/view	60 s	60 s	30 s

wedge-shaped sectors of hollow rods with a diameter ranging from 1.5 to 3.0 mm. For the three scans, it was filled with about 37 MBq ^{99m}Tc. Each of the scans was performed on the same dual head e.cam Fixed 180° clinical gamma camera of Siemens Medical Solutions, equipped with one or two pinhole collimators with interchangeable aperture plates (Nuclear Fields International B.V.), the design of which was inspired by Schramm *et al.* [97]. They were all followed by an identical, but shorter scan of the Bequé phantom [11] to obtain accurate estimates of the geometrical camera parameters (see section 3.1.1).

The first time, the phantom was scanned to evaluate the spatial resolution in the initial rat brain studies (see section 7.2). Therefore, the clinical gamma camera was equipped with one single pinhole collimator having an aperture diameter of 3.0 mm. The pinhole center was positioned at about 38 mm from the AOR. All photons with a measured energy within the 20% photopeak energy window were collected in a 256×200 matrix of 1.95 mm square pixels for each of the 64 viewing angles, equally spread over 360°. Each projection image was acquired in 60 s. The activity distribution was reconstructed in an image space of 40×40×40 cubic voxels of 1.2 mm using the OSEM algorithm with decreasing number of subsets [55,

116]: 15×16, 15×12, 15×8, 15×4, 15×2, and 15×1 (number of global iterations × number of subsets). Resolution recovery was performed with the 7-ray method (see section 3.1.3), the intrinsic resolution of the detector was modeled as a Gaussian with a FWHM of 4 mm, and the scatter was estimated by fitting a Gaussian to the projection data. Given the small size and low density of the phantom, attenuation could be neglected. As can be seen from the left image of Fig. 7.1, the rods with a diameter of 2.1 mm and larger can be clearly discerned from each other.

A few months later, a multipinhole collimator with 7 apertures of 1.5 mm diameter, focusing at a point at 50 mm from the central pinhole was used to image the phantom. It was designed to improve both the sensitivity and the spatial resolution for rat brain imaging (see [10], p.53), and was positioned somewhat further from the AOR (at ±54 mm) than the single pinhole, because of the focusing distance of the design. The same imaging protocol was used, but an additional energy window of equal width was positioned at the left side of the photopeak window to estimate the amount of scattered photons in this latter window (dual energy window (DEW) scatter correction, see section 3.2.1). The phantom activity was reconstructed in an 96×96×120 image space with cubic voxels of 0.8 mm. The following iteration scheme was used for reconstruction: 10×16, 10×12, 10×8, 10×4, 10×2 and 10×1. The image quality was clearly improved and all rods were well separable (see central image in Fig. 7.1).

Recently, the phantom was rescanned with the newly designed set of multipinhole plates attached to the two pinhole collimators (see Fig. 6.4 and 6.5). As the sensitivity increased by at least a factor of two, the acquisition time was halved. The design was optimized for focused mouse imaging, hence the distance to the AOR was reduced to about 34 mm. The data were corrected for scatter, using the DEW technique (see section 3.2.1), and for decay (see section 3.2.3). The reconstructed image space consisted of 72×72×88 0.6 mm cubic voxels, and because the dual head system doubles the calculation time compared to single head, the reconstruction time was kept within limits by reducing the amount of iterations to 2×16, 2×8, 2×4, 3×2 and 4×1. The accuracy of the estimated geometrical parameters was improved by using the refined calibration method (see section 6.2.3). The combination of the design optimization, the reduced distance to the AOR, which increased the sensitivity with a factor of $2.5 = (54/34)^2$, and the improved calibration elevated the image quality to a higher level, as shown in the right image of Fig. 7.1.

An overview of the most important acquisition and reconstruction parameters of these three scans is given in table 7.1.

7.2 Rat brain imaging

In chapter 8 of [10], the first small animal pinhole SPECT study performed in our lab was summarized. It concerned a rat brain study executed on a single head GE Millenium MPR camera with a single pinhole collimator, having a focal length of about 240 mm and an aperture diameter of 3.0 mm. For subsequent

rat brain experiments, the dual head e.cam Fixed 180° clinical gamma camera of Siemens Medical Solutions was used, equipped with, at that point in time, one pinhole collimator (Nuclear Fields International B.V.). The first images were still acquired with a single pinhole collimator with a focal distance of about 170 mm and an aperture diameter of 3.0 mm. The good phantom study results, obtained with the multipinhole design consisting of 7 apertures on a circle with 39 mm radius, an aperture diameter of 1.5 mm and focusing at a point at 50 mm distance (see section 7.1), encouraged us to proceed with the rat brain studies using the multipinhole collimator, though.

Before routinely scanning the rats with the multipinhole collimator, the improvement in image quality was first verified by scanning a normal rat twice, once with either collimator. The rat was injected with about 145 MBq of ^{123}I-FP-CIT, as usual, which binds to the dopamine transporters, accumulating in the left and right striatum. Because we determined earlier that the striatum-to-cerebellum uptake ratio remained more or less constant between 1 h and 5 h post injection (p.i.), the order of the scans should not influence the contrast in the brain. First, the animal was scanned with the multipinhole collimator (at 1.5 h p.i.), next using the single pinhole collimator (at 3.5 h p.i.). Each of the acquisitions was followed by a calibration scan to estimate the geometrical camera parameters (see section 3.1.1). The acquisition protocols as well as the distance between the pinhole center and the AOR were identical for the two animal scans in order to eliminate all influences on the image quality other than those of the collimator. Projection data were collected in 256×200 matrices with square pixels of 1.95 mm from 64 angular views (2 × 30 s/view for each animal scan), equally distributed over 360°. The detector intrinsic resolution was modeled as a Gaussian with a FWHM of 4 mm. The scatter was estimated using the triple energy window (TEW) method, described in section 3.2.1. Given the relatively short duration of the scans compared to the long half-life of ^{123}I (13.2 h), the decay was considered to be negligible. Attenuation was neglected as well, because of the small dimensions of the rat head. The activity distribution was reconstructed in a 96×96×120 image space with 0.8 mm cubic voxels, using the OSEM algorithm with gradually reduced subsets: 10×16, 10×12, 10×8, 10×4, 10×2, and 10×1.

In Fig. 7.2, a transaxial and coronal slice through the striata are shown for the two scans next to each other to facilitate image quality comparison. Because of the four times larger pinhole aperture area, the sensitivity of the single pinhole collimator is comparable to that of the 7-pinhole collimator, hence the noise is similar. However, for the same reason the resolution was expected to be better for the latter, which is confirmed by the experiment. Indeed, the activity of the left and right striatum is better separated and the contrast with the rest of the brain is higher for the multipinhole case. Also the uptake in the Harderian glands (behind the eyes of the rat) is less smoothed out. A possible disadvantage of the multipinhole collimator is its reduced ability to reconstruct the body activity, because of its smaller FOV. A more extensive discussion on this topic was provided in section 6.6.

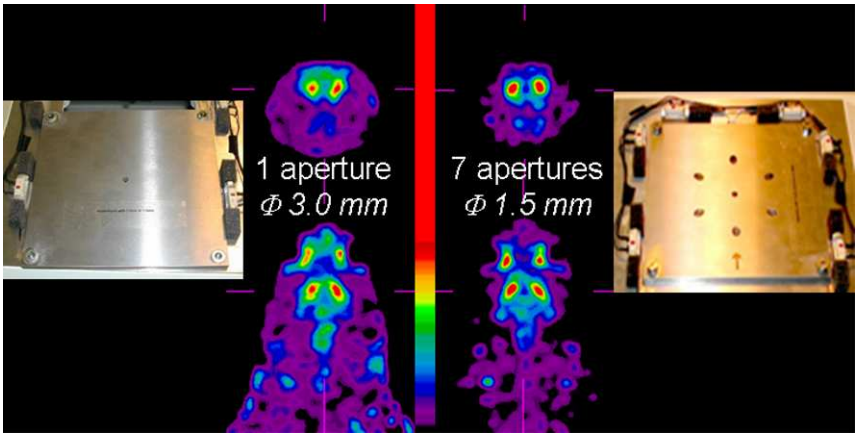

Figure 7.2: Comparison of the reconstruction image quality obtainable in the brain of a rat injected with 145 MBq of ^{123}I-FP-CIT, using (left image) a single pinhole collimator having a 3.0 mm aperture diameter and (right image) a multipinhole collimator consisting of 7 apertures with an aperture diameter of 1.5 mm: (top) transaxial and (bottom) coronal slices.

7.3 Rabbit heart imaging

7.3.1 Necrosis imaging

In our radiopharmacy department, a new SPECT tracer with high avidity for necrosis (cell death resulting in scar), mono-[^{123}I]iodohypericin (^{123}I-MIH), was synthesized and a preliminary evaluation of its uptake in a reperfused hepatic infarction rat model and in an occlusive myocardial infarction rabbit model was performed using conventional SPECT imaging and ex-vivo studies [82]. To study the tracer distribution over time, a new experiment was set up in which scans of various myocardial infarction rabbit models were acquired at multiple time points (2-3.5 h, 9-11 h and 22-24 h p.i.) [42]. As the resolution of the clinical gamma camera was too low to provide reasonable activity localization, single pinhole SPECT imaging with an aperture diameter of 3.0 mm was used instead. In addition, micro-PET $^{13}NH_3$ perfusion imaging was performed on the same rabbits to confirm the presence of the infarct and to enable comparison of the infarct delineation in the pinhole SPECT images with that of the perfusion defect in the micro-PET images. However, because both images contain little anatomical information and because registration of the images by just positioning the infarct inside the defect is not acceptable for a validation study, another registration approach was requisite. The use of fiducial markers visible in both SPECT and PET was not an option, because the micro-PET and series of pinhole SPECT images were acquired with large time gaps in between. Therefore, the rabbit was taken out of the bed and was allowed to wake up in between the scans, hence requiring repositioning. Sufficient information for registration could be obtained from an additional CT and micro-PET transmission

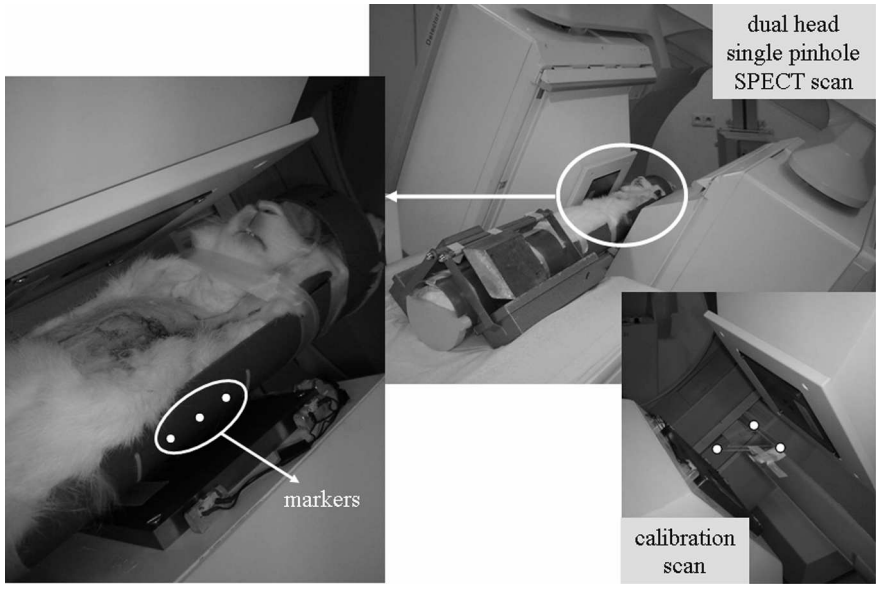

Figure 7.3: Pictures of a dual head single pinhole SPECT acquisition. The rabbit heart was positioned in the center of the FOV. Markers were attached to the rabbit bed to enable CT-SPECT registration. A calibration scan was performed immediately after the pinhole SPECT scan.

scan using a ^{57}Co source. The former was taken immediately after each series of pinhole SPECT scans by transporting the bed carefully between the two scanners. Hence, these images could easily be registered rigidly using five fiducial markers visible in both imaging modalities, also enabling attenuation correction of the pinhole SPECT images (see section 3.2.2). Fig. 7.3 and Fig. 7.4 show a picture of the pinhole SPECT[1] and CT acquisition, respectively. The micro-PET transmission scan was performed immediately before the micro-PET emission scan and was registered with it automatically, since they were acquired on the same camera without changing the rabbit's position (see Fig. 7.5). The transmission scan was then used for attenuation correction of the emission scan. Because the rabbit was always positioned in a similar way, i.e. by streching the body as much as possible, the first analysis of the data could be done using (sometimes manually guided) rigid registration between the two images containing anatomical information, namely the CT and the micro-PET transmission image, with mutual information as the objective function [72]. An overview of the complete registration process is given in Fig. 7.6. Since all images are now in the same space, the pinhole SPECT image and the micro-PET emission image can be combined, yielding a nice representation of the left ventricle, which can be automatically delineated. This delineation can then be copied to the individual images, enabling quantification of the infarcted region and

[1] At the time of this first rabbit study, only one pinhole collimator was available at our department.

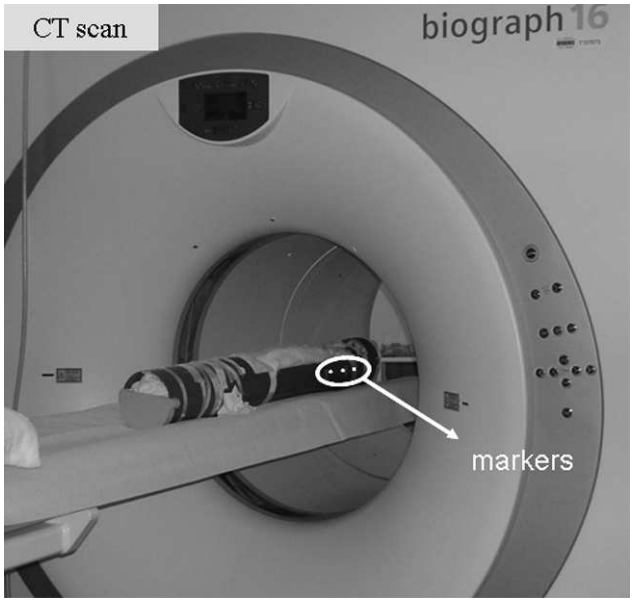

Figure 7.4: Pictures of a CT acquisition. The rabbit was scanned immediately after each series of pinhole SPECT scans. The markers attached to the rabbit bed (see also Fig. 7.3) are visible both in the pinhole SPECT and in the CT image.

the perfusion defect, respectively. It could be concluded that the infarcts can be well delineated in the ^{123}I-MIH images obtained at 9 h p.i. (and later). Longitudinal and transverse cardiac micro-PET and pinhole SPECT images are shown in [42].

7.3.2 Simultaneous necrosis and apoptosis imaging

From this result, a second experiment was set up to simulataneously visualize necrosis and apoptosis, non-organized and organized cell death, in a group of rabbits with an acute reperfused myocardial infarction. As an apoptosis avid tracer, ^{99m}Tc-labeled annexin A5 [40] was injected at the same time as the necrosis avid ^{123}I-MIH. Because the former tracer was expected to yield good images already at an earlier time point, four subsequent pinhole SPECT scans of 35 min were performed between 7 h p.i. and 10 h p.i. The ^{99m}Tc-labeled annexin A5 could not be injected before the micro-PET transmission scan, because the photopeak energies of ^{57}Co (122 keV) and ^{99m}Tc (140 keV) are too close to each other. To allow the study of one rabbit to be finished in one day, the SPECT tracers were injected (via ear vein) between the micro-PET transmission and emission scan. The complete study protocol is depicted in Fig. 7.7.

For this study, the registration of the two anatomical images was improved by performing it non-rigidly using again mutual information as objective function [27]. An example of such registration is shown in Fig. 7.8, with the contours of the CT

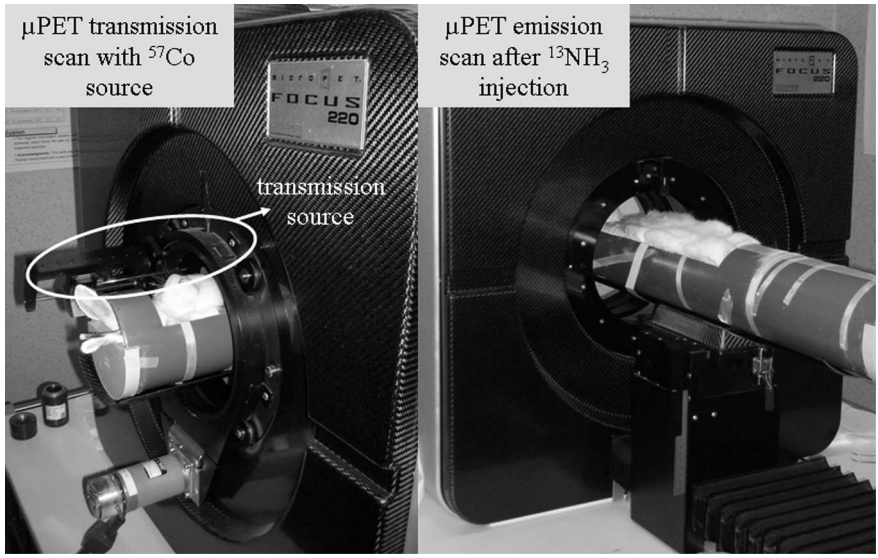

Figure 7.5: Pictures of a micro-PET acquisition. First, a transmission scan of the rabbit heart is performed. Next, the PET perfusion tracer $^{13}NH_3$ is injected in the ear vein. A micro-PET emission scan is started immediately after the injection.

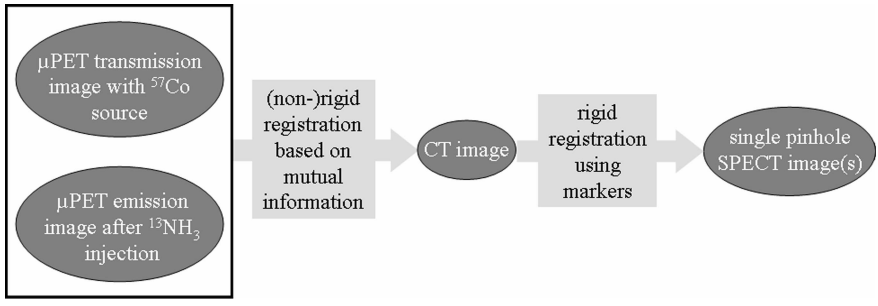

Figure 7.6: Flow diagram of the registration.

image (top) overlaid on the micro-PET transmission image (bottom). Furthermore, a second single pinhole collimator (Nuclear Fields International B.V.) was attached to the second detector of the dual head clinical gamma camera (e.cam Fixed 180°, Siemens Medical Solutions), reducing the required scan time to obtain the same image quality by a factor of two. Because two different SPECT tracers were injected with isotopes having a photopeak energy close to each other (^{99m}Tc (140 keV) and ^{123}I (159 keV)), crosstalk correction of the measured pinhole SPECT data was required, as explained in section 3.2.4. The resulting reconstructed images of the ^{123}I-MIH and the ^{99m}Tc-labeled annexin A5 activity distribution are shown in Fig. 7.9 (center) and (bottom), respectively. The corresponding slices of the registered micro-PET emission image are presented in Fig. 7.9 (top), and the

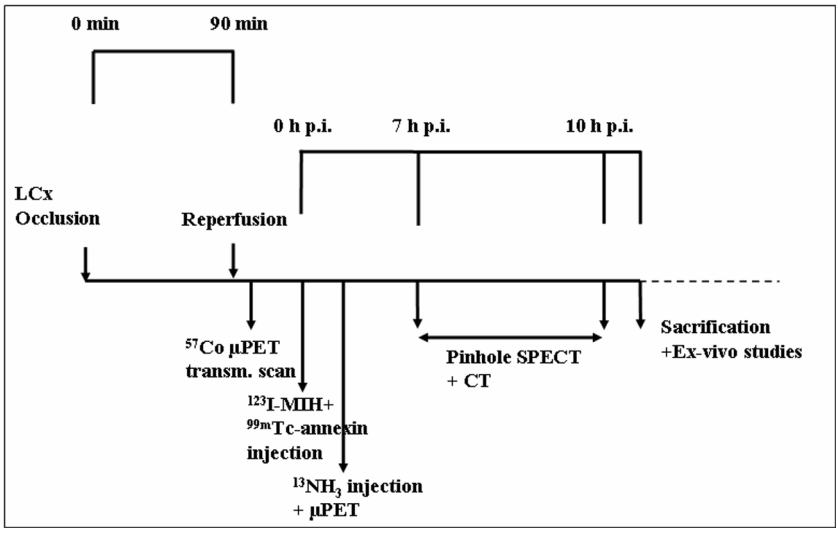

Figure 7.7: Study protocol of the second rabbit experiment (see section 7.3.2).

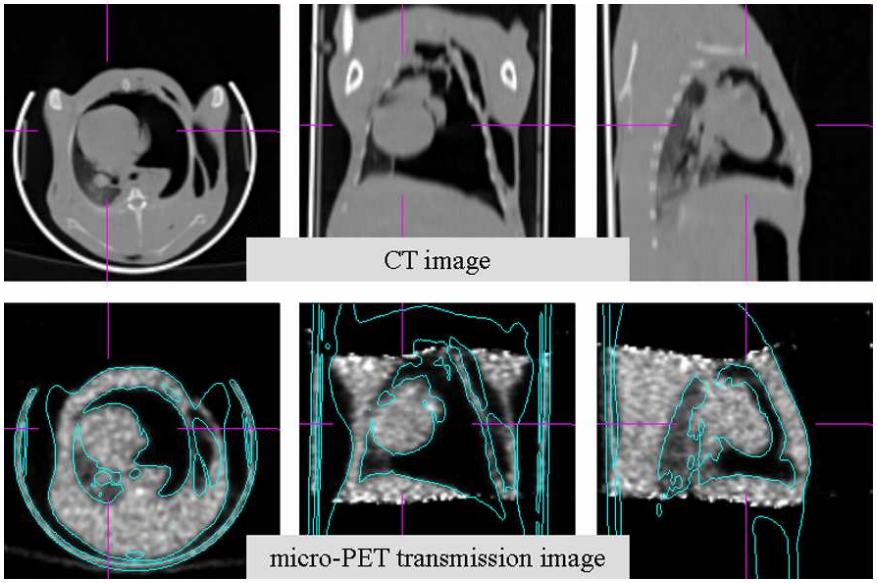

Figure 7.8: Reconstructed images of the CT scan (top) and the micro-PET transmission scan (bottom) of the same rabbit: (left) transaxial, (center) coronal and (right) sagittal slice. The scans were co-registered non-rigidly using mutual information. Both images were also transformed to the pinhole SPECT image space using rigid registration based on the fiducial markers. The contours originate from the CT image.

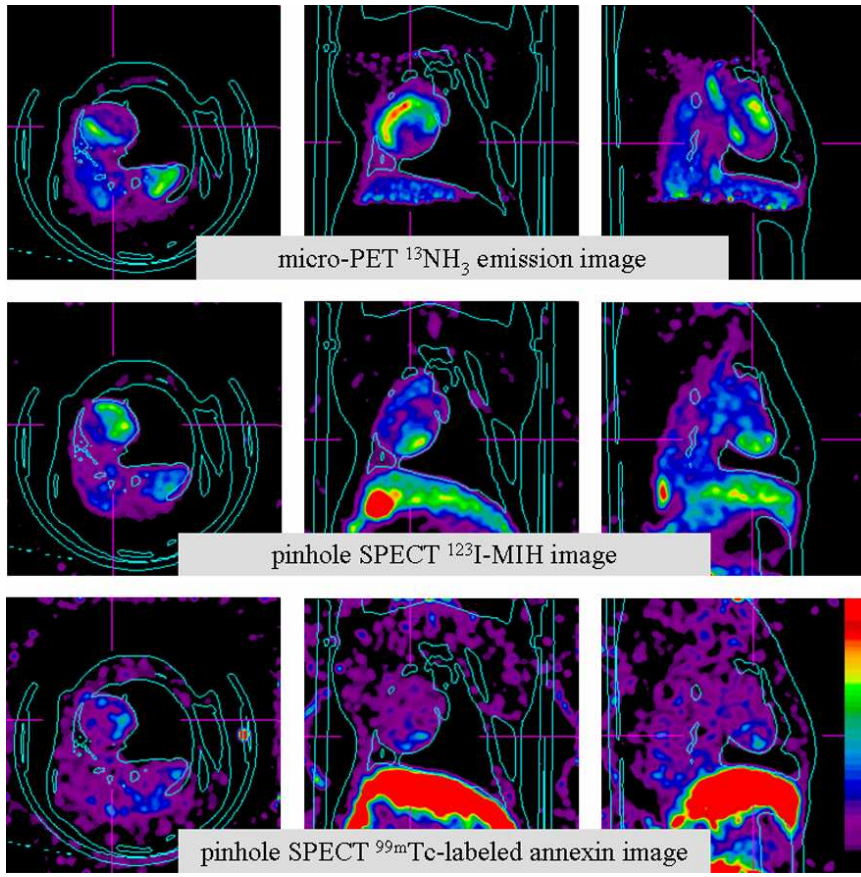

Figure 7.9: Reconstructed images of the corresponding micro-PET emission scan (top) and the dual isotope pinhole SPECT scan (center: ^{123}I-MIH and bottom: ^{99m}Tc-labeled annexin A5 image). The micro-PET emission scan underwent the same transformation as the transmission scan to be registered to the pinhole SPECT images. The contours originate from the registered CT image of Fig. 7.8 (top).

overlaid contours were obtained from the registered CT image of the same rabbit (see Fig. 7.8). From these images, we can again conclude that the necrotic tissue in the infarcted region fits well the perfusion defect. The contrast enhanced slightly with the elapsed time since the injection. In addition, some apoptosis was visible in (parts of) the infarcted region too (see Fig. 7.9 (bottom)). The myocardial infarction could already successfully be delineated in the ^{99m}Tc-labeled annexin A5 images obtained at 7 h p.i. [40].

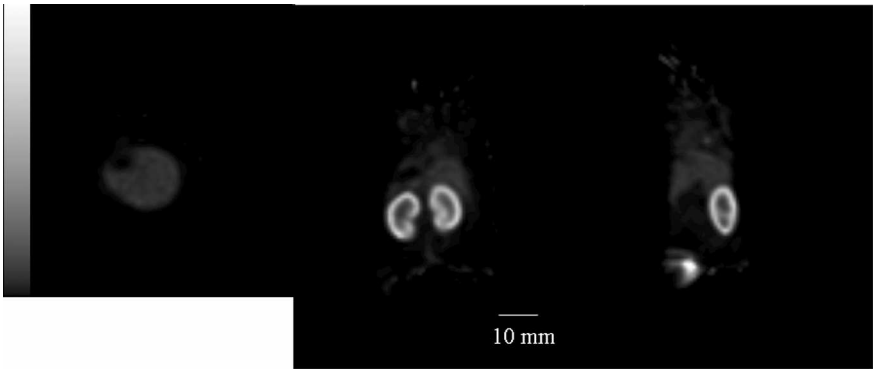

Figure 7.10: Transaxial (left), coronal (center) and sagittal slice (right) of a normal mouse (1 h p.i.), injected with 15.0 MBq of ^{99m}Tc-labeled annexin A5. These images were also shown in Fig. 6.11.

7.4 Mouse imaging

7.4.1 Apoptosis imaging

Next to the investigation of necrosis avid tracers, our lab is, among other things, also seeking for a good tracer for the visualization of apoptosis in collaboration with the university of Maastricht [40]. Various types of ^{99m}Tc-labeled annexin A5 are currently being tested for in vivo imaging of apoptosis. As for the necrosis avid tracers, the ^{99m}Tc-labeled annexin A5 is first tested in a hepatic apoptosis model. The final goal is to visualize apoptosis in tumors after therapy in order to assess therapy response. One of the studies involving pinhole SPECT imaging is briefly discussed below. Since a few months, the new multipinhole plates, optimized for focused mouse imaging, are routinely used for these kinds of studies (see chapter 6). Typically, the data are collected in 256×200 matrices with square pixels of 1.95 mm for 64 viewing angles (30 s/view), equally spread over 360°. After the mouse scan(s), a calibration scan is performed. The measured data are reconstructed using the OSEM algorithm with an equivalent of 66 global iterations in an image space of 96×96×120 cubic voxels of 0.8 mm.

To verify whether one of these ^{99m}Tc-labeled annexin A5 variants is specific for apoptosis, a simple experiment was set up. First, a baseline pinhole SPECT scan of a normal mouse was performed 1 h after the injection of ±15.0 MBq of ^{99m}Tc-labeled annexin A5. Two days later, the mouse was treated with anti-Fas monoclonal antibodies (mAb), which induce apoptosis in the liver. The same tracer was injected 1.5 h post treatment (±15.4 MBq) and the animal was rescanned 1 h p.i. of the tracer. Significant increase in liver uptake was expected. A second mouse underwent the same anti-Fas treatment, but half an hour before tracer injection (±11.3 MBq) an amount of cold (i.e. non-radioactive) annexin A5 was injected, hence at least partial saturation was expected, leading to a decreased liver uptake compared to the uptake in the first anti-Fas treated mouse. These expectations

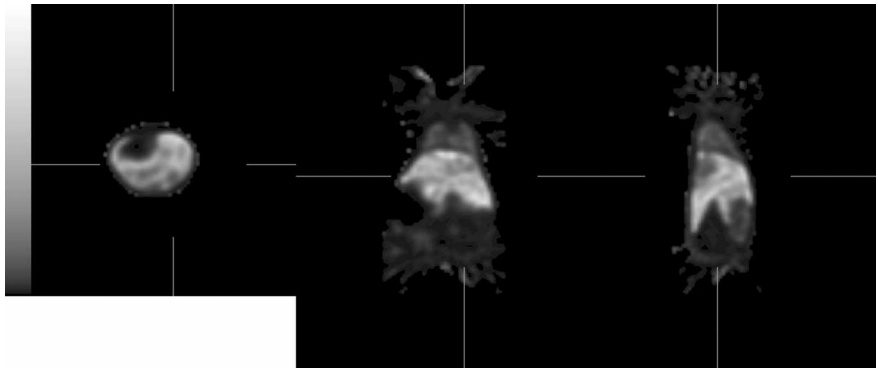

Figure 7.11: Transaxial (left), coronal (center) and sagittal slice (right) of the first anti-Fas treated mouse (1 h p.i.), injected with 15.4 MBq of ^{99m}Tc-labeled annexin A5.

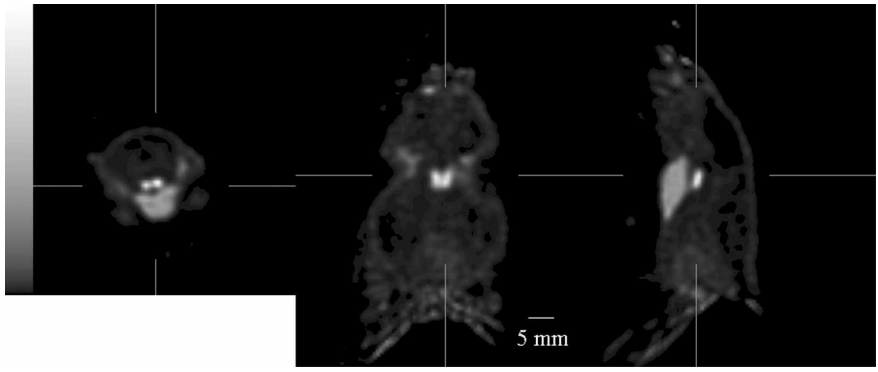

Figure 7.12: Transaxial (left), coronal (center) and sagittal slice (right) through the thyroid of a normal mouse (10 min p.i.), injected with ±29.6 MBq of $^{99m}TcO_4^-$. The same images were shown in Fig. 6.12.

were confirmed by biodistribution studies as well as by the pinhole SPECT images. A transaxial, coronal and sagittal slice of the baseline scan were already shown in Fig. 6.11 as an illustration of the performance of the new multipinhole designs, and are repeated in Fig. 7.10. A homogeneous liver uptake and high kidney uptake are visible. This stands in vivid contrast against the very high liver uptake in the first anti-Fas treated mouse (see Fig. 7.11). The uptake of the second mouse, which was pretreated with cold annexin A5, was very similar to the baseline image (image not shown).

7.4.2 Thyroid imaging

Once the new multipinhole plates were extensively tested for mouse imaging with simulations (section 6.5.1), phantom experiments (sections 6.5.2 and 7.1) and mouse scans (sections 6.5.3 and 7.4.1), their spatial resolution performance was evaluated by thyroid imaging in two normal mice. They were scanned 10 min after pertechnetate ($^{99m}TcO_4^-$) injection ($\pm$29.6 MBq). The data collection was very similar to those of the experiment in section 7.4.1. The measured data are reconstructed using the OSEM algorithm with an equivalent of 155 global iterations in an image space of 96×96×120 cubic voxels of 0.6 mm. A transaxial and coronal slice through the thyroid of one of the mice is shown in Fig. 7.12 (identical to Fig. 6.12).

This experiment was performed as a pilot study of a future follow-up experiment for thyroid therapy planning, using targeted sunitinib therapy [131]. Therefore, absolute quantification will be required. Thanks to the acquisition and reconstruction of a homogeneous cylinder with known activity concentration, and due to the accurate sensitivity modeling (using flood source measurements, see section 3.1.2), a global scale factor could be calculated, yielding images in Bq/mm^3.

7.5 Future studies

7.5.1 Necrosis imaging

In our radiopharmacy department, many new necrosis avid tracers have been synthesized and await in vivo testing in small laboratory animals. One of these is a new variant on the ^{123}I-MIH tracer, namely mono-[^{123}I]iodohypericin monocarboxylic acid (^{123}I-MIHA) [41], for which a faster blood clearance is expected, meaning earlier myocardial infarct visualization should be possible. Indeed, the early ^{123}I-MIH images were hampered by the high blood pool activity in the heart, yielding low contrast. Other necrosis avid tracers developed in our radiopharmacy lab are e.g. $^{99m}Tc(CO)_3$-labeled pamoid acid derivatives [39] and ^{99m}Tc-labeled bisindole. As a preliminary test, these tracers have already been evaluated in three different models for necrosis, namely reperfused hepatic infarction, ethanol induced liver necrosis and ethanol induced muscular necrosis, all in rats. Next, they will be studied in the clinically more relevant, but also more complex myocardial infarction models (permanent occlusion, reperfusion, etc.).

The most obvious choice would be to resort again to rabbit models, as we already yielded successful outcome with these. However, working with rabbits has many disadvantages compared to rats and mice. First of all, they are large and therefore costly in various ways, namely in purchase cost, housing cost, more surgical material, a higher amount of anaesthetics and a higher tracer dose are required, etc. Mice, on the other hand, are very small, making the surgery more complex and requiring a very high spatial resolution of the pinhole SPECT and micro-PET camera. Cardiac gating could help to improve the reachable resolution, but not all cameras can handle the 300-500 heart beats/min and given the often sparse uptake of necrotic

avid tracers, the registration between the different phases in the cycle will be a real challenge. Therefore, our preference would go to myocardial rat models. Although the new multipinhole designs were developed for mouse imaging, they should also perform well for imaging rats.

Studies similar to the rabbit heart imaging experiments, explained in section 7.3, will be set up for these tracers in the near future, using myocardial rat models. Because in our lab we are not experienced in imaging rat hearts, it might be interesting to first scan the heart of a normal rat using a validated tracer, such as ^{99m}Tc-MIBI, to get an idea about the spatial resolution and image quality that can be obtained with the pinhole SPECT and the micro-PET camera. This was also done before routinely scanning rabbit hearts. No problems are expected though, since cardiac rat imaging has been performed since many years in the V.U.Brussel on various pinhole SPECT cameras [118]. The images obtained with the different modalities (micro-PET, pinhole SPECT and CT) will be registrated in the same way as described in section 7.3 and depicted in Fig. 7.6.

7.5.2 Apoptosis imaging

The next experiment that is being planned in the scope of apoptosis imaging will study the killing effect of a particular chemotherapy on tumor cells. Effective therapy kills tumor cells within 3 days after therapy. Therefore, imaging of apoptosis enables specific and early assessment of therapy response.

As a tumor model, some tumor tissue is implanted in the spleen of severe combined immunodeficient (SCID) mice. If the model is successful, the tumor grows and reaches the desired size after about three weeks. This spleen tumor is preferred to a subcutaneously grown tumor, because the former has an improved vascularization, facilitating tracer uptake. After three weeks, a fast MRI scan will be performed to measure the tumor size. The mice with sufficiently large tumors are then selected for further investigation. These will be imaged on the micro-MRI scanner to visualize the anatomy from lungs to upper legs, and, if possible, also to visualize the vascularization and the perfusion in the tumor. Next, a baseline pinhole SPECT scan is taken of the FOV around the spleen 4 h p.i. of ^{99m}Tc-labeled annexin A5. Immediately afterwards, a CT scan will be acquired to enable the registration between the micro-MRI and the pinhole SPECT image. Similar to the rabbit heart experiments, a number of fiducial markers visible in SPECT and CT will be used for their registration (see section 7.3). Because little difference can be made between the various organs, such as liver, stomach and spleen (all soft tissue), a contrast agent will be injected to improve the contrast, but up till now we do not have any experience with this agent in mice (Fenestra^{TM}, [105]). If it clearly highlights the spleen and the tumor, the micro-MRI scan can probably be omitted for further experiments. After the pinhole SPECT and CT scan, chemotherapy is started. After one day of chemotherapy, a second pinhole SPECT and CT scan are performed to enable comparison of the amount of apoptosis in the tumor, which will be localized based on the registered MRI image. The main difficulty of this study will be the registration between the micro-MRI and the CT image, possibly combined with

some anatomical information visible in the pinhole SPECT image, e.g. the liver and the kidneys.

7.6 Discussion

During this PhD, we aimed for increasing the image quality of a pinhole SPECT system for small animal imaging. We focused on high sensitivity, rather than high resolution, because often low tracer uptake is expected. The dose per unit (body) weight injected in small animals is often already quite large compared to that in human studies, hence administering even higher doses is not an option. On the contrary, the currently injected doses are often too high and should be diminished [44]. Especially for follow-up studies, they risk to induce therapeutic effects, thereby possibly compromising the study's outcome. These relatively high doses might also involve a large injected mass (chemical quantity), which on its turn also might influence the outcome of the study [67]. In addition, the growing interest for multi-modality imaging (e.g. combination of SPECT and CT) further increases the dose. When performing small animal imaging, generally the impact of the radiation dose is not explored well enough.

A few years ago, we purchased a second pinhole collimator in order to double the sensitivity and reduce the required dose by a factor of two. For the rabbit experiments we chose to use pinhole plates with an aperture diameter of 3 mm, rather than 1.5 mm, because these yielded sufficiently accurate spatial resolution for visualizing the left ventricle of a (beating) rabbit heart. Doubling the diameter, quadrupled the sensitivity. Unfortunately, despite all this, still high doses in the order of 100 MBq needed to be injected to reach sufficient image quality with a 35 min pinhole SPECT scan. During the experiments, the rabbits also received extra radiation due to the micro-PET transmission and emission scan, and the CT scan. The latter was performed on a human PET/CT scanner, on which a low dose protocol was selected.

For mouse imaging, we designed a new set of multipinhole plates (see chapter 6). Although mice are significantly smaller than rats, keeping the aperture diameters at 1.5 mm was not hampering the analysis of the executed mouse studies. Even the bilobal structure of a mouse thyroid could be discerned (see Fig. 7.12). The smaller pinhole to AOR distance for mice (compared to rats) and the optimization of the multipinhole plates yielded high quality images for administered doses of about 15 MBq. Often also a CT scan is performed, which increases the radiation dose for the animal. Therefore, the gathered anatomical information would best be included during SPECT reconstruction to improve the image quality, not only for attenuation correction, but also for e.g. partial volume correction [2, 15].

7.7 Conclusion

In this chapter, it has been illustrated with both phantom and animal experiments that the image quality of our pinhole SPECT system has improved over the last four years. In addition, the increasing number of preclinical studies performed on this camera proves that it has established its position as an important in vivo imaging tool, next to micro-PET, micro-CT, micro-MRI, bioluminescence imaging, etc. This establishment is a general trend seen in the small animal imaging field. Another trend is the use of multiple imaging modalities for one study, often on combined scanners, such as a micro-PET/micro-CT (which is similar to the evolution in the clinic). The lack of such combined scanners requires accurate intermodality image registration, as discussed in many of the above small animal experiments. The growing interdisciplinary collaboration, of which the recently inaugurated molecular small animal imaging center (MoSAIC) is a perfect example, will certainly stimulate the popularity of the pinhole SPECT system, although a dedicated micro-SPECT system available during day time would make its use more attractive. In addition, one should pay sufficient attention to the total radiation dose given to the animal during the whole experiment.

Chapter 8

Fisher information-based evaluation of image quality for time-of-flight PET

To illustrate that the image quality evaluation method, derived in chapter 4, can be applied to many other emission and transmission tomography systems, it has been used to compare time-of-flight (TOF) PET systems with different time resolutions to conventional PET systems. In addition, the influence of the time resolution model accuracy on the reconstruction image quality has been evaluated with this method to study the counterintuitive results presented in [26], indicating that one should choose the TOF model too wide to yield the best contrast-to-noise ratio.

[1]The use of time-of-flight (TOF) information during positron emission tomography (PET) reconstruction has been found to improve the image quality. In this work we quantified this improvement using two existing methods: (1) a published analytical expression only valid for a central point in a large uniform disk source, and (2) efficient analytical approximations for post-filtered maximum likelihood expectation maximization (MLEM) reconstruction with a fixed target resolution, predicting the image quality in a pixel or in a small region of interest based on the Fisher information matrix. Using this latter method the weighting function for filtered backprojection reconstruction of TOF PET data proposed by Watson can be derived. The image quality was investigated at different locations in various software phantoms. Simplified as well as realistic phantoms, measured both with TOF PET systems and with a conventional PET system, were simulated. Since the time resolution of the system is not always accurately known, the effect on the image quality of using an inaccurate kernel during reconstruction was also examined with

[1]This chapter has been submitted as a full article to *IEEE Transactions on Medical Imaging*: K. Vunckx, L. Zhou, S. Matej, M. Defrise, J. Nuyts. Fisher information-based evaluation of image quality for time-of-flight PET. *submitted to IEEE Trans. Med. Imag.* Only minor changes concerning notational consistency and lay-out have been performed.

the Fisher information-based method. First, we confirmed with this method that the variance improvement in the center of a large uniform disk source is proportional to the disk diameter and inversely proportional to the time resolution. Next, image quality improvement was observed in all pixels, but in eccentric and high-count regions the contrast-to-noise ratio (CNR) increased slower than in central and low- or medium-count regions. Finally, the CNR was seen to decrease when the time resolution was inaccurately modeled (too narrow or too wide) during reconstruction. Although the optimum is rather flat, using an inaccurate TOF kernel tends to introduce artifacts in the reconstructed image.

8.1 Introduction

In the 1980s considerable research interest emerged for the use of time-of-flight (TOF) information in positron emission tomography (PET). However, due to the lack of fast high efficiency scintillators, this promising route was abandoned until in the 1990s the development of new scintillators, such as lutetium orthosilicate (LSO) and lanthanum bromide ($LaBr_3$), renewed interest in TOF PET. The effect on the image quality of using TOF information during PET reconstruction has been studied extensively by many groups. With analytical calculations [73, 101, 109, 110, 132], (Monte Carlo) simulations [24, 51, 60, 63, 74, 89, 106, 135], observer studies [90] and experimental data [24,61,107,127,134] it was shown that the image quality increases if timing information is exploited. Most of the gain induced by TOF is obtained by reduced variance. Many analytical approaches to predict the image quality are, however, restricted to simple objects. And on the other hand, simulations and phantom experiments are very time-consuming or give noisy results due to low-count statistics.

In this work, we use an analytical method, based on approximate expressions for the Fisher information matrix, to predict the impulse response and (co)variance of individual pixels of three phantoms imaged with various 2D TOF PET systems, as well as with a conventional PET system.

During reconstruction, the finite TOF resolution is usually modeled as a Gaussian with a full width at half maximum (FWHM) Δt, or equivalently $\Delta x = c\Delta t/2$, with Δx the localization uncertainty of the TOF PET system, c the speed of light, and Δt the time resolution. This Gaussian is often called the TOF kernel. We studied the effect of using an inaccurate TOF kernel, because Δt is not always accurately known and might depend on the count rate [107], and because of the counterintuitive results reported in [26], which indicated that using a wider kernel slightly improved the contrast versus noise trade-off.

8.2 Theory

8.2.1 Previous analytical calculation of TOF variance

In 1981, Tomitani derived a formula to evaluate the variance of a central pixel in a very large (with respect to Δx) uniform disk source with diameter D, reconstructed with a filtered backprojection (FBP) method using TOF information [110]. He proved that confidence weighted FBP, i.e. weighting the backprojection with the TOF kernel, ensures minimal variance $(\mathrm{Var}_{TOF,min})^2$, and calculated the variance reduction due to TOF by comparing it to the variance obtainable with conventional PET ($\mathrm{Var}_{conv,min}$):

$$\mathrm{Var}_{TOF,min} \approx \frac{b^2}{8}\frac{a\Delta x}{\Delta r^3}, \text{ provided that } D >> \Delta x \tag{8.1}$$

and

$$\frac{\mathrm{Var}_{conv,min}}{\mathrm{Var}_{TOF,min}} \approx \frac{b}{2\sqrt{\pi}}\frac{D}{\Delta x} = 0.66\frac{D}{\Delta x} \tag{8.2}$$

with $b = \sqrt{8\ln 2}$, a the amount of detected coincidences per unit area, and Δr the resolution of the reconstructed image, (both Δx and Δr represent the FWHM).

Because of the rotational symmetry of the phantom, these expressions for a central pixel also hold for weighted least squares (WLS) reconstruction. Indeed, the weights to be applied are then identical for all projection angles. Consequently, the expressions also apply to maximum a posteriori (MAP) or post-smoothed maximum likelihood expectation maximization (MLEM) in cases where the non-negativity constraint can be ignored.

8.2.2 Fisher information-based image quality prediction

Basic equations

In emission tomography, the linearized local impulse response (LLIR) and the covariance in a reconstructed pixel are often used as image quality measures. In [37,94] efficient analytical approximations for the LLIR and the covariance of a pixel j were proposed for converged MAP reconstruction:

$$l^j(\Lambda) \approx [\boldsymbol{F} + \beta\boldsymbol{U}]^{-1}\boldsymbol{F}e^j \tag{8.3}$$

$$\mathrm{Cov}^j(\Lambda) \approx [\boldsymbol{F} + \beta\boldsymbol{U}]^{-1}\boldsymbol{F}[\boldsymbol{F} + \beta\boldsymbol{U}]^{-1}e^j \tag{8.4}$$

$$\text{with } \boldsymbol{F} = \boldsymbol{A^T C_Y^{-1} A}$$

[2] In [110], the reconstructed image represents the amount of photon pairs emitted during acquisition time. Therefore, variance increases with a. More often, the activity per pixel or per unit volume is reconstructed. Then, variance decreases with increasing a, and a comes in the denominator in eq. (8.1). As a is eliminated anyhow in eq. (8.2), the original equation is maintained.

where $\boldsymbol{F}$ is the Fisher information matrix (which - in emission tomography - can be calculated by a forward projection $\boldsymbol{A}$, weighted by the inverse of the covariance matrix $\boldsymbol{C_Y}$ of the phantom measurement $\boldsymbol{Y}$, and followed by a backprojection $\boldsymbol{A^T}$, with $^{\boldsymbol{T}}$ denoting transpose), β is the smoothing parameter, $\boldsymbol{U}$ is the Hessian of the quadratic prior, used for regularization, and e^j is the j-th unit vector.

To enable comparison between different systems at equal (uniform) spatial resolution, we adapted the above equations to approximate post-smoothed MLEM with a fixed target resolution (see chapter 4). Essentially, we assumed $[\boldsymbol{F}+\beta\boldsymbol{U}]^{-1}$ could be approximated by $\boldsymbol{PG}$, with $\boldsymbol{P}$ an isotropic Gaussian post-smooth filter that tries to impose the given target resolution and $\boldsymbol{G}$ an approximate pseudoinverse of the Fisher information matrix $\boldsymbol{F}$. This yielded the following equations:

$$l^j(\Lambda) \approx \boldsymbol{PGF}e^j \tag{8.5}$$
$$\mathrm{Cov}^j(\Lambda) \approx \boldsymbol{PGFG^TP^T}e^j. \tag{8.6}$$

If local shift-invariance is assumed, $\boldsymbol{F}$ can be turned into a circulant matrix $\boldsymbol{F}^j$, where each row is a shifted version of the j-th row. Accordingly, also $\boldsymbol{G}$ and $\boldsymbol{P}$ become j-dependent (and get therefore a superscript ^{j}). Equations (8.3)-(8.6) can then be calculated by convolutions in the spatial domain, or - more efficiently - by multiplications in the Fourier domain [94]. Consequently, equations (8.5) and (8.6) changed into[3]:

$$l^j(\Lambda) \approx \boldsymbol{P}^j\boldsymbol{G}^j\boldsymbol{F}^j e^j \tag{8.7}$$
$$\mathrm{Cov}^j(\Lambda) \approx \boldsymbol{P}^j\boldsymbol{G}^j\boldsymbol{F}^j\boldsymbol{G}^{jT}\boldsymbol{P}^j e^j. \tag{8.8}$$

The j-th elements of $l^j(\Lambda)$ and $\mathrm{Cov}^j(\Lambda)$ are the contrast recovery coefficient (CRC) and the variance (Var) in pixel j, respectively. Combined they yield the contrast-to-noise ratio (CNR), often used as an image quality measure:

$$\mathrm{CNR} = \frac{\mathrm{CRC}}{\sqrt{\mathrm{Var}}}. \tag{8.9}$$

Extension to regions of interest

Assuming local shift-invariance, the filters found for an individual pixel j (see equations (8.7) and (8.8)) should be good approximations for all pixels of a small region of interest (ROI) centered at j. Therefore, the post-smoothed LLIR (l^{ROI}) and the

[3]The transpose of the second $\boldsymbol{P^j}$ in equation (8.8) can be omitted, since the same Gaussian filter, which was optimized to ensure the target resolution in pixel j, is applied to the whole image.

variance (Var^{ROI}) of the ROI can be approximated as

$$l^{ROI}(\Lambda) \;\approx\; Q_I \left.\begin{bmatrix} 0 \\ \vdots \\ 1/r \\ 1/r \\ 1/r \\ \vdots \\ 0 \end{bmatrix}\right\} \text{pixels in ROI} \tag{8.10}$$

$$Var^{ROI}(\Lambda) \;\approx\; \begin{bmatrix} 0 \;\ldots\; \frac{1}{r} \;\frac{1}{r} \;\frac{1}{r} \;\ldots\; 0 \end{bmatrix} Q_V \begin{bmatrix} 0 \\ \vdots \\ 1/r \\ 1/r \\ 1/r \\ \vdots \\ 0 \end{bmatrix} \tag{8.11}$$

with $Q_I = \boldsymbol{P}^j \boldsymbol{G}^j \boldsymbol{F}^j$ and $Q_V = \boldsymbol{P}^j \boldsymbol{G}^j \boldsymbol{F}^j \boldsymbol{G}^{jT} \boldsymbol{P}^j$, which can be obtained from equations (8.7) and (8.8), and with r the number of pixels in the ROI.

Extension to mismatched TOF kernels

We can easily include the reconstruction TOF kernel in equations (8.5) and (8.6). First, we substitute $\boldsymbol{F}$ by $\boldsymbol{A^T C_Y^{-1} A}$, with $\boldsymbol{A}$ and $\boldsymbol{A^T}$ the forward and backward projection matrix with the correct kernel (i.e. in agreement with the measurement). Similarly, $\boldsymbol{B}$ and $\boldsymbol{B^T}$ are defined as the forward and backward projection matrix modeling the reconstruction TOF kernel with inaccurate time resolution. Next, we identify which projection and backprojection operations need to model the real measurements, and which the reconstruction. For the latter, $\boldsymbol{A}$ and $\boldsymbol{A^T}$ are substituted by $\boldsymbol{B}$ and $\boldsymbol{B^T}$, respectively. This yields:

$$l^j(\Lambda) \approx \boldsymbol{P}[\boldsymbol{B^T C_Y^{-1} B}]^{ps} \boldsymbol{B^T C_Y^{-1} A} e^j \tag{8.12}$$

$$\mathrm{Cov}^j(\Lambda) \approx \boldsymbol{P}[\boldsymbol{B^T C_Y^{-1} B}]^{ps} \boldsymbol{B^T C_Y^{-1} B} \; ([\boldsymbol{B^T C_Y^{-1} B}]^{ps})^T \boldsymbol{P} e^j \tag{8.13}$$

where ^{ps} denotes approximate pseudoinverse, $\boldsymbol{A}e^j$ represents the impulse measurement, and $\boldsymbol{B}^T {\boldsymbol{C_Y}}^{-1}$ and $\boldsymbol{P}[\boldsymbol{B}^T {\boldsymbol{C_Y}}^{-1} \boldsymbol{B}]^{ps}$ can be seen as the (weighted) backprojection and the post-smooth and reconstruction filter, respectively, similar to FBP reconstruction (see section 8.2.3). The covariance matrix $\mathrm{Cov}^j(\Lambda)$ is computed by propagating the Poisson noise on the data through the reconstruction operator using a quadratic approximation. Because the reconstruction operator uses the inaccurate TOF kernel, the covariance matrix is a function of $\boldsymbol{B}$ and not of $\boldsymbol{A}$. To make these approximations more efficient, the same local shift-invariance assumption can be used as for deriving equations (8.7) and (8.8).

8.2.3 Fisher information-based kernel derivation for FBP of TOF PET

The above Fisher information-based approximations can also be used to determine the optimal weighting function for FBP reconstruction of the central point in a rotationally symmetrical positron emitting object, imaged with a TOF PET system. Because of the rotational symmetry, the weights are independent of the angle, and WLS reduces to least squares (LS). As mentioned in section 8.2.1, in that case the Fisher information-based approximations, which are based on a linearization of MLEM reconstruction, are valid for predicting the image quality of (W)LS and FBP reconstruction, and vice versa.

To find this weighting kernel, we start from a comparison between the (simplified) approximation for the LLIR for MLEM (or WLS)

$$l^j(\Lambda) \approx [\boldsymbol{A^T C_Y^{-1} A}]^{-1} \boldsymbol{A^T C_Y^{-1} A} e^j \tag{8.14}$$

and the expression for weighted FBP from [127] (in the frequency domain)

$$I(\nu) = \frac{\int d\theta W(\hat{u},\nu) M(\theta,\nu)}{\int d\theta W(\hat{u},\nu) G(\nu \cdot \hat{u})}, \tag{8.15}$$

$$\text{with } M(\theta,\nu) = I(\nu) G(\nu \cdot \hat{u}), \tag{8.16}$$

where $\hat{u}$ is a 2D unit vector in the projection direction at angle θ, $I(\nu)$ represents the 2D Fourier transform (FT) of the activity distribution in the object, $W(\hat{u},\nu)$ is the 2D FT of the weighting function applied during backprojection, $M(\theta,\nu)$ is the 2D FT of the measured projection data at angle θ, and $G(\nu \cdot \hat{u})$ is a 2D function of frequency that varies only in the direction of $\hat{u}$, in which it represents the 1D FT of the Gaussian TOF kernel. Expressions (8.14) and (8.15)-(8.16) can be split up into three subsequent steps: the (impulse) measurement, the weighted backprojection operation and the reconstruction filter (see table 8.1).

If an object with a Gaussian shape and standard deviation σ_{obj} is assumed, these three main parts can easily be calculated (see appendix B). The results are shown in the last row of table 8.1, where $\text{Gauss}_{\text{iD}}\{\sigma_x^2\}$ denotes an i-dimensional Gaussian with a standard deviation of σ_x, and σ_{TOF} is the standard deviation of the TOF kernel. The backprojection weighting function $\text{Gauss}_{\text{1D}}\{\sigma_{TOF}^2(1 + \frac{\sigma_{TOF}^2}{\sigma_{obj}^2})\}$ corresponds to that proposed in [128]. Reducing the object to a point source ($\sigma_{obj} = 0$), turns this weighting function into a Gaussian with infinite standard deviation, hence the optimal FBP reconstruction method for a (central) point source is regular unweighted FBP with the standard ramp filter, as was noted in [128]. For a uniform disk phantom with infinite extent ($\sigma_{obj} = \infty$), the standard deviation of the Gaussian weight becomes σ_{TOF}, meaning confidence weighted FBP then yields minimal variance, which agrees with the prediction in [110].

Table 8.1: Comparison between the expressions for linearized ML and weighted FBP reconstruction of an impulse (measured with a TOF PET system), and derivation of an analytical expression for a Gaussian object.

	reconstruction filter		weighted backprojection		impulse measurement
linearized ML	$[\boldsymbol{A^T C_Y^{-1}\ A}]^{-1}$	$\cdot$	$\boldsymbol{A^T\ C_Y^{-1}}$	$\cdot$	$\boldsymbol{A}\ e^j$
weighted FBP	$\left(\int d\theta W(\hat{u},\nu)G(\nu\cdot\hat{u})\right)^{-1}$	$\cdot$	$\int(d\theta W(\hat{u},\nu)$	$\cdot$	$I(\nu)G(\nu\cdot\hat{u}))$
expression for Gaussian object (see appendix B)	$\left[\frac{1}{\|\|\vec{x}\|\|}\text{Gauss}_{2\text{D}}\{\sigma^2_{TOF}(2+\frac{\sigma^2_{TOF}}{\sigma^2_{obj}})\}(\vec{x})\right]^{-1}$	$\otimes$	$\sum_\theta(\text{Gauss}_{1\text{D}}\{\sigma^2_{TOF}(1+\frac{\sigma^2_{TOF}}{\sigma^2_{obj}})\}(\vec{x}\cdot\hat{u})\otimes\text{Gauss}_{1\text{D}}\{\sigma^2_{TOF}\}(\vec{x}\cdot\hat{u})\cdot\delta(\vec{x}\cdot\hat{u}^\perp))$		

8.3 Simulations

8.3.1 Homogeneous disk, no attenuation

For the first experiment, two homogeneous disk phantoms with a diameter of 20 cm and 35 cm were simulated in order to mimic a 2D slice of a slim and a heavy patient, respectively. We examined the reconstruction image quality in the central pixel, obtainable with 12 different idealized 2D TOF PET tomographs with a time resolution Δt ranging from 100 to 1500 ps FWHM, and with a conventional PET system. For each system, the variance in this pixel was calculated twice: first from the approximation derived by Tomitani (equation (8.2)) and second from the Fisher information-based approximation (equation (8.8)).

The simulations produced sinograms of size 336x336(x84) (detector pixels x projection angles (x time bins[4])) for (TOF) PET, with a spatial and time sampling of 0.2 cm and 53.3 ps, respectively. The image space consisted of 336x336 square pixels of 0.2 cm. Post-smoothing ensured a resolution of 0.6 cm FWHM. Attenuation, scatter, randoms and detector resolution were not modeled.

8.3.2 Homogeneous ellipse

Since 2D transaxial slices of a patient are usually more ellipse-shaped and attenuation is not negligible, a water-filled ($\mu = 0.096$ cm^{-1}) elliptical phantom with the same area as the 35 cm diameter disk phantom was simulated. The long axis-to-short axis diameter ratio (D_a/D_b) was taken 1.56, which results in a D_a and D_b of 43.8 cm and 28.0 cm, respectively. Using equation (8.8), the variance was examined in three points: the central pixel and two pixels located along the two axis of the ellipse at a distance of 80% of $D_a/2$ and $D_b/2$ from the center, respectively (see Fig. 8.1(a)).

The same TOF and non-TOF PET systems were simulated as for the previous phantom. Also the image parameters were left unchanged. Attenuation was modeled, but scatter, randoms and detector resolution were not considered in the simulation.

8.3.3 Realistic 2D thorax phantom

To get a feeling of the gain that can be expected from imaging a real patient with a TOF PET system, a 2D thorax phantom with realistic activity distribution and attenuation values was simulated (see Fig. 8.1(b)). The phantom was obtained by thresholding the CT image of a clinical FDG-PET/CT scan of a patient with several tumors in the lungs. The mean linear attenuation coefficient was calculated in each region and scaled to fit typical values at 511 keV to build the attenuation

[4]For all simulations the time bins were equally distributed over the complete field of view, which was defined by the number of detector pixels. The time bin spacing was thus constant for TOF PET systems with different time resolutions (within the same simulation study).

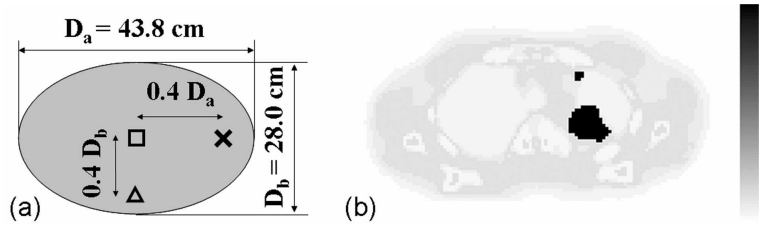

Figure 8.1: Illustration (a) of the dimensions of the water-filled ellipse and the location of the investigated points, and (b) of the realistic 2D thorax phantom (activity distribution).

map. Next, these regions were assigned a realistic uptake value, based on the corresponding values in the PET image.

The image quality of the thorax phantom was evaluated for two systems, i.e. a TOF PET system with a time resolution of 500 ps FWHM and a conventional PET system. The variance image for either PET system was obtained in two different manners. First, the variance was calculated in each pixel using equation (8.8). Next, the variance image was derived from the post-smoothed MLEM reconstruction of 300 projection data sets of the phantom corrupted with semi-random Poisson noise. The MLEM reconstructions were accelerated using ordered subsets [55]. OSEM was used to accelerate convergence, and the number of subsets was gradually reduced to ensure convergence to the maximum likelihood solution. The used iteration scheme was 15×32, 10×16, 5×8, 5×4, 3×2, 3×1 (global iterations × number of subsets), corresponding to 709 sub-iterations (updates). Dividing the variance image of the non-TOF by that of the TOF PET system will show the variance improvement (also called gain in the rest of the chapter) throughout the phantom.

The intrinsic resolution of the detector was taken 0.5 cm FWHM. The sinograms were of size 192×192(×96) for (TOF) PET, with a radial sampling of 0.3375 cm. The TOF data were sorted in 96 time bins of 45 ps to cover the whole FOV (4.32 ns = 64.8 cm). The image space had 192×192 square pixels of 0.3375 cm. The target resolution was 1.2 cm FWHM. No scatter nor randoms were modeled.

8.3.4 Effect of TOF kernel accuracy

As a last simulation study, the effect on the image quality of modeling the time resolution with an inaccurate kernel during reconstruction is investigated. Because we want to compare the results of our study (obtained with the Fisher information-based method) to those presented in [26] (based on the reconstruction of noisy projection data sets), the simulation parameters were taken as similar as possible. Since in this work the contrast is directly obtained from the impulse response, a homogeneous disk phantom of 27 cm diameter is simulated instead of a hot-spheres phantom of the same size. The mean and the variance on the mean in a 1.3 cm diameter ROI at 7 cm from the center were then calculated from equations (8.10) and

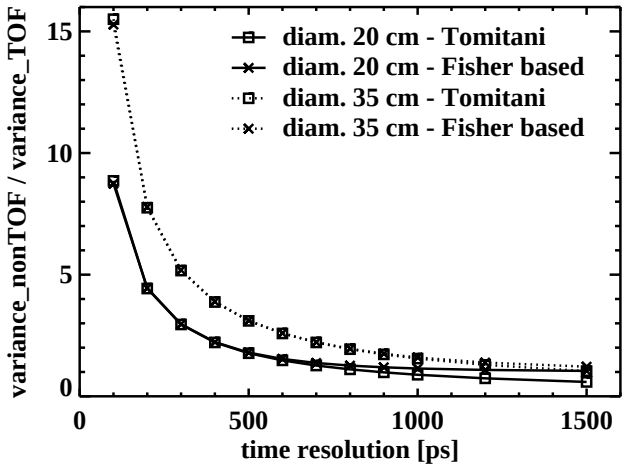

Figure 8.2: Simulation 1: Variance improvement due to the use of TOF information plotted versus the time resolution of the TOF PET systems. The image quality of the central pixel of two uniform disk phantoms with a diameter of 20 (solid lines) and 35 cm (dotted lines), respectively, was investigated with two methods: (squares) Tomitani's method (equation (8.2)), and (crosses) the Fisher information-based method (equation (8.8)).

(8.11). The CNR can simply be derived from these two values (see equation (8.9)).

The time resolution of the simulated TOF PET scanner was modeled as a Gaussian with a FWHM of 300 ps. The image quality obtained with a variety of reconstruction TOF kernel resolutions, i.e. 150, 225, 300, 375, 450, and 600 ps FWHM, was evaluated using (8.12) and (8.13). The attenuation of water was modeled, but scatter, randoms and detector resolution were not considered. The dimensions of the sinogram and of the image space were 336x336x48 and 336x336, respectively. The spatial sampling was 0.2 cm, the time sampling was 93.3 ps, and the pixel size was taken 0.2x0.2 cm^2. A target resolution of 0.6 cm FWHM was imposed.

8.4 Results

8.4.1 Homogeneous disk, no attenuation

In Fig. 8.2, the variance improvement in the central pixel of both the 20 cm (solid lines) and the 35 cm (dotted lines) diameter uniform disk source obtained due to the use of TOF information is plotted with respect to the time resolution Δt of the TOF PET systems. Two prediction methods are compared: (1) Tomitani's approximation (results depicted with squares) and (2) the Fisher information-based method (results plotted as crosses). The predictions of the two methods closely

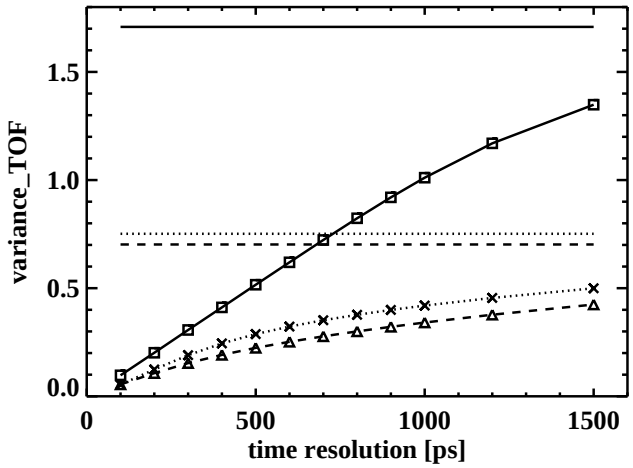

Figure 8.3: Simulation 2: Variance in 3 points of a homogeneous water-filled ellipse is plotted with respect to the time resolution of the tested systems. The horizontal lines show the results for the conventional PET system. The long and short axis diameter is 43.8 cm and 28.0 cm, respectively. The central pixel (squares, solid lines), the eccentric pixel on the long axis (crosses, dotted lines) and on the short axis (triangles, dashed lines) were investigated.

match. The accuracy is better for good time resolutions and for a large diameter. The approximation of Tomitani predicts that for smaller phantoms the image quality is better using a conventional PET system than using a TOF PET system with bad time resolution. This is because the assumption $D >> \Delta x$ that was made to derive equation (8.2) is no longer valid.

8.4.2 Homogeneous ellipse

Fig. 8.3 plots the variance for the three pixels in the water-filled ellipse versus the time resolution of the TOF PET systems. The horizontal lines depict the variance obtained with the conventional PET system. For all PET systems the variance in the central pixel (squares, solid lines) is clearly higher than the variance in the eccentric pixels (crosses, dotted lines and triangles, dashed lines). The variance in the eccentric pixel on the short axis (triangles, dashed lines) is slightly lower than that on the long axis (crosses, dotted line).

The evolution of the improvement in variance in the three points is denoted in table 8.2. The gain was shown for first generation, current generation and future generation TOF PET systems with a time resolution of 1500, 500 and 100 ps, respectively. The eccentric pixels start to benefit from the TOF information already at modest time resolutions (factors 1.50 and 1.65 for eccentric points vs. a factor 1.27 for the central one at Δt =1500 ps), but the variance decreases faster with

Table 8.2: Variance improvement in three points of a water-filled ellipse.

Δt	100 ps	500 ps	1500 ps
Central point	17.58	3.31	1.27
Point at $0.4D_a$	13.92	2.61	1.50
Point at $0.4D_b$	12.75	3.13	1.65

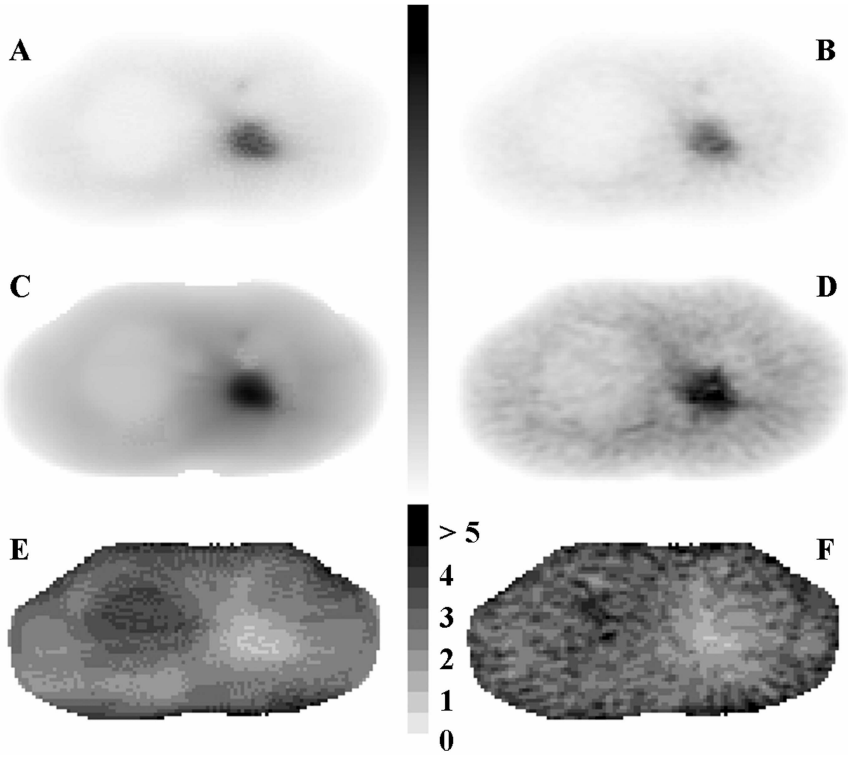

Figure 8.4: Simulation 3: Evaluation of the effect of the use of TOF PET for a realistic 2D thorax phantom. Variance images expected for a TOF PET system with a time resolution of 500 ps FWHM (top row) and for a conventional PET system (middle row) were obtained with the Fisher information-based method (first column) as well as with the reconstruction of 300 noisy projection data sets (second column). From these variance images the corresponding distribution of the variance improvement was calculated (bottom row).

improved time resolution in the central pixel (gain close to 18 for the central pixel vs. 13-14 for the eccentric ones).

8.4.3 Realistic 2D thorax phantom

The calculated variance and gain images of the thorax phantom (see Fig. 8.1(b)) are shown in Fig. 8.4. The left column contains the variance and gain images predicted with the Fisher information-based method, in the right column the corresponding images obtained from the reconstruction of 300 noisy projection data sets are shown. The variance images expected from the TOF PET system with $\Delta t = 500$ ps FWHM are shown on the first row. The variance images predicted for the conventional PET system can be seen on the middle row. The last row illustrates the distribution of the variance improvement over the thorax phantom, calculated with both methods.

From the first two rows in Fig. 8.4 it is clear that the variance reduces when TOF information is available during reconstruction. As Δt decreases the variance images look more and more similar to the thorax image (see Fig. 8.1(b)), because imaging with excellent time resolution results in an image of the phantom corrupted by Poisson noise. From the gain images (see Fig. 8.4E and F), we can conclude that the variance reduction is minor in the high count regions and up to a factor 4-5 in the large low active lung. The predictive value of the approximate method is very good.

8.4.4 Effect of TOF kernel accuracy

In Fig. 8.5, the mean (top), the variance on the mean (center) and the CNR of the ROI (bottom) are plotted with respect to the reconstruction TOF kernel. The left column shows the results for the standard case, where $\boldsymbol{P}^j$ was the Gaussian post-smooth filter that imposes the 6 mm FWHM target resolution. As can be seen, both the mean and the variance increase with increasing kernel width. When the kernel was taken too narrow (< 300 ps), the mean decreased faster than the variance. On the contrary, when the kernel was taken too wide (> 300 ps), the mean increased slower than the variance. As a result, the best contrast versus variance trade-off was obtained using the correct kernel (300 ps FWHM).

One should note, however, that - due to the fixed target resolution - the mean value in the ROI was expected to be constant. The fact that it is not, can be explained by investigating the shape of the post-smoothed impulse response. For the narrowest and widest kernel, profiles of these are drawn as a dashed line in the left and right top graph of Fig. 8.6, respectively. The solid curve represents the ideal ROI after post-smoothing with a Gaussian filter with 6 mm FWHM (i.e. the target resolution). From the top images a clear under- and overshoot can be observed for the narrow and wide kernel, respectively. Correspondingly, sidelobes and undershoots outside the FWHM range are observed in the bottom row images, which are a zoomed-in version of the top ones.

To force the mean value in the ROI to be constant, $\boldsymbol{P}^j$ should ensure that not only the width but also the shape of the post-filtered impulse response agrees with the target Gaussian filter. The results obtained with this optimal post-filter are shown on the right column of Fig. 8.5. Again the mean, the variance and the CNR of the ROI were plotted versus the reconstruction TOF kernel. Obviously,

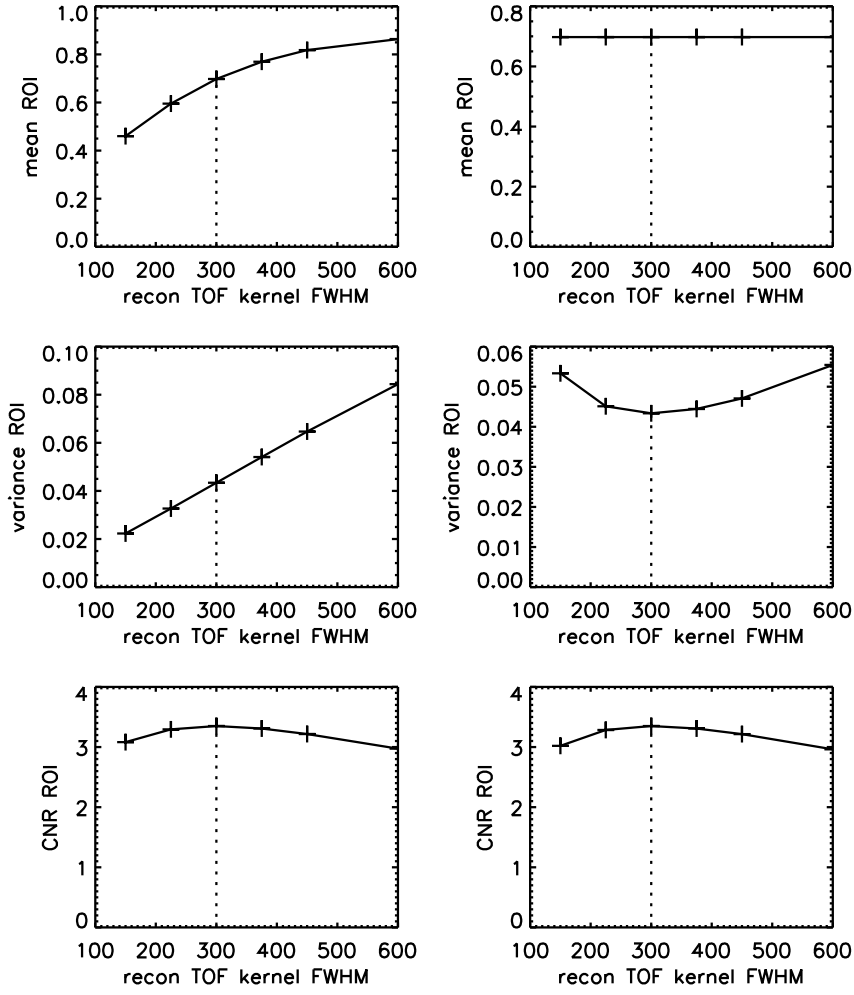

Figure 8.5: Simulation 4: Mean, variance on the mean, and CNR of the eccentric ROI in the 27 cm diameter homogeneous sphere (described in section 8.3.4) plotted with respect to the TOF kernel used during reconstruction. The real TOF kernel had a resolution of 300 ps. Left: Gaussian post-filter. Right: optimal post-filter.

the mean of the ROI is now fixed and equal to the value obtained with the 300 ps FWHM reconstruction kernel and Gaussian post-smoothing (see top left graph of the same figure). All effects of the reconstruction kernel accuracy are now contained by the variance, or equivalently, by the CNR. A very similar CNR curve, with the same optimum, was found using the optimal post-filter instead of the Gaussian post-smooth filter.

8.5 Discussion

Tomitani's approximations (8.1) and (8.2) were most accurate for central pixels in objects that are much larger than the time resolution. This observation was expected, because these approximations were derived for the center of an infinitely large homogeneous disk source.

As TOF information reduces the randoms fraction significantly, even larger gains might be within reach. The effect of randoms on the image quality of TOF PET was discussed in [23] based on experimental data, and an extended version of equation (8.2) including the influence of randoms was proposed. In the Fisher information-based method simple models for randoms, scatter, etc. can easily be included to study their effect on the image quality. The method is also readily extensible to 3D TOF PET, where its relevance will increase, since repeated reconstructions become very time-consuming.

For conventional PET it is known that the variance is lower in an eccentric pixel than in a central one, because the mean intersection length between the object and the projection lines through the pixel is shorter. Therefore, the surrounding activity contributes less to these projections and thereby also to the noise in the eccentric pixel. This effect decreases with improving time resolution of a TOF PET system, because the region of the object that influences the reconstruction of a pixel is determined by the extent of the TOF kernel and no longer only by the object boundaries. As a result, the relative variance gain achieved by the TOF information is lower for eccentric pixels. However, attenuation is independent of the TOF resolution and this effect still results in a much lower variance in eccentric pixels.

In Fig. 8.4E and F the variance in the tumor is seen to decrease slower than the variance in the rest of the thorax. This can be explained as follows. In conventional PET, the measured activity is backprojected along the complete line-of-response. The activity fraction deposited in the tumor, but originating from the surrounding tissue is relatively lower than the contribution of tumor activity to the activity in other tissues. In TOF PET, this crosstalk decreases due to the finite time resolution, which results in a reduced variance. In the tumor, however, this crosstalk was already low, hence the benefit is lower. For the same reason, the lung at the left side of the image gains more than the lung at the right side. Indeed, the former is positioned much farther from the hot tumors than the latter, and will therefore benefit already at 500 ps time resolution.

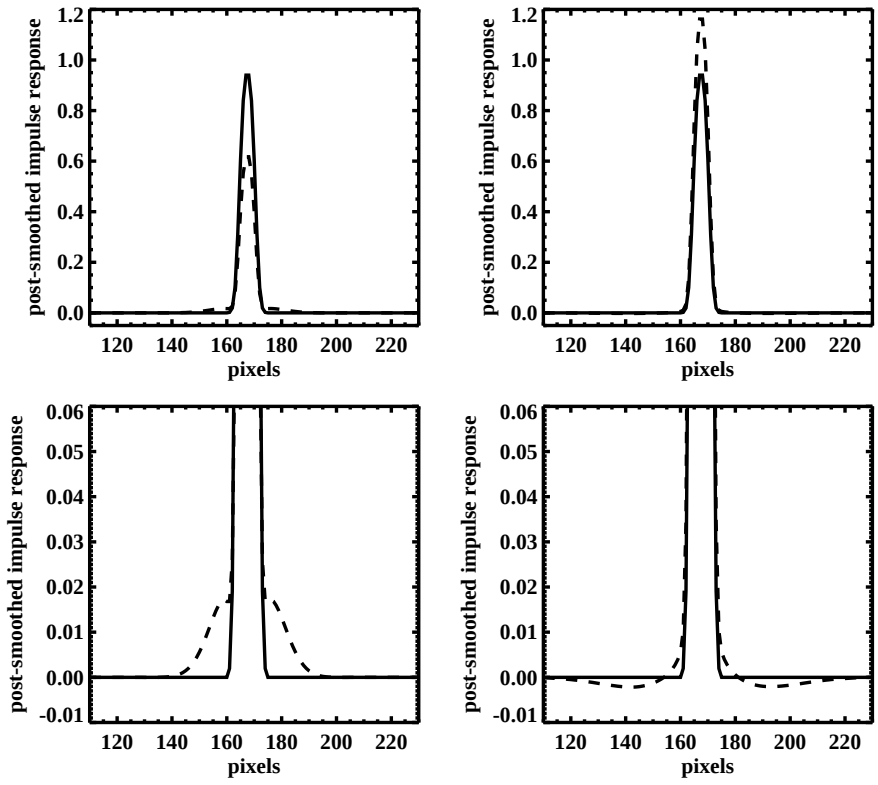

Figure 8.6: Simulation 4: Illustration of the artifacts in the post-smoothed impulse response caused by using an inaccurate TOF kernel during reconstruction. The solid lines show the ideal ROI post-smoothed with a Gaussian with a FWHM of 6 mm (target resolution). The dashed lines plot the post-smoothed impulse response obtained with a too narrow kernel (left) and a too wide kernel (right), respectively. Top row: full range. Bottom row: zoomed-in on the bottom part of the impulse response.

The analytical approximations, based on the calculation of the Fisher information matrix, predict accurately the image quality of post-filtered MLEM reconstructions. Both equations (8.7) and (8.8) and equations (8.12) and (8.13) were applied to estimate the image quality in different points in various phantoms, imaged with (TOF) PET systems, and validated with repeated simulations (results only shown for the thorax phantom, Fig. 8.4). Discrepancies between the simulations and the analytical approximations were only found in regions of very low activity, where the Fisher information-based method underestimated the CNR that could be attained by post-filtered MLEM. In these low activity regions, the non-negativity constraint in the MLEM algorithm contributes significantly to the image quality, but this constraint is not represented in the linearized model of the reconstruction used by the

analytical approximations.

In [123] some results were slightly different from those presented in this chapter. The differences in the outcome of the Fisher information-based method are mainly due to more accurately modeling the Gaussians of the TOF kernels and of the post-smooth filters. The tails of the Gaussians were only cut-off at three instead of two standard deviations distance from the mean. In both cases, the values were normalized such that the total equals one, resulting in a decreased maximum value of the Gaussian. Thanks to this more accurate modeling, the curves in Fig. 8.2 better match those obtained with Tomitani's approximation.

Also the variance images of the thorax were slightly different in [123], especially the one based on reconstructions of noisy non-TOF PET data (see Fig. 8.4D, underestimation of the variance in the lung in [123]). In this chapter, the reconstructions were run for an equivalent of 709 MLEM iterations instead of 214 in [123], because the reconstructions were not yet converged. Since the reconstruction of non-TOF PET data converges slower than that of TOF PET data, this change had more effect on Fig. 8.4D than on Fig. 8.4B. As the approximate method predicts the variance of MLEM post-smoothed after convergence, the agreement between the analytically calculated variance images and those based on reconstructions improved, and the gain is accurately predicted all over the phantom.

The efficiency of the Fisher information-based method allows rapid evaluation of the effect of different parameters (such as the object shape, the attenuation, the time resolution and the randoms fraction) on the reconstruction image quality of a few individual pixels or ROIs. To obtain complete variance images faster methods are available [136]. To speed-up the calculation of the variance images, the pixel size was increased from 0.2 cm to 0.3375 cm, which is still clinically relevant. Correspondingly, the target resolution was increased, because a minimal amount of post-smoothing is required for stability and accuracy of the approximations.

A mismatch between the actual TOF kernel and the kernel assumed for reconstruction could easily be incorporated in the approximations, as shown by equations (8.12) and (8.13). The use of these equations is subject to some restrictions, though. In cases where the FWHM of the reconstruction TOF kernel is larger than the real time resolution, problems might occur when investigating pixels or small ROIs near the edge of the object. The projection of the impulse, which is filtered with the reconstruction TOF kernel, has to be divided by the projection of the phantom (factor $\boldsymbol{C_Y^{-1}}$ in equations (8.12) and (8.13)), which is filtered with the real, narrower TOF kernel. Consequently, the tails of the TOF kernel then might be divided by a very small number (in order not to divide by zero), because the activity of the point is spread further than the activity of the phantom. This results first in asymmetric undershoot artifacts, as illustrated in the right image of Fig. 8.7, which shows the (zoomed-in) profile in the column direction through the center of the predicted post-smoothed impulse response, obtained with the 600 ps FWHM TOF reconstruction kernel (the real kernel was 300 ps). A similar asymmetry is apparent in the impulse response calculated with post-smoothed iterative reconstruction, but the prediction of the undershoots is not accurate. For more eccentric pixels or larger resolution differences, the approximations become increasingly inaccurate or even

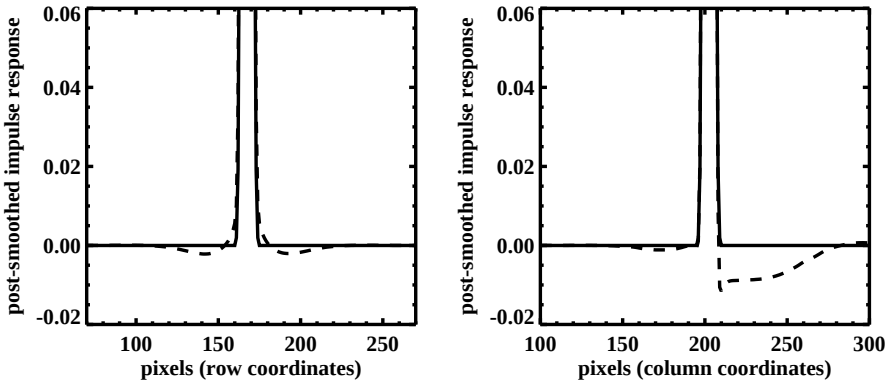

Figure 8.7: Illustration of asymmetric undershoot artifacts. The left graph is identical to the bottom right plot of Fig. 8.6, except for the x-range. It represents the (zoomed-in) profile in the row direction through the center of the post-smoothed impulse response of the eccentric ROI. The right graph shows the profile in the column direction.

instable. Careful use of these approximations is therefore recommended.

From the curves in the top left graph of Fig. 8.5, we found that the mean value in the ROI, and thus also the contrast, decreases if the reconstruction kernel is chosen too narrow, and increases when the kernel is taken too wide. This effect and its cause are very similar to what is observed when a reconstruction algorithm incorporates a model of the finite resolution of the detectors, that either under- or overestimates the width of the corresponding detector point spread function [95].

The observations in Fig. 8.5 (top left) are in agreement with the findings in [26]. However, from the same experiment we could also conclude that the CNR is optimal when using the correct kernel during reconstruction, whereas in [26] the increased contrast seemed to overcompensate the increase in noise. The main differences between the two methods are the way the figure of merit (FOM) for the noise is calculated, and the reconstruction method used/approximated. In [26] the noise was determined from the pixel-to-pixel percent standard deviation (%SD) in background ROIs, averaged over 60 background ROIs. The variance (or standard deviation) on the mean value of the ROI is considered to be a more accurate and more representative noise FOM. In [26] the image quality was evaluated after different numbers of iterations, but no matched resolution was assured, which makes it very difficult to compare image quality. Also convergence speed might differ for different TOF kernels. In this work, we have post-smoothed the MLEM reconstructions, run until convergence, to overcome these difficulties.

The CNR curves in the bottom row of Fig. 8.5 indicate that small deviations from the real kernel, and thus also from the effective time resolution, only have a minor effect on the image quality as measured by the CNR. However, these inaccuracies also induce artifacts, which may affect for instance the quantitative accuracy.

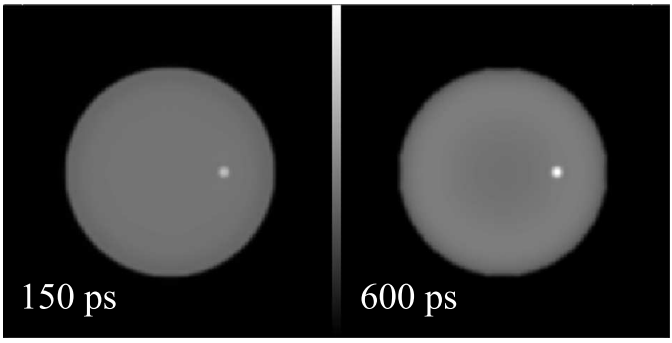

Figure 8.8: Homogeneous 27 cm diameter disk with an impulse in a 1.3 cm diameter ROI at 7 cm from the center, after reconstruction with a TOF kernel with a FWHM of (left) 150 ps, (right) 600 ps. The real TOF kernel was 300 ps.

These artifacts arise because the measured activity needs to be explained by a different model than the one of the measurement. For kernels that are too narrow, some of the original activity is deposited in side lobes (see Fig. 8.6, left column). This is necessary to explain the measured activity that cannot be accounted for by the narrow reconstruction kernel. For kernels that are too wide (see Fig. 8.6), undershoots are needed to cancel the activity that is projected on the detectors at a large distance from the exact projection location, but that was not measured, since the real TOF kernel is narrower. In both cases (too narrow and too wide) not only edge effects are to be expected, but also the quantification will be incorrect. This is also illustrated in Fig. 8.8, where two reconstruction images of the same noiseless projection data set are shown. The software phantom described in section 8.3.4 was measured with a TOF PET system with a time resolution of 300 ps FWHM. The activity in the eccentric ROI was doubled compared to the background activity. The post-smoothed OSEM reconstruction was run with 709 updates (equivalent to 709 MLEM iterations) and a TOF kernel with a FWHM of 150 and 600 ps was used to obtain the left and right image in Fig. 8.8, respectively. In Fig. 8.9 the vertical and horizontal profiles through the center of the ROI are plotted for the too narrow (dotted line), correct (solid line) and too wide (dashed line) TOF kernel. The same artifacts as found in Fig. 8.6 can be recognized.

We can also conclude that the artifacts due to the use of a too narrow kernel are much more localized than the ones caused by a too wide kernel. A conservative choice of the width is therefore preferable. Likewise, in [95] the artifacts due to a convolution kernel over-modeling the resolution were more severe then when the model was too modest. In [115] similar artifacts were observed after reconstruction of simulated TOF PET data with mismatched TOF kernels. The importance of these artifacts in reconstruction images of measured data is still to be verified.

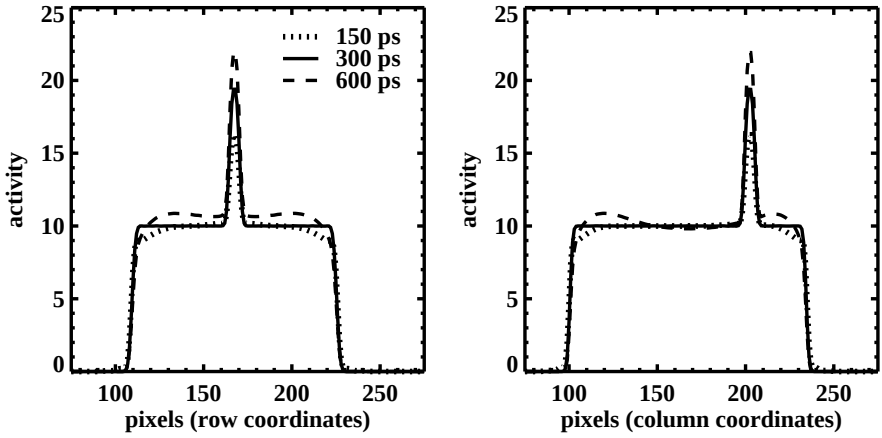

Figure 8.9: The vertical (left) and horizontal profiles (right) through the center of the ROI of the reconstructed images of Fig. 8.8 are plotted as a dotted line (150 ps), solid line (300 ps) and dashed line (600 ps).

8.6 Conclusion

Analytical Fisher information-based approximations were used to evaluate the image quality of simple and more realistic phantoms imaged with 2D (TOF) PET systems. The linearized local impulse response, the covariance matrix and the contrast-to-noise ratio in individual pixels and small regions of interest were calculated to compare TOF PET systems with different time resolutions with each other and with a conventional PET system. The approximations were validated with the post-filtered MLEM reconstruction of hundreds of noisy projection data sets. TOF information was found to improve the image quality in all pixels, although less benefit was seen in eccentric and hot regions, since they already performed well in conventional PET. Using a too narrow or too wide TOF kernel for reconstruction tends to decrease the image quality and to cause artifacts in the reconstructed image.

Chapter 9

General conclusion

9.1 Main contributions

The most important contributions of this work can be subdivided into four main topics. The scientifically most relevant one is probably the derivation, validation and application of an efficient method for tomographic image quality evaluation. We focused on single and multipinhole SPECT, but this method can be applied to any tomographic emission or transmission system, as was illustrated for time-of-flight (TOF) PET. This topic is elaborated in more detail in section 9.1.1. The developed method was subsequently used for multipinhole SPECT design optimization for one specific application, namely focused mouse imaging. Besides determining the optimal design parameters, multiple solutions to reduce multiplexing artifacts were presented, as discussed in section 9.1.2. In addition, the image quality can be improved by better modeling the acquisition during reconstruction in all possible ways. An overview of the most important enhancements with respect to the status at the beginning of this PhD [10] is given in section 9.1.3. Last but not least, the impact of this work on the application of pinhole SPECT in preclinical studies is discussed in section 9.1.4.

9.1.1 Image quality evaluation

To compare various tomographic systems, we evaluated the quality of the reconstructed images they yield quantitatively. For that purpose, we impose a fixed spatial resolution; hence the best system is the one providing the lowest variance. As this is object-dependent, a typical object for the investigated application domain needs to be chosen. To enable a thorough investigation of many different single and multipinhole SPECT designs, an accurate and efficient image quality evaluation method was required. In this PhD thesis, analytical approximations predicting the linearized local impulse response (LLIR) and the covariance matrix of a certain image voxel were derived from those proposed for maximum a poste-

riori (MAP) reconstruction image quality in [37, 79, 93, 94]. The LLIR provides, however, information about both the resolution and the noise in that voxel. As one can trade in resolution to decrease the noise, and vice versa, one of these two should be fixed to allow e.g. comparison between two pinhole collimator designs. Therefore, the approximations were adapted to predict the image quality for a predefined target resolution. However, fixing the spatial resolution is quite complex and hard to automate for MAP reconstruction, whereas it is straightforward for post-smoothed maximum likelihood expectation maximization (MLEM) reconstruction. For that reason, approximations were derived for predicting the image quality of post-smoothed MLEM with an imposed target resolution, which are equivalent to those for MAP with a uniform resolution (see chapter 4). After successful validation of this method for various single and multipinhole collimator designs used for imaging two distinct software phantoms, the method was applied to gain insight in the influence of the multiple collimator design parameters on the image quality.

A second, very interesting application of this method was the investigation of the effect of overlap in the projection images on the reconstruction image quality (see chapter 5). The usefulness of the extra sensitivity obtained due to overlap is an often debated topic in the pinhole SPECT research field. Based on the evaluation of many multipinhole collimator designs with and without overlap, it could be concluded that, once the complete detector area has been used, the extra sensitivity due to overlap can only compensate for the increased ambiguity of the measurement, but cannot improve the image quality. Furthermore, removing the overlap, e.g. by inserting septa, improves the contrast-to-noise ratio (CNR), especially in the central field of view. This is at the cost of the CNR of some voxels at the edges. The uncertainty about the origin of the detected photons in the overlap zones of the projection images are also known to cause multiplexing artifacts. Because these artifacts as well as truncation artifacts are not well identified by the CNR, reconstruction images of noise-free projection data were also investigated to study the image quality.

To illustrate that the derived approximations are generally applicable in SPECT and PET applications, they were used to study another currently extensively investigated research topic, namely the quantification of the obtainable gain in image quality due to the use of time-of-flight information during PET reconstruction (see chapter 8). This was calculated by dividing the predicted variance of a conventional PET camera by that of a TOF PET system with a specified time resolution. These results were compared to the gain in variance, expressed by an analytical formula which is only valid for the central pixel in a large, homogeneous disk phantom [110]. A very nice correspondence could be noticed between the results of the two methods, confirming that indeed the gain in such central pixel increases linearly with the size of the disk and is inversely proportional to the time resolution of the TOF PET camera. It was also shown that the approximate method could be used to derive the weighting function for filtered backprojection reconstruction of TOF PET data, proposed by Watson (see appendix B). Next, the image quality was studied in many image pixels of simple as well as more realistic software phantoms for various PET systems only differing in time resolution. TOF information was found to improve

the image quality in all pixels, but less pronounced in eccentric and hot regions, because there the reconstruction image quality was already very high for conventional PET. The influence of the TOF kernel accuracy on the CNR was also investigated with the approximate method, because the time resolution of a TOF PET camera is not always known precisely. This study indicated that using a too narrow or too wide kernel reduces the CNR and induces artifacts in the reconstruction image.

9.1.2 Multipinhole SPECT design optimization and artifact reduction

Supported by the knowledge gathered from the image quality evaluation studies of various pinhole SPECT systems with and without overlap (see chapters 4 and 5), the approximations for the LLIR and covariance in a voxel were used to optimize the pinhole SPECT collimator design for one specific application, namely focused mouse imaging (see chapter 6). From a very large group of tested pinhole designs, the design providing the best overall CNR in a restricted part of a simplistic mouse phantom was selected. For the ease of designing and manufacturing, some overlap was allowed in the projection images. Therefore, multiplexing artifacts were expected. To reduce their influence on the reconstruction image quality, the pinhole apertures were slightly displaced to form an irregular pattern. A second pinhole plate, for dual head imaging, was designed based on the first one to further decrease the multiplexing artifacts. After testing this set of multipinhole designs with simulations, the plates were manufactured. Next, its performance was further evaluated with phantom studies and mouse experiments. The residual multiplexing artifacts can be strongly reduced by defining the body support of the imaged subject from a fast reconstruction and using it during the final reconstruction as the volume responsible for all measured activity.

9.1.3 Improvements in pinhole SPECT reconstruction

An accurate method for analytically calculating the pinhole sensitivity was presented in section 3.1.2. The sensitivity can be factorized in a distance-dependent and a distance-independent component. The latter is computed with a ray-driven method, taking into account the intersection length of the projection rays with the collimator material. This method has been compared to Monte Carlo simulations and flood source measurements in collaboration with the university of Ghent [103]. All three approaches resulted in very similar sensitivity images. The deviations can be explained by manufacturing errors or inaccuracies and by the lack of accurate modeling of the detector in the analytical method. The analytical method is especially useful for computer simulations of the forward and backward projection through a pinhole collimator. For reconstructing measured data, however, the use of measured sensitivities is the best choice, provided that they are appropriately processed.

To reduce the effect of scatter in the reconstruction image, a dual and triple energy window (DEW and TEW) scatter correction method have been implemented

in the pinhole SPECT reconstruction software. All current pinhole SPECT acquisitions of laboratory animals injected with either a ^{99m}Tc- or ^{123}I-labeled tracer are routinely performed with a DEW and TEW setting, respectively. From these measurements the amount of scattered photons registered in the photopeak window can be accurately estimated (see section 3.2.1).

Furthermore, correction methods for attenuation, decay and crosstalk between ^{99m}Tc and ^{123}I have been implemented and are now routinely used for the reconstruction of the small animal scans (see sections 3.2.2-3.2.4). These corrections in combination with the measured sensitivity images and a correction factor obtained from the reconstruction of a measured homogeneously filled phantom with accurately known activity concentration, yield quantitatively correct reconstruction images, which express the activity distribution in Bq/mm^3.

The software for multipinhole calibration was improved by automating the time-consuming data processing step. In addition, a refined calibration method, similar to the one developed at the university of Brussels [29], was implemented. From a phantom measurement it was confirmed that its application yields enhanced spatial resolution in the reconstruction images. Especially the data collected with the second head of our pinhole SPECT system benefit from the improved camera modeling (see chapter 6). Furthermore, a theoretical study of the geometrical acquisition parameters indicated that only two point sources are required to uniquely specify the geometry of a multipinhole SPECT, compared to three point sources for single pinhole SPECT [11] (see appendix A). The distance between these point sources does not need to be known, hence making it easier to combine a phantom or animal scan with a calibration scan in one acquisition. This is in agreement with the findings in [126].

9.1.4 Applications

The many small animal pinhole SPECT scans, that were planned in the scope of preclinical experiments, have been the driving force for the majority of the software and hardware improvements described in this work. Almost every new experiment protocol induced an update of the software, ranging from handling scatter, over correcting for crosstalk, to the rigid or non-rigid registration of multimodality images. At the hardware side, first the available pinhole collimator was thickened to reduce the detection of scattered photons. This was especially relevant for the ^{123}I measurements, suffering from the high energy photopeaks. Based on Monte Carlo simulations (university of Ghent), the new thickness was determined, hence ensuring that the fraction of detected scattered photons is significantly reduced. Next, a second collimator was purchased to double the sensitivity of the pinhole SPECT camera. It can also be used to halve the acquisition time or the dose of radioactivity to be administered. In the mean while, thicker single pinhole plates were manufactured and a set of optimized multipinhole plates was designed and ordered. In addition, a rescaled calibration phantom as well as a set of fiducial markers for CT-SPECT registration were produced for rabbit scans. All of these changes have led to a continuous increase in image quality, which is responsible for the growing

popularity of the pinhole SPECT camera in our department.

9.2 Suggestions for future work

In this section, suggestions are made for future applications of the developed image quality evaluation method (see section 9.2.1), for multipinhole SPECT design optimization and artifact reduction (see section 9.2.2), and for possible improvements in the pinhole SPECT reconstruction (see section 9.2.3). The latter can be induced by improved camera modeling, the use of a priori information, or changes in the imaging protocol.

9.2.1 Image quality evaluation

Many different types of dedicated small animal SPECT systems have been developed over the past decade. Examples are the LinoView^{TM} miniSPECT of Linoview Systems [124], the X-SPECT^{TM} and FLEX Triumph^{TM} of Gamma Medica-Ideas, the HiSPECT and NanoSPECT/CT of Bioscan [88, 97] and the various U-SPECT systems of MILabs [8, 9, 114]. The image quality evaluation method described in this work could be used to compare these systems for specific applications, provided that a detailed system description is available. Currently, this method is also being used in our lab to evaluate the performance of rotating slat collimation against that of parallel hole collimation for planar and 3D SPECT imaging [137]. Of course, many other applications could be thought of.

In chapter 8, the image quality evaluation method was applied to a simple model of 2D TOF PET. Scatter and random detections were not taken into consideration, though, despite their quite high share in conventionally measured PET data. With experimental data, it has however been shown for example, that the use of time-of-flight information can significantly reduce the amount of measured randoms [23], and therefore their degrading influence on the reconstruction image quality. Models for the scatter and randoms could be included in the approximations for the LLIR and the covariance matrix to study their effect on the image quality. The approximations can also easily be extended to 3D TOF PET, where the efficiency advantage compared to repeated reconstructions is much higher.

As illustrated by the above applications, the image quality evaluation method developed in this work is a very interesting tool. However, as for every method, it also has some drawbacks. One of these is the fact that multiplexing and truncation artifacts are not translated into a lower CNR. This is not due to an inaccuracy of the approximations, though, it is intrinsic to the CNR. In contrast to the CNR, the covariance image is expected to contain information about these artifacts, but this topic requires further investigation. Another disadvantage is that the linearization of the approximations does not allow to include the non-negativity constraint, which bounds the MLEM and MAP reconstructions. Therefore, they become less accurate for the image quality prediction of voxels in low-count regions. It is still an open question how this non-negativity constraint can be modeled.

The approximation for predicting the covariance matrix can also be useful in the context of numerical observers, often applied to compare imaging systems or reconstruction algorithms for their performance on a specific task [4,7]. Indeed, the ideal (prewhitening) observer requires the computation of the inverse covariance matrix. The efficient approximation based on the Fisher information matrix yields a significant time gain and has been successfully applied in the domain of numerical observers before [14, 38, 85, 92, 133]. The extension to predict the covariance matrix of post-smoothed MLEM with an imposed target resolution might facilitate the comparison of different systems at equal resolution. In addition, it was found that regularization is usually inessential, meaning that for most observers an unregularized reconstruction method exists that achieves the ideal SNR for the specified detection task [38]. Furthermore, the approximations can be applied to verify whether the ranking of the image quality or detectability at a specific target resolution, yielded by different imaging systems or reconstruction algorithms, varies with the size of the region of interest or changes if the resolution is degraded or improved by post-smoothing more or less, respectively.

9.2.2 Multipinhole SPECT design optimization and artifact reduction

In this work, a pinhole collimator design was optimized for focused mouse imaging (see chapter 6). Some overlap between the projections through the different apertures was allowed to facilitate the designing and the manufacturing. However, the study described in chapter 5 indicated that overlap is not beneficial, and that overlap removal improves the image quality. Therefore, it is probable that a better design can be obtained by avoiding or removing all overlap. Additional advantages of such an overlap-free design are that the measured activity can be reconstructed without multiplexing artifacts by definition, and that the reconstruction will converge faster. The question remains, however, how overlap can best be avoided or removed, and how the pinholes are best positioned. The design process will thus need to be repeated from scratch, except for the application specification. In addition, as many rat heart scans are planned, it might be interesting to have an optimized pinhole collimator for focused rat imaging as well.

9.2.3 Improvements in pinhole SPECT reconstruction

Improved camera modeling

Theoretical study revealed that the geometrical acquisition parameters of a multipinhole SPECT sytem can be uniquely determined from the measurement of only two point sources (see appendix A for details). Although nice results were reported in [126], our preliminary calibration tests, based on measured data, indicated that the accuracy of the method is lower when the distance between the point sources is not used. However, providing knowledge about the interaperture distances seemed

to improve the accuracy of the parameter estimation. This method awaits further validation before it can be used for phantom and small animal studies.

The currently used projection and backprojection methods, namely the 7-ray and the precalculation method (see section 3.1.3), ignore the fraction of rays traveling through the edges of the pinhole apertures, called edge penetration. This means that the diameter of the penetrating rays of photons is slightly underestimated, as is the blurring effect of the pinhole aperture. The effect of edge penetration becomes increasingly important with decreasing aperture diameter. For the 7-ray method, edge penetration can easily be modeled by positioning the outer projection rays closer to the edge of the aperture. The location can be calculated based on expressions for the effective diameter. This has already been implemented, but still requires validation. For the precalculation method, currently the intersecting ellipses of each cone, defined by a detector pixel and the pinhole aperture, with the voxel planes parallel to the detector are calculated and all voxels inside these ellipses are stored by their index and weight. To model the edge penetration, the voxels around these ellipses could be assigned a weight decreasing with the normalized distance to the center of the ellipse, i.e. the initial edge voxels are at a distance equal to one. This is, however, only one possible solution, and further research is required to develop an accurate and time and storage efficient method.

Furthermore, the precalculation projection and backprojection method has currently only been implemented for a perfect circular orbit camera motion. Thus, it cannot yet handle parameters like tilt and twist, outputs from the calibration method. Therefore, this projection method has so far only been used for simulation studies, where speed is often a very important factor. The reconstructions of the phantom and small animal pinhole SPECT measurements were all performed with the very slow 7-ray method, but as most reconstructions are run overnight, the discomfort is limited. Nevertheless, it would be useful to extend the precalculation method, so that it can be applied to accelerate the reconstructions of the SPECT measurements as well. Indeed, in case of attenuation correction, or when using a body contour, multiple reconstructions need to be calculated subsequently, hence speed-up would be well appreciated. If one also wants to apply the refined calibration parameters, which are slightly different for every projection angle, a creative solution should be found, because currently only the projection information for one view is stored. The most straightforward method would be to displace (and resample) the reconstruction image with respect to the pinhole collimator, according to the small camera movements.

The use of a priori information

The newly designed set of multipinhole plates provide high quality reconstruction images. However, these images might suffer from multiplexing and truncation artifacts, as mentioned earlier. A simple solution to diminish these artifacts and to enhance the image quality was proposed in this work (see section 6.4.1), and consisted of using the body support during image reconstruction. Currently, the body support is defined either from a fast initial image reconstruction or from a registered

CT image. This involves many subsequent manual and semi-automated steps. For the processing of a pinhole SPECT reconstructed image, often first a restrictive volume is drawn, followed by thresholding, or a region is grown from a manually selected point. In some cases volume filling techniques have to be applied. To ensure that the body support is not chosen too small, the obtained volume is smoothed. The CT image can typically easily be thresholded. The difficult part is usually the registration of the CT with the pinhole SPECT image, as they represent very different distributions. Also this body support is best smoothed a little. It would be interesting to (semi-)automate this body support definition. For some mouse and rat studies fiducial markers will be used for registration in the near future, as was done for the rabbit experiments (see section 7.3). It might be useful to apply these markers to all pinhole SPECT scans after which a CT scan will be performed, even though it is not always initially meant for combined usage with the pinhole SPECT image.

In our small animal experiments, anatomical information is often available from CT or MRI images for various reasons, e.g. for tumor localization or for attenuation correction. Using this information in an appropriate way during reconstruction, for example as a prior in maximum a posteriori (MAP) reconstruction, can increase the image quality [15, 22, 47, 69, 85]. However, most of these methods require an accurate registration and segmentation of the anatomical image. This is also the case for the anatomy-based MAP algorithm available in our lab [2], which was successfully applied to a micro-PET and a pinhole SPECT rat brain image. For this purpose, an MRI rat brain atlas image had to be manually segmented [20]. As this is time-consuming and error-prone, other techniques were recently suggested, for which image segmentation is not required [16, 84, 102]. These methods have the potential to further improve the pinhole SPECT image quality.

Improving the imaging protocol

As mentioned above, the reconstructed images can express the activity distribution in Bq/mm^3. However, for some studies it is important to cancel out the effect of the injected dose and of the weight of the animal, hence providing images in standardized uptake value (SUV), as defined by

$$\mathrm{SUV}_j = \frac{\text{tracer concentration in voxel } j}{\text{average tracer concentration}} \tag{9.1}$$

$$= \frac{\text{tracer amount in Bq/g in voxel } j}{\text{total dose in Bq/total weight in g}} \tag{9.2}$$

This conversion is straightforward, but will probably be inaccurate for small animals like mice, because often a significant amount of tracer gets stuck in the tail due to a bad injection. A possible solution could be to perform a quick scan of the tail, as no details are required, to estimate the amount of tracer left in there.

Currently, pinhole SPECT scans are routinely performed in step-and-shoot mode. This means that the detector head moves to a certain projection angle and stops

there for a measurement during a short period of time, typically 30 or 60 s; then it proceeds to the next angle for another measurement and so on. Since the introduction of the second pinhole collimator reduced the requisite imaging time to 64 views of 30 s, the overhead time to move the camera between the projection angles has become quite significant. Therefore, it is worth considering scanning in continuous mode, where the camera is moving at a fixed speed around the subject while detecting photons. The gathered data are accumulated over small viewing angles and stored in matrices, hence the projection data are stored in the same way as before. This might cause some loss in spatial resolution, but preliminary test scans have indicated that the image degradation is minimal. Further validation experiments are required, especially with respect to the effect of the rotation speed on the calibration accuracy, before this technique can be used for preclinical studies.

Bibliography

[1] A. Andreyev, M. Defrise, and C. Vanhove. Pinhole SPECT reconstruction using blobs and resolution recovery. *IEEE Trans. Nucl. Sci.*, 53(5):2719–2728, 2006.

[2] K. Baete, J. Nuyts, W. Van Paesschen, P. Suetens, and P. Dupont. Anatomical based FDG-PET reconstruction for the detection of hypo-metabolic regions in epilepsy. *IEEE Trans. Med. Imag.*, 23(4):510–519, 2004.

[3] G. Bal, G. L. Zeng, R. M. Lewitt, Z. Cao, and P. D. Acton. Study of different pinhole configurations for small animal tumor imaging. In *Conference Record of the IEEE Nucl. Sci. Symp. and Med. Imag. Conf.*, volume 5, pages 3133–3137, Rome, Italy, 2004.

[4] H. H. Barrett, J. L. Denny, R. F. Wagner, and K. J. Myers. Objective assessment of image quality. II. Fisher information, Fourier crosstalk, and figures of merit for task performance. *J. Opt. Soc. Am. A*, 12(5):834–852, 1995.

[5] H. H. Barrett and K. Myers. *Foundations of image science*. John Wiley & Sons, 2003.

[6] H. H. Barrett, D. W. Wilson, and B. M. W. Tsui. Noise properties of the EM algorithm: I. Theory. *Phys. Med. Biol.*, 39(5):833–846, 1994.

[7] H. H. Barrett, J. Yao, J. P. Rolland, and K. J. Myers. Model observers for assessment of image quality. *Proc. Natl. Acad. Sci. USA*, 90(21):9758–9765, 1993.

[8] F. J. Beekman, F. van der Have, B. Vastenhouw, A. J. A. van der Linden, P. P. van Rijk, J. P. H. Burbach, and M. P. Smidt. U-SPECT-I: A novel system for submillimeter-resolution tomography with radiolabeled molecules in mice. *J. Nucl. Med.*, 46(7):1194–1200, 2005.

[9] F. J. Beekman and B. Vastenhouw. Design and simulation of a high-resolution stationary SPECT system for small animals. *Phys. Med. Biol.*, 49(19):4579–4592, 2004.

[10] D. Bequé. MicroSPECT imaging of small laboratory animals. In *Ph.D. thesis*, Katholieke Universiteit Leuven, Belgium, 2005.

[11] D. Bequé, J. Nuyts, G. Bormans, P. Suetens, and P. Dupont. Characterization of acquisition geometry of pinhole SPECT. *IEEE Trans. Med. Imag.*, 22(5):599–612, 2003.

[12] D. Bequé, C. Vanhove, A. Andreyev, J. Nuyts, and M. Defrise. Correction for imperfect camera motion and resolution recovery in pinhole SPECT. In *Conference Record of the IEEE Nucl. Sci. Symp. and Med. Imag. Conf.*, volume 4, pages 2507–2510, Rome, Italy, 2004.

[13] S. C. Blankespoor, X. Xu, K. Kalki, J. K. Brown, H. R. Tang, C. E. Cann, and B. H. Hasegawa. Attenuation correction of SPECT using X-ray CT on an emission-transmission CT system: myocardial perfusion assessment. *IEEE Trans. Nucl. Sci.*, 43(4):2263–2274, 1996.

[14] P. Bonetto, J. Qi, and R. M. Leahy. Covariance approximation for fast and accurate computation of channelized Hotelling observer statistics. *IEEE Trans. Nucl. Sci.*, 47(4):1567–1572, 2000.

[15] J. E. Bowsher, V. E. Johnson, T. G. Turkington, R. J. Jaszczak, C. E. Floyd, and R. E. Coleman. Bayesian reconstruction and use of anatomical a priori information for emission tomography. *IEEE Trans. Med. Imag.*, 15(5):673–686, 1996.

[16] J. E. Bowsher, J. E. Yuan, L. W. Hedlund, T. G. Turkington, G. Akabani, A. Badea, W. C. Kruylo, C. T. Wheeler, G. P. Cofer, M. W. Dewhirst, and G. A. Johnson. Utilizing MRI information to estimate 18F-FDG distributions in rat flank tumors. In *Conference Record of the IEEE Nucl. Sci. Symp. and Med. Imag. Conf.*, volume M2-157, Rome, Italy, 2004.

[17] T. F. Budinger. Time-of-flight positron emission tomography: status relative to conventional PET. *J. Nucl. Med.*, 24(1):73–78, 1983.

[18] Z. Cao, G. Bal, R. Accorsi, and P. D. Acton. Optimal number of pinholes in multi-pinhole SPECT for mouse brain imaging - a simulation study. *Phys. Med. Biol.*, 50(19):4609–4624, 2005.

[19] R. E. Carson, Y. Yan, B. Chodkowski, T. K. Yap, and M. E. Daube-Witherspoon. Precision and accuracy of regional radioactivity quantitation using the maximum likelihood EM reconstruction algorithm. *IEEE Trans. Med. Imag.*, 13(3):526–537, 1994.

[20] C. Casteels, P. Vermaelen, J. Nuyts, A. Van Der Linden, V. Baekelandt, L. Mortelmans, G. Bormans, and K. Van Laere. Construction and evaluation of multitracer small-animal PET probabilistic atlases for voxel-based functional mapping of the rat brain. *J. Nucl. Med.*, 47(11):1858–1866, 2006.

[21] S. K. Chitneni, C. M. Deroose, H. Fonge, R. Gijsbers, N. Dyubankova, J. Balzarini, Z. Debyser, L. Mortelmans, A. M. Verbruggen, and G. M. Bormans. Synthesis and biological evaluation of an (123)I-labeled bicyclic nucleoside analogue (BCNA) as potential SPECT tracer for VZV-tk reporter gene imaging. *Bioorg. Med. Chem. Lett.*, 17(12):3458–3462, 2007.

[22] C. Comtat, P. E. Kinahan, J. A. Fessler, T. Beyer, D. W. Townsend, M. Defrise, and C. Michel. Clinically feasible reconstruction of whole-body PET/CT data using blurred anatomical labels. *Phys. Med. Biol.*, 47(1):1–20, 2002.

[23] M. Conti. Effect of randoms on signal-to-noise ratio in TOF PET. *IEEE Trans. Nucl. Sci.*, 53(3):1188–1193, 2006.

[24] M. Conti, B. Bendriem, M. Casey, M. Chen, F. Kehren, C. Michel, and V. Panin. First experimental results of time-of-flight reconstruction on an LSO PET scanner. *Phys. Med. Biol.*, 50(19):4507–4527, 2005.

[25] H. Cramér. *Mathematical methods of statistics*. Princeton University Press, 1946.

[26] M. E. Daube-Witherspoon, S. Surti, S. Matej, M. Werner, S. Jayanthi, and J. S. Karp. Influence of time-of-flight kernel accuracy in TOF-PET reconstruction. In *Conference Record of the IEEE Nucl. Sci. Symp. and Med. Imag. Conf.*, volume 3, pages 1723–1727, San Diego, CA, USA, 2006.

[27] K. De Moor, J. Nuyts, L. Plessers, S. Stroobants, F. Maes, and P. Dupont. Non-rigid registration with position dependent rigidity for whole body PET follow-up studies. In *Conference Record of the IEEE Nucl. Sci. Symp. and Med. Imag. Conf.*, volume 6, pages 3502–3506, San Diego, CA, USA, 2006.

[28] M. Defrise, P. E. Kinahan, D. W. Townsend, C. Michel, M. Sibomana, and D. F. Newport. Exact and approximate rebinning algorithms for 3-D PET data. *IEEE Trans. Med. Imag.*, 16(2):145–158, 1997.

[29] M. Defrise, C. Vanhove, and J. Nuyts. Perturbative refinement of the geometric calibration in pinhole SPECT. *IEEE Trans. Med. Imag.*, 27(2):204–214, 2008.

[30] A. P. Dempster, N. M. Laird, and D. B. Rubin. Maximum likelihood estimation from incomplete data via the EM algorithm. *J. Royal Statist. Soc.*, Ser. B(39):1–38, 1977.

[31] F. P. DiFilippo. Design and performance of a multi-pinhole collimation device for small animal imaging with clinical SPECT and SPECT-CT scanners. *Phys. Med. Biol.*, 53(15):4185–4201, 2008.

[32] L. A. Feldkamp, L. C. Davis, and J. W. Kress. Practical cone-beam algorithms. *J. Opt. Soc. Am. A*, 1(6):612–619, 1984.

[33] J. A. Fessler. Mean and variance of implicitly defined biased estimators (such as penalized maximum likelihood): Applications to tomography. *IEEE Trans. Image Proc.*, 5(3):493–506, 1996.

[34] J. A. Fessler. Spatial resolution and noise tradeoffs in pinhole imaging system design: a density estimation approach. *Optics Express*, 2(6):237–253, 1998.

[35] J. A. Fessler. Analytical approach to regularization design for isotropic spatial resolution. In *Conference Record of the IEEE Nucl. Sci. Symp. and Med. Imag. Conf.*, volume 3, pages 2022–2026, Portland, Oregon, USA, 2003.

[36] J. A. Fessler and S. D. Booth. Conjugate-gradient preconditioning methods for shift-variant image reconstruction. *IEEE Trans. Image Proc.*, 8(5):688–699, 1999.

[37] J. A. Fessler and W. L. Rogers. Spatial resolution properties of penalized-likelihood image reconstruction: space-invariant tomographs. *IEEE Trans. Image Proc.*, 5(9):1346–1358, 1996.

[38] J. A. Fessler and A. Yendiki. Channelized Hotelling observer performance for penalized-likelihood image reconstruction. In *Conference Record of the IEEE Nucl. Sci. Symp. and Med. Imag. Conf.*, volume 2, pages 1040–1044, Norfolk, Virginia, USA, 2002.

[39] H. Fonge, S. Chitneni, J. Lixin, K. Vunckx, K. Prinsen, J. Nuyts, L. Mortelmans, G. Bormans, Y. Ni, and A. Verbruggen. Necrosis avidity of ^{99m}Tc(CO)$_3$-labeled pamoid acid derivatives: synthesis and preliminary biological evaluation in animal models of necrosis. *Bioconj. Chem.*, 18(6):1924–1934, 2007.

[40] H. Fonge, M. de Saint Hubert, K. Vunckx, D. Rattat, J. Nuyts, G. Bormans, Y. Ni, C. Reutelingsperger, and A. Verbruggen. Preliminary in vivo evaluation of a novel 99mTc-labeled HYNIC-cys-annexin A5 as an apoptosis imaging agent. *Bioorg. Med. Chem. Lett.*, 18(13):3794–3798, 2008.

[41] H. Fonge, L. Jin, H. Wang, Y. Ni, G. Bormans, and A. Verbruggen. Synthesis and preliminary evaluation of mono-[^{123}I]iodohypericin monocarboxylic acid as a necrosis avid imaging agent. *Bioorg. Med. Chem. Lett.*, 17(14):4001–4005, 2007.

[42] H. Fonge, K. Vunckx, H. Wang, Y. Feng, L. Mortelmans, J. Nuyts, G. Bormans, A. Verbruggen, and Y. Ni. Non-invasive detection and quantification of acute myocardial infarction in rabbits using MONO-[123I] iodohypericin μSPECT. *Eur. Heart Journal*, 29(2):260–269, 2008.

[43] T. Funk, P. Després, and W. C. Barber. A multipinhole small animal SPECT system with submillimeter spatial resolution. *Med. Phys.*, 33(5):1259–1268, 2006.

[44] T. Funk, M. Sun, and B. H. Hasegawa. Radiation dose estimate in small animal SPECT and PET. *Med. Phys.*, 31(9):2680–2686, 2004.

[45] S. Geman and D. Geman. Stochastic relaxation, Gibbs distributions, and the Bayesian restoration of images. *IEEE Trans. Pattern Anal. Machine Intell.*, PAMI-6(6):721–741, 1984.

[46] S. Ghoorun, K. Baete, J. Nuyts, W. Groenewald, and P. Dupont. The influence of attenuation correction and reconstruction techniques on the detection of hypoperfused lesions in brain SPECT images. *Nucl. Med. Comm.*, 27(10):765–772, 2006.

[47] G. Gindi, M. Lee, A. Rangarajan, and G. Zubal. Bayesian reconstruction of functional images using anatomical information as priors. *IEEE Trans. Med. Imag.*, 12(4):670–680, 1993.

[48] A. L. Goertzen, D. W. Jones, J. Seidel, K. Li, and M. V. Green. First results from the high-resolution mouseSPECT annular scintillation camera. *IEEE Trans. Med. Imag.*, 24(7):863–867, 2005.

[49] M. J. E. Golay. Point arrays having compact, nonredundant autocorrelations. *J. Opt. Soc. Am.*, 61:272–273, 1971.

[50] P. J. Green. Bayesian reconstructions from emission tomography data using a modified EM algorithm. *IEEE Trans. Med. Imag.*, 9(1):84–93, 1990.

[51] R. L. Harrison, S. B. Gillispie, A. M. Alessio, P. E. Kinahan, and T. K. Lewellen. The effect of object size, attenuation, scatter, and random coincidences on signal to noise ratio in simulations of time-of-flight positron emission tomography. In *Conference Record of the IEEE Nucl. Sci. Symp. and Med. Imag. Conf.*, volume 4, pages 1900–1904, Puerto Rico, USA, 2005.

[52] T. Hebert and R. Leahy. A generalized EM algorithm for 3-D Bayesian reconstructions from Poisson data using Gibbs priors. *IEEE Trans. Med. Imag.*, 8(2):194–202, 1989.

[53] J. Y. Hesterman, M. A. Kupinski, L. R. Furenlid, D. W. Wilson, and H. H. Barrett. The multi-module, multi-resolution system (M^3R): A novel small-animal SPECT system. *Med. Phys.*, 34(3):987–993, 2007.

[54] P. J. Huber. *Robust statistics*. John Wiley & Sons, 1981.

[55] H. M. Hudson and R. S. Larkin. Accelerated image reconstruction using ordered subsets of projection data. *IEEE Trans. Med. Imag.*, 13(4):601–609, 1994.

[56] T. Ichihara, K. Ogawa, N. Motomura, A. Kubo, and S. Hashimoto. Compton scatter compensation using the triple-energy window method for single- and dual-isotope SPECT. *J. Nucl. Med.*, 34(12):2216–2221, 1993.

[57] M. Ivanovic, D. A. Weber, and S. Loncaric. Multi-pinhole collimator optimization for high resolution SPECT imaging. In *Conference Record of the IEEE Nucl. Sci. Symp. and Med. Imag. Conf.*, volume 2, pages 1097–1101, Albuquerque, New Mexico, USA, 1997.

[58] R. J. Jaszczak, K. L. Greer, C. E. Floyd, C. C. Harris, and R. E. Coleman. Improved SPECT quantification using compensation for scattered photons. *J. Nucl. Med.*, 25(8):893–900, 1984.

[59] R. J. Jaszczak, J. Li, H. Wang, M. R. Zalutsky, and R. E. Coleman. Pinhole collimation for ultra-high-resolution, small-field-of-view SPECT. *Phys. Med. Biol.*, 39(3):425–437, 1994.

[60] C.-M. Kao, D. Yun, Q. Xie, and C.-T. Chen. An investigation of the potential benefits in trading energy resolution for timing resolution in time-of-flight positron emission tomography. In *Conference Record of the IEEE Nucl. Sci. Symp. and Med. Imag. Conf.*, volume 4, pages 2564–2569, San Diego, CA, USA, 2006.

[61] J. S. Karp, S. Surti, M. E. Daube-Witherspoon, and G. Muehllehner. Benefit of time-of-flight in PET: experimental and clinical results. *J. Nucl. Med.*, 49(3):462–470, 2008.

[62] A. Katsevich. Analysis of an exact inversion algorithm for spiral cone-beam CT. *Phys. Med. Biol.*, 47(15):2583–2597, 2002.

[63] J. A. Kimdon, J. Qi, and W. W. Moses. Effect of random and scatter fractions in variance reduction using time-of-flight information. In *Conference Record of the IEEE Nucl. Sci. Symp. and Med. Imag. Conf.*, volume 4, pages 2571–2573, Portland, Oregon, USA, 2003.

[64] P. E. Kinahan and J. G. Rogers. Analytic 3D image reconstruction using all detected events. *IEEE Trans. Nucl. Sci.*, 36(1):964–968, 1989.

[65] P. E. Kinahan, D. W. Townsend, T. Beyer, and D. Sashin. Attenuation correction for a combined 3D PET/CT scanner. *Med. Phys.*, 25(10):2046–2053, 1998.

[66] H. Kudo, M. Courdurier, F. Noo, and M. Defrise. Tiny a priori knowledge solves the interior problem. In *Conference Record of the IEEE Nucl. Sci. Symp. and Med. Imag. Conf.*, volume 6, pages 4068–4075, Honolulu, Hawaii, USA, 2007.

[67] M. P. Kung and H. F. Kung. Mass effect of injected dose in small rodent imaging by SPECT and PET. *Nucl. Med. Biol.*, 32(7):673–678, 2005.

[68] E. Lauwers, D. Bequé, K. Van Laere, J. Nuyts, G. Bormans, L. Mortelmans, C. Casteels, L. Vercammen, O. Bockstael, B. Nuttin, Z. Debyser, and V. Baekelandt. Non-invasive imaging of neuropathology in a rat model of alpha-synuclein overexpression. *Neurobiol. Aging*, 28(2):248–257, 2007.

[69] R. M. Leahy and X. Yan. Incorporation of anatomical MR data for improved functional imaging with PET. In *Internat. Conf. on Inform. Proc. in Med. Imag.*, pages 105–120, Berlin, Germany, 1991.

[70] C. S. Levin and E. J. Hoffman. Calculation of positron range and its effect on the fundamental limit of positron emission tomography system spatial resolution. *Phys. Med. Biol.*, 44(3):781–799, 1999.

[71] R. M. Lewitt. Processing of incomplete measurement data in computed tomography. *Med. Phys.*, 6(5):412–417, 1979.

[72] F. Maes, A. Collignon, D. Vandermeulen, G. Marchal, and P. Suetens. Multimodality image registration by maximization of mutual information. *IEEE Trans. Med. Imag.*, 16(2):187–198, 1997.

[73] A. Mallon, P. Grangeat, and P. X. Thomas. Comparison between three-dimensional positron emission tomography with and without time-of-flight measurement. In *Conference Record of the IEEE Nucl. Sci. Symp. and Med. Imag. Conf.*, volume 2, pages 988–990, Orlando, Florida, USA, 1992.

[74] R. M. Manjeshwar, Y. Shao, and F. P. Jansen. Image quality improvements with time-of-flight positron emission tomography for molecular imaging. In *IEEE Internat. Conf. Acoust., Speech, and Signal Proc. Proceedings*, volume 5, pages v/853–v/856, Philadelphia, Pennsylvania, USA, 2005.

[75] S. R. Meikle, R. R. Fulton, S. Eberl, M. Dahlbom, K.-P. Wong, and M. J. Fulham. An investigation of coded aperture imaging for small animal SPECT. *IEEE Trans. Nucl. Sci.*, 48(3):816–821, 2001.

[76] S. R. Meikle, P. Kench, A. G. Weisenberger, R. Wojcik, M. F. Smith, S. Majewski, S. Eberl, R. R. Fulton, A. B. Rosenfeld, and M. J. Fulham. A prototype coded aperture detector for small animal SPECT. *IEEE Trans. Nucl. Sci.*, 49(5):2167–2171, 2002.

[77] L. J. Meng and N. H. Clinthorne. A modified uniform Cramer-Rao bound for multiple pinhole aperture design. *IEEE Trans. Med. Imag.*, 23(7):896–902, 2004.

[78] L. J. Meng, W. L. Rogers, N. H. Clinthorne, and J. A. Fessler. Feasibility study of compton scattering enhanced multiple pinhole imager for nuclear medicine. *IEEE Trans. Nucl. Sci.*, 50(5):1609–1617, 2003.

[79] L. J. Meng and D. K. Wehe. Feasibility study of using hybrid collimation for nuclear environment imaging. *IEEE Trans. Nucl. Sci.*, 50(4):1103–1110, 2003.

[80] S. P. Mok, Y. Wang, and B. M. W. Tsui. Quantification of the multiplexing effect in multi-pinhole small animal SPECT. In *Conference Record of the IEEE Nucl. Sci. Symp. and Med. Imag. Conf.*, volume M07-01, San Diego, CA, USA, 2006.

[81] F. Natterer. Determination of tissue attenuation in emission tomography of optically dense media. *Inverse Problems*, 9(6):731–736, 1993.

[82] Y. Ni, D. Huyghe, K. Verbeke, P. A. de Witte, J. Nuyts, L. Mortelmans, F. Chen, G. Marchal, A. M. Verbruggen, and G. M. Bormans. First preclinical evaluation of mono-[^{123}I]iodohypericin as a necrosis-avid tracer agent. *Eur. J. Nucl. Med. Mol. Imaging*, 33(5):595–601, 2006.

[83] F. Noo, R. Clackdoyle, C. Mennessier, T. A. White, and T. J. Roney. Analytic method based on identification of ellipse parameters for scanner calibration in cone-beam tomography. *Phys. Med. Biol.*, 45(11):3489–3508, 2000.

[84] J. Nuyts. The use of mutual information and joint entropy for anatomical priors in emission tomography. In *Conference Record of the IEEE Nucl. Sci. Symp. and Med. Imag. Conf.*, volume 6, pages 4149–4154, Honolulu, Hawaii, USA, 2007.

[85] J. Nuyts, K. Baete, D. Bequé, and P. Dupont. Comparison between MAP and post-processed ML for image reconstruction in emission tomography when anatomical knowledge is available. *IEEE Trans. Med. Imag.*, 24(5):667–675, 2005.

[86] J. Nuyts and J. A. Fessler. A penalized-likelihood image reconstruction method for emission tomography, compared to postsmoothed maximum-likelihood with matched spatial resolution. *IEEE Trans. Med. Imag.*, 22(9):1042–1052, 2003.

[87] K. Ogawa, M. Nakajima, and S. Yuta. A reconstruction algorithm from truncated projections. *IEEE Trans. Med. Imag.*, 3(1):34–40, 1984.

[88] M. B. Pissarek, A.-M. Oros-Peusquens, and N. U. Schramm. Challenge by the murine brain: Multi-pinhole SPECT of ^{123}I-labelled pharmaceuticals. *J. Neurosci. Methods*, 168(2):282–292, 2008.

[89] D. G. Politte. Image improvements in positron-emission tomography due to measuring differential time-of-flight and using maximum-likelihood estimation. *IEEE Trans. Nucl. Sci.*, 37(2):737–742, 1990.

[90] L. M. Popescu and R. M. Lewitt. Comparison between TOF and non-TOF PET using a scan statistic numerical observer. In *Conference Record of the IEEE Nucl. Sci. Symp. and Med. Imag. Conf.*, volume 3, pages 1774–1780, San Diego, CA, USA, 2006.

[91] W. H. Press, B. P. Flannery, S.A. Teukolsky, and W. T. Vetterling. *Numerical recipes in C: the art of scientific computing (Second edition).* Cambridge University Press, 1992.

[92] J. Qi and R. H. Huesman. Theoretical study of lesion detectability of MAP reconstruction using computer observers. *IEEE Trans. Med. Imag.*, 20(8):815–822, 2001.

[93] J. Qi and R. M. Leahy. A theoretical study of the contrast recovery and variance of MAP reconstructions from PET data. *IEEE Trans. Med. Imag.*, 18(4):293–305, 1999.

[94] J. Qi and R. M. Leahy. Resolution and noise properties of MAP reconstruction for fully 3-D PET. *IEEE Trans. Med. Imag.*, 19(5):493–506, 2000.

[95] A. J. Reader, P. J. Julyan, H. Williams, D. L. Hastings, and J. Zweit. EM algorithm system modeling by image-space techniques for PET reconstruction. *IEEE Trans. Nucl. Sci.*, 50(5):1392–1397, 2003.

[96] P. Rizo, P. Grangeat, and R. Guillemaud. Geometric calibration method for multiple-head cone-beam SPECT system. *IEEE Trans. Nucl. Sci.*, 41(6):2748–2757, 1994.

[97] N. U. Schramm, G. Ebel, U. Engeland, T. Schurrat, M. Béhé, and T. M. Behr. High-resolution SPECT using multipinhole collimation. *IEEE Trans. Nucl. Sci.*, 50(3):315–320, 2003.

[98] L. A. Shepp and Y. Vardi. Maximum likelihood reconstruction for emission tomography. *IEEE Trans. Med. Imag.*, 1(2):113–122, 1982.

[99] M. F. Smith and R. J. Jaszczak. The effect of gamma ray penetration on angle-dependent sensitivity for pinhole collimation in nuclear medicine. *Med. Phys.*, 24(11):1701–1709, 1997.

[100] M. F. Smith, S. R. Meikle, S. Majewski, and A. G. Weisenberger. Design of multipinhole collimators for small animal SPECT. In *Conference Record of the IEEE Nucl. Sci. Symp. and Med. Imag. Conf.*, volume 4, pages 2291–2295, Portland, Oregon, USA, 2003.

[101] D. L. Snyder. Some noise comparisons of data-collection arrays for emission tomography-systems having time-of-flight measurements. *IEEE Trans. Nucl. Sci.*, 29(1):1029–1033, 1982.

[102] S. Somayajula, E. Asma, and R. Leahy. PET image reconstruction using anatomical information through mutual information based priors. In *Conference Record of the IEEE Nucl. Sci. Symp. and Med. Imag. Conf.*, volume M11-354, Puerto Rico, USA, 2005.

[103] S. Staelens, K. Vunckx, J. De Beenhouwer, F.J. Beekman, Y. D'Asseler, J. Nuyts, and I. Lemahieu. GATE simulations for optimization of pinhole imaging. *Nucl. Inst. & Meth. A*, 569(2):359–363, 2006.

[104] J. W. Stayman and J. A. Fessler. Compensation for nonuniform resolution using penalized-likelihood reconstruction in space-variant imaging systems. *IEEE Trans. Med. Imag.*, 23(3):269–284, 2004.

[105] C. E. Suckow and D. B. Stout. MicroCT liver contrast agent enhancement over time, dose and mouse strain. *Mol. Imaging Biol.*, 10(2):114–120, 2008.

[106] S. Surti, J. S. Karp, L. M. Popescu, M. E. Daube-Witherspoon, and M. Werner. Investigation of time-of-flight benefit for fully 3-D PET. *IEEE Trans. Med. Imag.*, 25(5):529–538, 2006.

[107] S. Surti, A. Kuhn, M. E. Werner, A. E. Perkins, J. Kolthammer, and J. S. Karp. Performance of Philips Gemini TF PET/CT scanner with special consideration for its time-of-flight imaging capabilities. *J. Nucl. Med.*, 48(3):471–480, 2007.

[108] C. R. Tenney. Gold pinhole collimators for ultra-high resolution Tc-99m smallvolume SPECT. In *Conference Record of the IEEE Nucl. Sci. Symp. and Med. Imag. Conf.*, volume 3, pages 22/44–22/46, Lyon, France, 2000.

[109] M. M. Ter-Pogossian, N. A. Mullani, D. C. Ficke, J. Markham, and D. L. Snyder. Photon time-of-flight-assisted positron emission tomography. *J. Comput. Assist. Tomogr.*, 5(2):227–239, 1981.

[110] T. Tomitani. Image reconstruction and noise evaluation in photon time-of-flight assisted positron emission tomography. *IEEE Trans. Nucl. Sci.*, 28(6):4582–4589, 1981.

[111] T. Tomitani. An edge detection algorithm for attenuation correction in emission CT. *IEEE Trans. Nucl. Sci.*, 34(1):309–312, 1987.

[112] H. K. Tuy. An inversion formula for cone-beam reconstruction. *SIAM J. Appl. Math.*, 43(3):546–552, 1983.

[113] F. van der Have and F. J. Beekman. Photon penetration and scatter in micro-pinhole imaging: a Monte Carlo investigation. *Phys. Med. Biol.*, 49(8):1369–1386, 2004.

[114] F. van der Have, B. Vastenhouw, and F. Beekman. U-SPECT-II: A versatile sub-half-mm resolution small animal SPECT system. *J. Nucl. Med.*, 48(Supplement 2):47P, 2007.

[115] S. Vandenberghe, S. Matej, M. E. Witherspoon, J. S. Karp, and I. Lemahieu. Determining timing resolution from TOF-PET emission data. In *Conference Record of the IEEE Nucl. Sci. Symp. and Med. Imag. Conf.*, volume 4, pages 2727–2731, Honolulu, Hawaii, USA, 2007.

[116] C. Vanhove, M. Defrise, P. R. Franken, H. Everaert, F. Deconinck, and A. Bossuyt. Interest of the ordered subsets expectation maximization (OS-EM) algorithm in pinhole single-photon emission tomography reconstruction: a phantom study. *Eur. J. Nucl. Med. Mol. Imaging*, 27(2):140–146, 2000.

[117] C. Vanhove, M. Defrise, T. Lahoute, and A. Bossuyt. Three-pinhole collimator to improve axial spatial resolution and sensitivity in pinhole SPECT. *Eur. J. Nucl. Med. Mol. Imaging*, 35(2):407–415, 2008.

[118] C. Vanhove, T. Lahoutte, M. Defrise, A. Bossuyt, and P.R. Franken. Reproducibility of left ventricular volume and ejection fraction measurements in rat using pinhole gated SPECT. *Eur. J. Nucl. Med. Mol. Imaging*, 32(2):211–220, 2005.

[119] K. Vunckx, D. Bequé, M. Defrise, and J. Nuyts. Single and multipinhole collimator design evaluation method for small animal SPECT. In *Conference Record of the IEEE Nucl. Sci. Symp. and Med. Imag. Conf.*, volume 4, pages 2223–2227, Puerto Rico, USA, 2005.

[120] K. Vunckx, D. Bequé, M. Defrise, and J. Nuyts. Single and multipinhole collimator design evaluation method for small animal SPECT. *IEEE Trans. Med. Imag.*, 27(1):36–46, 2008.

[121] K. Vunckx, M. Defrise, D. Bequé, C. Vanhove, A. Andreyev, and J. Nuyts. Geometrical calibration and aperture configuration design in multi-pinhole SPECT. In *IEEE Internat. Symp. on Biomed. Imag.*, pages 1403–1406, Paris, France, 2008.

[122] K. Vunckx and J. Nuyts. Effect of overlapping projections on reconstruction image quality in multipinhole SPECT. In *Conference Record of the IEEE Nucl. Sci. Symp. and Med. Imag. Conf.*, volume 5, pages 2826–2833, San Diego, CA, USA, 2006.

[123] K. Vunckx, L. Zhou, S. Matej, M. Defrise, and J. Nuyts. Fisher information-based evaluation of image quality for time-of-flight PET. In *Conference Record of the IEEE Nucl. Sci. Symp. and Med. Imag. Conf.*, volume 6, pages 4129–4136, Honolulu, Hawaii, USA, 2007.

[124] S. Walrand, A. van Dulmen, H. van Rossem, and S. Pauwels. Acquisition of linograms in SPET: implementation and benefits. *Eur. J. Nucl. Med. Mol. Imaging*, 29(9):1188–1197, 2002.

[125] Y. Wang and B. M. W. Tsui. Application of crosstalk concept to assessment of multi-pinhole collimator designs in small animal SPECT imaging. In *Conference Record of the IEEE Nucl. Sci. Symp. and Med. Imag. Conf.*, volume M16-8, San Diego, CA, USA, 2006.

[126] Y. C. Wang and B. M. W. Tsui. Pinhole SPECT with different data acquisition geometries: Usefulness of unified projection operators in homogeneous coordinates. *IEEE Trans. Med. Imag.*, 26(3):298–308, 2007.

[127] C. C. Watson. An evaluation of image noise variance for time-of-flight PET. *IEEE Trans. Nucl. Sci.*, 54(5):1639–1647, 2007.

[128] C. C. Watson. An improved kernel for analytical time-of-flight PET reconstruction. In *Conference Record of the IEEE Nucl. Sci. Symp. and Med. Imag. Conf.*, volume 4, pages 2721–2726, Honolulu, Hawaii, USA, 2007.

[129] A. Welch, R. Clack, F. Natterer, and G. T. Gullberg. Toward accurate attenuation correction in SPECT without transmission measurements. *IEEE Trans. Med. Imag.*, 16(5):532–541, 1997.

[130] D. W. Wilson, B. M. W. Tsui, and H. H. Barrett. Noise properties of the EM algorithm. II. Monte Carlo simulations. *Phys. Med. Biol.*, 39(5):847–872, 1994.

[131] P. Wolter, H. Dumez, and P. Schöffski. Sunitinib and hypothyroidism. *N. Engl. J. Med.*, 356(15):author reply 1580–1581, 2007.

[132] W.-H. Wong, N. A. Mullani, E. A. Philippe, R. Hartz, and K. L. Gould. Image improvement and design optimization of the time-of-flight PET. *J. Nucl. Med.*, 24(1):52–60, 1983.

[133] Y. Xing, I.-T. Hsiao, and G. Gindi. Rapid calculation of detectability in Bayesian single photon emission computed tomography. *Phys. Med. Biol.*, 48(22):3755–3773, 2003.

[134] M. Yamamoto, D. C. Ficke, and M. M. Ter-Pogossian. Experimental assessment of the gain achieved by the utilization of time-of-flight information in a positron emission tomograph (Super PETT I). *IEEE Trans. Med. Imag.*, 1(3):187–192, 1982.

[135] T. Yamaya, T. Obi, M. Yamaguchi, and N. Ohyama. High-resolution image reconstruction method for time-of-flight positron emission tomography. *Phys. Med. Biol.*, 45(11):3125–3134, 2000.

[136] Y. Zhang-O'Connor and J. A. Fessler. Fast predictions of variance images for fan-beam transmission tomography with quadratic regularization. *IEEE Trans. Med. Imag.*, 26(3):335–346, 2007.

[137] L. Zhou, K. Vunckx, and J. Nuyts. Comparison between parallel hole and rotating slat collimation: planar image quality evaluation by Fisher information-based method. In *Conference Record of the IEEE Nucl. Sci. Symp. and Med. Imag. Conf.*, Dresden, Germany, Oct. 2008.

List of publications

International Journals

1. S. Staelens, **K. Vunckx**, J. De Beenhouwer, F. Beekman, Y. D'Asseler, J. Nuyts, and I. Lemahieu. GATE simulations for optimization of pinhole imaging. *Nucl. Inst. & Meth. A*, 569(2):359–363, 2006.

2. S. Celen, T. de Groot, J. Balzarini, **K. Vunckx**, C. Terwinghe, P. Vermaelen, L. Van Berckelaer, H. Vanbilloen, J. Nuyts, L. Mortelmans, A. Verbruggen, and G. Bormans. Synthesis and evaluation of a ^{99m}Tc-MAMA-propyl-thymidine complex as a potential probe for in vivo visualization of tumor cell proliferation with SPECT. *Nucl. Med. Biol.*, 34(3):283–291, 2007.

3. H. Fonge, S. K. Chitneni, J. Lixin, **K. Vunckx**, K. Prinsen, J. Nuyts, L. Mortelmans, G. Bormans, Y. Ni, and A. Verbruggen. Necrosis avidity of ^{99m}Tc(CO)$_3$-labeled pamoic acid derivatives: synthesis and preliminary biological evaluation in animal models of necrosis. *Bioconj. Chem.*, 18(6):1924–1934, 2007.

4. **K. Vunckx**, D. Bequé, M. Defrise, and J. Nuyts. Single and multipinhole collimator design evaluation method for small animal SPECT. *IEEE Trans. Med. Imag.*, 27(1):36–46, 2008.

5. H. Fonge, **K. Vunckx**, H. Wang, Y. Feng, L. Mortelmans, J. Nuyts, G. Bormans, A. Verbruggen, and Y. Ni. Non-invasive detection and quantification of acute myocardial infarction in rabbits using mono-[123I] iodohypericin SPECT. *Eur. Heart Journal*, 29(2):260–269, 2008.

6. **K. Vunckx**, P. Suetens, and J. Nuyts. Effect of overlapping projections on reconstruction image quality in multipinhole SPECT. *IEEE Trans. Med. Imag. - special issue on Fully-3D reconstruction of medical images*, 27(7):972–983, 2008.

7. H. Fonge, M. De Saint-Hubert, **K. Vunckx**, D. Rattat, J. Nuyts, G. Bormans, Y. Ni, C. Reutelingsperger, and A. Verbruggen. Preliminary in vivo evaluation of a novel 99mTc-labeled HYNIC-cys-annexin A5 as an apoptosis imaging agent. *Bioorg. Med. Chem. Lett.*, 18(13):3794–3798, 2008.

8. **K. Vunckx**, L. Zhou, S. Matej, M. Defrise, and J. Nuyts. Fisher information-based evaluation of image quality for time-of-flight PET. submitted to *IEEE Trans. Med. Imag.*

International Conference Proceedings

1. **K. Vunckx**, D. Bequé, M. Defrise, and J. Nuyts. Single and multipinhole collimator design evaluation method for small animal SPECT. In *Conference Record of the IEEE Nucl. Sci. Symp. and Med. Imag. Conf.*, volume 4, pages 2223–2227, Puerto Rico, USA, 2005.

2. **K. Vunckx**, and J. Nuyts. Effect of overlapping projections on reconstruction image quality in multipinhole SPECT. In *Conference Record of the IEEE Nucl. Sci. Symp. and Med. Imag. Conf.*, volume 5, pages 2826–2833, San Diego, CA, USA, 2006.

3. **K. Vunckx**, L. Zhou, S. Matej, M. Defrise, and J. Nuyts. Fisher information-based evaluation of image quality for time-of-flight PET. In *Conference Record of the IEEE Nucl. Sci. Symp. and Med. Imag. Conf.*, volume 6, pages 4129–4136, Honolulu, Hawaii, USA, 2007.

4. **K. Vunckx**, M. Defrise, D. Bequé, C. Vanhove, A. Andreyev, and J. Nuyts. Geometric calibration and aperture configuration design in multi-pinhole SPECT. In *IEEE Internat. Symp. on Biomed. Imag.*, pages 1403–1406, Paris, France, 2008.

International Conference Abstracts

1. S. Staelens, **K. Vunckx**, D. Bequé, Y. D'Asseler, J. Nuyts, and I. Lemahieu. GATE multi-pinhole simulations: optimization of design parameters. In *Book of abstracts of the 3rd Internat. Conf. on Imag. Technol. in Biomed. Sci.*, page 138, 2005, Milos Island, Greece.

2. H. Fonge, **K. Vunckx**, Y. Ni, J. Nuyts, L. Mortelmans, H. Wang, T. de Groot, P. Vermaelen, G. Bormans, and A. Verbruggen. Non-invasive in vivo detection and quantification of myocardial infarction in rabbits using mono-[123I]iodohypericin as a necrosis avid tracer agent. In *Society of Nuclear Medicine's 54th Annual Meeting, J. Nucl. Med. 2007*, volume 48 (Suppl. 2), page 179P, June 2-6, 2007, Washington, DC, USA.

3. H. Fonge, **K. Vunckx**, J. Lixin, H. Wang, K. Prinsen, C. Lemmens, D. Rattat, L. Mortelmans, J. Nuyts, G. Bormans, Y. Ni, S. van den Borne, L. Hofstra, C. Reutelingsperger, and A. Verbruggen. Non invasive in vivo SPECT imaging of apoptosis and necrosis in rabbits with a novel site specific ^{99m}Tc-labelled Annexin-A5-HYNIC derivative and mono-[123I] iodohypericin after

acute reperfused myocardial infarction. *Annual Congress of the Eur. Assoc. of Nucl. Med.*, October 13-17, 2007, Copenhagen, Denmark (Marie Curie Award Nominee).

4. K. Prinsen, Y. Ni, J. Zhang, M. De Saint-Hubert, **K. Vunckx**, C. Lemmens, L. Zhou, L. Mortelmans, J. Nuyts, G. Bormans, and A. Verbruggen. Radiosynthesis and preliminary evaluation in rats of a novel ^{99m}Tc-labelled necrosis avid imaging agent. *Europ. Symp. on Radiopharmacy and Radiopharmaceuticals*, April 24-27, 2008, Skopje, Macedonia.

5. M. De Saint-Hubert, E. Devos, K. Prinsen, F. M. Mottaghy, J. Nuyts, **K. Vunckx**, P. Vermaelen, S. Stroobants, L. Mortelmans, C. Reutelingsperger, A. Verbruggen, and D. Rattat. *In vitro* and *in vivo* evaluation of second generation Annexin-A5 labelled with ^{99m}Tc or ^{99m}Tc-tricarbonyl as imaging agents for apoptosis. *Annual Congress of the Eur. Assoc. of Nucl. Med.*, October 11-15, 2008, Munich, Germany.

6. **K. Vunckx**, J. Nuyts, B. Vanbilloen, M. De Saint-Hubert, D. Vanderghinste, D. Rattat, F. Mottaghy, and M. Defrise. Optimized multipinhole design for mouse imaging. *IEEE Nucl. Sci. Symp. and Med. Imag. Conf.*, October 19-25, 2008, Dresden, Germany.

7. L. Zhou, **K. Vunckx** and J. Nuyts. Comparison between parallel hole and rotating slat collimation: planar image quality evaluation by Fisher information-based method. *IEEE Nucl. Sci. Symp. and Med. Imag. Conf.*, October 19-25, 2008, Dresden, Germany.

National Symposium Abstracts

1. **K. Vunckx**, L. Zhou, S. Matej, M. Defrise, and J. Nuyts. Time-of-flight PET: image quality analysis. *Symposium of the Belgian Hospital Physicist Association*, Februari 8-9, 2008, Leuven, Belgium.

2. **K. Vunckx**, and J. Nuyts. Effect of overlapping projections on reconstruction image quality in multipinhole SPECT. *Symposium of the Belgian Hospital Physicist Association*, Februari 2-3, 2007, Liège, Belgium.

3. **K. Vunckx**, D. Bequé, and J. Nuyts. Evaluation of single and multipinhole collimator designs for small animal SPECT. *Symposium of the Belgian Society of Nuclear Medicine*, May 20-22, 2005, Knokke, Belgium.

Invited Talks

1. **K. Vunckx** and J. Nuyts. Effect of (multi)pinhole collimator design on the reconstruction image quality of small animal SPECT. *UMC Utrecht*, January 7, 2008, Utrecht, The Netherlands.

International Scientific Project Meetings

1. **K. Vunckx**, M. Defrise, K. Van Laere, and J. Nuyts. Pinhole microSPECT: novel approaches. *Joint DiMI/EMIL annual meeting*, May 15-17, 2006, INSTN, Saclay, France.

2. **K. Vunckx**, J. Nuyts, B. Vanbilloen, M. De Saint-Hubert, D. Vanderghinste, D. Rattat, F. Mottaghy, and M. Defrise. Optimized multipinhole design for mouse imaging. *Joint DiMI/EMIL annual meeting*, June 1-3, 2008, University Hospital Gasthuisberg, Leuven, Belgium.

Master Thesis

1. W. Jansen and **K. Vunckx**. Prosodiemodellering in spraakherkenning. Katholieke Universiteit Leuven, Belgium, 2004.

Curriculum Vitae

Kathleen Vunckx was born in Turnhout, Belgium, on October 23rd, 1981. In 1999, she started her studies at the Faculty of Engineering of the Katholieke Universiteit Leuven in Belgium. In 2004, she graduated magna cum laude as a Master of Applied Sciences and Engineering: Electro-technical engineer ICT in multimedia and signal processing. Inspired by the technical challenges in medical imaging, Kathleen started her PhD in September 2004 at the Faculty of Engineering, Department of Electrical Engineering (ESAT), center for Processing of Speech and Images (PSI), laboratory of Medical Imaging Computing (MIC) in Leuven, Belgium. As a researcher of the Nuclear Medicine division of the university hospital Gasthuisberg, she was able to fruitfully synergize theory and practice of medical imaging research in a realistic context, and valorize her results in several preclinical experiments. The achieved results in her PhD and the many open challenges in this domain strongly motivate Kathleen to continue her research on statistical image reconstruction of small animal as well as human emission data.

Scientific training

1. Short Course: "Statistical methods for image reconstruction" by J. Qi, F. J. Beekman and B. De Man. IEEE NSS-MIC, Puerto Rico, USA, October 25th, 2005.

2. Short Course: "Image quality" by K. J. Myers, H. H. Barrett, M. A. Kupinski, B. Gallas, E. Frey. IEEE NSS-MIC, San Diego, CA, USA, October 31th, 2006.

3. Short Course: "Programming & medical applications using graphics hardware" by A. Sitek, G. Pratx and S. Prevrhal. IEEE NSS-MIC, Honolulu, Hawaii, USA, October 29th, 2007.

Appendix A

Multipinhole SPECT calibration

Here, we provide a more elaborated version of the derivation presented in the appendix of [121] to determine the amount of point sources required for multipinhole SPECT calibration. Notations and parameterization are based on [11].

A.1 Introduction

For single pinhole SPECT (and cone-beam CT), the camera detector geometry can be described by the 7 parameters depicted in Fig. 3.1, namely f, e_u, e_v, d, m, ϕ and ψ. The mechanical offset in the direction parallel to the AOR n can be chosen zero by an appropriate choice of the origin of the coordinate system. For multipinhole SPECT, however, this axial mechanical offset can be non-zero for many apertures, despite a smart origin choice. In that case, the projections (u_{ij}, v_{ij}) of a the point source j with cylindrical coordinates (r_j, α_j, z_j), through aperture i, can be written as (see (A.36)-(A.40) in [10])

$$u_{ij} = f_i \frac{M_1 + Z_1 + R_1}{N} + M_1 + e_u \tag{A-1}$$

$$v_{ij} = f_i \frac{M_2 + Z_2 + R_2}{N} + M_2 + e_v \tag{A-2}$$

$$
\begin{aligned}
\text{with } M_1 &= m_i \cos\psi - n_i \sin\psi \\
M_2 &= m_i \sin\psi + n_i \cos\psi \\
Z_1 &= z_j \cos\phi \sin\psi \\
Z_2 &= -z_j \cos\phi \cos\psi \\
R_1 &= r_j(-\cos\gamma\cos\psi + \sin\gamma\sin\phi\sin\psi) \\
R_2 &= -r_j(\cos\gamma\sin\psi + \sin\gamma\sin\phi\cos\psi) \\
N &= d_i + r_j\cos\phi\sin\gamma - z_j\sin\phi \\
\gamma &= \alpha_j - \theta
\end{aligned}
$$

We assume that the point sources are not put on the AOR, so $r_j > 0$. As explained above, one of the axial mechanical offsets can be set to zero, hence $n_1 = 0$. To verify whether the point source projections provide sufficient information for unique geometrical calibration, we assume there exist two different sets of solutions that explain the measured point source projections, namely $\{f_i, d_i, m_i, n_i, \phi, \psi, e_u, e_v, r_j, \alpha_j, z_j\}$ and $\{\tilde{f}_i, \tilde{d}_i, \tilde{m}_i, \tilde{n}_i, \tilde{\phi}, \tilde{\psi}, \tilde{e}_u, \tilde{e}_v, \tilde{r}_j, \tilde{\alpha}_j, \tilde{z}_j\}$, $i = 1 \ldots I, j = 1 \ldots J$, with I the total number of apertures and J the total amount of point sources. We will try to proof that these solutions are identical for a certain (minimum) number of apertures and point sources. Imposing that both sets yield the observed projections (u_{ij}, v_{ij}), results in the following equations (similar to (16)-(25) in [11]):

$$\tilde{\psi} = \psi \tag{A-3}$$

$$\tilde{f}_i = f_i \frac{\cos\tilde{\phi}}{\cos\phi} \tag{A-4}$$

$$\tilde{\alpha}_j = \alpha_j \tag{A-5}$$

$$\frac{\tilde{n}_i}{\tilde{r}_j} + \frac{\tilde{d}_i \sin\tilde{\phi} - \tilde{z}_j}{\tilde{r}_j \cos\tilde{\phi}} = \frac{n_i}{r_j} + \frac{d_i \sin\phi - z_j}{r_j \cos\phi} \tag{A-6}$$

$$\frac{\tilde{d}_i - \tilde{z}_j \sin\tilde{\phi}}{\tilde{r}_j \cos\tilde{\phi}} = \frac{d_i - z_j \sin\phi}{r_j \cos\phi} \tag{A-7}$$

$$\frac{\tilde{m}_i}{\tilde{r}_j} = \frac{m_i}{r_j} \tag{A-8}$$

$$(\tilde{m}_i - m_i)\cos\psi - (\tilde{n}_i - n_i)\sin\psi + (\tilde{e}_u - e_u) \tag{A-9}$$

$$= f_i \frac{\sin\psi}{\cos\phi}(\sin\phi - \sin\tilde{\phi}) \tag{A-10}$$

$$(\tilde{m}_i - m_i)\sin\psi + (\tilde{n}_i - n_i)\cos\psi + (\tilde{e}_v - e_v) \tag{A-11}$$

$$= -f_i \frac{\cos\psi}{\cos\phi}(\sin\phi - \sin\tilde{\phi}) \tag{A-12}$$

$$f_i + d_i = R \text{ and } \tilde{f}_i + \tilde{d}_i = \tilde{R} \tag{A-13}$$

Equations (A-6) and (A-7) are written differently from the ones proposed in [11], but are equivalent to expressions (19) and (20) of [11], extended with the non-zero mechanical offsets n_i and $\tilde{n}_i$:

$$\frac{\tilde{z}_j}{\tilde{r}_j} = a\frac{z_j}{r_j} + b\frac{d_i}{r_j} + \frac{1}{\cos\tilde{\phi}}\left(\frac{\tilde{n}_i}{\tilde{r}_j} - \frac{n_i}{r_j}\right) \tag{A-14}$$

$$\frac{\tilde{d}_i}{\tilde{r}_j} = a\frac{d_i}{r_j} + b\frac{z_j}{r_j} + \frac{\sin\tilde{\phi}}{\cos\tilde{\phi}}\left(\frac{\tilde{n}_i}{\tilde{r}_j} - \frac{n_i}{r_j}\right), \tag{A-15}$$

where a and b are defined as:

$$\begin{aligned} a &= \frac{1 - \sin\phi\sin\tilde{\phi}}{\cos\phi\cos\tilde{\phi}} \\ b &= \frac{\sin\tilde{\phi} - \sin\phi}{\cos\phi\cos\tilde{\phi}}. \end{aligned}$$

Equation (A-7) follows directly from the equations (45) and (49) of [11]:

$$\tilde{g} = g \tag{A-16}$$

$$g = \frac{d_i - z_j\sin\phi}{r_j\cos\phi}. \tag{A-17}$$

To derive (A-6) we insert a and b in (A-14) and multiply with $\cos\tilde{\phi}$ to obtain:

$$\frac{\tilde{z}_j\cos\tilde{\phi}}{\tilde{r}_j} = \frac{z_j(1 - \sin\phi\sin\tilde{\phi}) + d_i(\sin\tilde{\phi} - \sin\phi)}{r\cos\phi} + \frac{\tilde{n}_i}{\tilde{r}_j} - \frac{n_i}{r_j}$$

which can be rewritten as:

$$\frac{\tilde{z}_j\cos\tilde{\phi}}{\tilde{r}_j} = \frac{z_j - d_i\sin\phi}{r_j\cos\phi} + \frac{\sin\tilde{\phi}(d_i - z_j\sin\phi)}{r_j\cos\phi} + \frac{\tilde{n}_i}{\tilde{r}_j} - \frac{n_i}{r_j}$$

Applying (A-7), the second term can be rewritten, yielding:

$$\frac{\tilde{z}_j\cos\tilde{\phi}}{\tilde{r}_j} = \frac{z_j - d_i\sin\phi}{r_j\cos\phi} + \frac{\tilde{d}_i\sin\tilde{\phi} - \tilde{z}_j\sin^2\tilde{\phi}}{\tilde{r}_j\cos\tilde{\phi}} + \frac{\tilde{n}_i}{\tilde{r}_j} - \frac{n_i}{r_j}$$

The left hand side of this expression is moved to the right hand side into the second term to obtain

$$\frac{z_j - d_i\sin\phi}{r_j\cos\phi} + \frac{\tilde{d}_i\sin\tilde{\phi} - \tilde{z}_j}{\tilde{r}_j\cos\tilde{\phi}} + \frac{\tilde{n}_i}{\tilde{r}_j} - \frac{n_i}{r_j} = 0,$$

which is identical to (A-6).

From (A-3) we can conclude that one aperture and one point source are sufficient to uniquely define ψ. To simplify the remaining equations, we precorrect the data for ψ by rotating the point source projections (u_{ij}, v_{ij}) over ψ:

$$u'_{ij} = u_{ij}\cos\psi + v_{ij}\sin\psi \quad \text{(A-18)}$$
$$v'_{ij} = -u_{ij}\sin\psi + v_{ij}\cos\psi \quad \text{(A-19)}$$

which yields

$$u'_{ij} = f_i\frac{m_i - r_j\cos\gamma}{N} + m_i + e'_u \quad \text{(A-20)}$$
$$v'_{ij} = f_i\frac{n_i - z_j\cos\phi - r_j\sin\gamma\sin\phi}{N} + n_i + e'_v \quad \text{(A-21)}$$

$$\text{with } e'_u = e_u\cos\psi + e_v\sin\psi$$
$$e'_v = -e_u\sin\psi + e_v\cos\psi.$$

This is equivalent to setting $\psi = 0$ and replacing (e_u, e_v) with rotated versions (e'_u, e'_v) in the original equations.

In the next section, the number of apertures is set to 2 ($I = 2$) in the above equations in order to investigate whether two point sources are sufficient for multipinhole SPECT calibration.

A.2 Two apertures, one point source

If we precorrect the data for ψ, as mentioned above, (A-3)-(A-13) turn into the following equations[1], where $i = 1, 2$ (two apertures) and j is omitted since only one point source is envisaged:

$$\tilde{\psi} = \psi \quad \text{(A-22)}$$
$$\tilde{f}_i = f_i\frac{\cos\tilde{\phi}}{\cos\phi} \quad \text{(A-23)}$$
$$\tilde{\alpha} = \alpha \quad \text{(A-24)}$$
$$\frac{\tilde{n}_i}{\tilde{r}} + \frac{\tilde{d}_i\sin\tilde{\phi} - \tilde{z}}{\tilde{r}\cos\tilde{\phi}} = \frac{n_i}{r} + \frac{d_i\sin\phi - z}{r\cos\phi} \quad \text{(A-25)}$$
$$\frac{\tilde{d}_i - \tilde{z}\sin\tilde{\phi}}{\tilde{r}\cos\tilde{\phi}} = \frac{d_i - z\sin\phi}{r\cos\phi} \quad \text{(A-26)}$$
$$\frac{\tilde{m}_i}{\tilde{r}} = \frac{m_i}{r} \quad \text{(A-27)}$$
$$\tilde{m}_i + \tilde{e}_u = m_i + e_u \quad \text{(A-28)}$$
$$\tilde{n}_i - n_i + \tilde{e}_v - e_v = f_i\frac{\sin\tilde{\phi} - \sin\phi}{\cos\phi} \quad \text{(A-29)}$$

$$f_i + d_i = R \text{ and } \tilde{f}_i + \tilde{d}_i = \tilde{R} \quad \text{(A-30)}$$

[1]Note that we reused the same notation for the electrical shifts, namely e_u and e_v instead of e'_u and e'_v, for notational simplicity.

Rewriting (A-27) and (A-28) as

$$\tilde{m}_i = \frac{\tilde{r}}{r} m_i \quad \text{and} \quad \tilde{m}_i = m_i + e_u - \tilde{e}_u, \tag{A-31}$$

yields

$$e_u - \tilde{e}_u = \left(\frac{\tilde{r}}{r} - 1\right) m_1 = \left(\frac{\tilde{r}}{r} - 1\right) m_2. \tag{A-32}$$

Consequently, if we require $m_1 \neq m_2$, we obtain

$$\tilde{r} = r \tag{A-33}$$
$$\tilde{e}_u = e_u \tag{A-34}$$
$$\tilde{m}_i = m_i. \tag{A-35}$$

Thus, the set of equations is reduced to

$$\tilde{f}_1 = f_1 \frac{\cos\tilde{\phi}}{\cos\phi} \tag{A-36}$$
$$\tilde{f}_2 = f_2 \frac{\cos\tilde{\phi}}{\cos\phi} \tag{A-37}$$
$$\frac{\tilde{d}_1 \sin\tilde{\phi} - \tilde{z}}{\cos\tilde{\phi}} = \frac{d_1 \sin\phi - z}{\cos\phi} \tag{A-38}$$
$$\tilde{n}_2 + \frac{\tilde{d}_2 \sin\tilde{\phi} - \tilde{z}}{\cos\tilde{\phi}} = n_2 + \frac{d_2 \sin\phi - z}{\cos\phi} \tag{A-39}$$
$$\frac{\tilde{d}_1 - \tilde{z}\sin\tilde{\phi}}{\cos\tilde{\phi}} = \frac{d_1 - z\sin\phi}{\cos\phi} \tag{A-40}$$
$$\frac{\tilde{d}_2 - \tilde{z}\sin\tilde{\phi}}{\cos\tilde{\phi}} = \frac{d_2 - z\sin\phi}{\cos\phi} \tag{A-41}$$
$$\tilde{e}_v = e_v + f_1 \frac{\sin\tilde{\phi} - \sin\phi}{\cos\phi} \tag{A-42}$$
$$\tilde{n}_2 + \tilde{e}_v = n_2 + e_v + f_2 \frac{\sin\tilde{\phi} - \sin\phi}{\cos\phi} \tag{A-43}$$
$$\tilde{d}_1 - \tilde{d}_2 = \tilde{f}_2 - \tilde{f}_1 \tag{A-44}$$

If we select an arbitrary value for $\tilde{\phi}$, then we have nine linear equations in the 7 unknowns $\tilde{e}_v, \tilde{z}, \tilde{d}_1, \tilde{d}_2, \tilde{f}_1, \tilde{f}_2$ and $\tilde{n}_2$. However, there are only 7 independent equations. Combining the difference between (A-37) and (A-36) and the difference between (A-41) and (A-40) yields (A-44), because $d_2 - d_1 = f_1 - f_2$. Similarly, the difference between (A-39) and (A-38) is identical to the difference between (A-43)

and (A-42). The remaining equations can be solved, so a solution can be found for any value of $\tilde{\phi}$. The solution is:

$$\tilde{f}_1 = f_1 \frac{\cos\tilde{\phi}}{\cos\phi} \tag{A-45}$$

$$\tilde{f}_2 = f_2 \frac{\cos\tilde{\phi}}{\cos\phi} \tag{A-46}$$

$$\tilde{e}_v = e_v + f_1 \frac{\sin\tilde{\phi} - \sin\phi}{\cos\phi} \tag{A-47}$$

$$\tilde{n}_2 = n_2 + (f_2 - f_1) \frac{\sin\tilde{\phi} - \sin\phi}{\cos\phi} \tag{A-48}$$

$$\tilde{d}_1 = \frac{d_1(1 - \sin\phi\sin\tilde{\phi}) + z(\sin\tilde{\phi} - \sin\phi)}{\cos\phi\cos\tilde{\phi}} \tag{A-49}$$

$$\tilde{z} = \tilde{d}_1 \sin\tilde{\phi} - \cos\tilde{\phi} \frac{d_1 \sin\phi - z}{\cos\phi} \tag{A-50}$$

$$\tilde{d}_2 = \tilde{d}_1 + \tilde{f}_1 - \tilde{f}_2. \tag{A-51}$$

Consequently, a SPECT-scan of a single point source is insufficient to uniquely determine the seven geometrical parameters of a dual aperture pinhole system.

A.3 Three or more apertures, one point source

Adding a pinhole aperture adds three independent equations with three additional variables $\tilde{f}_3, \tilde{d}_3$ and $\tilde{n}_3$. Hence, a single point source is insufficient for the calibration of a rotating multipinhole system.

A.4 Fixing the distance between the apertures

Usually, either the pinhole collimator is rigid, or it consists of an interchangeable pinhole plate. So, in most cases, the distance between the apertures is fixed. Thus, one could determine that distance once and for all, and fix it to the correct value in subsequent calibration parameter calculations. This yields the additional equation

$$(\tilde{f}_2 - \tilde{f}_1)^2 + (\tilde{m}_2 - \tilde{m}_1)^2 + \tilde{n}_2^2 = (f_2 - f_1)^2 + (m_2 - m_1)^2 + n_2^2. \tag{A-52}$$

Because of (A-35), this reduces to

$$(\tilde{f}_2 - \tilde{f}_1)^2 + \tilde{n}_2^2 = (f_2 - f_1)^2 + n_2^2. \tag{A-53}$$

Unfortunately, in many practical designs, the distance between the pinhole apertures and the detector will be the same for all apertures, implying that $f_1 = f_2$ and $\tilde{f}_1 = \tilde{f}_2$. In that case, the equation above is always satisfied because of (A-42) and (A-43). For these designs, the knowledge of the distance between the pinhole apertures is thus of no use.

A.5 Two pinhole apertures and two point sources

To investigate whether the addition of a second point source makes the solution to the calibration problem unique, the two equations (A-38) for the apertures 1 and 2 are combined, yielding

$$\frac{\tilde{z}_1 - \tilde{z}_2}{\cos\tilde{\phi}} = \frac{z_1 - z_2}{\cos\phi}. \tag{A-54}$$

In addition, the combination of the equations (A-40) for the two apertures yields

$$(\tilde{z}_1 - \tilde{z}_2)\frac{\sin\tilde{\phi}}{\cos\tilde{\phi}} = (z_1 - z_2)\frac{\sin\phi}{\cos\phi}. \tag{A-55}$$

If we choose the point sources such that $z_1 \neq z_2$, both equations can only be satisfied simultaneously if $\sin\tilde{\phi} = \sin\phi$. Inserting this into the other equations, one obtains that the two sets of geometric parameters are identical, hence two point sources without information about their distance to each other are required and sufficient to calibrate a rotating dual or multipinhole camera, provided that $r_j > 0$, $m_1 \neq m_2$ and $z_1 \neq z_2$.

Appendix B

Optimization weighted FBP for TOF PET

In this appendix, the derivation of the expression in the last row of table 8.1 is discussed in more detail. In equation (8.14) the factor $[\boldsymbol{A^T C_Y^{-1} A}]^{-1}$ represents a deblurring filter, $\boldsymbol{A^T\ C_Y^{-1}}$ is a weighted backprojection operator, and $\boldsymbol{A}e^j$ is the projection of a point source. To derive an FBP expression from this, we consider the central pixel j in a 2D Gaussian object (as in [128]):

$$\text{Gauss}_{\text{2D}}\{\sigma^2_{obj}\}(\vec{x}) = \frac{1}{2\pi\sigma^2_{obj}} \exp(\frac{-x^2-y^2}{2\sigma^2_{obj}}), \tag{A-1}$$

with $\vec{x} = (x, y)$ the location vector in the spatial domain. We first consider the operator $\boldsymbol{A^T C_Y^{-1} A}$ by analyzing step by step what it produces when applied to image e^j. $\boldsymbol{A}e^j$ is a TOF sinogram. It is independent of the angle, and zero everywhere except for the central line of response (LOR) at $l = 0$:

$$\boldsymbol{A}e^j(l, \tau, \theta) = \text{Gauss}_{\text{1D}}\{\sigma^2_{TOF}\}(\tau) \cdot \delta(l), \tag{A-2}$$

with l the LOR index, τ the TOF dimension, and θ the projection angle. $\boldsymbol{C_Y}$ is the covariance matrix of the phantom measurement. Because the measurement noise is Poisson distributed, $\boldsymbol{C_Y}$ is a diagonal matrix with the measurement in each sinogram pixel as its diagonal elements. We only need these elements for $l = 0$, so

$$\begin{aligned} \boldsymbol{C_Y}(0, \tau, \theta) &= Y(0, \tau, \theta) \\ &= \text{Gauss}_{\text{1D}}\{\sigma^2_{TOF} + \sigma^2_{obj}\}(\tau). \end{aligned} \tag{A-3}$$

Then

$$\boldsymbol{C_Y^{-1}} \boldsymbol{A}e^j(l, \tau, \theta) \propto \text{Gauss}_{\text{1D}}\{\sigma^2_{TOF}(1 + \frac{\sigma^2_{TOF}}{\sigma^2_{obj}})\}(\tau) \cdot \delta(l), \tag{A-4}$$

where the equal sign was dropped because a constant factor has been ignored.

$\boldsymbol{A^T}$ represents again a convolution with the TOF kernel, followed by a summation over all angles, such that

$$\begin{aligned} &\boldsymbol{A^T C_Y^{-1} A} e^j(\vec{x}) \qquad \text{(A-5)} \\ &\propto \sum_\theta \text{Gauss}_{1\text{D}}\{\sigma_{TOF}^2(2+\frac{\sigma_{TOF}^2}{\sigma_{obj}^2})\}(\vec{x}\cdot\hat{u})\cdot\delta(\vec{x}\cdot\hat{u}^\perp) \\ &\approx \frac{1}{|\vec{x}|}\text{Gauss}_{2\text{D}}\{\sigma_{TOF}^2(2+\frac{\sigma_{TOF}^2}{\sigma_{obj}^2})\}(\vec{x}). \end{aligned}$$

with $\hat{u}$ and $\hat{u}^\perp$ the 2D unit vectors in the projection direction at angle θ and the perpendicular direction, respectively. The last expression is an approximation based on the continuous case, with $|\vec{x}|$ denoting the vector norm. $[\boldsymbol{A^T C_Y^{-1} A}]^{-1}$ is the corresponding deblurring. Finally, $\boldsymbol{A^T\ C_Y^{-1}}$ is obtained by removing the smoothing of $\boldsymbol{A}$ in equation (A-5). Thus, the weighted backprojection of sinogram Y becomes

$$\boldsymbol{A^T C_Y^{-1}} Y \propto \sum_\theta \text{Gauss}_{1\text{D}}\{\sigma_{TOF}^2(1+\frac{\sigma_{TOF}^2}{\sigma_{obj}^2})\} \otimes Y \qquad \text{(A-6)}$$

Consequently, the "optimal" backprojection kernel for FBP reconstruction of a Gaussian object is a Gaussian kernel with $\sigma^2 = \sigma_{TOF}^2(1+\sigma_{TOF}^2/\sigma_{obj}^2)$. This same expression was proposed by Watson in [128], based on heuristic arguments. This FBP-kernel is only "optimal" in the sense that with this kernel, FBP is the best shift invariant approximation of a WLS reconstruction for the central pixel of a Gaussian object. The approximation is very good (but not perfect) for the central pixel, and worse for all others, because the WLS reconstruction would apply a different weighted backprojection and a different reconstruction filter for every pixel. These filters are the rows of $\boldsymbol{A^T\ C_Y^{-1}}$ and $[\boldsymbol{A^T C_Y^{-1} A}]^{-1}$, respectively. Moreover, any other object would yield a different backprojection weight, which in general is not rotationally symmetrical.